

# Light-Meson Spectroscopy with COMPASS

B. Ketzer<sup>a</sup>, B. Grube<sup>b</sup>, D. Ryabchikov<sup>c,b</sup>

<sup>a</sup>Universität Bonn, Helmholtz-Institut für Strahlen- und Kernphysik, 53115 Bonn, Germany

<sup>b</sup>Technische Universität München, Physik-Department, 85748 Garching, Germany

<sup>c</sup>State Scientific Center Institute for High Energy Physics of National Research Center “Kurchatov Institute”, 142281 Protvino, Russia

---

## Abstract

Despite decades of research, we still lack a detailed quantitative understanding of the way quantum chromodynamics (QCD) generates the spectrum of hadrons. Precise experimental studies of the hadron excitation spectrum and the dynamics of hadrons help to improve models and to test effective theories and lattice QCD simulations. In addition, QCD seems to allow hadrons beyond the three-quark and quark-antiquark configurations of the constituent-quark model. These so-called exotic hadrons contain additional constituent (anti)quarks or excited gluonic fields that contribute to the quantum numbers of the hadron. Hadron spectroscopy is currently one of the most active fields of research in hadron physics. The COMPASS experiment at the CERN SPS is studying the excitation spectrum of light mesons, which are composed of up, down, and strange quarks. The excited mesons are produced via the strong interaction, i.e. by Pomeron exchange, by scattering a 190 GeV/c pion beam off proton or nuclear targets. On heavy nuclear targets, in addition the electromagnetic interaction contributes in the form of quasi-real photon exchange at very low four-momentum transfer squared. COMPASS has performed the most comprehensive analyses to date of isovector resonances decaying into  $\eta\pi$ ,  $\eta'\pi$ , or  $\pi^-\pi^-\pi^+$  final states. In this review, we give a general and pedagogical introduction into scattering theory and the employed partial-wave analysis techniques. We also describe novel methods developed for the high-precision COMPASS data. The COMPASS results are summarized and compared to previous measurements. In addition, we discuss possible signals for exotic mesons and conclude that COMPASS data provide solid evidence for the existence of the manifestly exotic  $\pi_1(1600)$ , which has quantum numbers forbidden for a quark-model state, and of the  $a_1(1420)$ , which does not fit into the quark-model spectrum. By isolating the contributions from quasi-real photon exchange, COMPASS has measured the radiative widths of the  $a_2(1320)$  and, for the first time, that of the  $\pi_2(1670)$  and has tested predictions of chiral perturbation theory for the process  $\pi^- + \gamma \rightarrow \pi^-\pi^-\pi^+$ .

*Keywords:* light-meson spectroscopy, exotic mesons, hybrid mesons, partial-wave analysis, isobar model, diffractive dissociation, quasi-real photoproduction, chiral dynamics

*PACS:* 11.80.Et, 11.80.Gw, 12.38.Qk, 12.39.Mk, 13.25.Jx, 13.60.Le, 13.85.Hd, 14.40.Be, 14.40.Rt, 25.20.Lj

---

(Submitted to *Progress in Particle and Nuclear Physics*)

## Contents

<b>1</b>	<b>Introduction</b>	<b>5</b>
----------	---------------------	----------

---

*Email addresses:* [bernhard.ketzer@uni-bonn.de](mailto:bernhard.ketzer@uni-bonn.de) (B. Ketzer), [bgrube@tum.de](mailto:bgrube@tum.de) (B. Grube), [dmitry.ryabchikov@ihep.ru](mailto:dmitry.ryabchikov@ihep.ru) (D. Ryabchikov)

<b>2 Phenomenology of Mesons</b>	<b>10</b>
2.1 The Quark Model . . . . .	10
2.1.1 Quantum Numbers of Mesons . . . . .	10
2.1.2 The Meson Spectrum . . . . .	13
2.2 Regge Trajectories . . . . .	15
2.3 Exotic Mesons . . . . .	17
2.4 Lattice QCD . . . . .	18
<b>3 Strong Interactions</b>	<b>21</b>
3.1 Scattering Theory . . . . .	21
3.1.1 $S$ -Matrix . . . . .	21
3.1.2 Kinematics of Two-Body Reactions . . . . .	24
3.1.3 Cross Sections . . . . .	25
3.1.4 Partial-Wave Expansion and Breit-Wigner Resonances . . . . .	27
3.1.5 Analytic Structure of the Amplitude . . . . .	31
3.1.6 Discontinuities . . . . .	34
3.1.7 $K$ -Matrix . . . . .	35
3.1.8 Dispersion Relations . . . . .	35
3.1.9 $N$ -over- $D$ Method . . . . .	37
3.1.10 Final-State Interactions . . . . .	37
3.2 Regge Theory . . . . .	38
3.2.1 Motivation . . . . .	38
3.2.2 Regge Poles and Particles . . . . .	41
3.2.3 Differential and Total Cross Section . . . . .	42
3.3 Duality in Hadron Interactions . . . . .	44
3.4 Chiral Perturbation Theory . . . . .	44
<b>4 Experimental Methods</b>	<b>46</b>
4.1 Production of Excited Light Mesons at COMPASS . . . . .	46
4.2 The COMPASS Experiment . . . . .	49
4.2.1 Setup for Hadron Beams . . . . .	49
4.2.2 Beam Line . . . . .	51
4.2.3 Target Region . . . . .	51
4.2.4 Large-Angle Spectrometer . . . . .	53
4.2.5 Small-Angle Spectrometer . . . . .	56
4.2.6 Trigger and Data Acquisition . . . . .	56
4.2.7 Event Reconstruction . . . . .	57
4.2.8 Offline Event Selection . . . . .	58
<b>5 Partial-Wave Analysis Formalism</b>	<b>61</b>
5.1 Analysis Model . . . . .	61
5.1.1 Ansatz . . . . .	61
5.1.2 Decay Amplitude . . . . .	62
5.1.3 Parameterization of Propagator Terms . . . . .	65
5.1.4 Coordinate Systems . . . . .	66
5.1.5 Examples for Decay Amplitudes . . . . .	67
5.1.6 Symmetrization of the Decay Amplitudes . . . . .	68
5.1.7 Extension of the Model to Several Intermediate States . . . . .	68
5.2 Stage I: Partial-Wave Decomposition in Kinematic Cells . . . . .	71
5.2.1 Incoherent Background Contributions . . . . .	72
5.2.2 Spin-Density Matrix and Rank . . . . .	72
5.2.3 Parity Conservation and Reflectivity . . . . .	73

5.2.4	Normalization . . . . .	76
5.2.5	Unbinned Extended Maximum Likelihood Fit . . . . .	78
5.2.6	Observables . . . . .	81
5.2.7	Comparison of Partial-Wave Analysis Model and Data . . . . .	82
5.2.8	Discussion of the Partial-Wave Analysis Method . . . . .	83
5.2.9	Freed-Isobar Partial-Wave Analysis . . . . .	87
5.3	Stage II: Resonance-Model Fit of Spin-Density Matrix . . . . .	89
5.3.1	Resonance Model . . . . .	90
5.3.2	$t'$ -Dependent Observables . . . . .	93
5.3.3	Fit Method . . . . .	95
5.3.4	Discussion of the Resonance Model . . . . .	96
5.3.5	Analytical Unitary Model . . . . .	97
<b>6</b>	<b>Results from Pion-Difraction Data</b>	<b>100</b>
6.1	COMPASS Data Samples . . . . .	100
6.1.1	The $\eta\pi^-$ and $\eta'\pi^-$ Data Samples . . . . .	100
6.1.2	The $\pi^-\pi^-\pi^+$ Data Samples . . . . .	101
6.2	Analysis Models . . . . .	101
6.2.1	$\eta^{(\prime)}\pi^-$ Partial-Wave Decomposition . . . . .	102
6.2.2	$\eta^{(\prime)}\pi^-$ Resonance-Model Fits . . . . .	105
6.2.3	$\pi^-\pi^-\pi^+$ Partial-Wave Decomposition . . . . .	106
6.2.4	$\pi^-\pi^-\pi^+$ Resonance-Model Fits . . . . .	109
6.3	Results . . . . .	112
6.3.1	The $J^{PC} = 0^{-+}$ Sector . . . . .	112
6.3.2	The $J^{PC} = 1^{++}$ Sector . . . . .	116
6.3.3	The $J^{PC} = 1^{-+}$ Sector . . . . .	122
6.3.4	The $J^{PC} = 2^{++}$ Sector . . . . .	129
6.3.5	The $J^{PC} = 2^{-+}$ Sector . . . . .	133
6.3.6	The $J^{PC} = 4^{++}$ Sector . . . . .	138
<b>7</b>	<b>Primakoff Production of <math>\pi^-\pi^-\pi^+</math></b>	<b>143</b>
7.1	Extraction of Primakoff Process via $t'$ Spectrum . . . . .	144
7.2	Model for Partial-Wave Decomposition in the Primakoff Kinematical Region . . . . .	146
7.3	Results for $a_2(1320)$ and $\pi_2(1670)$ from Partial-Wave Decomposition . . . . .	149
7.4	Radiative Widths of $a_2(1320)$ and $\pi_2(1670)$ . . . . .	151
7.5	Test of Chiral Perturbation Theory . . . . .	154
<b>8</b>	<b>Conclusions and Outlook</b>	<b>156</b>
<b>Acknowledgments</b>		<b>160</b>
<b>Appendices</b>		<b>161</b>
<b>A</b>	<b><math>n</math>-Body Phase-Space Element</b>	<b>161</b>
<b>B</b>	<b>Wigner <math>D</math>-Function</b>	<b>161</b>
<b>C</b>	<b>Angular Distribution for Two-Body Decay</b>	<b>162</b>
<b>D</b>	<b>List of Angular-Momentum Barrier Factors</b>	<b>163</b>
<b>E</b>	<b>Chung-Trueman Parameterization of the Spin-Density Matrix</b>	<b>163</b>

<b>F</b> Maximization of the Likelihood Function and Uncertainty Estimation	<b>164</b>
<b>G</b> Numerical Calculation of Integral Matrices	<b>165</b>
<b>H</b> Additional Observables	<b>166</b>
<b>I</b> Resonance Parameters of $a_J$ and $\pi_J$ Mesons	<b>167</b>
<b>J</b> Effect of $\phi_{GJ}$ Smearing on the Partial-Wave Decomposition of $\pi^-\pi^-\pi^+$	<b>167</b>
References	169

## 1. Introduction

The understanding of the fundamental building blocks of matter has been a long-standing quest of mankind. According to the Greek philosopher Empedocles (around 500 B.C.), the universe is composed of Air, Fire, Water, and Earth. It was Democritus (460 to 371 B.C.) who had the vision of fundamental indivisible constituents [1]:

By convention [there is] sweet and by convention [there is] bitter,  
by convention [there is] hot, by convention [there is] cold, by convention [there is] color;  
but in reality [there are only] atoms<sup>1</sup> and void.

In: SEXTUS EMPIRICUS  
*Against the Mathematicians VII.135.*

It took more than 2000 years before in the 19th century Mendeleev and Meyer noticed patterns in the chemical properties of the chemical elements, indicating an underlying symmetry and hinting at atoms as the basic constituents of chemical elements.

This strategy was later to be repeated to find even more fundamental building blocks of matter. In the 20th century, scattering experiments with momentum transfers large enough to probe the internal structure of the colliding objects subsequently revealed the substructure of atoms, which are systems of negatively charged electrons and a positively charged nucleus bound together by the electromagnetic force, and that of atomic nuclei, which are composed of protons and neutrons held together by the nuclear or strong force. In addition to protons and neutrons, a large number of other strongly interacting particles, both with half-integer spin (called baryons<sup>2</sup>) and integer spin (called mesons<sup>3</sup>), was observed in experiments with cosmic rays and later at particle accelerators. The lightest member of the meson family is the pion, which was discovered by Powell in 1947. The kaon, the lightest particle containing strange quarks, was observed by Rochester and Butler in 1947. Many heavier mesons and baryons followed, suggesting that pions, protons and neutrons (i.e. nucleons) were merely the lightest members of a large family of strongly interacting particles. Most of the heavier species of mesons and baryons are extremely unstable and decay after a very short time of the order of  $10^{-24}$  s. Today, more than 200 mesons and more than 100 baryons have been identified [5].

As for the chemical elements, such a proliferation of particles called for a systematic order in the zoo of hadrons. Sorting the then-known baryons and mesons by their quantum numbers strong isospin and strangeness, which are known to be conserved in strong interactions,<sup>4</sup> hinted towards a further substructure of these strongly interacting particles. In the 1960s, Gell-Mann and Zweig suggested that hadrons could be made of more elementary objects called quarks. Three types or flavors of quarks, up (u), down (d), strange (s), carrying different charge, isospin, and strangeness were required to explain the quantum numbers of the observed hadrons. What started out merely as a mathematical tool, soon turned out to become reality, when electron-scattering experiments at SLAC began to show that protons did indeed contain point-like constituents, called partons by Feynman. In the 1970s, experiments colliding high-energy electrons with their antiparticles, positrons, revealed the existence of heavier types of quarks, carrying new quantum numbers called charm and bottomness (or beauty). In 1999, the sixth and heaviest quark, called top, was observed at Fermilab.

According to our present-day understanding, matter is composed of fundamental point-like fermions, i.e. particles with spin  $\hbar/2$ , which are summarized in Table 1. While the quarks experience the strong

<sup>1</sup>From Ancient Greek ἄτομος meaning indivisible.

<sup>2</sup>The term baryon was coined by A. Pais [2] and was derived from the Greek word “βαρύς” for heavy, because at that time most known particles that were considered elementary had lower masses than the baryons.

<sup>3</sup>Originally, C. D. Anderson and S. H. Neddermeyer proposed the term “mesotron” [3] that was derived from the Greek word “μέσος” for intermediate for particles with masses between that of the electron and the proton. The term was later changed to meson [4].

<sup>4</sup>The strong isospin characterizes the approximate symmetry of the strong interaction between proton and neutrons, or u and d quarks, which is explicitly broken by the small mass difference between u and d. In the rest of the paper, the term “isospin” always refers to the strong isospin.

Table 1: Fundamental fermions with quantum numbers  $Q$  (charge),  $I$  (strong isospin),  $I_3$  ( $z$ -component of strong isospin),  $S$  (strangeness),  $C$  (charm),  $B$  (beauty or bottomness),  $T$  (topness), strong  $Y$  (hypercharge). Except for  $I$ , which follows the standard quantum mechanics rules for addition of angular momenta, all other quantum numbers are additive. The masses given for the quarks are so-called current masses and are determined in the  $\overline{\text{MS}}$  renormalization scheme at a scale of 2 GeV [6]. The mass values for electron and muon are rounded. For the precise values of the lepton masses and their uncertainties see [5].

Fermion	Mass [MeV/ $c^2$ ]	$Q$ [ $e$ ]	$I$	$I_3$	$S$	$C$	$B$	$T$	$Y$	Generation
$e^-$	0.511		-1	0	0	0	0	0	0	I
$\nu_e$			0	0	0	0	0	0	0	
$\mu^-$	105.658		-1	0	0	0	0	0	0	II
$\nu_\mu$			0	0	0	0	0	0	0	
$\tau^-$	1776.86		-1	0	0	0	0	0	0	III
$\nu_\tau$			0	0	0	0	0	0	0	
u	$2.16^{+0.49}_{-0.26}$	$+\frac{1}{3}$	$\frac{1}{2}$	$+\frac{1}{2}$	0	0	0	0	$\frac{1}{3}$	I
d	$4.67^{+0.48}_{-0.17}$	$-\frac{2}{3}$	$\frac{1}{2}$	$-\frac{1}{2}$	0	0	0	0	$\frac{1}{3}$	
c	$(1.27 \pm 0.02) \cdot 10^3$	$+\frac{1}{3}$	0	0	0	1	0	0	0	II
s	$93^{+11}_{-5}$	$-\frac{2}{3}$	0	0	-1	0	0	0	$-\frac{2}{3}$	
t	$(172.9 \pm 0.4) \cdot 10^3$	$+\frac{1}{3}$	0	0	0	0	0	1	0	III
b	$(4.18^{+0.03}_{-0.02}) \cdot 10^3$	$-\frac{2}{3}$	0	0	0	0	-1	0	0	

force, the leptons do not. The stable matter around us is entirely composed of fermions of the first generation, i.e. electrons and up and down quarks. The heavier fermions can be produced in high-energy particle collisions at accelerators or in cosmic-ray interactions. While the masses of the charged leptons can be measured directly, the masses of the quarks need to be determined indirectly, since they are confined inside hadrons and never appear as isolated particles (see below). The quark masses given in Table 1 are so-called current masses, which are the mass values of the bare quarks appearing in the QCD Lagrangian [6]. They are determined by comparing measured hadron properties with calculations, e.g. using Lattice QCD (see Section 2.4) or chiral perturbation theory (see Section 3.4) for the case of light quarks. In order to render the physical quantities calculated from the theory finite, a renormalization scheme needs to be applied, which requires the introduction of a scale parameter  $\mu$ . The most commonly applied scheme in QCD perturbation theory is the  $\overline{\text{MS}}$  scheme and a typical scale is  $\mu = 2 \text{ GeV}$ .

In the standard model of particle physics, the lepton number, i.e. the number of leptons minus the number of antileptons,  $N_l - N_{\bar{l}}$ , is a strictly conserved quantity. Similarly, the baryon number  $\mathcal{B}$  is strictly conserved. Quarks are assigned  $\mathcal{B} = +1/3$ , antiquarks  $\mathcal{B} = -1/3$ , while leptons have  $\mathcal{B} = 0$ . By convention, the non-zero flavor quantum number of a quark ( $I_3$ ,  $S$ ,  $C$ ,  $B$ , or  $T$ ) carries the same sign as its charge<sup>5</sup>. The generalized Gell-Mann–Nishijima formula relates the charge (in units of the elementary charge  $e$ ) to the other additive quantum numbers of the quarks,

$$Q = I_3 + \frac{\mathcal{B} + S + C + B + T}{2} . \quad (1)$$

Flavor quantum numbers are conserved in strong interactions, which is reflected in the conservation

<sup>5</sup>We use sans serif fonts for the flavor quantum numbers  $S$ ,  $C$ ,  $B$ , and  $T$  in order to distinguish them from quantities introduced later, e.g. the charge-conjugation parity  $C$ .

of the strong hypercharge  $Y$ ,<sup>6</sup> defined as

$$Y = \mathcal{B} + \mathcal{S} - \frac{\mathcal{C}}{3} + \frac{\mathcal{B}}{3} - \frac{\mathcal{T}}{3}. \quad (2)$$

In quantum field theory, the interactions between fermions are described by the exchange of virtual particles of rest mass  $m$ , so-called gauge bosons. The exchanged particle is assigned a 4-momentum  $q$ , which is the difference between the 4-momenta of the particles entering and leaving the interaction vertex. Since in general  $q^2 \neq m^2$  for virtual particles, they are commonly referred to as “not being on their mass shell”, which means that they do not obey the relativistic relation between energy  $E$ , rest mass  $m$ , and three-momentum  $\mathbf{p}$ ,

$$E^2 = m^2 + \mathbf{p}^2 \quad (3)$$

between energy  $E$ , rest mass  $m$ , and momentum  $p$ .<sup>7</sup> The virtual particles couple to a conserved property generally called charge. The electromagnetic interaction between particles carrying electric charge, for example, is described in Quantum Electrodynamics (QED) by the exchange of virtual photons, massless electrically neutral spin-1 particles. The range of the force is given by the Compton wavelength of the virtual particle:

$$\lambda = \frac{1}{m}. \quad (4)$$

Yukawa postulated that the short-range interaction between nucleons is due to the exchange of massive integer-spin particles, which he identified as pions.

In Quantum Chromodynamics (QCD), the field theory of strong interaction, the interaction between quarks is mediated by the exchange of massless spin-1 particles called gluons, which couple to the strong charge or color. There are three different strong charges, or colors, termed red, green, and blue. In contrast to photons, however, the gluons also carry charge, i.e. color, themselves and hence can also couple to themselves.<sup>8</sup> It is this self-interaction of the gluons which generates a wealth of new phenomena for strongly interacting particles, the two most important being confinement and asymptotic freedom of quarks, which will be explained in the following. At large momentum transfers, corresponding to distance scales much smaller than the size of a nucleon of about 1 fm, the quarks inside hadrons behave essentially as free particles. This asymptotic freedom allows the interaction to be treated perturbatively with a small coupling parameter  $\alpha_s$  as series expansion parameter. It is in this regime, where predictions from QCD have been verified to very high precision. For larger distance scales approaching  $\mathcal{O}(1 \text{ fm})$ , the cloud of virtual gluons and  $q\bar{q}$  pairs around quarks modifies their effective strong charge, similarly to the screening of the electric charge by the cloud of virtual photons fluctuating into  $e^+e^-$  pairs. Due to the self-interaction of gluons, however, there is an anti-screening of the strong charge, leading to an increased coupling strength at larger distances. This can be modeled by a potential between stationary quarks that consists of a Coulomb-like term for small distances  $r$  and increases linearly for larger distances, i.e.

$$V(r) = -\frac{4}{3} \frac{\alpha_s}{r} + k r, \quad (5)$$

resembling a string with a constant string tension  $k$  (see Section 2.2). With increasing distance, the energy density stored in the string becomes high enough to create a new quark-antiquark pair from the vacuum. As a consequence, free quarks are not observed in nature.<sup>9</sup> It is one of the major questions of modern physics, how this phenomenon of confinement emerges from the underlying theory of QCD.

---

<sup>6</sup>There are different definitions of the hypercharge, e.g.  $Y = \mathcal{B} + \mathcal{S} \pm \mathcal{C} + \mathcal{B} \pm \mathcal{T}$ , such that all quarks have fractional  $Y$ , which causes the hypercharge of all hadrons to be integer. Our definition follows [7], which defines  $Y$  in  $\text{SU}(3)_{\text{flavor}}$  from the generator  $\lambda_8$ , i.e.  $Y = 1/\sqrt{3}\lambda_8$ . This definition centers the weight diagrams for  $\text{SU}(4)_{\text{flavor}}$  around zero also for  $\mathcal{C} \neq 0$ .

<sup>7</sup>Unless explicitly stated, we use natural units, i.e.  $\hbar = c = 1$ .

<sup>8</sup>This is sometimes referred to as Yang-Mills theory, a gauge theory with non-Abelian symmetry.

<sup>9</sup>By the same argument, there are also no free gluons. As the quarks, they are confined into hadrons. Hence the range of the strong interaction is limited to  $\mathcal{O}(1 \text{ fm})$  although the gluons are massless, i.e. Eq. (4) does not apply.

In order to account for confinement, hadrons are postulated to be color-neutral objects, or, more precisely, color-singlets, which are invariant under rotations in color space. The simplest possible configurations to obtain color-neutral objects are combinations of three quarks of different color each, or of a quark and an antiquark of a given color and the corresponding anti-color (or complementary color). Experiments on deep-inelastic scattering of leptons ( $e^-$ ,  $\mu$ , or  $\nu$ ) off protons and neutrons established that the nucleon is a complicated dynamic system composed of three valence quarks, which account for the quantum numbers of the nucleon, and an infinite sea of virtual quarks, antiquarks, and gluons. Almost 50% of the total momentum of the nucleon is carried by the gluons and only about 30% of the spin 1/2 of the nucleon is carried by the quarks [8]. While the hard scattering processes between the lepton and the quark can be precisely calculated in QCD, the parton distribution functions (PDF), that describe the momentum and spin degrees of freedom of quarks and gluons inside the nucleon, cannot be calculated from first principles. The large effective coupling at distance scales  $\mathcal{O}(1\text{ fm})$  corresponding to hadrons makes it impossible to solve QCD in this regime by a series expansion in the effective coupling parameter. While a wealth of experimental data and phenomenological models on PDFs is available for nucleons, very little is known about the quark and gluon structure of the lightest mesons.

Similarly, the excitation spectrum of strongly interacting particles is still far from being understood, despite a 50-year long history of world-wide experimental and theoretical efforts. Various models and effective theories have been developed to describe composite systems of quarks and gluons and their complex excitation spectrum. Despite its conceptual simplicity, neglecting the afore-mentioned dynamic internal structure, the constituent-quark model, which is discussed in more detail in Section 2.1, can explain many properties of observed hadrons. Based on the concept of flavor symmetry, mesons are described in the quark model as bound states of an effective quark-antiquark system, while baryons are composed of three effective quarks. QCD, however, allows for a much larger variety of color-singlet bound systems, including multi-quark states, molecule-like systems, or, owing to the fact that also gluons carry the charge of the strong interaction, systems where gluons explicitly contribute to the quantum numbers of the hadronic state. It is one of the most important questions in present-day hadronic physics whether such states exist or not.

Recently, precise ab-initio calculations of the properties of ground-state baryons and mesons were performed by solving QCD on a discrete space-time lattice (lattice QCD) (see e.g. Ref. [9] for a review). First qualitative results have been obtained for excited states. It is still a long way, however, until lattice QCD will yield precision calculations for excited states decaying into multi-particle final states.

On the experimental side, a plethora of excited hadronic states has been observed at proton and electron accelerators. Only in the last 15 years with the advent of high-intensity particle beams, modern particle detectors, and readout technology, it became possible to collect sufficiently large data samples both in the light and heavy-quark sectors to achieve the statistical precision to observe first signs of states not fitting into the  $q\bar{q}$  or  $qqq$  model of mesons and baryons. At the same time, many states predicted by the quark model are still unobserved or need confirmation. The COMPASS experiment is one of the key-players in the light-quark sector. This review will summarize the current status of results from this experiment and put them into perspective with respect to the ultimate goal of explaining the structure of hadrons in terms of quarks and gluons, the fundamental building blocks of Quantum Chromodynamics.

The paper is structured as follows: After an introduction into the strong interaction and its embedding in the Standard Model of particle physics in Section 1, we review the phenomenology of mesons in Section 2. Starting from the quark model and the concept of flavor symmetry, we discuss the expected multiplet structure of mesons and the excitation spectrum of light mesons and confront it with experimental results. The experimentally observed approximate linear relation (“Regge trajectories”) between spin and mass-squared of mesons is shown to arise from a simple string model. Finally, we define the notion of exotic mesons, and show how lattice QCD may contribute to resolving some of the open questions. Section 3 gives a general and pedagogical overview over some of the theoretical concepts employed to analyze scattering experiments using the  $S$ -matrix approach. We

discuss the kinematics for general two-body reactions and introduce the partial-wave expansion for spinless particles. Resonances are introduced both in the Breit-Wigner approximation and as poles of the analytic  $S$ -matrix in the complex plane. The consequences of unitarity of the  $S$ -matrix are discussed. Models which satisfy unitarity of the partial-wave amplitudes, like the  $K$ -matrix or the  $N$ -over- $D$  method are briefly introduced. The consequences of unitarity on production reactions and final-state interactions are discussed. We continue by explaining some of the important concepts underlying Regge theory, which lead to an asymptotic description of scattering processes at high energies. The section ends with a brief discussion of chiral perturbation theory, which is the low-energy limit of QCD. Section 4.1 describes the dominant reaction mechanisms in the COMPASS kinematic domain, i.e. at high energies of the incoming particle beam, before Section 4 introduces the COMPASS experimental apparatus used for hadron spectroscopy. Based on the more general account in Section 3, Section 5 provides a detailed derivation of the partial-wave analysis (PWA) formalism used to decompose the measured data into partial-wave amplitudes with a given spin-parity assignment. Special attention is paid to new developments which are expected to reduce the model-dependence of the analysis, like the freed-isobar PWA (Section 5.2.9), or help to better constrain the fit by fulfilling some of the fundamental properties of the  $S$ -matrix (Section 5.3.5). In Section 6 we finally present the most important results from the analysis of diffractive dissociation reactions, while in Section 7 we discuss the results from Primakoff reactions. The review closes with conclusions and an outlook in Section 8. In several appendices we provide more detailed mathematical formulae, which are useful for PWA practitioners.

## 2. Phenomenology of Mesons

In the following section, we review some phenomenological aspects of mesons. The quark model by Gell-Mann and Zweig explains the multiplet structure of observed mesons when classified by total spin, isospin and strong hypercharge, by identifying them as composite objects of a quark and an antiquark (see Section 2.1.1). The excitation spectrum can be calculated in the quark model by parameterizing the quark-antiquark interaction by effective Hamiltonians, which include a Coulomb-like attractive potential that dominates at small separations, and a linearly increasing potential that dominates for larger distances. We confront a recent relativistic quark-model calculation with present-day experimental data (see Section 2.1.2). A linear confining potential between more fundamental constituents is also needed to explain the approximate linear relation between the total spin and the squared mass for certain groups of mesons (“Regge trajectories”), which had been noticed even before the advent of the quark model in the early 1960s. A simple model of a rotating string first proposed by Nambu is presented as illustration in Section 2.2. Regge theory, which will be summarized in Section 3.2, links the observed trajectories to the forces between quarks and to the high-energy behavior of the scattering amplitude. Regge trajectories can help to assign experimentally observed resonances to states predicted by quark models. States not fitting the model predictions are generally termed exotic. We discuss candidates for light exotic states (see Section 2.3) and show that lattice QCD, providing hints towards the structure of the meson spectrum from first principles, also predicts the existence of a group of exotic states called hybrids (see Section 2.4).

### 2.1. The Quark Model

In general, the term quark model refers to a class of models, which describe the properties of hadrons by effective degrees of freedom carried by valence quarks. For baryons, the number of valence quarks is given by the net number of quarks of a given flavor,  $N_q - N_{\bar{q}}$ . As their counterparts, the valence electrons in atoms, valence quarks determine the quantum numbers, the excitation spectrum, and the interactions of hadrons. While the quark structure and the quantum numbers of hadrons in quark models are determined based on symmetry considerations and static quark content, the determination of the excitation spectrum, i.e. the masses and widths of states, requires the inclusion of the dynamics of the interaction, usually based on effective Hamiltonians.

#### 2.1.1. Quantum Numbers of Mesons

All additive quantum numbers mentioned in Table 1 also apply to bound systems of quarks. Mesons carry baryon number  $\mathcal{B} = 0$ , i.e. in their simplest form they are composed of a quark and an antiquark of the same (flavorless<sup>10</sup> or hidden-flavor mesons) or a different flavor (open flavor mesons). Containing only additive quantum numbers, both the Gell-Mann–Nishijima formula Eq. (1) and the hypercharge Eq. (2) apply to individual quarks as well as bound systems of quarks. In addition to the baryon number and the flavor quantum numbers, mesons are characterized by the quantum numbers  $J^{PC}$ <sup>11</sup>, with the total angular momentum  $J = 0, 1, 2, \dots$ , and the parity  $P = \pm 1$ , specifying the symmetry of the wave function under reflection through a point in space. Neutral flavorless mesons are eigenstates of the particle-antiparticle conjugation operator and thus have a defined charge conjugation parity  $C = \pm 1$ . The concept of  $C$ -parity can be extended to include the charged combinations  $u\bar{d}$  and  $d\bar{u}$  by introducing the the  $G$  parity, defined as charge conjugation followed by a  $180^\circ$  rotation in isospin space about the  $y$  axis. Flavored mesons have one or two of the quantum numbers strangeness  $S$ , charm  $C$ , or bottomness  $B$  different from zero. All the quantum numbers mentioned above are conserved in strong interactions.

Light mesons, as well as light baryons, with a given  $J^P$  can be classified in multiplets according to their isospin and hypercharge, or, equivalently, the strangeness  $S$  (see Eq. (2)). Figures 1a and 1b

---

<sup>10</sup>Here,  $u$  and  $d$  are considered the same flavor because of isospin symmetry.

<sup>11</sup>They are related to the Poincaré symmetry of relativistic field theories.

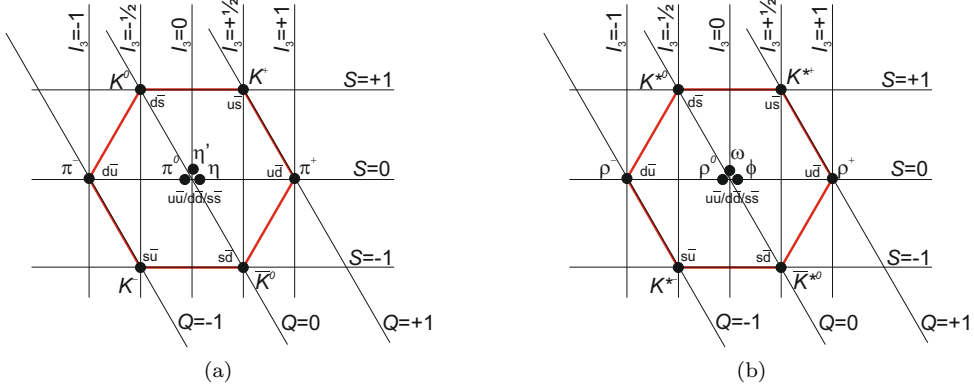


Figure 1: Nonets of ground-state (a) pseudoscalar, (b) vector mesons, classified by the  $z$  component of the strong isospin  $I_3$  and the strangeness  $S$ .

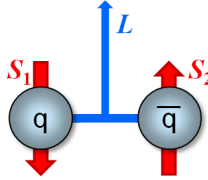


Figure 2: A meson in the quark model.

show the corresponding nonets of the lightest pseudoscalar ( $J^P = 0^-$ ) and vector ( $J^P = 1^-$ ) mesons, respectively. This systematics is explained in the quark model of Gell-Mann [10] and Zweig [11] by extending the  $SU(2)_{\text{iso}}$  symmetry group of the strong isospin to  $SU(3)_{\text{flavor}}$ , with the triplet ( $u, d, s$ ) of light quarks being the fundamental representation, and combining it with the symmetry groups  $SU(2)_{\text{spin}}$  for spin and  $SO(3)_{\text{orb}}$  for orbital angular momentum between the quarks:

$$SU(3)_{\text{flavor}} \otimes SU(2)_{\text{spin}} \otimes SO(3)_{\text{orb}}. \quad (6)$$

The flavor symmetry is of course only approximate, since  $m_s > m_{u,d}$ . In the quark model, mesons are described as bound states of a quark  $q$  and an antiquark  $\bar{q}'$ , while baryons are composed of three quarks, both forming singlets in color space  $SU(3)_{\text{color}}$ .

In the  $L$ - $S$  coupling scheme,<sup>12</sup> the spins of the  $q\bar{q}'$  pair couple to the total intrinsic spin  $S = 0, 1$ . The total spin  $J$  of the system is the vector sum of the total intrinsic spin  $S$  and the relative orbital angular momentum  $L$  with quantum number  $|L - S| \leq J \leq (L + S)$  (cf. Fig. 2).

The meson nonets for a given  $J^P$  combination are obtained by combining the  $SU(3)_{\text{flavor}}$  quark triplet with the antiquark triplet, resulting in nine possible combinations, transforming like an octet and a singlet in  $SU(3)_{\text{flavor}}$  space:

$$3 \otimes \bar{3} = 8 \oplus 1, \quad (7)$$

where the dimensions of the multiplets are used to label their irreducible representations. The flavor wave functions of the isoscalar (i.e.  $I = 0$ ) flavor singlet and octet combinations are

$$\psi_1 = \sqrt{\frac{1}{3}} (u\bar{u} + d\bar{d} + s\bar{s}) \quad \text{and} \quad \psi_8 = \sqrt{\frac{1}{6}} (u\bar{u} + d\bar{d} - 2s\bar{s}), \quad (8)$$

<sup>12</sup>The  $L$ - $S$  coupling scheme is a good basis to characterize systems consisting of only light or heavy quarks. For heavy-light systems  $Q\bar{q}$ , heavy-quark symmetry implies that in the limit  $m_Q \rightarrow \infty$  the spin of the heavy quark and the total angular momentum  $j$  of the light quark are separately conserved [12, 13], corresponding to the  $j$ - $j$  coupling scheme in atomic physics.

respectively. The flavor wave functions of the isovector (i.e.  $I = 1$ ) triplet are<sup>13</sup>

$$\left( d\bar{u}, \sqrt{\frac{1}{2}} (u\bar{u} - d\bar{d}), -u\bar{d} \right). \quad (9)$$

The states with open strangeness are  $d\bar{s}$ ,  $u\bar{s}$ ,  $s\bar{u}$ , and  $s\bar{d}$ . The  $SU(3)_{\text{flavor}}$  singlet and octet states with  $I = 0$  generally mix to produce the physical mesons  $A$  and  $B$ , i.e.

$$\begin{pmatrix} A \\ B \end{pmatrix} = \begin{pmatrix} \cos\theta & -\sin\theta \\ \sin\theta & \cos\theta \end{pmatrix} \begin{pmatrix} \psi_1 \\ \psi_8 \end{pmatrix}, \quad (10)$$

with a mixing angle  $\theta_P$  between  $-10^\circ$  and  $-20^\circ$  for the pseudoscalar ground states  $A = \eta$  and  $B = \eta'$ , and  $\theta_V = 36.4^\circ$  for the vector ground states  $A = \omega$  and  $B = \phi$  [7]. The latter is close to ideal mixing, such that  $\phi \approx s\bar{s}$ .

Introducing the heavier charm quark into the model extends the symmetry by one dimension to  $SU(4)_{\text{flavor}}$ , which, however, is strongly broken due to the much heavier  $c$  quark.

In the quark model, the quantum numbers  $P$ ,  $C$ , and  $G$  of the mesons are given by

$$P = (-1)^{L+1}, \quad C = (-1)^{L+S}, \quad \text{and} \quad G = (-1)^{L+S+I}. \quad (11)$$

This gives rise to meson states with quantum numbers

$$J^{PC} = 0^{-+}, 0^{++}, 1^{--}, 1^{+-}, 1^{++}, 2^{--}, 2^{-+}, 2^{++}, \dots. \quad (12)$$

States with  $P = (-1)^J$  are called *natural-parity* states, those with  $P = (-1)^{J+1}$  *unnatural parity* states. The *naturality* of a state is defined by

$$\eta \equiv P(-1)^J = \pm 1, \quad (13)$$

and is  $+1$  for the natural-parity series states  $0^+$ ,  $1^-$ ,  $2^+$ , ..., and  $-1$  for the unnatural-parity series states  $0^-$ ,  $1^+$ ,  $2^-$ , .... The spectroscopic notation  $n^{2S+1}L_J$  is used to fully designate a given  $q\bar{q}'$  state, with  $n = n_r + 1$  numbering radial excitations ( $n_r$  is the number of radial nodes).<sup>14</sup>

The  $C$  parity ( $\pm 1$ ) is commonly used not only for neutral flavorless mesons, which are eigenstates of the particle-antiparticle conjugation operator, but also for the charged members of an isospin triplet, or sometimes even for all members of an  $SU(3)_{\text{flavor}}$  nonet. In these cases, it is understood to be defined through the neutral component of the corresponding multiplet.

The naming scheme for mesons reflects their quantum numbers, and is given in Table 2. The total spin  $J$  is added as a subscript except for the pseudoscalar ( $J^{PC} = 0^{-+}$ ) and vector ( $1^{--}$ ) mesons. Light isoscalar states, which generally are a mixture of  $(u\bar{u} + d\bar{d})$  and  $s\bar{s}$  (see Eq. (10)), may be distinguished by adding a prime ('') or by the pair  $(\omega, \phi)$ . For mesons with open flavor, the natural-parity series states are tagged by a star, while the unnatural parity series states do not carry a star. Particle states have positive flavor quantum number  $S$ ,  $C$ , or  $B$  (e.g.  $K^0$ ,  $K^+$ ,  $D^0$ ,  $D^+$ ), while antiparticle states have negative ones. Radial excitations of the  $q\bar{q}'$  system carry the same name as the corresponding ground state.

<sup>13</sup>The minus sign that appears in the  $I_3 = 0$  and  $-1$  components in Eq. (9) is a convention, which allows the  $SU(2)_{\text{iso}}$  quark doublet and the antiquark doublet to transform in exactly the same way under isospin rotations or ladder operations. Such a representation is, in general, not possible in  $SU(3)_{\text{flavor}}$ .

<sup>14</sup>Note that the convention used in the quark model is different from atomic physics, where the principal quantum number  $n = n_r - L - 1$  with  $L$  being the orbital angular momentum quantum number.

Table 2: Naming scheme of mesons (inspired by Ref. [14]). The quoted  $C$  parity is defined for the flavorless states of the corresponding multiplet with  $I_3 = S = C = B = 0$ .

$q\bar{q}'$ content	$I$	$^{2S+1}L_J = {}^1(\text{even})_J$	${}^1(\text{odd})_J$	${}^3(\text{even})_J$	${}^3(\text{odd})_J$
		$J^{PC} = (0, 2, \dots)^{-+}$	$(1, 3, \dots)^{+-}$	$(1, 2, \dots)^{--}$	$(0, 1, \dots)^{++}$
$d\bar{u}, u\bar{u} - d\bar{d}, u\bar{d}$	1	$\pi_J$	$b_J$	$\rho_J$	$a_J$
$u\bar{u} + d\bar{d}, s\bar{s}$	0	$\eta_J, \eta'_J$	$h_J, h'_J$	$\omega_J, \phi_J$	$f_J, f'_J$
$u\bar{s}, d\bar{s}$	$\frac{1}{2}$	$K_J$	$K_J$	$K_J^*, K_J$	$K_J^*, K_J$
$c\bar{c}$	0	$\eta_c$	$h_c$	$\psi$	$\chi_c$
$b\bar{b}$	0	$\eta_b$	$h_b$	$\Upsilon$	$\chi_b$
$c\bar{u}, c\bar{d}$	$\frac{1}{2}$	$D_J$	$D_J$	$D_J^*, D_J$	$D_J^*, D_J$
$c\bar{s}$	0	$D_{sJ}$	$D_{sJ}$	$D_{sJ}^*, D_{sJ}$	$D_{sJ}^*, D_{sJ}$
$u\bar{b}, d\bar{b}$	$\frac{1}{2}$	$B_J$	$B_J$	$B_J^*, B_J$	$B_J^*, B_J$
$s\bar{b}$	0	$B_{sJ}$	$B_{sJ}$	$B_{sJ}^*, B_{sJ}$	$B_{sJ}^*, B_{sJ}$
$c\bar{b}$	0	$B_{cJ}$	$B_{cJ}$	$B_{cJ}^*, B_{cJ}$	$B_{cJ}^*, B_{cJ}$

### 2.1.2. The Meson Spectrum

There is a large variety of different models to calculate the spectrum of mesons [15]. Typically the dynamics of the quark-antiquark interaction is parameterized by effective Hamiltonians with the following ingredients:

- Effective masses of constituent, i.e. “dressed”, valence quarks of  $m_u = m_d \approx 0.3 \text{ GeV}$  and  $m_s \approx 0.5 \text{ GeV}$ ,
- an attractive potential  $\propto 1/r$  due to one-gluon exchange,  $r$  being the interquark distance,
- a long-range confining potential  $\propto r$ ,
- a chromomagnetic spin-spin interaction  $\propto \mathbf{S}_1 \cdot \mathbf{S}_2$  (cf. Fig. 2).

In Fig. 3 the spectrum of light flavorless mesons calculated in a relativistic quark model (RQM) [16] is compared with the masses of the experimentally observed mesons [5]. The RQM spectrum is displayed by horizontal lines. The energy levels for the non-strange isotriplet and isosinglet wave functions are displayed by two lines next to each other, with  $I = 1$  shifted to the left and  $I = 0$  to the right, while the pure  $s\bar{s}$  combinations with  $I = 0$  are indicated by single lines shifted to the right. Mixing of states with  $I = 0$  is neglected in this model, except for the pseudoscalar ground states, where the  $\eta\text{-}\eta'$  mixing scheme of Ref. [17] is applied. The corresponding spectroscopic symbols are given below the  $J^{PC}$  values. Experimental results for all mesons below a mass of 2.5 GeV appearing in the full listing of the Particle Data Group (PDG) [5] are displayed as data points, with the uncertainties on the masses as error bars. Full dots denote established states, open circles non-established states, which need confirmation, while open squares indicate states in the “Further States” listing of the PDG. As for the RQM states, the experimental states with  $I = 1$  are shifted to the left, the ones with  $I = 0$  to the right. The assignment to RQM states follows [16], except in a few cases where the PDG entries changed in the meantime. States appearing in the “Further States” listing of the PDG are included only if they were explicitly assigned to RQM states. Blue data points indicate states which have been assigned to RQM states, while red data points designate states which have not been assigned, and are thus considered potentially supernumerary. Blue lines indicate assignment, while red lines designate states, which are expected from the RQM, but where a corresponding state has not yet been found by experiments.

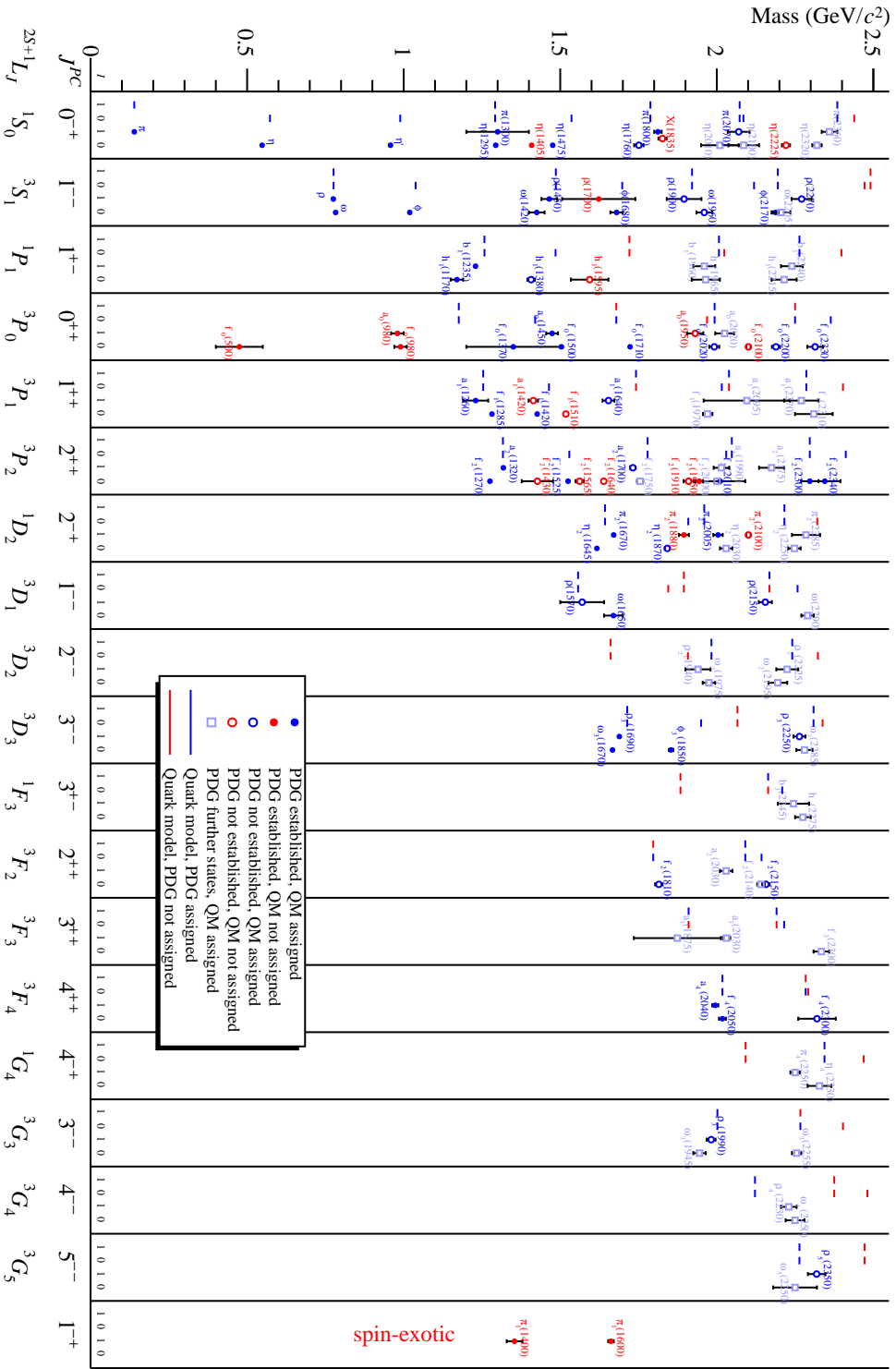


Figure 3: Mass spectrum of light flavorless mesons sorted by their  $J^{PC}$  quantum numbers. Data points indicate the masses of experimentally observed mesons with their corresponding uncertainties [5]. The PDG names are given immediately above or below the corresponding data point. Horizontal lines show the results for  $q\bar{q}'$  states from a relativistic quark model [16], with the spectroscopic notation given below the  $J^{PC}$  values. See text for detailed explanation.

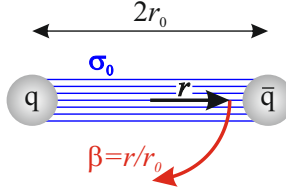


Figure 4: String model of a meson, proposed by Nambu [19] in order to explain the approximate linear relation between spin and mass squared for groups of mesons.

Despite its conceptual simplicity, the quark model is quite successful in explaining the overall structure of the observed spectrum of mesons, especially for the ground states of pseudoscalar and vector mesons. However, many radial and orbital excitations of quark-antiquark systems predicted by the model have not yet been observed experimentally (red lines). On the experimental side, there are noticeable and often well-established states, which lack a correspondence or a clear assignment to quark model nonets. Prominent cases can be found in the scalar sector with  $J^{PC} = 0^{++}$ , in the axial-vector and tensor sectors with  $J^{PC} = 1^{++}$  and  $2^{++}$ , respectively, and in the sector with spin-exotic quantum numbers  $J^{PC} = 1^{-+}$ , which will be discussed in more detail below.

## 2.2. Regge Trajectories

In parallel to the development of the quark model, it was noted by Chew and Frautschi [18] that hadrons can be arranged in groups, which exhibit an approximate linear dependence of the spin  $J$  on their mass  $M$  squared,

$$J(M) = \alpha(0) + \alpha' M^2, \quad (14)$$

with  $\alpha(0)$  being the  $y$ -axis intercept and  $\alpha'$  the slope of the so-called Regge trajectory. This observation provided another hint that hadrons were composite objects of more fundamental entities. An attractive interpretation was given by Nambu in terms of a simple string model [19]. In this model, massless quarks are bound to the ends of a string (or flux tube) of length  $2r_0$  with constant energy density  $\sigma_0$  per unit length (at rest):

$$\sigma_0 = dE_0 / dr. \quad (15)$$

For massless quarks, the ends of the string may move at the speed of light with respect to the center of momentum of the string, and the velocity of the string element at a radius  $r$  is  $\beta(r) = r/r_0$  (with  $c \equiv 1$ ), see Fig. 4 for illustration. The energy (or mass-equivalent) stored in this string element is

$$dE = \gamma(r) dE_0 = \gamma(r) \sigma_0 dr, \quad (16)$$

with  $\gamma(r) = [1 - \beta^2(r)]^{-1/2}$ . The total energy in the rotating string is then

$$E = 2\sigma_0 \int_0^{r_0} dr \gamma(r) = \pi\sigma_0 r_0, \quad (17)$$

i.e. a potential that increases linearly with the quark separation  $r_0$ , corresponding to a total relativistic mass

$$M = \pi\sigma_0 r_0. \quad (18)$$

Similarly, the angular momentum of the rotating string element is

$$dJ = r \beta(r) \gamma(r) dE_0, \quad (19)$$

and the total angular momentum

$$J = 2\sigma_0 \int_0^{r_0} dr r \beta(r) \gamma(r) = \frac{M^2}{2\pi\sigma_0}. \quad (20)$$

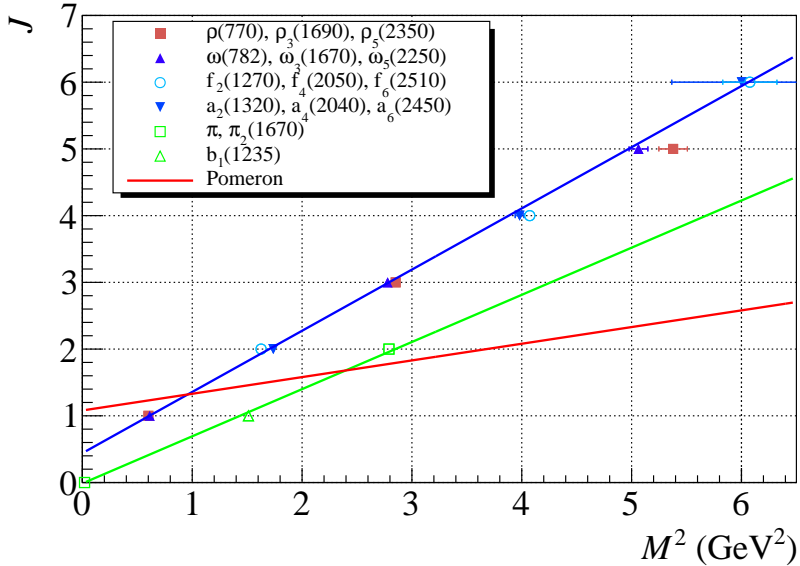


Figure 5: Chew-Frautschi plot exhibiting the linear dependence of  $\alpha(t) = J$  on the squared mass  $M^2$  of radial-ground-state-mesons.

The slope of the trajectory in this model is therefore

$$\alpha' = \frac{1}{2\pi\sigma_0} . \quad (21)$$

Figure 5 shows a so-called Chew-Frautschi plot, displaying the experimentally observed mesons  $\{\rho, \rho_3, \rho_5\}$ ,  $\{\omega, \omega_3, \omega_5\}$ ,  $\{f_2, f_3, f_4\}$ ,  $\{a_2, a_4, a_6\}$ ,  $\{\pi, \pi_2\}$ , and  $\{b_1\}$  in the  $(\alpha(t) = J)$  versus  $(t = M^2)$  plane. All the mesons listed above are characterized in the quark model by being in the radial ground state ( $n = 1$ ). Within the groups, the mesons have the same isospin  $I$ , intrinsic spin  $S$ , and parity  $P$ , while the total spin  $J$  and the orbital momentum  $L$  increase by two units, respectively. The first four series apparently fall on a single trajectory (blue line), characterized by spin  $S = 1$ , natural parity and  $J = L + S$ . A fit of Eq. (14), gives  $\alpha(0) = 0.440 \pm 0.011$  and  $\alpha' = 0.917 \pm 0.016 \text{ (GeV)}^{-2}$ <sup>15</sup>. With Eq. (21), one finds for the string tension  $\sigma_0$ , or, equivalently, the slope  $k$  of the linear confining potential in Eq. (5),  $\sigma_0 = 0.880 \pm 0.016 \text{ GeV/fm}$ . This number is in qualitatively good agreement with the value of  $k = 0.72 \text{ GeV/fm}$  extracted from a fit to the energy levels of heavy quarkonia (see e.g. [20]).

Similarly, the pion series  $\{\pi, \pi_2\}$  and the  $b_1$  form a separate, almost degenerate trajectory (green line), characterized by  $S = 0$  ( $J = L$ ) and unnatural parity. Its slope, however, is slightly different as it is dominated by the ground state  $\pi$ . This indicates the dual nature of the  $\pi$  as a ground-state meson and a Goldstone boson of spontaneous chiral symmetry breaking (see e.g. Ref. [21] and references therein). Radially excited meson states are observed to fall on trajectories with slopes similar to their parent  $n = 1$  trajectories, but shifted to higher masses. They are hence called daughter trajectories. Linear trajectories for quark-model meson families can be observed not only in the  $M^2$ - $J$  plane, but also in the  $M^2$ - $n_r$  plane (see e.g. Ref. [16]),  $n_r$  being the number of radial nodes of the wave function.

<sup>15</sup>For the fit, we used the experimental uncertainties of the meson masses as given by [5], and scaled the resulting parameter uncertainties by the reduced  $\chi^2$  of the fit.

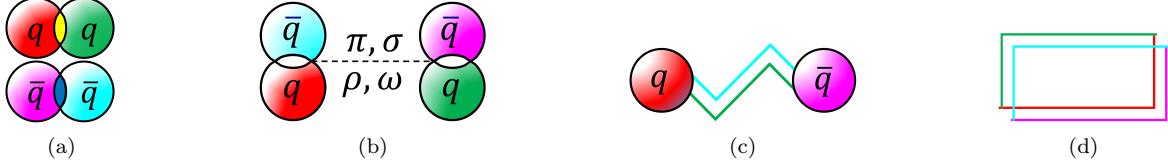


Figure 6: Examples of non- $q\bar{q}'$  configurations of mesons, which are allowed by QCD: (a) tetraquark, (b) molecule, (c) hybrid, and (d) glueball.

In addition, Fig. 5 includes the so-called Pomeron trajectory,

$$\alpha_{\mathbb{P}}(M^2) = \alpha_{\mathbb{P}}(0) + \alpha'_{\mathbb{P}} M^2, \quad (22)$$

$$\alpha_{\mathbb{P}}(0) = 1 + \epsilon_{\mathbb{P}}, \quad (23)$$

with  $\epsilon_{\mathbb{P}} = 0.08$  and  $\alpha'_{\mathbb{P}} = 0.25 \text{ GeV}^{-2}$  [22] (red line), for which so far no corresponding mesons could be identified (see Section 3.2 for the interpretation of this trajectory).

### 2.3. Exotic Mesons

Mesons which do not fit the simple  $q\bar{q}'$  quark model are generally called *exotic*. Indeed, QCD allows for a much richer spectrum of mesons, which includes configurations where more than two valence quarks contribute to the quantum numbers of the meson. The most prominent configurations are shown in Fig. 6. *Tetraquarks* (Fig. 6a) are color-singlet objects formed by a color-octet diquark and a color-octet anti-diquark bound by gluon exchanges. *Molecular* configurations (Fig. 6b) include two color-singlet  $q\bar{q}'$  pairs bound by long-range meson exchanges. Owing to the non-Abelian structure of QCD, additional configurations are possible, in which an excited gluonic field contributes to the quantum numbers of the meson. States with a valence color-octet  $q\bar{q}'$  pair neutralized in color by an excited gluon field are termed *hybrids* (Fig. 6c). Finally, due to the self-interaction of gluons, color-singlet states can in principle also be composed entirely of multiple gluonic excitations without valence quarks; such objects are generically called *glueballs* (Fig. 6d).

These configurations in principle allow for an extended set of quantum numbers compared to ordinary  $q\bar{q}'$  systems. States with flavor quantum numbers  $|I_3|, |S|, |C|$ , or  $|B| \geq 2$  are called *flavor-exotic*. No candidates for such states have been observed to date. Mesons with  $J^{PC}$  quantum numbers

$$J^{PC} = 0^{--}, 0^{+-}, 1^{-+}, 2^{+-}, \dots, \quad (24)$$

i.e. not fitting to Eqs. (11) and (12), are called *spin-exotic*. If observed, such states are considered strong candidates for gluonic excitations like hybrids or glueballs (which are then called *oddballs*), because the gluonic field may carry quantum numbers different from  $0^{++}$ . However, also molecular or multi-quark states may have spin-exotic quantum numbers. As can be seen in Fig. 3, there are two light-meson candidate states with spin-exotic quantum numbers listed by the PDG: the  $\pi_1(1400)$  and the  $\pi_1(1600)$  [5]. Their nature as a resonance has been the subject of a long-standing controversy, which has recently been resolved thanks to the data of the COMPASS experiment. This is discussed in more detail in Section 6.3.3. The unambiguous identification of exotic states with the same quantum numbers as ordinary  $q\bar{q}'$  mesons, so-called *crypto-exotic* mesons, is difficult because they will only appear as supernumerary states in the observed spectrum for a given  $J^{PC}$ , possibly mixing with the corresponding conventional  $q\bar{q}'$  states. For such states, their fitting into Regge trajectories (see Section 2.2) can be a useful criterion for their classification.

Experimental states labelled as “not assigned” (red data points) in the columns corresponding to  $q\bar{q}'$  configurations in Fig. 3 are potential candidates for supernumerary states, however, a full understanding of the  $q\bar{q}'$  spectrum is a prerequisite for claiming such states. There is evidence that the light scalar states indeed agree with a tetraquark interpretation. The recent observation of the

$a_1(1420)$  by COMPASS is another example of a potentially supernumerary state in the  $1^{++}$  sector, which will be discussed in more detail in Section 6.3.2.

The search for exotic states has been a central goal of hadron spectroscopy in the last 20 years [23–25]. In recent years, many new and unexpected resonance-like signals have been observed in the heavy-quark sector. Many of these so-called  $X, Y, Z$  states are candidates for exotic configurations of mesons. Similar studies in the light-quark sector are more challenging due to the wide and overlapping nature of the known resonances, but have also revealed possible candidates, in particular for hadrons with explicit gluonic degrees of freedom. Still, one expects to find not only single states, but whole multiplets of states with similar masses, similar to the  $q\bar{q}'$  multiplets. It remains an open question, whether these multiplets simply have evaded detection until now or whether they are not realized in nature as expected. In order to settle this fundamental question, large data sets with high statistical precision are needed. The unambiguous identification of exotic states requires experiments with complementary production mechanisms and the analysis of different final states. In Section 8, we will briefly discuss some running and upcoming high-precision experiments, which are expected to shed new light on the existence of exotic states in nature.

Last but not least, advanced analysis methods are needed, which overcome of some of the shortcomings of the traditional partial-wave techniques. These include analysis models that reduce or avoid bias or prejudice, and improved parameterizations of amplitudes that include reaction models and fulfill fundamental theoretical constraints such as unitarity, analyticity, and crossing symmetry. Some important steps in this direction have been pioneered by the COMPASS experiment in collaboration with JPAC<sup>16</sup> and will be reported in Section 6.

Recently, numerical calculations using the method of lattice QCD (see Section 2.4) started to make predictions on the multiplet structure of exotic hadrons, which may be used as a guideline in the experimental searches [27–30].

#### 2.4. Lattice QCD

Lattice QCD is presently the only available rigorous ab-initio method that can consistently describe the physics of binding and decay of hadrons [31–33]. It is a form of lattice gauge theory as proposed by K. G. Wilson in Ref. [34], where calculations are performed in a discretized Euclidean space-time using a hypercubic lattice with lattice spacing  $a$ . The lattice spacing leads to a momentum cut-off  $\propto 1/a$  (ultraviolet regularization). In lattice QCD, the quark fields are placed at the lattice sites, while the gluon gauge fields are defined on the links that connect neighboring sites.

The calculations are performed numerically by using Monte Carlo techniques, i.e. by sampling possible configurations of the quark and gluon fields according to the probability distribution given by the QCD Lagrangian. This requires large computational resources provided only by supercomputers. Because of the employed Monte Carlo approach, only a finite number of configurations can be considered. This leads to statistical uncertainties of the lattice QCD results. The calculations are often performed at larger up and down quark masses than in nature. This limits the computational cost because it drastically reduces the number of virtual quark-antiquark loops that have to be taken into account. The employed up and down quark masses are commonly expressed in terms of the resulting (unphysical) pion mass.

In lattice QCD calculations, the extent of the space-time lattice is necessarily finite. In order to obtain physical results, several limits have to be taken: (i) the *continuum limit*, i.e. the extrapolation  $a \rightarrow 0$ , (ii) the *infinite-volume limit*, i.e. the extrapolation  $L \rightarrow \infty$ , and (iii) the *physical quark-mass limit*, i.e. the extrapolation to physical quark masses. Many present-day lattice calculations are already performed directly at or very close to the physical values of the quark masses (see e.g. Ref. [35]), so that the latter extrapolation becomes less of an issue and the dominant systematic effects are due to the finite spatial volume and discrete nature of the lattice. Unfortunately, lattice

---

<sup>16</sup>The Joint Physics Analysis Center (JPAC) is a collaboration of theorists working in hadron physics [26].

QCD calculations of excited hadron resonances still need to be performed at rather high pion masses as will be discussed further below.

Lattice QCD calculations have shown that QCD confines color [36–38]. The method was also used successfully to calculate various hadron properties, in particular the masses of ground-state hadrons (see e.g. Ref. [7]). The results match the experimental values with impressive precision, which shows that QCD indeed seems to be the correct theory also in the regime where the perturbation expansion in the strong coupling  $\alpha_s$  does not converge.

Compared to the ground-state hadrons, lattice QCD studies of the excitation spectrum of hadronic states are still performed further away from the physical point. However, tremendous progress has been made in the development of methods that are now able to extract towers of highly excited states and to determine the inner structure of these states (see e.g. Ref. [33] and references therein). The cubic spatial lattice breaks rotational invariance and hence makes the identification of spin states more difficult. It was found that with a sufficiently fine lattice spacing, the effects of the reduced rotational symmetry of a cubic lattice can be overcome. By correlating meson operators with definite spin with the irreducible representations of cubic rotations, it is possible to make spin assignments from lattice QCD simulations with a single lattice spacing. Another key improvement was the development of variational methods so that a large base of operators can be used in order to reliably extract many excited states and to probe their internal structure.

Figure 7 shows the spectrum of light non-strange mesons from the lattice QCD calculation in Ref. [29]. The spectrum is qualitatively similar to the one predicted by quark models (see Fig. 3), but lattice QCD predicts also the existence of exotic non- $q\bar{q}'$  states that are discussed in Section 2.3. The masses of the states depend on the pion mass used in the calculation. The lowest pion mass used in Ref. [29] is  $391\text{ MeV}/c^2$ , which is still far away from the physical point. Since the simulation did not include multi-hadron operators, the extracted states are quasi-stable and their masses are in general not identical to the resonance masses. For the same reason, this calculation cannot predict widths and decay modes of the states. For this, one still has to rely on models for most of the states.

Lattice QCD calculations are performed by applying periodic spatial boundary conditions to the quark and gluon fields. This means that within the cube of finite volume  $L_s^3$ , free particles can only have discrete three-momenta  $\vec{p} = (2\pi/L_s)(n_x, n_y, n_z)$  with integer  $n_i$ . Hence in scattering processes, multi-hadron states are limited to a discrete spectrum of states, which are the energies of the eigenstates of the QCD Hamiltonian in a finite box. The simplest case is the decay of a state into two (quasi-)stable particles, e.g. two pions. The energies of the two-particle state depend on the interactions between these particles. By inverting this relation, one can extract information about scattering amplitudes, e.g. scattering phase shifts, from the volume dependence of the discrete spectrum in a finite volume. This idea goes back to M. Lüscher [39, 40]. It was developed into a general method to calculate scattering amplitudes for all possible  $2 \rightarrow 2$  scattering processes of mesons by including hadron-hadron operators that, for example, represent  $\pi\pi$  or  $K\bar{K}$  systems with defined momenta of the particles (see Ref. [33] and references therein). The resonances, which may appear in these scattering processes, are extracted by analytic continuation of the scattering amplitude into the complex energy-plane, where the resonances appear as poles (see Section 3.1). Calculations of this kind have been performed, for example, for the  $\pi\pi$  system (see e.g. Refs. [41, 42]) and the coupled  $\pi\eta$  and  $K\bar{K}$  system (see Ref. [43]).

The calculations of scattering amplitudes performed so far were mostly of exploratory nature and were hence performed at rather large pion masses. Unfortunately, performing these kind of calculations closer to the physical point is not only a question of computational cost. With decreasing pion mass also the kinematical thresholds for three- and four-hadron channels decrease. In particular highly excited states couple strongly to such multi-hadron final states. However, the current method is not applicable to these channels. A complete finite-volume formalism for three or even more particles would therefore be a major breakthrough for the calculation of masses and decay modes of hadron resonances. Such a formalism is already under development (see Ref. [33] and references therein).

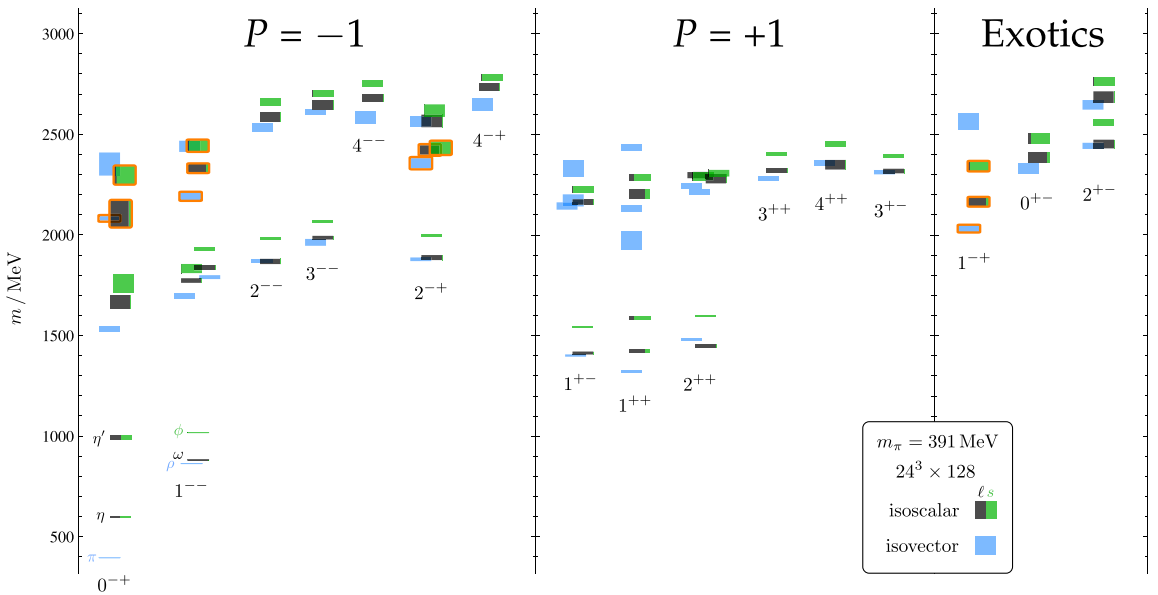


Figure 7: Spectrum of light non-strange isoscalar (blue boxes) and isovector mesons (green/black boxes) from a lattice QCD calculation performed on a  $24^3 \times 128$  lattice with a spatial lattice spacing of 0.12 fm and a temporal lattice spacing of 0.034 fm using unphysical up and down-quark masses that correspond to a pion mass of  $391 \text{ MeV}/c^2$  [29]. The height of the boxes correspond to the statistical uncertainty of the estimated masses. For the isoscalar states, the mixing contributions from up and down quarks are indicated by the black areas, the contributions from strange quarks by the green areas. Boxes outlined with orange represent the lightest states that have a large chromomagnetic gluonic component in their wave function. They can be interpreted as the lightest hybrid-meson supermultiplet (see Section 2.4).

### 3. Strong Interactions

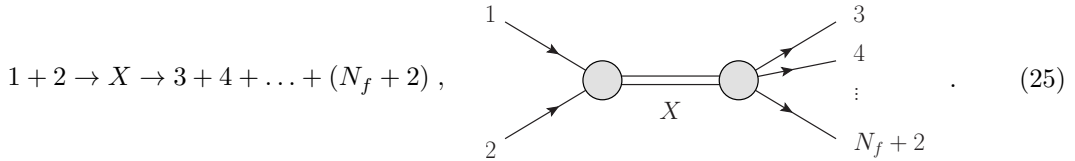
Quantum Chromodynamics is well established as the fundamental gauge field theory of strong interactions in the regime of large momentum transfers (see e.g. Ref. [44] and references therein), where it can be solved using perturbative methods. The non-Abelian structure of the  $SU(3)_{\text{color}}$  gauge symmetry group, however, introduces self-interactions between the gauge bosons, which lead to an increase of the effective strong coupling  $\alpha_s$  with decreasing momentum transfer. As a consequence, QCD is a strongly coupled theory in the regime of hadrons, which cannot be solved perturbatively. Instead, models and effective theories are employed to describe the phenomenology and dynamics of hadrons. As discussed in Section 2.4, more recently lattice QCD started to provide data on excited states by numerically investigating the scattering of light hadrons in a discrete and finite space-time volume.

Experimentally, hadronic resonances can be studied either in scattering experiments or in decays (cf. Section 4). The analysis and interpretation of both experimental and lattice data requires the implementation of theoretical amplitudes describing the reaction under study. In the following subsections, we will review some of the basic principles of scattering theory based on the  $S$ -matrix formulation. Although  $S$ -matrix theory, which was developed long before the advent of QCD, cannot be used to compute the strong interaction amplitudes from first principles, its fundamental properties provide important constraints for theoretical amplitudes.

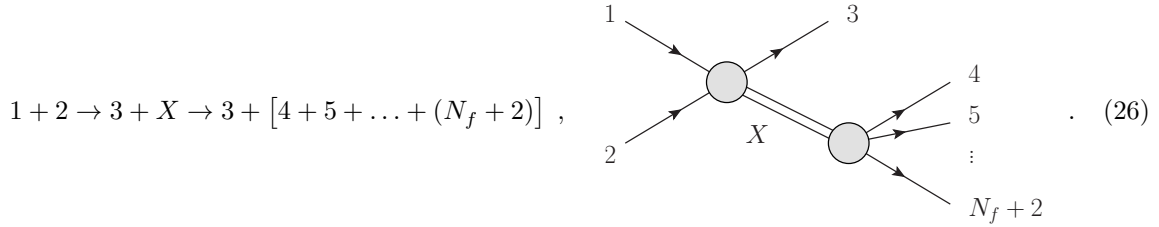
#### 3.1. Scattering Theory

##### 3.1.1. $S$ -Matrix

In a typical scattering experiment, a beam particle 1, e.g. from an accelerator, hits a target particle 2, which may either be at rest or also an accelerated particle, and the interaction between the two particles may result in the production of several new particles travelling in different directions. A resonance  $X$  may appear in direct formation experiments,



or together with a (spectator) recoil particle 3,



The operator connecting the initial and final states is called the  $S$ -matrix. In order to define the  $S$ -matrix, we start from an initial state  $|i\rangle$  at time  $t \rightarrow -\infty$ , usually consisting of two particles with four-momenta  $p_1, p_2$  and total four-momentum  $P_i = p_1 + p_2$ , which is scattered into a state  $|i'\rangle$  at time  $t \rightarrow +\infty$ , containing  $N_f$  particles with total four-momentum  $P_f = \sum_{b=3}^{N_f+2} p_b$ . The asymptotic states consist of non-interacting particles, implying a short-range interaction such as the strong force. The scattering process is described by the scattering operator  $S$ :

$$|i'\rangle = S |i\rangle . \quad (27)$$

Of all possible states contained in  $|i'\rangle$ , the detector projects out a particular final state  $|f\rangle$ . The probability amplitude for finding  $|f\rangle$  in  $|i'\rangle$  is given by

$$\langle f|i'\rangle = \langle f|S|i\rangle = S_{fi} , \quad (28)$$

with  $S_{fi}$  being the elements of the  $S$ -matrix. The probability of finding a final state  $|f\rangle$ , given  $|i\rangle$  as the initial state, is

$$|S_{fi}|^2 = |\langle f|S|i\rangle|^2 = \langle i|S^\dagger|f\rangle\langle f|S|i\rangle . \quad (29)$$

The full  $S$ -matrix therefore connects all possible initial states with all possible final states, and constitutes a complete description of all particle interactions. If  $|f\rangle$  forms a complete set of orthonormal states, then<sup>17</sup>

$$\sum_f |f\rangle\langle f| = \mathbb{1} . \quad (30)$$

Starting from the initial state  $|i\rangle$ , the probability of ending up in some final state must be unity:

$$1 = \sum_f |\langle f|S|i\rangle|^2 = \sum_f \langle i|S^\dagger|f\rangle\langle f|S|i\rangle = \langle i|S^\dagger S|i\rangle . \quad (31)$$

Since Eq. (31) must hold for any state  $|i\rangle$ , it follows that  $S^\dagger S = \mathbb{1}$ . In the same way, a final state  $|f\rangle$  must have originated from some initial state out of a complete set  $|i\rangle$ , from which one gets  $S S^\dagger = \mathbb{1}$ . Therefore, as a consequence of the conservation of probability,  $S$  is unitary:

$$S^\dagger S = S S^\dagger = \mathbb{1} . \quad (32)$$

The set  $|i'\rangle$  in Eq. (27) also contains states that have not experienced any interaction. They are usually separated out by defining the transition matrix element  $T_{fi}$  through<sup>18</sup>

$$S_{fi} = \delta_{fi} + iT_{fi} , \quad (33)$$

or in matrix form

$$S = \mathbb{1} + iT . \quad (34)$$

Inserting Eq. (34) into the unitarity condition Eq. (32), leads to the general unitarity relation for  $T$ :

$$T - T^\dagger = iT^\dagger T = iT T^\dagger , \quad (35)$$

or, in terms of the elements of  $T$ :

$$\begin{aligned} \frac{1}{i} [\langle f|T|i\rangle - \langle f|T^\dagger|i\rangle] &= \frac{1}{i} [\langle f|T|i\rangle - \langle i|T^*|f\rangle] = \frac{1}{i} (T_{fi} - T_{if}^*) \\ &= \langle f|T^\dagger T|i\rangle = \sum_j \langle f|T^\dagger|j\rangle\langle j|T|i\rangle = \sum_j \langle j|T^*|f\rangle\langle j|T|i\rangle \\ &= \sum_j T_{jf}^* T_{ji} , \end{aligned} \quad (36)$$

where we have made use of  $(T^\dagger)_{fi} = T_{if}^*$ . As in Eqs. (30) and (31), for continuum states the sum in Eq. (36) contains an integral  $\int \prod_{c=1}^{N_j} d^3 p_c / (2\pi)^3$  over all possible momenta of the  $N_j$  particles in the

---

<sup>17</sup>In the case of continuum states, i.e. states with a continuous momentum variable, the sum also contains an integral over all possible momenta for all final states.

<sup>18</sup>Some authors use a different definition, e.g. with a factor of 2 or a minus sign. We follow the definition by [45].

intermediate state  $j$ .<sup>19</sup> It is important to note that the intermediate-state particles in the unitarity relation are on their mass shells; they are not virtual particles as they appear e.g. in Feynman diagrams. If

$$T_{fi} = T_{if} , \quad (37)$$

which is generally true for  $2 \rightarrow 2$  reactions if the interaction is invariant with respect to parity transformation and time-reversal [45], we arrive at

$$\frac{1}{i} (T_{fi} - T_{fi}^*) \equiv 2 \operatorname{Im} T_{fi} = \sum_j T_{fj}^* T_{ji} . \quad (38)$$

Explicitly factoring out the conservation of four-momentum in the reaction, i.e.  $P_f = P_i$ , the elements of the transition matrix are usually written as [46]

$$iT_{fi} = (2\pi)^4 \delta^{(4)}(P_i - P_f) \prod_{a \in i} \frac{1}{\sqrt{2E_a}} \prod_{b \in f} \frac{1}{\sqrt{2E_b}} i\mathcal{M}_{fi} , \quad (39)$$

with the Lorentz-invariant matrix element or amplitude  $i\mathcal{M}_{fi}$  [47] that encodes the whole dynamic content of the transition and that can be calculated e.g. from Feynman rules in perturbation theory for elementary processes containing quarks and leptons. For low-energy hadronic interactions, effective Lagrangians may be employed to calculate the amplitude [48]. For light hadrons, chiral perturbation theory is the low-energy effective theory of QCD (see Section 3.4). For high energies, the framework of Regge theory, discussed in Section 3.2, provides some guidance on the asymptotic behavior of scattering amplitudes. The intermediate energy-regime is governed by hadronic resonances, for which no fundamental theory exists, and for which the amplitudes need to be parameterized using phenomenological models. Lorentz-invariance requires the invariant amplitude to be a Lorentz scalar, which may therefore be written as a function of Lorentz scalars only. In case of spinless particles, which we will assume here for simplicity,  $\mathcal{M}_{fi}$  is thus a function of scalar products of four-momenta only.

The unitarity condition Eq. (38) can be written in terms of the invariant amplitude  $\mathcal{M}_{fi}$  from Eq. (39) as

$$\frac{1}{i} (\mathcal{M}_{fi} - \mathcal{M}_{fi}^*) \equiv 2 \operatorname{Im} \mathcal{M}_{fi} = \sum_j \int d\Phi_{N_j} \mathcal{M}_{fj}^* \mathcal{M}_{ji} , \quad (40)$$

where one of the two  $\delta$ -functions was “cancelled” on both sides of the equation and the remaining one on the right-hand side was included in the Lorentz-invariant  $N$ -body phase-space element<sup>20</sup> for the intermediate state  $j$ :

$$d\Phi_N(P_i; p_1, \dots, p_N) = (2\pi)^4 \delta^{(4)}\left(P_i - \sum_{b=1}^N p_b\right) \prod_{b=1}^N \frac{d^3 p_b}{(2\pi)^3 2E_b} . \quad (41)$$

For  $N$  particles with fixed masses in the final state, there are  $3N$  three-momentum variables and 4 constraints from energy and momentum conservation. The effective dimension of  $d\Phi_N$  is hence  $3N - 4$ . For a two-body final state,  $d\Phi_2$  can be calculated directly by integrating out the  $\delta$ -function (see Eq. (60) below). For more particles,  $d\Phi_N$  can be calculated from  $d\Phi_2$  using the phase-space recurrence relation (see Appendix A). For 2-to-2 scattering, the unitarity condition Eq. (40) can be represented symbolically as

$$2 \operatorname{Im} \left\{ \text{Feynman diagram with } \mathcal{M}_{fi} \text{ in the loop} \right\} = \sum_j \int d\Phi_{N_j} \text{Feynman diagram with } \mathcal{M}_{ji} \text{ and } \mathcal{M}_{fj}^* . \quad (42)$$

<sup>19</sup>We use the indices  $a$ ,  $b$ , and  $c$  to enumerate the initial-state, final-state, and intermediate-state particles, respectively.

<sup>20</sup>We deviate from the convention used in [49] by including the factor  $(2\pi)^4$  in the phase-space element.

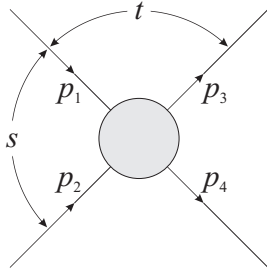


Figure 8: Two-body scattering process  $1 + 2 \rightarrow 3 + 4$ .

### 3.1.2. Kinematics of Two-Body Reactions

The decay of a resonance  $X$  into a multi-particle final state is commonly modeled as a sequence of two-body decays (see Section 5.1.2). Therefore, we restrict ourselves to two-body kinematics in the following. Consider two spinless particles with momenta  $\mathbf{p}_1$  and  $\mathbf{p}_2$  and masses  $m_1$  and  $m_2$ , which scatter to two particles with momenta  $\mathbf{p}_3$  and  $\mathbf{p}_4$  and masses  $m_3$  and  $m_4$ , as shown in Fig. 8. The four-momenta are defined as  $p_i = (E_i, \mathbf{p}_i)$ , where  $E_i^2 = m_i^2 + \mathbf{p}_i^2$  is the energy of particle  $i$ . The Lorentz-invariant Mandelstam variables are defined as

$$s = (p_1 + p_2)^2 = (p_3 + p_4)^2 = m_1^2 + m_2^2 + 2(E_1 E_2 - \mathbf{p}_1 \cdot \mathbf{p}_2) , \quad (43)$$

$$t = (p_1 - p_3)^2 = (p_2 - p_4)^2 = m_1^2 + m_3^2 - 2(E_1 E_3 - \mathbf{p}_1 \cdot \mathbf{p}_3) , \text{ and} \quad (44)$$

$$u = (p_1 - p_4)^2 = (p_2 - p_3)^2 = m_1^2 + m_4^2 - 2(E_1 E_4 - \mathbf{p}_1 \cdot \mathbf{p}_4) . \quad (45)$$

They satisfy

$$s + t + u = \sum_{i=1}^4 m_i^2 , \quad (46)$$

i.e. there are only two independent variables to fully characterize the scattering process for given masses  $m_i$ . The diagram in Fig. 8 not only describes the  $s$ -channel process  $1 + 2 \rightarrow 3 + 4$ , but, by reversing the signs of some of the four-momenta, also the  $t$ -channel process  $1 + \bar{3} \rightarrow \bar{2} + 4$  and the  $u$ -channel process  $1 + \bar{4} \rightarrow \bar{2} + 3$ .<sup>21</sup>

In the  $s$ -channel center-of-momentum frame, we have  $\mathbf{p}_1 = -\mathbf{p}_2 =: \mathbf{p}$  and  $\mathbf{p}_3 = -\mathbf{p}_4 =: \mathbf{q}$ , and thus

$$s = (E_1 + E_2)^2 = (E_3 + E_4)^2 , \quad (47)$$

$$t = m_1^2 + m_3^2 - 2(E_1 E_3 - |\mathbf{p}_1| |\mathbf{p}_3| \cos \theta_s) , \text{ and} \quad (48)$$

$$u = m_1^2 + m_4^2 - 2(E_1 E_4 - |\mathbf{p}_1| |\mathbf{p}_4| \cos \theta_s) , \quad (49)$$

with  $\theta_s$  the scattering angle between particle 1 and 3 in the  $s$ -channel center-of-momentum frame. The physically allowed region for the  $s$ -channel process is

$$s \geq (m_1 + m_2)^2 \quad \text{and} \quad -1 \leq \cos \theta_s \leq 1 . \quad (50)$$

The limiting values for  $t$  are  $t_0$  for  $\theta_s = 0$  and  $t_1$  for  $\theta_s = \pi$ :

$$t_0 = m_1^2 + m_3^2 - 2(E_1 E_3 \mp |\mathbf{p}_1| |\mathbf{p}_3|) . \quad (51)$$

---

<sup>21</sup>The channels are named after their respective energy invariants, as defined by Eqs. (43) to (45).

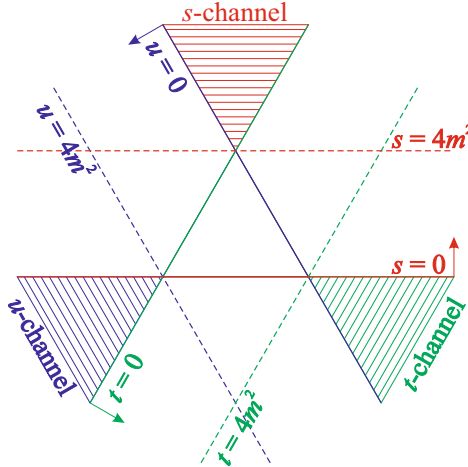


Figure 9: Mandelstam plot of the variables  $s$ ,  $t$ , and  $u$ . The physically allowed regions for the  $s$ -,  $t$ -, and  $u$ -channel process in the equal-mass case are indicated by the hashed triangles.

In order to deal with positive values, one usually defines

$$|t|_{\min} := -t_0 \quad (52)$$

and

$$t' := |t| - |t|_{\min}. \quad (53)$$

For the simple case of equal masses, i.e.  $m_i = m$  with  $i = 1 \dots 4$  and  $\mathbf{p}_1 = \mathbf{p}_3 = \mathbf{p}$ , we have

$$s = 4 \left( \mathbf{p}^2 + m^2 \right), \quad (54)$$

$$t = -2\mathbf{p}^2 (1 - \cos \theta_s), \text{ and} \quad (55)$$

$$u = -2\mathbf{p}^2 (1 + \cos \theta_s). \quad (56)$$

The boundaries of the physical region for the  $s$ -channel process are then given by  $s \geq 4m^2$ ,  $t \leq 0$ , and  $u \leq 0$ . For the  $t$ -channel process, they are  $t \geq 4m^2$ ,  $u \leq 0$ , and  $s \leq 0$ , and for the  $u$ -channel process  $u \geq 4m^2$ ,  $s \leq 0$ , and  $t \leq 0$ . Equation (46) defines a plane in the Cartesian coordinate system spanned by  $s$ ,  $t$ , and  $u$  with normal vector  $(1, 1, 1)$  and distance to the origin of  $4m^2/\sqrt{3}$ . More commonly, one plots the three axes  $s, t, u$  in one plane with the axes rotated by  $60^\circ$ <sup>22</sup> as shown in Fig. 9.

### 3.1.3. Cross Sections

The differential cross section for the inelastic scattering reaction  $1 + 2 \rightarrow 3 + 4 + \dots + (N_f + 2)$  is given by [49]<sup>23</sup>

$$d\sigma = \frac{1}{F} |\mathcal{M}_{fi}|^2 d\Phi_{N_f}(p_1 + p_2; p_3, \dots, p_{N_f+2}), \quad (57)$$

with the flux factor  $F$ , which for a general collinear collision between two particles is

$$F = 4 \left[ (p_1 \cdot p_2)^2 - m_1^2 m_2^2 \right]^{1/2}, \quad (58)$$

<sup>22</sup>In an equilateral triangle, the sum of the perpendicular distances from a point to the sides is constant, i.e. Eq. (46) is fulfilled by definition.

<sup>23</sup>If the colliding particles are unpolarized and if the spin states of initial and final-state particles are not measured in the experiment, the term  $|\mathcal{M}_{fi}|^2$  is assumed to include the incoherent averaging and summation over the spin states of the initial and the final-state particles, respectively.

and the Lorentz-invariant  $N_f$ -body phase-space element  $d\Phi_{N_f}$  (cf. Eq. (41)).

In the center-of-momentum frame for a two-body reaction  $1+2 \rightarrow 3+4$ , we have  $\sqrt{s} = E_1 + E_2 = E_3 + E_4$ ,  $|\mathbf{p}_1| = |\mathbf{p}_2| =: p$  and  $|\mathbf{p}_3| = |\mathbf{p}_4| =: q$ , and the flux factor in Eq. (58) and the phase-space element in Eq. (41) become

$$F = 4p\sqrt{s} \quad (59)$$

and

$$d\Phi_2 = \frac{1}{4\pi} \frac{q}{\sqrt{s}} \frac{d\Omega}{4\pi}, \quad (60)$$

respectively. Here,  $d\Omega = d\cos\theta_s d\phi$  is the solid-angle element around the scattering angle  $\theta_s = \angle(\mathbf{p}_1, \mathbf{p}_3)$ . The momenta  $p$  and  $q$  can be calculated by

$$p = \frac{1}{2\sqrt{s}} \lambda^{1/2}(s, m_1^2, m_2^2) \quad \text{and} \quad (61)$$

$$q = \frac{1}{2\sqrt{s}} \lambda^{1/2}(s, m_3^2, m_4^2) \quad (62)$$

using the Källén function

$$\begin{aligned} \lambda(a, b, c) &= a^2 + b^2 + c^2 - 2ab - 2bc - 2ca \\ &= \left[ a - \left( \sqrt{b} + \sqrt{c} \right)^2 \right] \left[ a - \left( \sqrt{b} - \sqrt{c} \right)^2 \right]. \end{aligned} \quad (63)$$

The differential cross section for two-body scattering is then, according to Eq. (57),

$$\frac{d\sigma}{d\Omega} = \frac{1}{64\pi^2 s} \frac{q}{p} |\mathcal{M}_{fi}|^2. \quad (64)$$

For spinless particles, the scattering probability is independent of the azimuthal angle  $\phi$ , and we get from Eq. (64), by using  $d\Omega = d\cos\theta_s d\phi$  together with Eq. (48) and integrating over the azimuthal angle  $\phi$ ,

$$\frac{d\sigma}{dt} = \frac{1}{64\pi s p^2} |\mathcal{M}_{fi}|^2. \quad (65)$$

For  $m_1 = m_2$ , this simplifies to

$$\frac{d\sigma}{dt} = \frac{1}{16\pi s (s - 4m^2)} |\mathcal{M}_{fi}|^2. \quad (66)$$

The total cross section for the scattering of particles 1 and 2 can be calculated by integrating Eq. (57) over the phase space and summing over all possible final states,

$$\sigma_{\text{tot}} = \frac{1}{F} \sum_f \int d\Phi_{N_f} \mathcal{M}_{fi}^* \mathcal{M}_{fi}. \quad (67)$$

Using the unitarity condition Eq. (40), the right-hand-side of this equation can be replaced by the imaginary part of the invariant amplitude for identical initial and final states, i.e.  $|f\rangle \equiv |i\rangle$ ,

$$\sigma_{\text{tot}} = \frac{2}{F} \text{Im} \mathcal{M}_{ii}. \quad (68)$$

This relation, which connects the total cross section to the forward elastic scattering amplitude  $\mathcal{M}_{ii}$  is known as the *optical theorem*. The optical theorem can be represented symbolically as

$$\sigma_{\text{tot}} = \frac{1}{2s} \sum_{N_f=2}^{\infty} \left| \begin{array}{c} \text{1} \\ \text{2} \end{array} \right\|_{N_f}^2 = \frac{1}{2s} \sum_{N_f=2}^{\infty} \left| \begin{array}{c} \text{1} \\ \text{2} \end{array} \right\|_{N_f} \left| \begin{array}{c} \text{1} \\ \text{2} \end{array} \right\|_{N_f} = \frac{1}{s} \text{Im} \left\{ \begin{array}{c} \text{1} \\ \text{2} \end{array} \right\|_{N_f} \left\| \begin{array}{c} \text{1} \\ \text{2} \end{array} \right\|_{N_f}. \quad (69)$$

The factor  $1/(2s)$  is the large- $s$  limit of  $2/F$  with  $F$  from Eq. (59).

### 3.1.4. Partial-Wave Expansion and Breit-Wigner Resonances

For a two-body reaction  $1 + 2 \rightarrow 3 + 4$ , there are 2 independent variables, which may be chosen to be  $s$  and  $t$ :  $\mathcal{M}_{fi} = \mathcal{M}_{fi}(s, t)$ . From Eqs. (54) and (55), one gets for the equal-mass case

$$\cos \theta_s = 1 + \frac{2t}{s - 4m^2}. \quad (70)$$

It is clear that  $t$  is a linear function of  $\cos \theta_s$  at fixed  $s$ . One can therefore use  $s$  and  $z_s := \cos \theta_s$  as independent variables. The amplitude for  $s$ -channel scattering of two spinless particles can then be expanded in a partial-wave series

$$\mathcal{M}_{fi}(s, t(s, z_s)) = \sum_{\ell=0}^{\infty} (2\ell + 1) t_{\ell, fi}(s) P_{\ell}(z_s). \quad (71)$$

Here we have assumed that the interaction potential is spherically symmetric, so that the relative orbital angular momentum  $\ell$  between initial-state and final-state particles, respectively, is a good quantum number and we can factorize the angular and the energy dependence into the Legendre polynomials  $P_{\ell}(z_s)$  and the  $s$ -channel partial-wave scattering amplitude  $t_{\ell, fi}(s)$ . The  $P_{\ell}(z_s)$  form a complete set of eigenfunctions of  $\ell$  and encode the angular distribution as a function of the center-of-momentum scattering angle  $\theta_s$ . They obey the orthonormality relation

$$\int_{-1}^1 dz P_n(z) P_m(z) = \frac{\delta_{nm}}{2n + 1}. \quad (72)$$

The  $t_{\ell, fi}(s)$  are in general complex functions, which describe the dynamics of the scattering process from initial state  $|i\rangle$  to final state  $|f\rangle$  in the partial wave  $\ell$ .

For  $2 \rightarrow 2$  scattering, the unitarity condition Eq. (40), using Eq. (60), reads

$$2 \operatorname{Im} \mathcal{M}_{fi} = \sum_j \int d\Phi_2 \mathcal{M}_{fj}^* \mathcal{M}_{ji} = \sum_j \frac{q_j}{4\pi \sqrt{s}} \int \frac{d\Omega}{4\pi} \mathcal{M}_{fj}^* \mathcal{M}_{ji}. \quad (73)$$

Inserting the partial-wave expansion Eq. (71) for  $\mathcal{M}_{fi}$ , we arrive at the unitarity condition for the partial-wave amplitudes

$$\operatorname{Im} t_{\ell, fi}(s) = \sum_j \rho_j(s) t_{\ell, f j}^*(s) t_{\ell, j i}(s), \quad (74)$$

with the two-body phase-space factor

$$\rho_j(s) = \frac{q_j}{8\pi \sqrt{s}} = \frac{1}{2} \Phi_2. \quad (75)$$

Here, we have made use of [50]

$$\int \frac{d\Omega}{4\pi} P_{\ell}(\cos \theta_1) P_n(\cos \theta_2) = \frac{\delta_{\ell n}}{2\ell + 1} P_{\ell}(\cos \theta), \quad (76)$$

where the integration is performed over all angles of the momentum vector  $\mathbf{k}$  of one of the two intermediate-state particles in the center-of-momentum frame. The angle  $\theta_1 = \angle(\mathbf{p}_1, \mathbf{k})$  denotes the angle between the momentum vectors of the initial and the intermediate-state particles in the center-of-momentum frame,  $\theta_2 = \angle(\mathbf{k}, \mathbf{p}_3)$  the angle between intermediate and final-state particles, and  $\theta = \angle(\mathbf{p}_1, \mathbf{p}_3)$  the angle between initial and final-state particles.<sup>24</sup> For the scattering of equal-mass

---

<sup>24</sup>The relation can be derived using the relation between Legendre polynomials and spherical harmonics for spin projection quantum number  $m = 0$ , i.e.  $Y_{\ell}^0 = \sqrt{\frac{2\ell+1}{4\pi}} P_{\ell}(\cos \theta)$ , the addition theorem, and the orthonormality of the spherical harmonics [51].

particles, the two-body phase-space factor in Eq. (75) is

$$\rho(s) = \frac{1}{16\pi} \sqrt{\frac{s-4m^2}{s}}. \quad (77)$$

Considering a single channel only, i.e. for given  $|i\rangle$ ,  $|j\rangle$ , and  $|f\rangle$ , the channel indices may be skipped and Eq. (74) can be reduced to

$$\text{Im } t_\ell(s) = t_\ell^*(s) \rho(s) t_\ell(s). \quad (78)$$

In the more general case, when  $T_{fi} \neq T_{if}$ , the left-hand-side of Eq. (36) is not equal to the imaginary part of the amplitude. The unitarity relation for partial-wave amplitudes then reads

$$t_\ell^\dagger(s) - t_\ell(s) = 2i t_\ell^\dagger(s) \rho(s) t_\ell(s). \quad (79)$$

For several coupled two-body channels, e.g. the  $\eta\pi-\eta'\pi$  analysis explained in Sections 6.2.1 and 6.2.2, Eqs. (78) and (79) are to be understood with  $t_\ell(s)$  being a matrix in channel space with the phase-space matrix  $\rho = \text{diag}(\rho_1, \rho_2, \dots, \rho_j)$ . A common parameterization satisfying the unitarity condition Eq. (78) for two-body scattering involving two channels  $i, j$  is [52]<sup>25</sup>

$$t_{\ell,ij}(s) = \frac{s_{\ell,ij}(s) - \delta_{ij}}{2i \sqrt{\rho_{ii}(s)} \sqrt{\rho_{jj}(s)}}, \quad (80)$$

with  $\delta_{ij}$  being the Kronecker delta symbol and  $s_{\ell,ij}$  the elements of a unitary  $2 \times 2$  matrix,

$$s_\ell(s) = \begin{pmatrix} \eta_\ell e^{2i\delta_{\ell,1}} & i\sqrt{1-\eta_\ell^2} e^{i(\delta_{\ell,1}+\delta_{\ell,2})} \\ i\sqrt{1-\eta_\ell^2} e^{i(\delta_{\ell,1}+\delta_{\ell,2})} & \eta_\ell e^{2i\delta_{\ell,2}} \end{pmatrix}. \quad (81)$$

The phase shifts  $\delta_{\ell,1}(s), \delta_{\ell,2}(s)$  and the inelasticity  $\eta_\ell(s) \in [0, 1]$  in the partial wave  $\ell$  are real numbers. The  $2 \times 2$  matrix of partial-wave transition amplitudes is then

$$t_\ell(s) = \begin{pmatrix} \frac{\eta_\ell e^{2i\delta_{\ell,1}} - 1}{2i\rho_{11}} & \frac{\sqrt{1-\eta_\ell^2} e^{i(\delta_{\ell,1}+\delta_{\ell,2})}}{2\sqrt{\rho_{11}} \sqrt{\rho_{22}}} \\ \frac{\sqrt{1-\eta_\ell^2} e^{i(\delta_{\ell,1}+\delta_{\ell,2})}}{2\sqrt{\rho_{11}} \sqrt{\rho_{22}}} & \frac{\eta_\ell e^{2i\delta_{\ell,2}} - 1}{2i\rho_{22}} \end{pmatrix}. \quad (82)$$

For inelastic scattering,  $\eta_\ell < 1$ , while for elastic scattering  $\eta_\ell = 1$ . In the latter case (single-channel elastic scattering), we can rewrite Eq. (80) as

$$\rho(s) t_\ell(s) = \frac{e^{2i\delta_\ell(s)} - 1}{2i} = e^{i\delta_\ell(s)} \sin \delta_\ell(s) = \frac{1}{\cot \delta_\ell(s) - i}. \quad (83)$$

The squared amplitude of a particular partial wave goes through a maximum for  $\delta_\ell(s = M_0^2) = (n + 1/2)\pi$  with  $n \in \mathbb{N}$ , corresponding to an isolated resonance at  $\sqrt{s} = M_0$ . The energy-dependence of the amplitude around the resonance mass can be investigated by performing a Taylor expansion of  $\cot \delta_\ell(\sqrt{s})$  around this maximum:

$$\begin{aligned} \cot \delta_\ell(\sqrt{s}) &= \cot \delta_\ell(M_0) + (\sqrt{s} - M_0) \left. \frac{d \cot \delta_\ell}{d \sqrt{s}} \right|_{\sqrt{s}=M_0} + \dots \\ &\simeq 0 + (\sqrt{s} - M_0) \left( -\frac{2}{\Gamma_0} \right), \end{aligned} \quad (84)$$

<sup>25</sup>This definition is made such that it reduces to the well-known form for non-relativistic potential scattering for the case of a single channel.

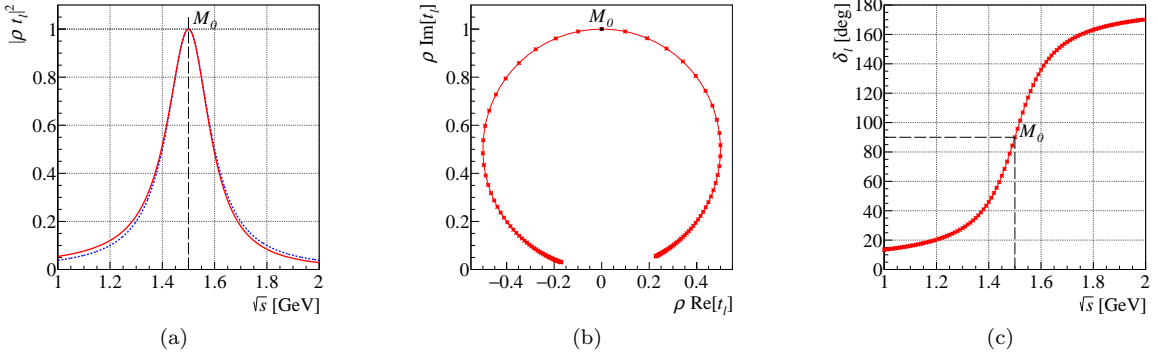


Figure 10: Breit-Wigner amplitude for elastic scattering through a fictitious resonance in the two-body partial wave with orbital angular momentum  $\ell$  with mass  $M_0 = 1500$  MeV and constant width  $\Gamma_0 = 200$  MeV. (a) Modulus squared of (red) the relativistic, Eq. (87), and (blue) the non-relativistic Breit-Wigner, Eq. (85). (b) Imaginary versus real part (Argand diagram), (c) phase  $\delta_\ell$  as a function of  $\sqrt{s}$  for the relativistic Breit-Wigner amplitude. The points in (b) and (c) are spaced equidistantly in 10 MeV bins of  $\sqrt{s}$  with  $s$  increasing in counter-clockwise direction from 1 to 2 GeV.

where the first derivative of  $\cot \delta_\ell$  with respect to  $\sqrt{s}$  at  $\sqrt{s} = M_0$  has been defined as  $(-2/\Gamma_0)$ .<sup>26</sup> Inserting this into Eq. (83) then gives

$$\rho(s) t_\ell(s) \simeq \frac{\Gamma_0/2}{M_0 - \sqrt{s} - i\Gamma_0/2} , \quad (85)$$

which is the non-relativistic form of the Breit-Wigner amplitude with constant width, denoted by the parameter  $\Gamma_0$  (full width at half maximum).<sup>27</sup> Using

$$M_0^2 - s = (M_0 + \sqrt{s}) (M_0 - \sqrt{s}) \simeq 2M_0 (M_0 - \sqrt{s}) \quad (86)$$

for  $\sqrt{s} \simeq M_0$ , Eq. (85) can be written as

$$\rho(s) t_\ell(s) \simeq \frac{M_0 \Gamma_0}{M_0^2 - s - i M_0 \Gamma_0} , \quad (87)$$

which is the relativistic, Lorentz-covariant form of the elastic Breit-Wigner amplitude with constant width.

Figure 10 displays the modulus squared, the imaginary versus the real part (Argand diagram), and the phase of  $\rho(s) t_\ell(s)$  as a function of  $\sqrt{s}$ . In Fig. 10a the relativistic form is compared to the non-relativistic form. For elastic scattering, the locus of  $\rho(s) t_\ell(s)$  follows a circle of unit diameter around the point  $0 + i/2$  in counterclockwise direction in the Argand diagram shown in Fig. 10b. When a threshold for inelastic processes is passed, we have  $\eta_\ell < 1$ , and the locus moves inward from the circle. The phase shift  $\delta_\ell$ , which is always measured with respect to some reference<sup>28</sup> undergoes a steep rise from 0 to  $180^\circ$  when the energy is varied across the resonance position (see Fig. 10c). It should be stressed that the Breit-Wigner approximation for Eq. (83) in Eq. (87) is only valid for isolated, narrow resonances in the vicinity of the resonance mass and sufficiently far from thresholds. For wider resonances, the opening of the phase space for the decay products across the resonance

<sup>26</sup>This relation can formally be derived from the radial solution of the non-relativistic Schrödinger equation for a spherically symmetric potential of finite range [53].

<sup>27</sup>A Fourier transformation of a wave function decaying exponentially with a time constant  $2/\Gamma_0$  leads to the same result as Eq. (85).

<sup>28</sup>Compare to the phase shift of a driven oscillator, which is measured with respect to the driving force.

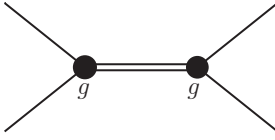


Figure 11: Feynman diagram for the amplitude for scattering of two particles via the exchange of a particle, cf. Eq. (89). The coupling at the vertices is  $g$ .

width has to be taken into account by replacing the constant width  $\Gamma_0$  in Eq. (87) by the dynamic width  $\Gamma(s)$  that will be discussed below:

$$\rho(s) t_\ell(s) \simeq \frac{M_0 \Gamma(s)}{M_0^2 - s - i M_0 \Gamma(s)} . \quad (88)$$

In quantum field theory, the relativistic Breit-Wigner amplitude with dynamic width corresponds to the amplitude for scattering of two particles via the exchange of a particle with mass  $m(s)$  and four-momentum squared  $q^2 = s$ , as depicted in Fig. 11,

$$t_\ell(s) = g \frac{1}{m^2(s) - q^2} g , \quad (89)$$

where  $g$  denotes the coupling at the vertices (assumed to be equal for equal-mass scattering) and  $1/[m^2(s) - q^2]$  is the propagator term. For the exchange of unstable particles, we make use of  $m(s) = M_0 - i\Gamma(s)/2$ . The two-body differential decay width of an unstable particle with mass  $M_0$  is [49]

$$d\Gamma = \frac{1}{2M_0} |g|^2 d\Phi_2 . \quad (90)$$

For coupling  $g$  independent of  $s$ , this yields  $M_0 \Gamma(s) = \rho(s) g^2$  with  $\rho(s)$  from Eq. (75). Using  $(M_0 - i\Gamma(s)/2)^2 = M_0^2 - i M_0 \Gamma(s) - \Gamma(s)^2/4 \approx M_0^2 - i M_0 \Gamma(s)$  for  $\Gamma(s) \ll M_0$ , Eq. (89) then becomes

$$t_\ell(s) = \frac{g^2}{M_0^2 - s - i \rho(s) g^2} , \quad (91)$$

which is equivalent to Eq. (88), but explicitly displays the phase-space factor  $\rho(s)$  in the denominator.

Close to the kinematic threshold  $s_{\text{thr}}$  of the reaction, the dependence of  $\Gamma(s)$  can be estimated from the asymptotic behavior of the Legendre polynomials in Eq. (71),  $P_\ell(z_s) \propto z_s^\ell$  for  $z_s \gg 1$ . From Eq. (55), we find that

$$z_s = \cos \theta_s = 1 + \frac{t}{2p^2} \quad (92)$$

for equal-mass  $2 \rightarrow 2$  scattering with  $p = q$ , implying that  $P_\ell(z_s) \propto 1/q^{2\ell}$  for small breakup-momenta  $q$ , which diverges for  $q \rightarrow 0$ , i.e. at threshold. In order for the full scattering amplitude Eq. (71) to remain finite, this divergence must be cancelled by the appropriate behavior of the partial-wave amplitudes as  $t_\ell \propto q^{2\ell}$ . We hence obtain for the threshold behavior of Eq. (88),

$$\rho(s) t_\ell(s) \propto q^{2\ell+1} , \quad (93)$$

where one power of  $q$  obviously arises from the phase-space factor on the left-hand-side of the equation (see Eq. (75)), and initial and final state each contribute a barrier factor of  $q^\ell$ . This indicates that partial waves with  $\ell > 0$  are suppressed by the centrifugal barrier close to threshold.<sup>29</sup> This barrier

<sup>29</sup>For the more general case of inelastic  $2 \rightarrow 2$  reactions with different masses and different orbital angular momenta  $\ell_i$ ,  $\ell_f$  in the initial and finite states, respectively, the corresponding partial-wave amplitude behaves as  $t_\ell \propto p^{\ell_i} q^{\ell_f}$ .

arises because the orbital angular momentum is given by  $q$  and the impact parameter between the particles, which is of the order of the range of the strong interaction, i.e. about 1 fm. This corresponds via the Heisenberg uncertainty relation to a range parameter of  $q_R \approx 200$  MeV. At small  $\sqrt{s}$ , i.e.  $q \lesssim q_R$ , higher orbital angular momenta are hence suppressed.

Provided that the denominator in Eq. (91) varies slowly compared to the numerator, i.e. the threshold behavior of  $g^2$  follows the one of  $t_\ell$ , we obtain for the threshold behavior of the dynamic width  $\Gamma(s)$

$$\Gamma(s) = \Gamma_0 \frac{M_0}{\sqrt{s}} \left( \frac{q}{q_0} \right)^{2\ell+1}, \quad (94)$$

with  $q$  and  $q_0$  being the breakup momenta at  $s$  and  $M_0^2$ , respectively (see Eq. (62)) and  $\Gamma_0$  being the width at  $s = M_0^2$ .

At high  $\sqrt{s}$ , far away from threshold, the behavior in Eq. (93), however, is no longer correct, because it would imply  $t_\ell \propto \sqrt{s}^{2\ell}$ , which violates the Froissart bound [54]. In order to enforce the correct threshold behavior and damp the indefinite growth at high energies, model-dependent form factors  $F_\ell$  are commonly introduced so that Eq. (94) becomes

$$\Gamma(s) = \Gamma_0 \frac{q}{\sqrt{s}} \frac{M_0}{q_0} \frac{F_\ell^2(q)}{F_\ell^2(q_0)}. \quad (95)$$

The most popular phenomenological parameterization for these barrier factors was derived by Blatt and Weisskopf [55] and later generalized by von Hippel and Quigg [56]. By solving the non-relativistic Schrödinger equation for a spherically symmetric potential with finite range  $R$  and a sharp boundary, they showed that the  $F_\ell$  can be expressed in terms of spherical Hankel functions of the first kind, which are given by

$$h_\ell^{(1)}(x) = (-i)^{\ell+1} \frac{e^{ix}}{x} \sum_{k=0}^{\ell} \frac{(\ell+k)!}{(\ell-k)! k!} \left( \frac{i}{2x} \right)^k. \quad (96)$$

The  $F_\ell$  are usually written as functions of  $z(s) := [q(s)/q_R]^2$ , i.e.

$$F_\ell^2(z) = \frac{1}{z |h_\ell^{(1)}(q/q_R)|^2}. \quad (97)$$

From Eqs. (96) and (97) it is apparent that for  $q \rightarrow 0$ ,  $F_\ell^2(z) \propto q^{2\ell}$ , consistent with Eq. (93). It is customary to normalize the barrier factor such that  $F_\ell(z=1) = 1$ . In Appendix D, we list the normalized barrier factors for  $\ell$  up to 6.

### 3.1.5. Analytic Structure of the Amplitude

In addition to being a unitary matrix, the  $S$ -matrix is postulated to be an analytic function of Lorentz-invariants [45], that are regarded as complex variables, everywhere in the complex plane, except for a few well-defined singularities related to the internal dynamics of the scattering process. These include poles, corresponding to stable particles or resonances, and branch points with cuts required by unitarity. It is these singularities, which characterize the analytic function. The physical amplitude corresponds to the boundary values of the analytic function for real-valued variables, e.g. the Mandelstam variables for the case of  $2 \rightarrow 2$  scattering of spinless particles.

The postulate of analyticity results from rather general causality arguments [50]. It also suggests that the same complex amplitude, analytically continued from the physical  $s$ -channel region to the physical regions of the  $t$ - and  $u$ -channel in the Mandelstam plane in Fig. 9, correctly describes also the crossed-channel processes. This assumption obviously holds in perturbation theory (Feynman diagrams), and seems plausible also for the case of hadron scattering.

As mentioned above, it is not possible to calculate the amplitude for a given process solely based on the properties of the  $S$ -matrix, i.e. unitarity, analyticity, and crossing symmetry. The theory rather

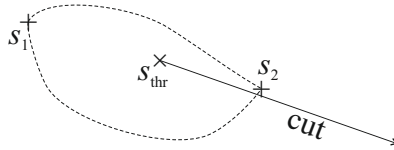


Figure 12: Analytic continuation of the amplitude along different paths around a branch point  $s_{\text{thr}}$ .

provides a framework for the development of models and offers constraints for the corresponding amplitudes, which may or may not be of concern for a particular application. In any case, the understanding of the analytic structure of amplitudes is essential for the interpretation of scattering and lattice QCD data and will be discussed in the following.

From the unitarity relations Eq. (40) or Eq. (74), it is clear that an intermediate state with  $N$  particles of mass  $m_1, \dots, m_N$  can only contribute to the imaginary part of the amplitude above the corresponding  $N$ -particle threshold, i.e. if  $s > s_{\text{thr}} \equiv \left(\sum_{i=1}^N m_i\right)^2$ . Considering for simplicity only particles with equal mass  $m$ , the thresholds are at  $4m^2, 9m^2, \dots$ . Below the three-body threshold, the imaginary part of the partial-wave amplitude is, according to Eq. (78) for a single  $2 \rightarrow 2$  channel,

$$\text{Im } t_\ell(s) \equiv \frac{t_\ell(s) - t_\ell^*(s)}{2i} = \rho(s) |t_\ell(s)|^2. \quad (98)$$

In the equal-mass case, the phase-space factor is given by Eq. (77). Hence for real  $s$ , the amplitude  $t_\ell(s)$  has a finite imaginary part in the physical region above the elastic threshold  $s_{\text{thr}} = 4m^2$ , which is the smallest  $s$  at which a two-particle state can exist. Below the elastic threshold the amplitude is purely real.

For complex  $s = s_{\text{thr}} + r \exp i(\theta \pm 2\pi n)$ , with  $n \in \mathbb{N}$ , the square root in the numerator of Eq. (77),  $\sqrt{s - s_{\text{thr}}} = \sqrt{r} \exp i(\theta/2 \pm \pi n)$ , has two different solutions, depending on the choice of  $n$ :

$$\sqrt{s - s_{\text{thr}}} = \begin{cases} +\sqrt{r} e^{i\theta/2} & \text{for } n = 0, 2, 4, \dots \\ -\sqrt{r} e^{i\theta/2} & \text{for } n = 1, 3, 5, \dots \end{cases} \quad (99)$$

The threshold  $s_{\text{thr}}$  is thus a branch point of the amplitude  $t_\ell(s)$ ; consequently, a cut is attached to the branch point, indicating that continuing  $t_\ell(s)$  from a point  $s_1$  to a point  $s_2$  along two paths on different sides of the branch point, as illustrated in Fig. 12, will result in different values of the amplitude. The different solutions of  $t_\ell(s)$  for the same value of  $s$  are visualized by two planes stacked on top of each other and connected along the branch cut (Riemann sheets), as shown in Fig. 13. Therefore, the amplitude  $t_\ell(s)$  has a discontinuity along the real axis for  $s > s_{\text{thr}}$ , i.e. the value of  $t_\ell(s)$  depends on whether one approaches the axis from above or from below, which will be further discussed in Section 3.1.6. The common convention is that the physical limit for  $s \geq s_{\text{thr}}$  is reached by approaching the real axis from above (“+ $i\epsilon$  prescription”),

$$t_\ell(s) = \lim_{\epsilon \rightarrow 0^+} t_\ell(s + i\epsilon). \quad (100)$$

The “physical” sheet (also called sheet I) is thus defined by  $n = 0, 2, \dots$  in Eq. (99) and is indicated in white in Fig. 13. The second sheet II is called “unphysical”, but, as we will see, may have a large influence on the amplitude along the physical axis. The opening of an additional channel, e.g. above the three-particle threshold  $9m^2$  for equal-mass particles, defines a new branch point and a corresponding cut. For  $n$  channels, there are  $2^n$  Riemann sheets. By convention, the cut corresponding to the lowest threshold is drawn along the positive real  $s$  axis, and thus passes through all other branch points, as indicated in Fig. 13. This is called the right-hand (or normal-threshold) cut, which is a consequence of unitarity when the amplitude is viewed as a function of complex variables. It has a clear dynamical origin, namely the opening of the two-particle threshold. In Eq. (77), another

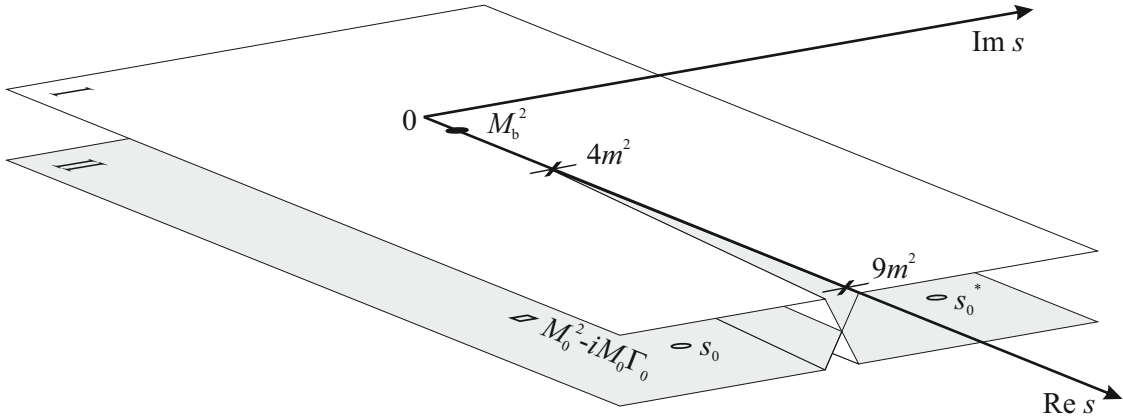


Figure 13: Riemann sheets and singularities of the partial-wave amplitude  $t_\ell(s)$  in the complex  $s$ -plane. The physical sheet is labelled I, the unphysical one II. Branch points are indicated by crosses. A conjugate pair of resonance poles on the second sheet ( $s_0, s_0^*$ ) is drawn as open circles, a bound state pole on the first sheet ( $M_b^2$ ) as a filled circle. A single resonance pole corresponding to a Breit-Wigner amplitude with mass  $M_0$  and constant width  $\Gamma_0$  (see Eqs. (85) and (87)) is indicated by a square.

branchpoint at  $s = 0$  appears, which we ignored up to now. It appears purely because of kinematics and is hence called a kinematic singularity. For the case of the phase-space factor, one can get rid of it by using e.g. the Chew-Mandelstam phase-space function [57–59], which is an analytic continuation of Eq. (77). In general, one usually tries to parameterize amplitudes such that they are free of kinematic singularities and focuses on the dynamic ones [50, 60, 61]. We will therefore continue to ignore the branch point at  $s = 0$  for our discussion on the analytic structure of the amplitude.

In addition to the branch points due to unitarity, the amplitude  $t_\ell$  may contain singularities, corresponding to the exchange of particles. Stable bound states appear as poles on the physical sheet on the real axis below the two-body threshold. Unstable resonances correspond to poles with a finite imaginary part in the lower half of the complex  $s$ -plane. In order for the resonance to have a noticeable effect on the physical amplitude, its pole needs to be near the physical region. It is therefore located on the second (or higher) Riemann sheet that is reached from the physical region by diving down under the threshold cut [62]. The analytic continuation of the amplitude  $t_\ell(s)$  from the physical plane to the second sheet can be performed using the Schwarz reflection principle [51], which states that the analytic continuation of a complex function  $f(z)$ , which is analytic in the upper half of the complex plane ( $\text{Im } z > 0$ ) and which has real boundary values on part of the real axis, to the lower half of the complex plane can be done via

$$f(z^*) = f^*(z). \quad (101)$$

This implies that, if  $t_\ell$  has a pole at complex  $s = s_0$ , there must be a corresponding pole at  $s = s_0^*$ , i.e. poles outside the real axis must occur in conjugate pairs for analytic amplitudes.

The Breit-Wigner amplitude with dynamic width in Eq. (91) indeed shows the behavior expected from analyticity: (i) There are no poles on the first sheet, except for a possible bound-state pole at  $s = M_b^2$  located on the real axis below the threshold  $4m^2$ , and (ii) if there is a complex a pole at  $s = s_0$  on the lower half of the second sheet, there is a conjugate pole at  $s = s_0^*$  on the upper half, as indicated in Fig. 13. It should be noted here that the Breit-Wigner amplitudes with constant width in Eqs. (85) and (87) only contain a pole at  $s = M_0^2 - i M_0 \Gamma_0$ , i.e. on the lower half plane of the unphysical sheet (see Fig. 13), and not the conjugate one in the upper half of sheet II. Hence the Breit-Wigner amplitudes with constant width violate analyticity. This may be acceptable far above

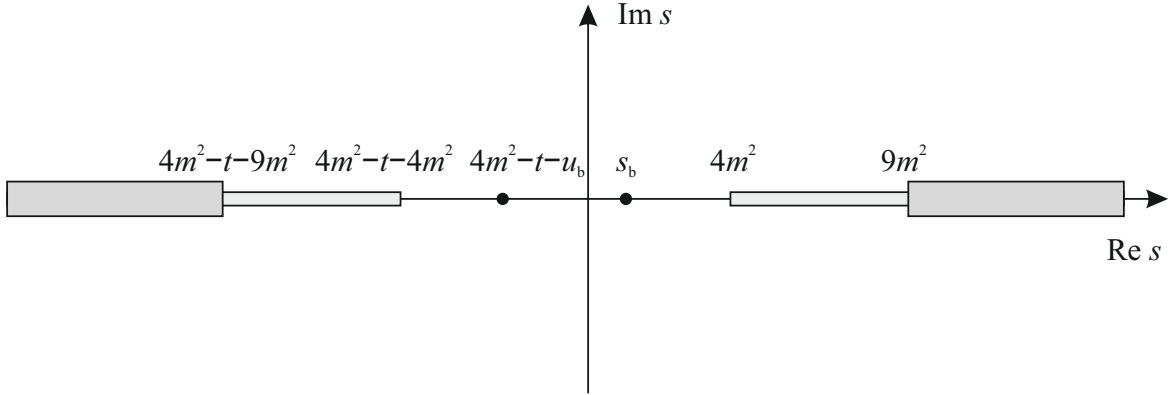


Figure 14: Singularities of the scattering amplitude on the physical sheet of the complex  $s$ -plane for equal-mass  $2 \rightarrow 2$  scattering and fixed  $t$ .  $s_b$  and  $u_b$  denote bound-state poles in the  $s$ - and  $u$ -channel, respectively. The boxes represent the branch points and associated unitarity cuts due to the opening of two- and three-body channels in the  $s$ - and  $u$ -reaction channels, respectively.

threshold, where the pole at  $s_0$  is much closer to the physical axis than  $s_0^*$ .<sup>30</sup> Therefore, its influence on the physical amplitude will be much stronger, while the conjugate pole at  $s_0^*$  will have a negligible effect. This is, however, no longer true close to threshold, where both poles contribute to the physical amplitude.<sup>31</sup>

Until now, we have investigated the analytic structure of the scattering amplitude for the  $s$ -channel process  $1 + 2 \rightarrow 3 + 4$ . Analyticity allows us to continue the amplitude from the physically allowed region for the  $s$ -channel to the  $t$ - and  $u$ -channel regions. Analogously to the  $s$ -channel, where a stable bound state with mass  $M_b < 4m^2$  gives rise to a pole of the amplitude at  $s = s_b \equiv M_b^2$  on the real axis of the physical sheet, a stable bound state in the  $u$ -channel leads to a pole at  $u = u_b$ . The corresponding position of the pole in the complex  $s$  plane is given by Eq. (46), which for equal-mass scattering yields  $s = 4m^2 - t - u_b$  with  $u_b < 4m^2$  and  $s, t < 0$  (see Fig. 9). Similarly, physical thresholds in the  $u$ -channel lead to branch cuts in the  $s$ -plane starting from the two-body branch point  $u = 4m^2$  and extending to infinity along the negative real axis (left-hand cut), as depicted schematically in Fig. 14 for fixed  $t$ . For decreasing  $t \leq 0$ , the  $u$ -channel pole and cut move to the right towards larger values of  $s$  and may even overlap the  $s$ -channel singularities.

### 3.1.6. Discontinuities

Using the Schwarz reflection principle Eq. (101), the partial-wave unitarity equation Eq. (78) can be written as

$$t_\ell(s) - t_\ell(s^*) = 2i t_\ell(s^*) \rho(s) t_\ell(s) , \quad (102)$$

and, taking the limit onto the physical region,

$$t_\ell(s_+) - t_\ell(s_-) = 2i t_\ell(s_-) \rho t_\ell(s_+) , \quad (103)$$

where we have defined  $\lim_{\epsilon \rightarrow 0+} t_\ell(s + i\epsilon) =: t_\ell(s_+)$  and  $\lim_{\epsilon \rightarrow 0+} t_\ell(s - i\epsilon) =: t_\ell(s_-)$ .<sup>32</sup> The left-hand-side of Eq. (103) is the difference of the values of  $t_\ell$  just above and just below the unitarity cut for  $s \geq 4m^2$ , i.e. the discontinuity of  $t_\ell$  across the cut:

$$\text{disc } t_\ell(s) := t_\ell(s_+) - t_\ell(s_-) = 2i t_\ell(s_-) \rho t_\ell(s_+) . \quad (104)$$

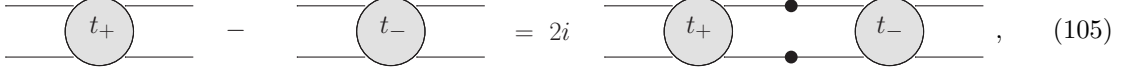
<sup>30</sup>The pole at  $s_0$  can be reached from the physical axis directly by diving under the right-hand cut, while in order to reach  $s_0^*$ , one has to go around the branch point at  $4m^2$ , as can be seen from Fig. 13.

<sup>31</sup>In fact, it is the interplay of the conjugate poles, which makes the amplitude real below threshold.

<sup>32</sup>The phase-space factor is understood to be calculated in the limit  $\rho(s_+)$ .

This derivation of the unitarity relation in terms of the discontinuity of partial-wave amplitudes started from Eq. (38), which relies on Eq. (37), and made use of the Schwarz reflection principle Eq. (101). It should be noted that even if Eq. (37) is not met, the general unitarity relation Eq. (79) can be expressed in terms of the discontinuity of a single analytic amplitude across the unitarity cut. This property of scattering amplitudes is called Hermitian analyticity [45, 63].

Equation (104) can be represented graphically as



$$\text{Diagram 1} - \text{Diagram 2} = 2i \text{Diagram 3}, \quad (105)$$

where  $t_{\pm}$  refer to the amplitudes  $t_{\ell}(s_{\pm})$ , respectively, and the dots indicate that the intermediate-state particles are on mass shell. Expressing the unitarity equations through discontinuity relations will turn out to be essential to combine unitarity with analyticity in so-called dispersion relations, as we will show below.

### 3.1.7. $K$ -Matrix

The unitarity relation Eq. (104) can be cast in a different form by multiplying both sides on the right by  $t_{\ell}^{-1}(s_+)$  and on the left by  $t_{\ell}^{-1}(s_-)$ :

$$t_{\ell}^{-1}(s_+) - t_{\ell}^{-1}(s_-) = -2i \rho(s). \quad (106)$$

Since the discontinuity of  $\rho$  is  $\rho(s_+) - \rho(s_-) = 2\rho(s)$  (cf. Eq. (99)), Eq. (106) is obviously fulfilled by<sup>33</sup>

$$t_{\ell}^{-1}(s) = K^{-1}(s) - i\rho(s), \quad (107)$$

where  $K^{-1}$  is a regular function free of the branch point at  $s = 4m^2$ , i.e.  $K^{-1}(s_+) = K^{-1}(s_-)$ . Hence  $K^{-1}$  must be real. Solving for  $t_{\ell}$ , we arrive at

$$t_{\ell}(s) = K(s) [1 - i\rho(s) K(s)]^{-1} = [1 - iK(s)\rho(s)]^{-1} K(s). \quad (108)$$

Choosing  $K(s) = g^2/(M_0^2 - s)$ , called a “bare” pole, where the parameters  $g$  and  $M_0$  do not have any direct physical meaning, we recover the relativistic Breit-Wigner amplitude Eq. (91). The advantage of this so-called  $K$ -matrix formalism [64, 65] is that one can sum resonance (and possible background) amplitudes in  $K$ , with the resulting  $t_{\ell}$  still being unitary, in contrast to summing resonance poles directly in  $t_{\ell}$ .

For more than one channel, Eq. (108) is to be understood in terms of matrices for  $t_{\ell}$ ,  $K$ , and  $\rho$  in channel space, similar to Eq. (74). One example of the application of the  $K$ -matrix formalism is the Flatté parameterization [66], which is commonly used to describe the  $f_0(980)$  (cf. Section 6.2.3). It has two decay channels,  $i := \pi\pi$  and  $j := K\bar{K}$  [5], with the threshold for  $K\bar{K}$  being very close to the resonance mass. Using Eq. (108) with bare poles  $K_{ij} = g_i g_j / (M_0^2 - s)$ , we arrive at

$$t_{\ell,ij}(s) = \frac{g_i g_j}{M_0^2 - s - i\rho_{ii}(s)g_i^2 - i\rho_{jj}(s)g_j^2}. \quad (109)$$

### 3.1.8. Dispersion Relations

As we saw in the previous sections, unitarity constrains the imaginary part of transition amplitudes. The theory of complex analytic functions provides a very powerful tool to reconstruct the full amplitude from its discontinuity by means of dispersion relations. For an in-depth treatment of

<sup>33</sup>It should be noted that the phase-space term  $\rho(s)$  in Eq. (107) is only one possible choice of functions that have a discontinuity of  $2\rho(s)$  across the normal-threshold cut and thus fulfill the unitarity condition Eq. (106). An example are the functions introduced by Chew and Mandelstam [57].

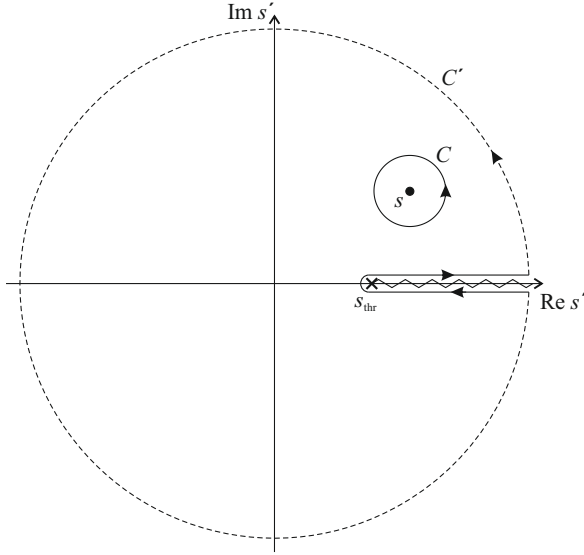


Figure 15: Contours for the Cauchy integral formula Eq. (110) for the calculation of  $f(s)$ , which are constructed such that  $f(s')$  is analytic everywhere inside and on the contour.

dispersion relations in scattering theory, see e.g. Refs. [45, 67]. Here, we only review some simple results based on Cauchy's integral formula [51], which states that

$$f(s) = \frac{1}{2\pi i} \oint_C ds' \frac{f(s')}{s' - s}, \quad (110)$$

with  $f(s')$  being an analytic function inside and on the closed contour  $C$ , and  $s$  any point inside of  $C$ . Since  $s' \neq s$  on the integration path along  $C$ , the integral is well-defined. The virtue of Eq. (110) is that once a function is known on a closed contour  $C$ , it is known everywhere in the region interior to  $C$ . If  $f(s')$  is free of singularities and has only one branch point at  $s' = s_{\text{thr}}$  and a corresponding cut extending from  $s_{\text{thr}}$  to  $+\infty$ , we can deform the contour  $C$  to  $C'$  such that its radius goes to infinity and that it excludes the branch cut, as shown in Fig. 15. Assuming that  $f(s')$  vanishes faster than  $1/s'$  for  $|s'| \rightarrow \infty$ , the circular integral along the dashed line in Fig. 15 does not contribute. The only remaining parts of the integral are the integrals along straight lines in opposite directions above and below the cut, i.e.

$$f(s) = \frac{1}{2\pi i} \int_{s_{\text{thr}}}^{\infty} ds' \frac{f(s'_+) - f(s'_-)}{s' - s} = \frac{1}{2\pi i} \int_{s_{\text{thr}}}^{\infty} ds' \frac{\text{disc } f(s')}{s' - s}. \quad (111)$$

Knowing the discontinuity of  $f(s')$  across the normal-threshold cut, we can reconstruct the full function everywhere in the complex plane by the dispersion integral Eq. (111). If  $f(s')$  does not fall off quickly enough at  $s' \rightarrow \infty$ , the convergence can be restored by applying Eq. (111) to  $f(s')$  divided by a polynomial in  $s'$ . Very often, a polynomial of first order is sufficient, i.e.

$$\tilde{f}(s') = \frac{f(s')}{s' - s_1}, \quad (112)$$

with the subtraction point  $s_1 \neq s$ . This, however, introduces a singularity in  $\tilde{f}(s')$  at  $s' = s_1$ , which has to be taken into account when enlarging the contour  $C$  to infinity in Fig. 15. The integral of

$\tilde{f}(s')$  around  $s_1$  can be calculated using the residue theorem [51]. As a result, we get the so-called once-subtracted dispersion integral,

$$f(s) = f(s_1) + \frac{s - s_1}{2\pi i} \int_{s_{\text{thr}}}^{\infty} ds' \frac{\text{disc } f(s')}{(s' - s_1)(s' - s)} . \quad (113)$$

The subtraction improves convergence of the dispersion integral at the expense of introducing a new subtraction constant  $f(s_1)$ , which has to be determined by external input, e.g. from data.<sup>34</sup>

### 3.1.9. *N-over-D* Method

As discussed in Section 3.1.7, the  $K$ -matrix provides a convenient way to take into account the constraints from unitarity on the partial-wave amplitudes, i.e. the right-hand cut. But, as mentioned in Section 3.1.5, partial-wave amplitudes may in addition have a left-hand cut related to crossed channels, which are associated with exchange processes. The *N-over-D* method allows us to explicitly include the left-hand singularities of the partial-wave amplitudes (see e.g. Ref. [47]). In order to do so, the partial-wave amplitude  $t_\ell$ , e.g. the parameterization for single-channel elastic scattering Eq. (83), is written as the quotient of two functions,

$$t_\ell(s) = \frac{N_\ell(s)}{D_\ell(s)} = N_\ell(s) D_\ell^{-1}(s) , \quad (114)$$

such that  $D_\ell(s)$  only contains the right-hand cut due to unitarity, while  $N_\ell(s)$  only has the left-hand cut, which depends on the exchanges in the crossed channels. Both functions may also contain possible poles in the respective channels. Note that poles in either function can always be represented by zeros of the other. Often,  $D_\ell(s)$  is parameterized to contain universal resonance poles in the  $s$ -channel, while  $N_\ell(s)$  is a smooth function representing background processes. The last expression in Eq. (114) is also valid in matrix form, i.e. for multiple coupled channels [68]. Rearranging Eq. (114) and using unitarity of  $t_\ell$  from Eq. (106), the discontinuity of  $D_\ell(s)$  across the right-hand cut can be expressed as

$$\text{disc } D_\ell(s) := D_\ell(s_+) - D_\ell(s_-) = \left[ t_\ell^{-1}(s_+) - t_\ell^{-1}(s_-) \right] N_\ell(s) = -2i \rho(s) N_\ell(s) . \quad (115)$$

Making use of Eq. (113), the general solution for Eq. (115) can be expressed as a once-subtracted dispersion integral around the subtraction point  $s_1 = 0$ :

$$D_\ell(s) = D_\ell(0) - \frac{s}{\pi} \int_{s_{\text{thr}}}^{\infty} ds' \frac{\rho(s') N_\ell(s')}{s'(s' - s)} . \quad (116)$$

Note that the unitarity condition can still be fulfilled if the subtraction constant  $D_\ell(0)$  is replaced by an analytic function  $D_{\ell,0}(s)$ , which does not have a branch point at  $s = 4m^2$  and no right-hand cut, e.g.  $K^{-1}(s)$  (see Section 3.1.7).

The connection of the *N-over-D* method to the  $K$ -matrix discussed in Section 3.1.7 is made by inserting Eq. (114) into Eq. (107), which yields

$$K_\ell^{-1} = (D_\ell + i \rho N_\ell) N_\ell^{-1} . \quad (117)$$

### 3.1.10. Final-State Interactions

Consider the production of a hadronic final state, e.g. in the decay of a heavier state or in the interaction of two particles (e.g. photoproduction or diffractive production), as shown in Fig. 16. The

---

<sup>34</sup>Even if  $\lim_{|s'| \rightarrow \infty} f(s') = 0$ , subtractions may sometimes be useful to damp the weight of  $f(s')$  at large  $s'$  where it is not known precisely, e.g. in chiral perturbation theory (see Section 3.4).



Figure 16: Amplitude for the production of a hadronic state, e.g. (a) in the decay of a heavier state or (b) in the interaction of two particles, including rescattering.

invariant transition amplitude for these processes, which we denote as  $\mathcal{A}_{fi}$  in order to distinguish it from  $\mathcal{M}_{fi}$ , which is used for the hadronic (re)scattering amplitude in the following, has to satisfy the unitarity relation Eq. (40). The right-hand-side of this relation includes the production of intermediate states  $j$  and the rescattering of these intermediate states to the final state. Assuming that the interaction between intermediate and final states only occurs through the strong interaction (final-state interaction), we can replace  $\mathcal{A}_{fj}^*$  by the scattering amplitude  $\mathcal{M}_{fj}^*$ . Performing a partial-wave expansion of the invariant amplitudes  $\mathcal{A}_{fi}$  and  $\mathcal{M}_{fj}$ , as in Eq. (71), we arrive at the unitarity relation for the partial-wave production amplitude  $a_\ell(s)$  (cf. Eq. (78)):

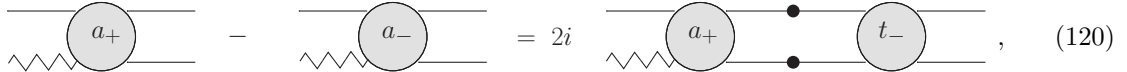
$$\text{Im } a_\ell(s) = t_\ell^*(s) \rho(s) a_\ell(s) . \quad (118)$$

Here,  $t_\ell$  denotes the scattering partial-wave amplitude, which describes the rescattering processes. In general, Eq. (118) again has to be understood as a matrix equation containing several channels. In case of a single open channel, i.e. for elastic rescattering (e.g. with  $t_\ell$  according to Eq. (83)), Eq. (118) implies that the phase of the production amplitude is equal to the one of the elastic rescattering amplitude, since  $\text{Im } a_\ell$  has to be real. This result is known as the Fermi-Watson theorem [69].

Equation (118) can be cast into a discontinuity relation (cf. Eq. (104)),

$$\text{disc } a_\ell(s) := a_\ell(s_+) - a_\ell(s_-) = 2i t_\ell(s_-) \rho a_\ell(s_+) , \quad (119)$$

or, graphically,



where  $a_\pm$  and  $t_\pm$  refer to  $a_\ell(s_\pm)$  and  $t_\ell(s_\pm)$ , respectively (cf. Eq. (105)).

A model based on Eq. (118) and making use of the techniques sketched in Sections 3.1.6 to 3.1.10 has been applied to the COMPASS data on  $\eta\pi$  and  $\eta'\pi$  final states in order to extract pole positions for  $a_2(1320)$ ,  $a_2(1700)$ , and  $\pi_1(1600)$  [70, 71], as discussed in Sections 5.3.5, 6.2.2, 6.3.3, and 6.3.4.

### 3.2. Regge Theory

#### 3.2.1. Motivation

The amplitude  $\mathcal{M}_{fi}(s, t)$  for the scattering of spinless particles in the  $s$ -channel can be expanded in a partial-wave series according to Eq. (71). For small  $s > s_{\text{thr}}$ , the scattering amplitude is dominated by resonances in the intermediate state (see Fig. 17a), e.g. the  $\Delta$  resonance in  $\pi^+ p$  scattering for  $\sqrt{s} \approx 1.2$  GeV. Consequently, the partial-wave series is expected to converge for a limited number of  $\ell$ . For large  $s$ , however, inelastic processes with multi-particle exchanges dominate (cf. Eq. (69)), and the  $s$ -channel expansion will no longer converge. There is, however, an interrelation between the cross section for high-energy  $s$ -channel scattering and the exchange of color-singlet clusters of quarks and gluons in the  $t$ -channel, as depicted in Fig. 17b. It turns out that reactions, for which the exchange of low-mass particles or resonances is allowed in the  $t$ -channel, have considerably higher cross sections than those, for which the exchanged quantum numbers do not correspond to resonances. The allowed quantum numbers for the  $t$ -channel exchanges are determined by the quantum numbers of the initial

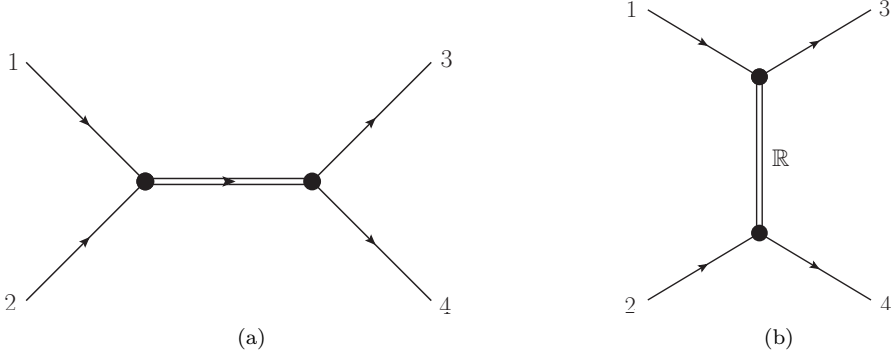


Figure 17: (a)  $s$ -channel scattering  $1+2 \rightarrow 3+4$  via the formation of a resonance in the intermediate state; (b)  $t$ -channel scattering via the exchange of a Reggeon  $\mathbb{R}$ .

and final states of the corresponding  $t$ -channel reaction  $1 + \bar{3} \rightarrow \bar{2} + 4$  (see Section 3.1.2). Examples are the reactions  $K^- p \rightarrow \pi^- \Sigma^+$  and  $\bar{p}p \rightarrow \bar{\Sigma}^- \Sigma^+$ , which are both strongly forward peaked and consequently have a large total cross section. Regge theory links this experimental observation to the fact that these reactions may proceed via  $t$ -channel exchange of  $K^*$  and  $K$  or  $K^*$ , respectively [72]. This is in contrast to the reactions  $K^- p \rightarrow \pi^+ \Sigma^-$  and  $\bar{p}p \rightarrow \bar{\Sigma}^+ \Sigma^-$ , which have a much smaller cross section with no strong dependence on the scattering angle [73, 74], because there are no known resonances with the necessary quantum numbers for  $t$ -channel exchange.

According to Eq. (4), the longest-range component of the force between two hadrons is provided by the exchange of the lightest color-singlet object carrying the quantum numbers required by conservation laws. The exchange of heavier particles will lead to contributions at shorter ranges. Therefore, Yukawa's simple one-pion exchange between interacting hadrons is merely a limiting case of a much more complicated picture. Regge theory provides the generalization of the one-pion exchange model and turned out to be very successful in describing high-energy scattering processes of hadrons.

In order to describe  $s$ -channel scattering processes at large  $s$  and small  $-t$ , we therefore start from a partial-wave expansion in the  $t$ -channel in the physically allowed region, i.e.  $t > 4m^2$  and  $s < 0$  (equal-mass case),

$$\mathcal{M}_{fi}(s(t, z_t), t) = \sum_{\ell=0}^{\infty} (2\ell + 1) t_{\ell, fi}(t) P_{\ell}(z_t), \quad (121)$$

with

$$z_t := \cos \theta_t = 1 + \frac{2s}{t - 4m^2} \quad (122)$$

being the scattering angle in the  $t$ -channel (cf. Eq. (70)).

Assuming that scattering at large  $s$  proceeds via the exchange of a single resonance of spin  $J$  in the  $t$ -channel (as in the one-pion-exchange approximation), only one partial wave of Eq. (121) will contribute:

$$\mathcal{M}_{fi}(s, t) = (2J + 1) t_J(t) P_J(z_t), \quad (123)$$

where we have skipped the channel indices on the right-hand side for clarity. At large  $z_t$ ,  $z_t \propto s$  from Eq. (122) and  $P_{\ell}(z_t) \propto z_t^{\ell}$ , which gives  $\mathcal{M}_{fi}(s, t) \propto s^J$ . Using the optical theorem Eq. (68), the total cross section is then expected to scale like  $\sigma_{\text{tot}} \propto s^{J-1}$  in the high- $s$  limit. For reactions proceeding via pion exchange, for example, the cross section would decrease as  $s^{-1}$ , while for those involving a  $\rho(770)$ , a constant total cross section would be predicted, and the exchange of a spin-2 particle would yield a linearly rising cross section. This, however, does not match the measured total cross sections, displayed in Fig. 18. For energies above the resonance region,  $\sqrt{s} \gtrsim 2.5$  GeV, the total

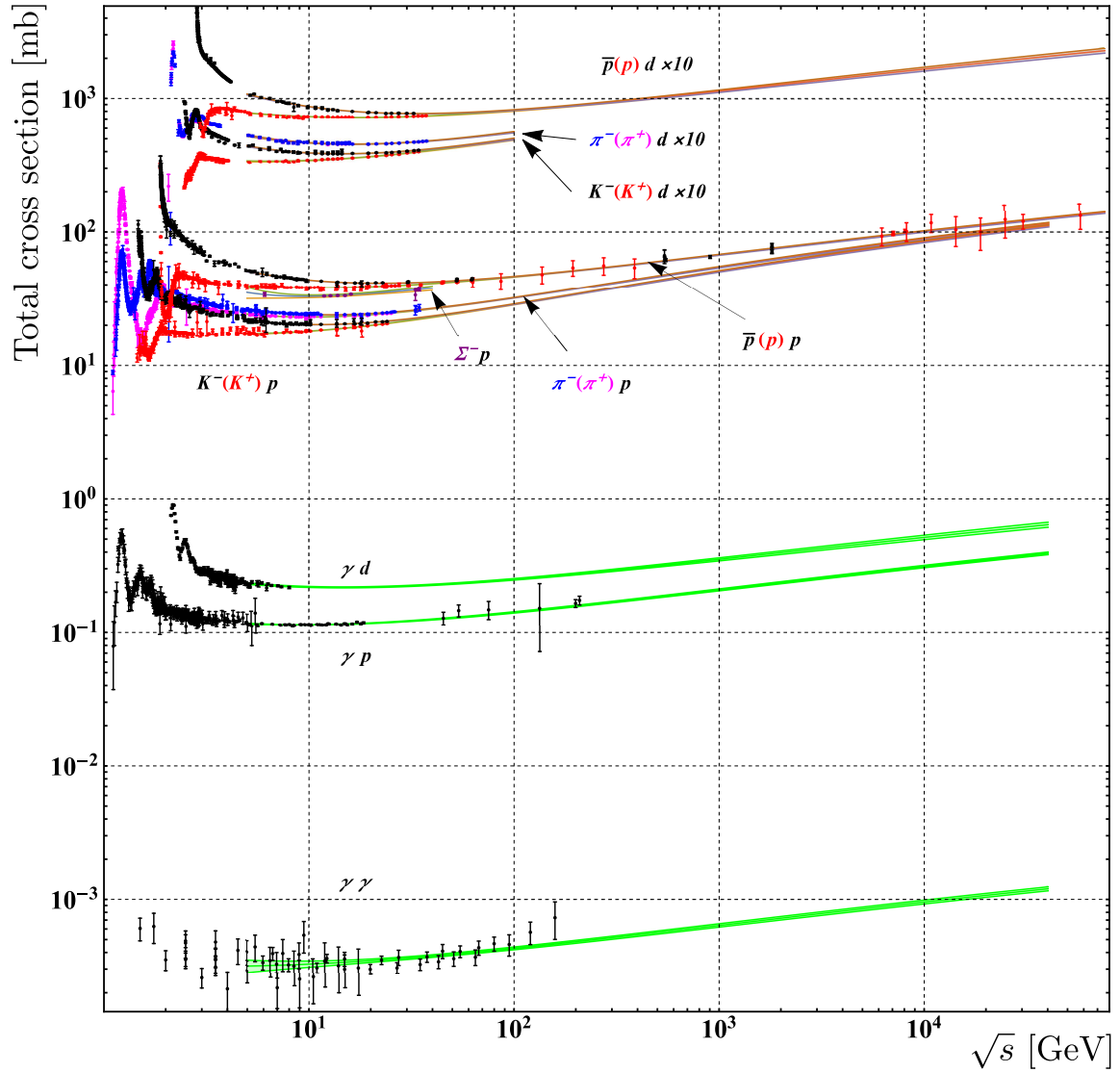


Figure 18: Total cross sections for hadronic,  $\gamma p$  and  $\gamma\gamma$  processes as a function of  $\sqrt{s}$  from Ref. [75].

cross sections first decrease with increasing energy, before they begin to show a very slow rise at large  $\sqrt{s} \gtrsim 20$  GeV. Instead of a single resonance, therefore, one has to consider the collective effect of exchanging all members of a family of resonances in the  $t$ -channel carrying the required quantum numbers in order to describe high- $s$  scattering processes.

The expansion in Eq. (121) in the physical  $t$ -channel region, however, cannot be directly applied to high-energy  $s$ -channel scattering, because  $z_t \propto s$  becomes large for  $s \rightarrow \infty$ . Since  $P_\ell(z_t) \propto z_t^\ell$  for large  $z_t$ , we would have  $P_\ell(z_t) \propto s^\ell$ , so that the series would diverge for large  $s$ . Instead, one has to start in the physical region for the  $t$ -channel where the series converges, i.e.  $t > 4m^2$  and  $s < 0$  (equal-mass case), sum up the series and then analytically continue to large values of  $s$ .

Regge theory provides the mathematical formalism to sum up the  $t$ -channel resonances [76]. It requires an extension of the  $t$ -channel partial-wave amplitudes  $t_\ell(t)$ , which enter in Eq. (121) only for integer values of  $\ell$ , to functions of *complex* angular momentum. We follow the convention to use the symbol  $\alpha$  to denote complex values of angular momentum, keeping the symbol  $\ell$  for integer values. It is thus assumed that in the complex angular momentum plane, or  $\alpha$ -plane, there exists an analytic function  $t(\alpha, t)$ , which satisfies

$$t(\alpha, t)|_{\alpha=\ell} = t_\ell(t) \quad \text{for } \ell = 0, 1, 2, \dots . \quad (124)$$

T. Regge showed that in non-relativistic potential scattering theory the Schrödinger equation for a radially symmetric potential  $V(r)$  can indeed be solved for complex angular momentum  $\alpha$ , yielding a unique analytical extension of the partial-wave amplitudes  $t_\ell(t)$ , provided that  $|t(\alpha, t)|$  has a limited asymptotic behavior for  $|\alpha| \rightarrow \infty$  (see e.g. Refs. [77, 78]). For scattering from a superposition of Yukawa potentials,  $t(\alpha, t)$  is found to be an analytic function except for a number of simple poles in the complex  $\alpha$ -plane called Regge poles or Reggeons, which depend on  $t$  and which we denote as  $\alpha_1(t), \alpha_2(t), \dots, \alpha_n(t)$ . The term “Regge trajectory” is used both for the paths traced out in the complex  $\alpha$ -plane by the functions  $\alpha_i(t)$  as  $t$  varies and for  $\text{Re}[\alpha_i(t)]$  plotted against  $t$ . As long as a Regge trajectory  $\alpha_i(t)$  remains far away from integer values  $\ell$  of  $\alpha$ , there will be little influence of the corresponding pole on  $t(\alpha, t)|_{\alpha=\ell}$ . But if one of the Regge trajectories,  $\alpha_n(t)$ , passes close to a particular integer value of  $\ell = J$  for a given  $t = t_0$ , such that  $\text{Re}[\alpha_n(t_0)] = J$  and  $\text{Im}[\alpha_n(t_0)] \ll 1$ , the amplitude  $t(\alpha, t)|_{\alpha=J}$  will be dominated by this Regge pole for  $t \approx t_0$ . The value of  $t_0$ , for which  $\alpha_n(t_0) \approx J$ , corresponds to the squared mass  $M_J^2$  of a strong interaction resonance with spin  $J$ .<sup>35</sup> A Regge trajectory passing very close to several integer values of  $\ell = 0, 1, 2, \dots$  along the real axis of the complex  $\alpha$ -plane as  $t$  increases thus predicts a sequence of resonances with spin  $J = 0, 1, 2, \dots$  with increasing masses. As was shown in Section 2.2, Fig. 5, the experimentally observed hadrons can indeed be arranged in such families of resonances, having the same quantum numbers  $I, I_3, P$ , and  $S$ . In addition to non-relativistic scattering theory, this observation provides another justification for the rather bold extension to complex angular momentum in Regge theory.

### 3.2.2. Regge Poles and Particles

In the vicinity of a Regge trajectory  $\alpha_n(t)$  passing close to integer values of  $\alpha$ , the amplitude corresponding to the exchange of a whole family of resonances on this trajectory will be dominated by the Regge pole in the complex  $\alpha$ -plane, so we can write it as

$$t(\alpha, t) = \frac{\beta(t)}{\alpha - \alpha_n(t)} . \quad (125)$$

Here,  $\beta(t)$  is the residue function at the pole, which determines the coupling of the pole to the external particles involved in the scattering process. By the definition Eq. (124),  $t(\alpha, t)$  has to be equal to the  $t$ -channel partial-wave amplitude  $t_\ell(t)$  for non-negative integer values of  $\alpha$ . The functions  $\alpha_i(t)$  and their residues are not predicted by theory. They trace out a path in the complex  $\alpha$ -plane

---

<sup>35</sup>A bound state of spin  $J$  will occur if a Regge trajectory passes *through* the point  $\alpha = J$  for a value of  $t < 4m^2$  [53].

when  $t$  changes (“Regge trajectories”, cf. Sections 2.2 and 3.2.1). For simplicity, we consider a linear trajectory, as suggested by the Chew-Frautschi plot in Fig. 5 (dropping the trajectory index),

$$\alpha(t) = \alpha(0) + \alpha' t, \quad (126)$$

with  $\alpha(t)$  passing close to integer values of  $\alpha$  at  $t = M_J^2$ , i.e.  $\alpha \approx \alpha(0) + \alpha' M_J^2$ . Then, according to Eq. (124), the  $t$ -channel partial-wave amplitude is

$$t_\ell(t) = t(\alpha, t)|_{\alpha=\ell} \simeq \frac{\beta(t)}{\alpha' (M_J^2 - t)}. \quad (127)$$

Substituting Eq. (125) into Eq. (121), yields the following expression for the partial-wave expansion of the invariant amplitude in the  $t$ -channel:

$$\mathcal{M}_{fi}(s(t, z_t), t) = \sum_{\ell=0}^{\infty} (2\ell + 1) \frac{\beta(t)}{\ell - \alpha(t)} P_\ell(z_t). \quad (128)$$

This expression can now be analytically continued to the  $s$ -channel physical region, making use of  $z_t \propto s$  (see Eq. (122)) and hence  $P_\ell(z_t) \propto z_t^\ell$  for large  $s$  and  $t < 0$  fixed. We then arrive at the characteristic power-law behavior of the invariant amplitude as a function of  $s$  for large  $s$  and fixed  $t$ , originating from the exchange of a single Regge trajectory of particles or resonances [72]:

$$\mathcal{M}_{fi}(s(t, z_t), t) \propto \sum_{\ell=0}^{\infty} (2\ell + 1) \frac{\beta(t)}{\ell - \alpha(t)} z_t^\ell \propto \beta(t) s^{\alpha(t)}. \quad (129)$$

### 3.2.3. Differential and Total Cross Section

Regge theory, according to Eq. (129), predicts that for large  $s$  and  $t < 0$  the amplitude of the  $s$ -channel reaction produced by a Regge pole in the  $t$ -channel has the form

$$\mathcal{M}_{fi} = h(t) \left( \frac{s}{s_0} \right)^{\alpha(t)} = h(t) e^{\alpha(t) \ln(s/s_0)}, \quad (130)$$

where  $h(t)$  collects all factors depending on  $t$ , and a mass scale  $s_0 := 1 \text{ GeV}^2$  of the order of hadron masses has been introduced to make the radix dimensionless. The differential cross section for a two-body process, Eq. (66), then asymptotically becomes

$$\frac{d\sigma}{dt} = \frac{1}{16\pi s^2} |\mathcal{M}_{fi}|^2 = \frac{|h(t)|^2 s_0^2}{16\pi} \left( \frac{s}{s_0} \right)^{2\alpha(t)-2}. \quad (131)$$

with  $\alpha(t)$  being the leading Regge trajectory,<sup>36</sup> which can be exchanged in the process. Experimentally, it is known that the differential cross section falls roughly exponentially with  $|t|$  for small  $|t|$ . The function  $h(t)$  can thus be approximated by an exponential form factor,  $h(t) \simeq g e^{bt/2}$ , with  $g$  being a coupling constant and  $b$  an exponential slope [53]. Substituting Eq. (126) into Eq. (131) yields

$$\begin{aligned} \frac{d\sigma}{dt} &= \frac{g^2 s_0^2}{16\pi} e^{bt} \left( \frac{s}{s_0} \right)^{2\alpha(0)-2} \left( \frac{s}{s_0} \right)^{2\alpha' t} \\ &= \frac{g^2 s_0^2}{16\pi} \left( \frac{s}{s_0} \right)^{2\alpha(0)-2} \exp \left\{ \left[ b + 2\alpha' \ln \left( \frac{s}{s_0} \right) \right] t \right\}. \end{aligned} \quad (132)$$

<sup>36</sup>In case of several Regge poles, the corresponding amplitudes need to be summed up. The trajectory that passes closest to real integer values of  $\alpha$  is the dominant one and called “leading trajectory”.

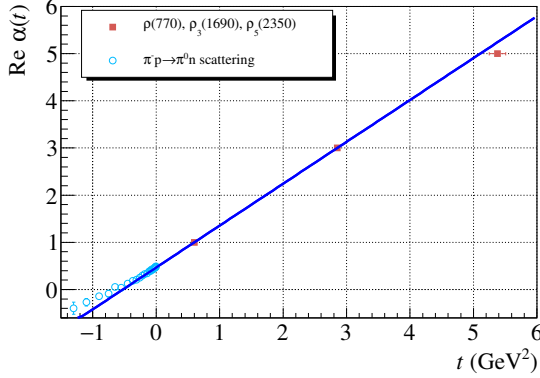


Figure 19: The  $\rho$  trajectory determined from physical particle masses for  $t > 0$ , and extrapolated to  $t < 0$ . The data points at  $t < 0$  are determined by measuring the cross section  $d\sigma/dt$  of the reaction  $\pi^- p \rightarrow \pi^0 n$  [79].

Because of the slope  $\alpha' > 0$  of the Regge trajectory, the forward peak toward  $|t| = |t|_{\min}$  of the differential cross section is expected to become sharper (“shrinks”) as  $\ln s$  increases.

The trajectory  $\alpha(t)$  at high  $s$  and  $t < 0$  can be determined by measuring the differential cross section  $d\sigma/dt$  as a function of  $s$ , and plotting  $\ln(d\sigma/dt)$  versus  $\ln s$  for fixed values of  $t$ . An example is the charge-exchange reaction  $\pi^- p \rightarrow \pi^0 n$ , which in the  $t$ -channel reaction  $\pi^- \pi^0 \rightarrow \bar{p}n$  has quantum numbers  $I = 1$ ,  $P = -1$ , and  $G = +1$ , and thus proceeds via exchange of the  $\rho$  trajectory. The measurement of the differential cross section therefore gives the continuation of the  $\rho$  trajectory to negative values of  $t$  [79]. Figure 19 shows the scattering data from Ref. [79] together with an extrapolation of the linear  $\rho$  trajectory fitted to the masses of  $\{\rho, \rho_3, \rho_5\}$  (cf. Fig. 5). The data can be reasonably well described with a single Regge pole, although some deviations at large values of  $-t$  can be seen, which may be due to additional contributions to the amplitude beyond the leading  $\rho$  trajectory.

The total cross section is related to the imaginary part of the forward elastic scattering amplitude via the optical theorem Eq. (68). Taking only the leading pole of the Regge amplitude at  $t = 0$ , we get for large  $s$

$$\sigma_{\text{tot}} \sim \frac{1}{2s} \text{Im} \mathcal{M}_{ii}(s, 0) \sim s^{\alpha(0)-1}. \quad (133)$$

Figure 18 suggests that the total cross sections approach a constant value for  $s \rightarrow \infty$ , implying  $\alpha(0) \simeq 1$  in Eq. (133). Since all of the known meson trajectories have  $\alpha(0) \lesssim 0.5$ , as has been shown in Fig. 5, a new trajectory with even signature<sup>37</sup> and the quantum numbers of the vacuum has been proposed [80] to be exchanged in scattering processes at high  $s$  in order to obtain an asymptotically constant total cross section. This trajectory is called the Pomeron trajectory  $\alpha_{\text{P}}$ . It has been included as a red line in Fig. 5. For elastic scattering  $1 + 2 \rightarrow 1 + 2$ , the corresponding  $t$ -channel process has a particle and its antiparticle in the initial and final states, respectively, i.e.  $1 + \bar{1} \rightarrow 2 + \bar{2}$ . The exchanged trajectory therefore must have vacuum quantum numbers, i.e.

$$\mathcal{B} = Q = I = S = C = B = 0 \quad \text{and} \quad P = G = C = S = +1. \quad (134)$$

The  $f$  mesons carry the required quantum numbers, but the  $y$ -axis intercept  $\alpha(0)$  of the corresponding Regge trajectory is too low (see Fig. 5). Since the Pomeron trajectory carries even signature, there is no pole and thus no corresponding physical particle near  $t = 0$ , because  $\alpha_{\text{P}}(0) = 1$  is a wrong signature

<sup>37</sup>The term “signature”  $S = \pm 1$  appears in the full expression for the amplitude from Regge theory (see e.g. Ref. [72]) and implies that the amplitude has poles only for even ( $S = +1$ ) or odd ( $S = -1$ ) integer values of  $\alpha(t)$ , and thus for even or odd partial waves.

point. The lowest-mass physical particle of the Pomeron trajectory could have  $\alpha_{\text{P}} = J = 2$ , but has not been identified uniquely until now. It seems plausible to assume that the flavorless exchange in elastic scattering is dominated by gluon ladders, in contrast to other Regge trajectories, which contain valence quarks. Glueballs are therefore discussed as good candidates for physical particle states on the Pomeron trajectory.

### 3.3. Duality in Hadron Interactions

So far, we have treated the two-body  $s$ -channel scattering reaction  $1+2 \rightarrow 3+4$  either via scattering through intermediate  $s$ -channel resonances (see Section 3.1) or via the exchange of resonances in the  $t$ -channel (see Section 3.2), suggesting that the  $s$ -channel resonance mechanism dominates at low energies, while the  $t$ -channel exchanges are responsible for the high-energy behavior of the amplitude (cf. also Fig. 17). These two pictures, however, are not independent of each other, as the discussion on experimental cross sections for certain reactions in Section 3.2.1 has shown. The two approaches are rather two alternative or *dual* ways of describing the same dynamics. One cannot easily combine the two pictures by simply adding the corresponding amplitudes without violating unitarity. The amplitude for a given  $s$ -channel reaction is in principle fully determined by summing up the infinite partial-wave series Eq. (71) in the  $s$ -channel. This, however, is technically difficult, because, at least at high center-of-momentum energies like at COMPASS, many high-spin waves will still contribute significantly to the sum. Therefore, in practice, one has to *truncate* the  $s$ -channel partial-wave expansion at some value of  $\ell$ . The contributions from higher-spin partial waves are then often taken into account by effective background terms, which are represented by  $t$ -channel exchanges. One example is the Deck-background (see Fig. 21d), which is further discussed in Section 4.1. It should be noted, however, that this is an *effective* description of the amplitude, which results from the truncation of the partial-wave series. The splitting is of course not unique and sometimes reaction-dependent. This may result in reaction-dependent resonance parameters [52]. The pole positions in the complex  $s$ -plane and their residues (i.e. couplings), however, should be universal and reaction-independent. Care has to be taken in order not to violate the unitarity condition for the  $S$ -matrix Eq. (32) when including background terms in a model. This has been studied extensively for two-body or quasi-two-body scattering (see e.g. Refs. [59, 64, 81]), and is currently being worked on for three-body scattering (see e.g. Refs. [82–85] and references therein).

### 3.4. Chiral Perturbation Theory

At present, QCD is compatible with all strong-interaction phenomena that are observed at high energies, i.e. in the region of asymptotic freedom. However, there still exists no analytical method to solve the QCD Lagrangian at low energies, i.e. in the confinement regime.

The masses of the three light quarks  $u$ ,  $d$ , and  $s$  are small compared to the masses of light hadrons. In the limit of zero masses of the light quarks, the left-handed and right-handed quark fields decouple from each other in the QCD Lagrangian. This leads to a  $SU(3)_{\text{flavor},L} \times SU(3)_{\text{flavor},R}$  symmetry, which is called *chiral symmetry*. This symmetry can be exploited to construct the low-energy effective field theory of QCD, where, instead of quarks and gluons, hadrons are the relevant degrees of freedom. This approach is called Chiral Perturbation Theory ( $\chi$ PT), which allows the calculation of amplitudes of strong-interaction processes by performing a systematic expansion in powers of the particle momenta (for details see e.g. Refs. [21, 48] and references therein). In this regard, it differs from the usual perturbative approach, which is a power-series expansion in the coupling constant of the interaction. The energy scale, defining the applicability of  $\chi$ PT, is defined by the mass of the pion. The  $\chi$ PT expansion contains universal and process-independent low-energy constants. The values of these constants have to be determined by experiments or by other theoretical calculations, such as lattice QCD. The leading-order mesonic Lagrangian contains two low-energy constants: the pion-decay constant and the scalar quark condensate. The most general next-to-leading-order Lagrangian contains 10 low-energy constants [86].

The spontaneous breaking of the chiral symmetry in the QCD vacuum leads to the occurrence of (almost) massless pseudoscalar Nambu-Goldstone bosons. They are identified with the observed  $\pi$ ,

$K$ , and  $\eta$  mesons, which have smaller masses than the lightest vector meson, the  $\rho(770)$ . In  $\chi$ PT, the small masses of the  $\pi$ ,  $K$ , and  $\eta$  mesons originate from the non-zero quark masses, which break the chiral symmetry explicitly.

Chiral perturbation theory has become a well-established method for describing low-energy interactions of the pseudoscalar octet mesons (see e.g. Ref. [21]). However, its applicability is limited to low-energy processes, typically below the threshold for production of resonances. For the calculation of resonance production, one must revert to lattice QCD (see Section 2.4) or models.

## 4. Experimental Methods

This section covers the experimental methods at our disposal to study the excitation spectrum of light mesons at COMPASS. After a discussion of the relevant physical processes in Section 4.1, we will describe the setup of the COMPASS experiment in Section 4.2, which is optimized to measure scattering reactions of high-energy hadron beams off a stationary target.

### 4.1. Production of Excited Light Mesons at COMPASS

A variety of experimental approaches has been developed to produce excited light-meson states and to study their properties [14]. Such resonances can be produced either in scattering experiments through the interaction of two colliding particles or as intermediate states in the decay of heavier states. Scattering experiments can be further categorized in production and formation experiments. In formation experiments, resonances are formed in the  $s$ -channel without a recoil particle. The invariant mass and the quantum numbers of the intermediate and the final state are fixed by the initial state. Hence formation experiments only yield final states with non-exotic quantum numbers. In production experiments, the total energy is shared between a multi-meson final state and a recoil particle. Hence measurements at a single center-of-momentum energy are sufficient to cover a wide mass range of the multi-meson final state. Since the quantum numbers of the produced multi-meson system are restricted only by the conservation laws of the interaction, both non-exotic and exotic states (see Section 2.3) can be produced. At high  $\sqrt{s}$ , production reactions via  $t$ -channel exchanges dominate the cross section. The dominant contributions in the COMPASS kinematic domain will be described in this section.

COMPASS is a production experiment where light mesons are produced in inelastic scattering of a  $\pi^-$  beam off proton or nuclear targets. At the COMPASS beam momentum of  $190\text{ GeV}/c$ , which corresponds to a center-of-momentum energy  $\sqrt{s}$  of approximately  $19\text{ GeV}$ , the total  $\pi^- p$  cross section is approximately  $24\text{ mb}$  [87, 88] (see also Fig. 18), whereas the elastic  $\pi^- p$  cross section is only about  $3\text{ mb}$  [89, 90]. This means that most of the scattering processes are inelastic. In these inelastic processes, particles may be produced in various ways. COMPASS has performed exclusive measurements of various produced final states. In this paper, we report on the  $\eta\pi p$ ,  $\eta'\pi p$ , and  $\pi^-\pi^-\pi^+ p$  final states. For the process  $\pi^- + p \rightarrow \pi^-\pi^-\pi^+ p$ , for example, a total cross section of  $635 \pm 61\text{ }\mu\text{b}$  was measured at a similar beam energy of  $205\text{ GeV}$  [91], which corresponds to  $18 \pm 2\%$  of the total 4-prong cross section<sup>38</sup> of about  $3.5\text{ mb}$  [89] and to about  $2.6\%$  of the total cross section.

In order to study excited mesons, we select processes, where the target proton scatters elastically (see Section 4). In these reactions, the produced final-state particles hence originate from the beam particle (see Fig. 20). These processes of the form  $\pi^- + p \rightarrow X + p$  are called *single-diffraction dissociation processes*<sup>39</sup> and are characterized by the relation  $s \gg m_X^2 \gg t$ , where  $s$  and  $t$  are the Mandelstam variables of the scattering process as defined in Eqs. (43) and (44) and  $m_X$  is the invariant mass of the  $X$  system. For a  $205\text{ GeV}$   $\pi^-$  beam, the pion single-diffraction cross section for the inclusive reaction  $\pi^- + p \rightarrow X + p$  was measured to about  $1.9 \pm 0.2\text{ mb}$  [92]. For the channel  $X = \pi^-\pi^-\pi^+$ , for example, it was found that about  $2/3$  of the total cross section of  $635 \pm 61\text{ }\mu\text{b}$  quoted above is due to dissociation of the beam pion, whereas about  $1/3$  is due to dissociation of the target proton [91].

At the center-of-momentum energy considered here, the strong interaction between the beam and the target particle is described by  $t$ -channel exchange of Reggeons (see Section 3.2). Since we require elastic scattering of the target proton, only isoscalar exchanges are possible and the reaction is dominated by Pomeron exchange. In addition, also exchange of the  $f_2$  trajectory is possible.

<sup>38</sup>This is the cross section for exclusive events with 4 charged outgoing tracks.

<sup>39</sup>The name diffraction originates from the resemblance of hadronic scattering processes with the diffraction of light waves by a black disk. For both phenomena, the measured intensity is characterized by a dominant forward peak, the diffraction peak, that is accompanied by a series of minima and maxima at characteristic values of  $t$  and the scattering angle, respectively, that depend on the size and shape of the object that the beam scatters off.

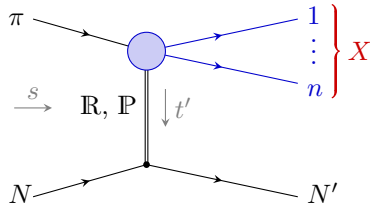


Figure 20: Production of an  $n$ -body system  $X$  via diffraction of a pion beam on a target nucleon  $N$ .

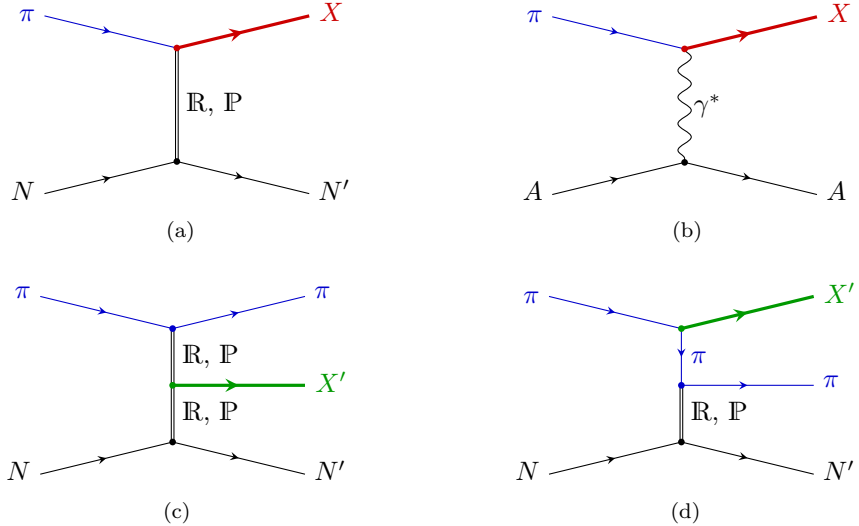


Figure 21: Production mechanisms of mesons for the COMPASS pion beam. (a) Diffractive production of an excited meson  $X$  by exchange of a Reggeon or Pomeron with the target nucleon  $N$ . (b) Production of an excited meson  $X$  by exchange of a quasi-real photon from the Coulomb field of the target nucleus  $A$ . (c) and (d): Examples for double-Regge exchange processes that constitute potential background for the processes in (a) and (b), if  $X'$  represents a subsystem of the final state that  $X$  decays into. E.g., for  $X \rightarrow 3\pi$ ,  $X'$  would represent the  $2\pi$  subsystem. For (a), (c), and (d), the target could also be a nucleus.

Because of the approximately exponential behavior of the differential cross section  $d\sigma/dt$  in Eq. (132), diffractive reactions are characterized by low values of the reduced four-momentum transfer squared  $t'$  (see Eq. (53)). We therefore limit our analyses to the range  $t' < 1(\text{GeV}/c)^2$ . Due to the small  $t'$ , the  $X$  system is produced at small scattering angles and carries most of the beam energy. This means that the  $X$  system is strongly forward boosted. In contrast, the recoiling target proton has only low momentum and is emitted under large angles with respect to the beam axis. Hence particles emitted from the target vertex are kinematically well separated from the particles of the  $X$  decay. This fact is also referred to as *rapidity gap*. We require a rapidity gap in the trigger condition of the experiment (see Section 4).

At low masses of the produced system  $X$ , it is known to be dominated by meson resonances. Figure 21a shows the diagram of such a reaction. The produced intermediate states  $X$  are very short-lived and dissociate via the strong interaction into the measured forward-going  $n$ -body final state that consists mostly of  $\pi$ ,  $K$ ,  $\eta$ , and  $\eta'$ .

The final states  $\eta\pi$ ,  $\eta'\pi$ , and  $\pi^-\pi^-\pi^+$  considered here have  $I^G = 1^-$  quantum numbers identical to those of the beam pion. Hence only states of the  $a_J$  and  $\pi_J$  families, which carry  $J^{PC}$  quantum numbers of  $J^{++}$  and  $J^{-+}$ , respectively, are accessible (see Table I.5). This means in particular, that only spin-exotic resonances with  $J^{PC} = 1^{-+}, 3^{-+}, \dots$  quantum numbers can be studied. Interest-

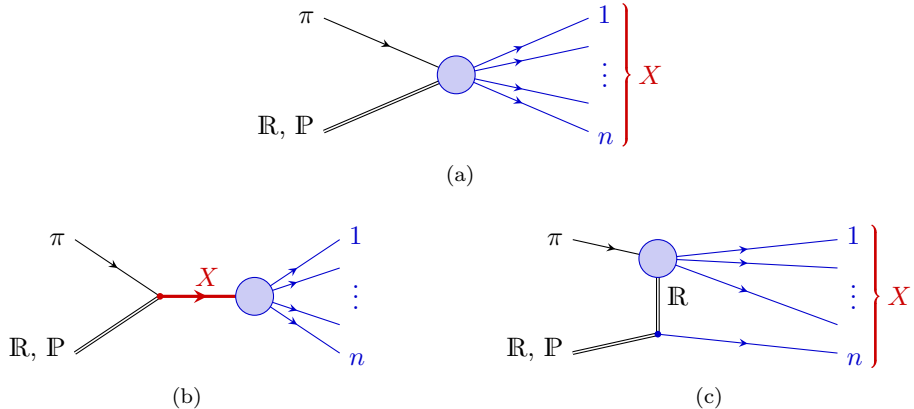


Figure 22: (a) Subprocess of the pion single-difraction process shown in Fig. 20. The blue blob in (a) contains  $s$ -channel processes that proceed via intermediate states  $X$  as shown in (b). In addition, also  $t$ -channel exchange processes contribute. (c) shows an example for such a process. Depending on the final state, the blue blob in (c) may contain further  $s$ -channel subprocesses, i.e. intermediate states  $X'$ , as well as  $t$ -channel subprocesses.

ingly, model calculations [24] and lattice QCD calculations (see Fig. 7) predict the lightest spin-exotic state to have  $J^{PC} = 1^{-+}$ .

In addition to the dominant Pomeron exchange also so-called *double-Regge exchange processes* contribute to the scattering cross section. In these processes, two Reggeons are exchanged and the produced forward-going particles do not originate from the decay of a common resonant intermediate state  $X$ . Hence for a given measured final state, double-Regge exchange processes constitute irreducible non-resonant background contributions to the resonance production in Fig. 21a. However, resonances still may appear in subsystems  $X'$  of the final state. Various Reggeons may be exchanged and Figs. 21c and 21d show only two examples of whole set of possible diagrams.

The exchanged Reggeons affect the kinematic distribution of the corresponding events. There are two special cases, which play a role in the analysis of COMPASS data. In *central-production reactions*, beam and target particle each scatter elastically and a resonance is produced by the fusion of two Reggeons as shown in Fig. 21c. Such processes are characterized kinematically by a fast scattered beam particle, which usually carries a larger momentum than the other final-state particles. Hence backgrounds from central production to diffractive reactions are usually small because they can be separated kinematically. Another class of double-Regge exchange processes is the so-called *Deck process* [93], where the resonant intermediate state is produced at the beam vertex and a pion is exchanged. The pion interacts with the target particle via Pomeron exchange and emerges as a final-state particle (see Fig. 21d). The Deck process is kinematically less well separable from single-difraction and therefore plays an important role in the analysis.

Regge theory allows us to factorize the beam vertex in Fig. 20 from the target vertex. In the partial-wave analysis model that will be discussed in Section 5.1, we consider only the subprocess  $\pi^- + R, P \rightarrow 1 + \dots + n$  as shown in Fig. 22a. We decompose the  $n$ -body system into partial waves by inserting a complete set of intermediate states  $X$  with well defined quantum numbers as shown in Fig. 22b. This is equivalent to resonance production as shown in Fig. 21a. In the considered subprocess, it corresponds to  $s$ -channel scattering. In addition, also  $t$ -channel processes may contribute. Figure 22c shows, as an example, one of the possible  $t$ -channel processes, which correspond to the non-resonant processes shown in Figs. 21c and 21d. As was discussed in Section 3.3,  $s$  and  $t$ -channel processes are related by duality. The applied truncated partial-wave expansion in the  $s$ -channel provides only an effective description of the data and the partial-wave amplitudes that are estimated from the data contain contributions from  $s$  as well as  $t$ -channel processes that need to be taken into account when modelling the partial-wave amplitudes in terms of resonances, which will be discussed in Section 5.3.

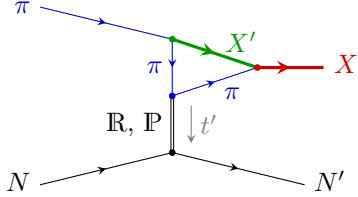


Figure 23: Example diagram for resonance production via rescattering in the Deck process.

Via rescattering, the  $t$ -channel processes discussed above may also contribute to resonance production. Figure 23 shows, as an example, the corresponding lowest-order diagram for a Deck process in Fig. 21d. Typically, these diagrams exhibit a different dependence on  $t'$  than the diagrams for direct resonance production in Fig. 21a.

In addition to the processes described above, which are manifestations of the strong interaction, also electromagnetic processes may contribute. In these so-called *Primakoff reactions*, the beam particle scatters off quasi-real photons in the Coulomb field of the target particle. Since the cross section is proportional to  $Z^2$ , where  $Z$  is the charge number of the target material, and the photons are mostly quasi-real, these processes contribute significantly only for nuclear targets with large  $Z$  and at extremely low  $t' < 10^{-3} (\text{GeV}/c)^2$  at COMPASS energies. Primakoff reactions allow us to study  $\pi^-$ - $\gamma$  reactions, which are difficult to measure otherwise. At low values of the  $\pi^-$ - $\gamma$  center-of-momentum energy, we test predictions from chiral perturbation theory (see Section 3.4); at higher values, we study photoproduction of resonances. Both topics will be covered in Section 7. The latter process is shown in Fig. 21b and we use it to measure the partial widths of radiative decays  $X \rightarrow \pi^- + \gamma$ , which due to their smallness are difficult to measure directly.

#### 4.2. The COMPASS Experiment

COMPASS [94] is a large-acceptance, high-resolution double-magnetic spectrometer, located at the M2 beam line of the CERN Super Proton Synchrotron (SPS). The beam line delivers high-energy and high-intensity secondary hadron and tertiary muon beams as well as a low-intensity electron beam. This makes COMPASS a unique laboratory to investigate non-perturbative aspects of QCD related to the structure and the spectroscopy of hadrons.

The partonic structure of nucleons is studied using hard electromagnetic reactions of naturally polarized 160 GeV/c beam muons with polarized target nucleons. As polarized targets, solid  ${}^6\text{LiD}$  and  $\text{NH}_3$  have been used in the past, inserted in a superconducting solenoid magnet providing an extremely homogeneous magnetic field of 2.5 T over a length of 130 cm along the beam axis.

Strong or electromagnetic interactions of the beam hadrons with different targets give access to the excitation spectrum of hadrons. For this part of the COMPASS physics program, large event samples of diffractive, central, and Primakoff production reactions of hadronic beam particles into final states containing charged and neutral particles have been gathered in several data taking periods in the years 2004, 2008, 2009, and 2012. Mesonic resonances and in particular spin-exotic states are being investigated in a variety of final states. In this review, we will focus on  $\eta\pi$ ,  $\eta'\pi$ , and  $\pi^-\pi^-\pi^+$ . A complete account of the configuration of COMPASS for the measurements with hadron beams in 2008 and 2009 can be found in Ref. [95]. In the following subsections, a short overview of the apparatus is given and some of the key equipments for the spectroscopy program are explained in more detail.<sup>40</sup>

##### 4.2.1. Setup for Hadron Beams

The COMPASS fixed-target setup is logically divided into four main sections along the beam direction. The first section comprises the *beam line* located upstream of the COMPASS target and

<sup>40</sup>For the Primakoff production of  $\pi^-\pi^-\pi^+$ , which is described in Section 7, the setup was slightly different in a few details, which can be found in Ref. [94].

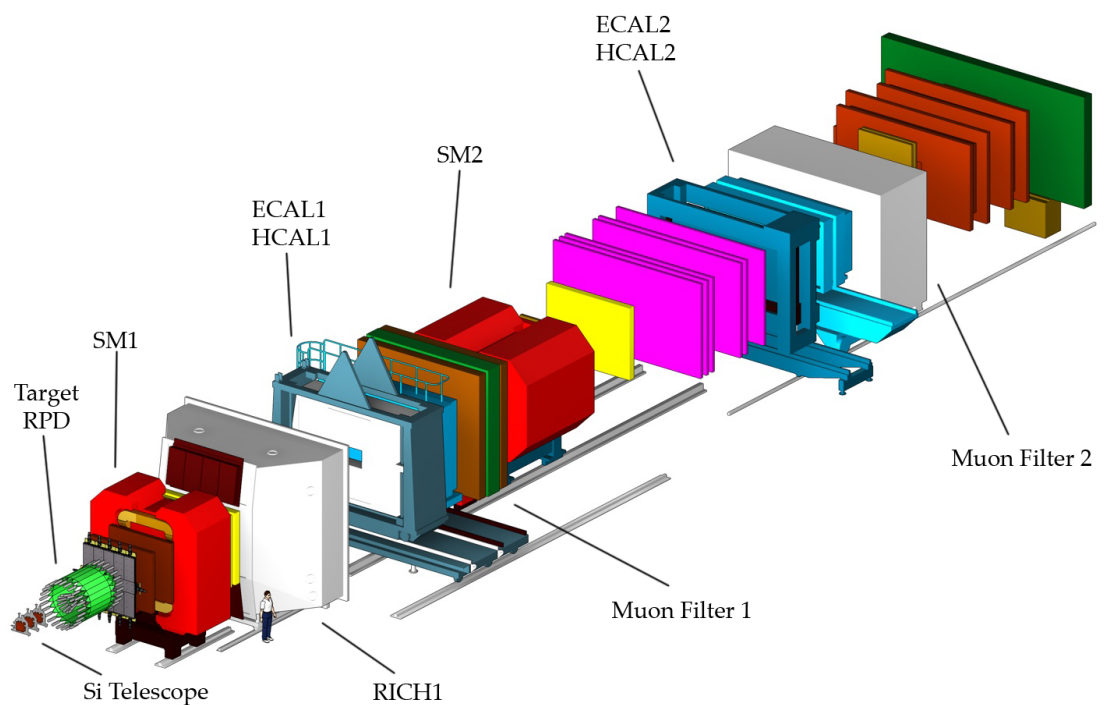


Figure 24: Three-dimensional view of the COMPASS setup for measurements with hadron beams [95]. The different colors indicate different detector types. The CEDAR detectors located about 30 m upstream of the target are not shown.

the detectors which identify the incoming beam particles (CEDAR) and measure their timing and their coarse positions (Scintillating Fibers, Beam Counter, Veto Detectors). The *target region* includes the various targets used for the measurements with hadron beams (liquid hydrogen and nuclear targets Pb, W, and Ni) and the detectors immediately surrounding them (Silicon Microstrip Vertex Detector, Recoil Proton Detector, Sandwich Veto Detector). The third section, called *Large-Angle Spectrometer* (LAS) includes the first dipole magnet (SM1), the tracking detectors up- and downstream of it, and the RICH1 detector for particle identification. The forth part, called *Small-Angle Spectrometer* (SAS), is located downstream of the LAS. It is built around the second dipole magnet (SM2) and includes several types of tracking detectors. Both LAS and SAS comprise a pair of electromagnetic and hadronic calorimeters, and a muon filter. Figures 24 and 25 show a three-dimensional and a top view of the COMPASS setup, respectively.

#### 4.2.2. Beam Line

The COMPASS setup is located at the end of the 1.13 km long M2 beam line of the CERN SPS accelerator. High-intensity secondary hadron beams are produced by slow extraction of 9 to  $12 \cdot 10^{12}$  protons per accelerator cycle with  $400 \text{ GeV}/c$  momentum from the SPS onto a 500 mm thick production target made of Beryllium. Particles emitted from the production target are captured using a set of 6 high-gradient, large-acceptance quadrupoles. Momentum and charge selection is performed in several dipole magnets and collimators along the beam line, with the goal to achieve a momentum resolution below 1%. The maximum beam momentum for the used beam-line optics is  $225 \text{ GeV}/c$ ; momenta up to  $280 \text{ GeV}/c$  can be reached with a slightly larger momentum spread. The results reported in this review have been obtained with a hadron beam of  $(190 \pm 1.4) \text{ GeV}/c$  momentum and an intensity of  $5 \cdot 10^6 \text{ s}^{-1}$  during the extraction from the SPS, which is typically 9.6 s long with a cycle time of 30 to 48 s. At  $190 \text{ GeV}/c$  momentum, the positive hadron beam contains  $p$  (74.6%),  $\pi^+$  (24%), and  $K^+$  (1.4%), the negative beam consists mainly of  $\pi^-$  (96.8%), but also contains small fractions of  $K^-$  (2.4%) and  $\bar{p}$  (0.8%).

Switching between different beams is done fully automatic by loading the corresponding beam elements configuration. This operation typically takes about thirty minutes. During data taking with hadron beams only the trajectory of the incident beam particle is measured, but not the magnitude of its momentum. The Beam Momentum Station (BMS), an equipment used for the determination of the incident momentum during measurements with a muon beam, is moved out of the hadron beam in order to minimize the material budget along the beam path. The momentum spread of the hadron beam arriving at the target is 1%. About 30 m upstream of the COMPASS target, two ChErenkov Differential counters with Achromatic Ring focus (CEDAR) identify and tag each incoming beam hadron.

#### 4.2.3. Target Region

Most of the data with hadron beams were collected using a cylindrical liquid-hydrogen target (see Fig. 26) with a diameter of 35 mm and a length of 400 mm along the beam direction, corresponding to 5.5% of a nuclear interaction length and 4.5% of a radiation length. The target cell is made of 125  $\mu\text{m}$  thick Mylar and surrounded by a cryostat tube made of 1.8 mm thick aluminum, both faces closed by 250  $\mu\text{m}$  thick Mylar windows. Inside the cell, the hydrogen is kept just at the phase transition point at a pressure of 1200 mbar, resulting in a small fraction of evaporated gas at the top. In order to allow for convection and heat exchange, the cylinder axis is tilted with respect to the beam axis by lowering the downstream end by 1 mm. During part of the data taking, the liquid-hydrogen target was removed and replaced with a specially designed solid-target holder, onto which several solid targets with different atomic numbers (Ni, Pb, W) and different thicknesses were mounted.

The recoil-proton trigger and the momentum-conservation criterion applied in the event selection suppress such events on average by about an order of magnitude. The remaining contributions consist predominantly of low-mass  $N^*$  produced at large  $t'$ . In diffractive reactions, target and beam vertex factorize, so that these events are expected to have only little effect on the production of the three-pion final state.

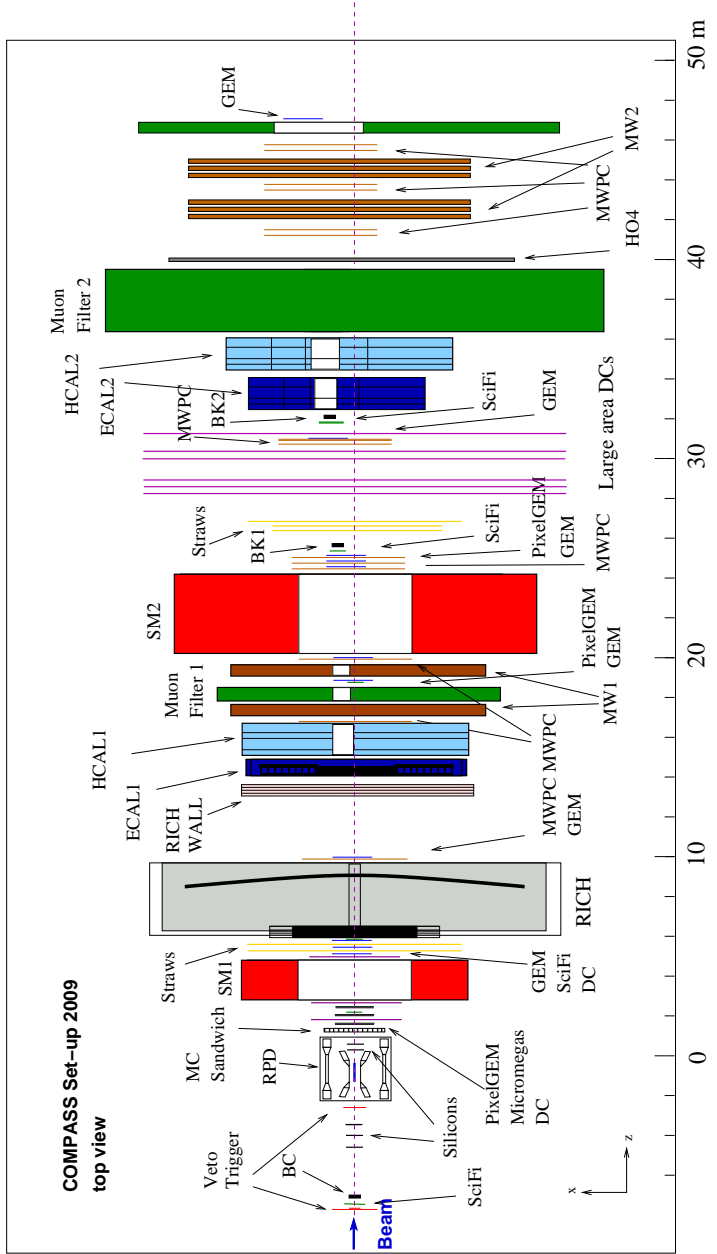


Figure 25: Top view of the COMPASS setup for data taking with hadron beams [95]. The labels indicated the various detectors, as referenced throughout this paper.

A dedicated time-of-flight detector, called Recoil Proton Detector (RPD), was installed around the target. This detector serves a two-fold purpose. First, it was used in the trigger to select single-diffractive events with a recoiling proton. Second, the information from this detector is used in the offline analysis (see Section 4.2.8) to fully reconstruct the produced final states and to ensure the exclusivity of the processes under investigation by measuring the velocity and the energy loss of particles recoiling from the target at angles between  $50^\circ$  and  $90^\circ$  with respect to the beam axis ( $z$  axis). With this information, double-diffraction events with simultaneous excitation of the target particle (see Section 4.1) were suppressed by about one order of magnitude. The PRD consists of two concentric barrels (“rings”) made of plastic scintillator slabs (12 for the inner ring with radius 12 cm, 24 for the outer ring with radius 75 cm), with a length of 50 cm and 115 cm, respectively. Each slab is read out from both sides by photomultiplier tubes, providing position resolutions along  $z$  of  $\sigma_z = 2.7$  cm and 5.0 cm for the inner and outer ring slabs, respectively. RPD straight radial track candidates are reconstructed by combining hits from the inner ring elements with the corresponding outer ring elements in the azimuthal range covered by the inner element.. The momenta of the recoil particles are calculated from the measured time-of-flight using the proton-mass hypothesis, applying a momentum correction to take into account the energy loss in the material crossed. Protons recoiling from the target at large angles can be identified by their energy loss in the outer ring up to a velocity of  $\beta = 0.4$ . A lower momentum cut-off of 270 MeV/ $c$  for detectable recoil protons is given by the energy loss in the target walls and the inner ring. This translates into a minimum momentum transfer of  $|t| = 0.07$  (GeV/ $c$ )<sup>2</sup>. For measurements with nuclear targets, the recoil particle is mostly stopped inside the target and hence does not reach the recoil detector.

For the precise determination of the interaction vertex position, the target is surrounded by 5 stations of Silicon Microstrip Detectors. Three stations are mounted upstream of the target. Together with a scintillating-fiber counter (SciFi1) installed about 7 m upstream of the target, these detectors measure the beam particle trajectory and its time before entering the target. Two other silicon stations are positioned immediately downstream of the target, still inside the RPD as indicated in Fig. 26, to measure the tracks of outgoing charged particles. One station comprises two silicon detectors, each read out by microstrips with a pitch of about 50  $\mu\text{m}$  on both sides, oriented in perpendicular directions. In order to resolve hit ambiguities, the strips of the two detectors in a station form a stereo angle of  $\pm 2.5^\circ$  with respect to the horizontal and vertical axes. The detectors are operated at a temperature of 200 K in order to minimize effects of radiation damage and to improve the signal-to-noise ratio. The vertex resolution achieved with this system is typically of the order of 1 mm along the beam axis and 15  $\mu\text{m}$  in the plane transverse to the beam, but of course depends strongly on the number of outgoing charged particles and their angles.

Immediately downstream of the RPD, a Sandwich Veto Detector [96] was installed in order to veto events with charged or neutral particles emitted at large polar angles with respect to the incident beam, thus enhancing single-diffractive reactions by requiring a rapidity gap between the forward-going system  $X$  and the recoil proton. Including the detector in the trigger logic increased the purity of the diffractive trigger by a factor of about 3.5. The detector consists of a sandwich of five layers of 5 mm thick lead plates, reinforced by 1 mm steel plates on each side, interspersed by five layers of plastic scintillators, the first three with a thickness of 10 mm, the last two with a thickness of 5 mm. The light from the scintillators is extracted by wavelength-shifting fibers and read out by photomultiplier tubes. The efficiency of the detector was determined to be 98% for minimum ionizing particles. It has a transverse size of  $2 \times 2 \text{ m}^2$  with an inner hole matching the opening angle of the RPD and the angular acceptance of the spectrometer.

#### 4.2.4. Large-Angle Spectrometer

The Large-Angle Spectrometer (LAS) connects immediately downstream of the target region and includes the detectors up- and downstream of the first dipole spectrometer magnet (SM1), located at a distance of about 4 m downstream of the target center and operated at a field integral of 1 Tm. Its large aperture matches the opening of the RPD and the Sandwich Veto. Tracking is performed using different types of planar gaseous detectors, depending on the surface to be covered, the expected

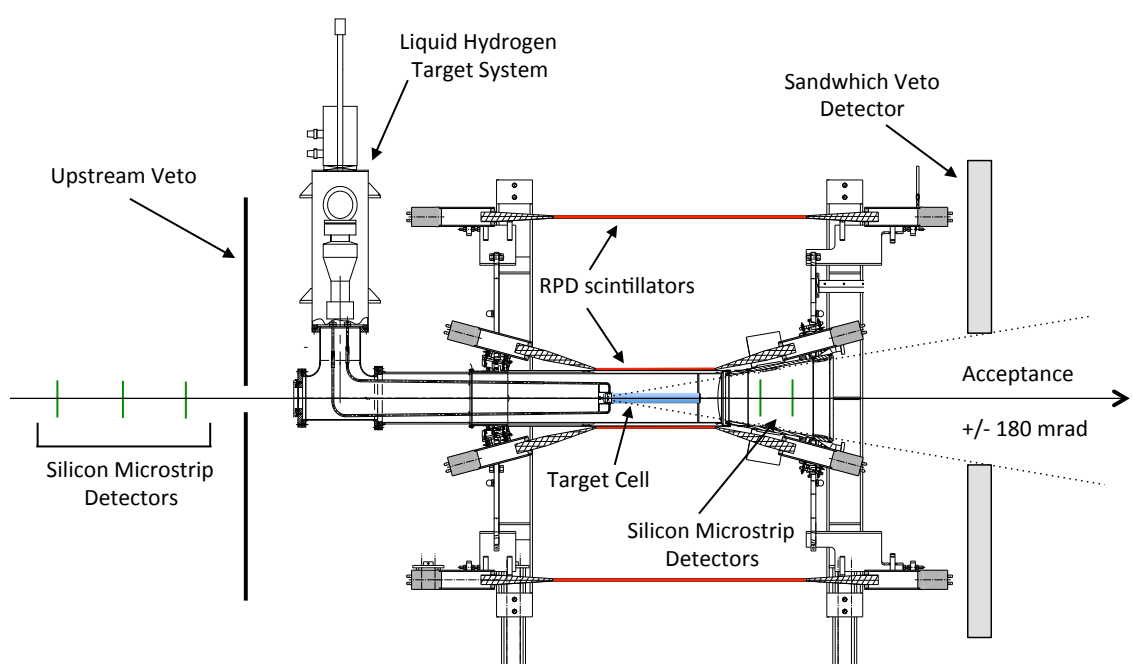


Figure 26: Side view of the target region with the liquid-hydrogen target [95].

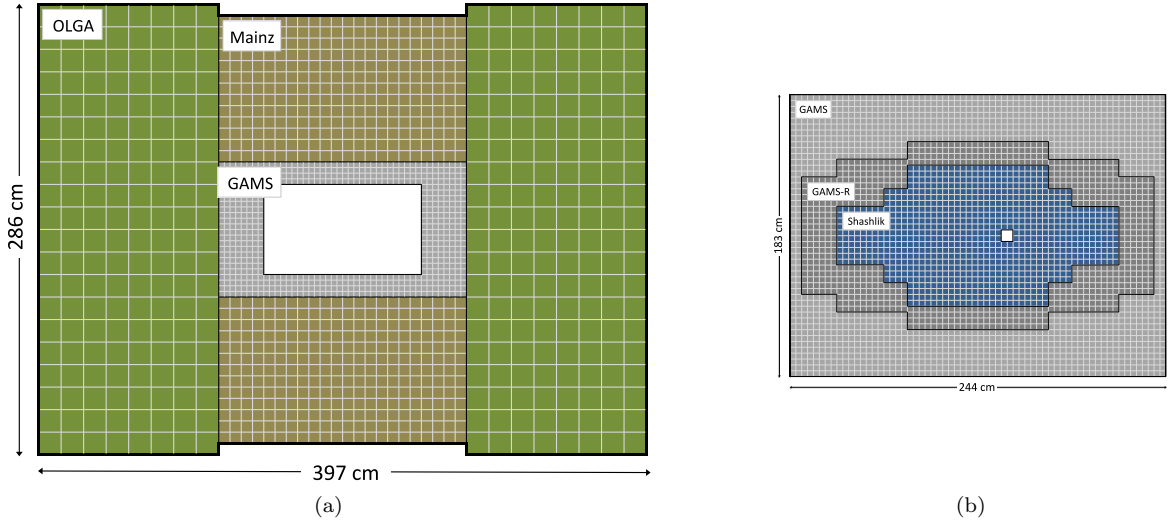


Figure 27: (a) Configuration of ECAL1 [95]. The central area is equipped with GAMS modules. The MAINZ modules are installed above and below the GAMS area. The OLGA modules cover the outer left and right regions. The names refer to the experiments where these modules were originally used. (b) Configuration of ECAL2 (corrected from [95]). The outer and intermediate regions are equipped with GAMS and radiation-hardened GAMS modules, respectively. The inner region is equipped with Shashlik sampling modules. The transverse sizes of all three types of modules are identical. The central beam hole of  $2 \times 2$  modules can be seen as a white spot.

rates and the required resolutions. The large-area tracking is performed by drift chambers, drift tubes, and multi-wire proportional chambers (MWPCs) with active areas up to  $5\text{ m}^2$ . All of them have central inactive areas with diameters of 20 to 30 cm, covered by Micropattern Gaseous Detectors with higher rate capabilities and better resolutions. Upstream of SM1, this region is covered by Micromegas (Micromesh Gaseous Structure) detectors, optimized for operation in hadron beams [95]. Downstream of SM1, GEM (Gas Electron Multiplier) detectors with a two-coordinate readout [97] are used for this purpose. Since both GEMs and Micromegas feature strip-pattered anodes, they have a central inactive region of 5 cm diameter in order to avoid excessive pile-up of signals on the central strips due to beam particles. For tracking directly in and close to the beam region, GEM detectors with pixelized anodes (PixelGEMs) [98] are installed in replacement of all but one scintillating-fibre counters previously used with the muon beam. The momentum resolution for charged particles with momenta from 1 up to about  $15\text{ GeV}/c$ , detected only in the LAS, was determined to be between 1.1 and 1.5%.

Charged hadrons are identified in a Ring-Imaging Cherenkov detector (RICH) filled with  $\text{C}_4\text{F}_{10}$  gas [99]. The Cherenkov light emitted by charged particles passing the radiator gas is focused by a large mirror onto two different types of photon detectors located outside of the geometrical acceptance of the spectrometer. In the peripheral region, MWPCs with CsI photocathodes are used, while the central region is instrumented with multi-anode photomultipliers. The RICH can be used to distinguish pions and kaons with momenta between 5 and  $43\text{ GeV}/c$  at a level of  $2.5\sigma$  or better.

Photons and electrons emitted at large angles are detected and identified in the first electromagnetic calorimeter (ECAL1), which consists of 1500 lead-glass modules of different types (see Fig. 27a). The Cherenkov light created by the charged particles in a shower is detected by photomultiplier tubes mounted to the downstream end face of each module. For neutral pions reconstructed from photon pairs detected in ECAL1, a mass resolution of  $8.8\text{ MeV}/c^2$  has been achieved after careful calibration of all modules.

Directly downstream of ECAL1 a hadronic calorimeter is installed to measure the energy of charged and neutral hadrons. Its 480 modules consist of 40 Fe/scintillator layers, each 20 cm and 5 cm thick,

adding up to 4.8 nuclear interaction lengths. The light produced in the active medium is measured by photomultiplier tubes (PMT).

The LAS is completed by a Muon Detection System consisting of a 60 cm thick iron absorber (Muon Filter 1) sandwiched between large-area drift-tube detectors (MW1).

#### 4.2.5. Small-Angle Spectrometer

Particles emitted from the target at angles smaller than  $\pm 30$  mrad and charged particles with momenta larger than about  $15 \text{ GeV}/c$  pass through central rectangular holes in the calorimeters and the muon absorber of the LAS and enter the Small-Angle Spectrometer (SAS). It includes the second spectrometer magnet (SM2), which is positioned about 22 m downstream of the target and has a higher bending power than SM1 with a field integral of  $4.4 \text{ Tm}$ . Similarly to the LAS, tracking of charged particles is performed using planar gaseous detectors of different active areas and resolutions: MWPCs and drift chambers for the large-area tracking, GEMs for the small-area tracking, scintillating fibres and PixelGEMs for the tracking in the beam. For charged particles detected both in the LAS and the SAS the momentum resolution is determined to be between 0.3 and 0.4%.

Photons are detected in the second electromagnetic calorimeter ECAL2, which is made of 3068 modules of three different types (see Fig. 27b): homogeneous lead-glass modules in the outer part and so-called Shashlik Pb/scintillator sampling modules in the inner part, used for their improved radiation hardness. The mass resolution for  $\pi^0$  reconstructed from photon pairs detected in ECAL2 is  $3.9 \text{ MeV}/c^2$ .

ECAL2 is followed immediately by the second hadronic calorimeter HCAL2, comprising 220 modules made of 36 Fe/scintillator layers read out by PMTs. For both calorimeters in the SAS, the acceptance is maximized by reducing the size of the central hole so that only the beam passes through.

A Muon Detection System comprising a 2.40 m thick concrete absorber (Muon Filter 2) and large-area drift-tube detectors (MW2) completes the spectrometer setup.

#### 4.2.6. Trigger and Data Acquisition

The trigger system of COMPASS serves several purposes. (i) It selects candidates for physics (or calibration) events in a high-intensity beam with a time delay of  $\lesssim 1 \mu\text{s}$ , (ii) it initiates the readout of all detectors, (iii) it distributes a precise reference clock to all front-end electronics modules with a frequency of  $38.88 \text{ MHz}$ , and (iv) it distributes a unique event identification to allow for the merging of the data streams from the individual detector front-ends.

Candidate physics events for hadron spectroscopy are identified by dedicated trigger elements detecting the incoming beam particle, a veto system discarding interactions outside of the target or outside of the spectrometer acceptance, and detectors which enhance the different final states under investigation. Figure 28 shows a schematic view of the hardware elements contributing to physics triggers for hadron spectroscopy.

Beam particles are detected by a coincidence of the analog sum of signals from SciFi1 (vertical fibres) and a scintillator disk with 3.2 cm diameter (Beam Counter) installed 50 cm downstream of SciFi1. These elements also serve as a time reference for the trigger with a resolution of  $(450 \pm 50) \text{ ns}$ . The veto system comprises two scintillator disks of 3.5 cm diameter (Beam Killers) installed 25 m and 33 m downstream of the target, their coincidence inhibiting non-interacting beam particles, the Sandwich Veto (see Section 4.2.3), and three scintillator hodoscopes located upstream of the target.

Diffractive reactions in the liquid-hydrogen target with a recoiling proton are selected by requiring signals in both rings of the RPD (see Section 4.2.3). Target pointing in azimuthal direction is assured by requiring coincidences in matching segments of inner and outer rings. Pions and  $\delta$ -electrons are suppressed by correlating the energy loss in the inner and outer ring using combinations of signals with two different thresholds. The requirement of a signal in both rings selects events with a squared momentum transfer larger than  $|t| \approx 0.07 (\text{GeV}/c)^2$ . In order to also record reactions with smaller values of  $|t|$ , a Multiplicity Counter positioned downstream of the RPD in front of the Sandwich Veto was used for part of the data taking with nuclear targets. This counter selects events with more than a given number (one or two) of minimum ionizing charged particles in the final state,

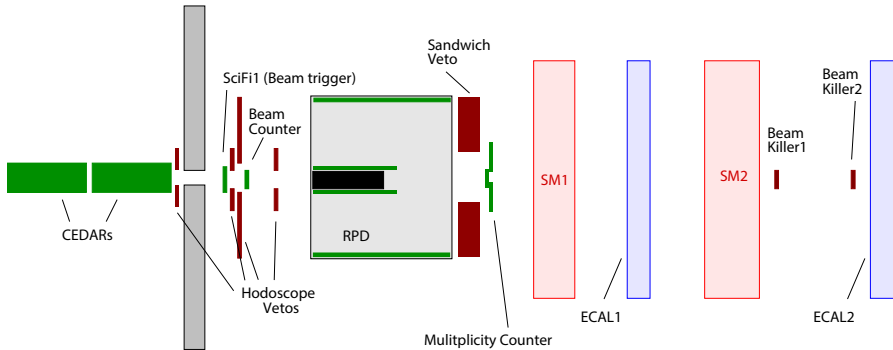


Figure 28: Arrangement of trigger elements in the spectrometer (schematic side view, not to scale) [95].

irrespective of  $|t|$ . Events with a high-energy photon in the final state, e.g. via the Primakoff reaction  $\pi^- + A \rightarrow \pi^- \gamma + A$ , are selected by triggering on photons with energies larger than a given threshold (40 or 60 GeV) detected in the central part of the ECAL2 calorimeter. Last but not least, a trigger on incoming beam kaons using the signals from both CEDARs is used.

Adding up all different triggers, the rate of recorded events at nominal beam intensity of  $5 \cdot 10^6 \text{ s}^{-1}$  amounts to  $3$  to  $4 \cdot 10^4 \text{ s}^{-1}$  with an average event size of 40 kB. This large instantaneous data rate is averaged out to about 300 MB/s over the typical SPS spill structure by using large buffers at every stage of the data acquisition chain. The detector signals are collected by dedicated front-end electronics and are digitized in custom-made TDC<sup>41</sup> or sampling ADC<sup>42</sup> modules. The digitized data from several detector front-ends are then transmitted to about 150 data concentrator modules located in VME<sup>43</sup> crates for easy control and power supply. From there the merged data from several detectors are transmitted via optical fibers to Readout Buffer PCs. These distribute the data from a given event through a Gbit Ethernet switch to Event Builder PCs, which temporarily store the raw data before they are transferred to permanent storage in the CERN data center. The Event Builder PCs also run online monitoring and calibration tasks.

#### 4.2.7. Event Reconstruction

The entities for data recording and processing are so-called *runs* which typically contain data from 100 SPS spills. During data taking, the raw data are split up in files of 1 GB size each with about 1200 such files per run. The reconstruction of the raw data is performed using the software framework CORAL (COMPASS Reconstruction Algorithm) [94]. The first steps of the reconstruction are (i) decoding and mapping, i.e. the translation of raw data to hits in terms of physical detector channels, including amplitude and time information if applicable, and (ii) clustering, i.e. the combination of hits adjacent in space to reconstruction clusters. The latter step requires a precise knowledge of the relative positions in space of sensitive detector elements, e.g. wires, strips, or pixels. These are determined by an iterative software alignment procedure using tracks recorded at low beam intensity both with spectrometer magnets off and on.

The next steps of the reconstruction depend on the detector type. The information from the tracking detectors is used to reconstruct charged-particle tracks and to determine their momenta from the bending by the two spectrometer magnets. The association of detector clusters to track candidates is performed by first searching for straight track segments in regions without or negligible magnetic field and without large amounts of material. These segments are then bridged across the

<sup>41</sup>Time-to-digital converter; measures signal time.

<sup>42</sup>Analog-to-digital converter; measures signal amplitude.

<sup>43</sup>The Versa Module Eurocard standard defines a bus protocol as well as mechanical and electrical interfaces.

magnets and absorber walls by extrapolation and matching within a variable road width and by comparing the track segments to a dictionary of reconstructable tracks. The precise determination of the track momentum and of the charge sign is finally done using a Kalman filter for track fitting.

The vertexing algorithm attempts to combine beam-particle tracks reconstructed in the beam telescope and any number of final-state-particle tracks reconstructed in the spectrometer to form primary vertices. The optimal vertex positions are determined using a Kalman filter which progressively tests the contribution of each track to the overall  $\chi^2$  of the vertex. Secondary vertices from decays of long-lived unstable particles are constructed from pairs of two oppositely charged spectrometer-tracks, which do not contain a beam track.

Clusters in the electromagnetic calorimeters may contain showers from several incident particles overlapping in space and time. In order to disentangle the individual contributions, several shower profiles, which have been pre-determined from single electron or photon events, are fitted to the reconstructed clusters in the plane transverse to the beam direction, until a good description is reached. In order to optimize the energy resolution, the cell responses are calibrated using  $\pi^0$  reconstructed from events containing at least two photons.

#### 4.2.8. Offline Event Selection

The events selected by the hardware triggers (see Section 4.2.6) contain reactions of various beam-particle species into a variety of final states. The analysis of the data set proceeds by selecting exclusive events corresponding to a given reaction channel. The final states may comprise both charged and neutral particles.

In the following, we discuss the criteria for offline event selection, which are common to all analyses. As example, the steps are illustrated for  $\eta^{(\prime)}\pi p$  and  $\pi^-\pi^-\pi^+ p$  final states produced by incoming  $\pi^-$  scattering on a proton target.

1. Events from a given physics trigger are selected by requiring that the corresponding trigger bit is set for the event.
2. A primary vertex (see Section 4.2.7) between the beam particle and the forward-going charged particles is required to be formed in a fiducial volume within the target. Charge conservation between incoming and outgoing particles needs to be fulfilled. In case more than one vertex candidate has been found by the vertexing algorithm, usually the one with the better  $\chi^2$  value is chosen. Figure 29 shows the spatial distribution of primary vertices for events with three forward-going charged particles.
3. In case of final states containing neutral short-lived particles decaying to photons, e.g.  $\pi^0$  or  $\eta$ , photon showers reconstructed by the calorimeters are selected by requiring that
  - (a) no charged-particle track is associated with the shower,
  - (b) the time difference between the beam track and the calorimeter shower does not exceed a certain maximum value,
  - (c) the shower energies are above certain thresholds (typically 1 GeV for ECAL1 and 4 GeV for ECAL2),
  - (d) the shower is reconstructed in a geometrical position that is not obstructed from the target by a large amount of material.

Based on the energy of the reconstructed photons, their three-momenta are determined by assuming that they originate from the primary vertex. Final-state  $\pi^0$  or  $\eta$  are selected by combining photon pairs and applying a cut on the two-photon invariant mass. Figure 30 shows the two-photon invariant mass distribution from the reaction  $\pi^- + p \rightarrow \pi^-\pi^-\pi^+\gamma\gamma + p$ .

4. Transverse momentum conservation at the interaction vertex is ensured by requiring exactly one recoil track detected in the RPD that is back-to-back with the forward-going system reconstructed in the spectrometer in the plane perpendicular to the beam direction (“coplanarity cut”).

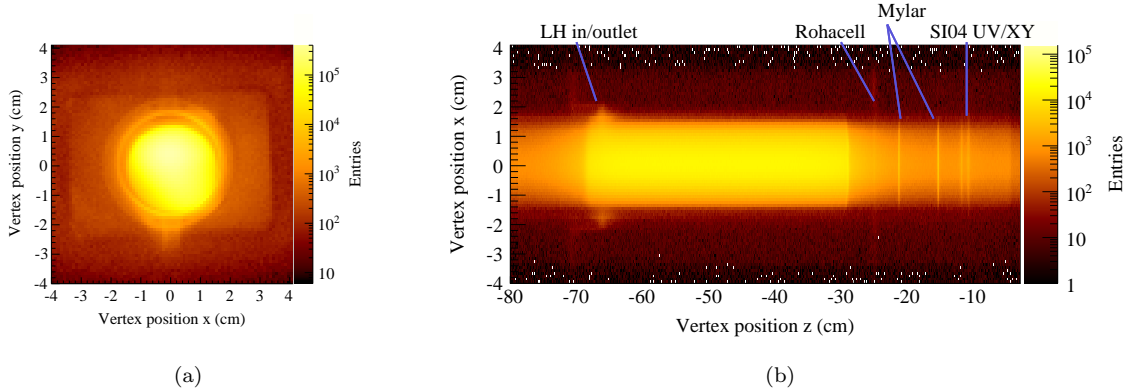


Figure 29: Spatial distribution of the primary vertices for the liquid-hydrogen target for events with three forward-going charged particles [95], (a) in the plane perpendicular to the beam direction and (b) in the horizontal plane with  $z$  along the beam.

5. Energy conservation is enforced by requiring that the energy sum of all final-state particles corresponds to the nominal beam energy within a window given by the momentum spread of the beam (“exclusivity cut”). Figure 31 shows the total energy calculated from all reconstructed final-state particles including the recoil proton for the reaction  $\pi^- + p \rightarrow \pi^- \pi^- \pi^+ + p$ .
6. Depending on the reaction under study, the beam particle may be required to be tagged or vetoed by the CEDAR detectors.
7. In the same way, tagging and vetoing of forward-going final-state particles by the RICH may be required. In Fig. 32, the Cherenkov angles for reconstructed rings are shown as a function of the particle momenta. The bands correspond to different particle types and can be used for identification.
8. Further kinematical cuts, e.g. on the rapidity of the fastest particle, defined by<sup>44</sup>

$$y = \frac{1}{2} \ln \frac{E + p_z}{E - p_z} , \quad (135)$$

or on the Feynman- $x$  variable, defined by

$$x_F := \frac{p_z}{p_{z \max}} \approx \frac{2p_z \text{ CM}}{\sqrt{s}} , \quad (136)$$

may be applied in order to select or remove events from production reactions with distinct kinematics, e.g. central production (see Section 4.1).

<sup>44</sup>Here, the  $z$  direction is defined by the measured direction of the beam particle.

<sup>45</sup>Figure 30 is an unpublished auxiliary plot from the analysis presented in Ref. [101].

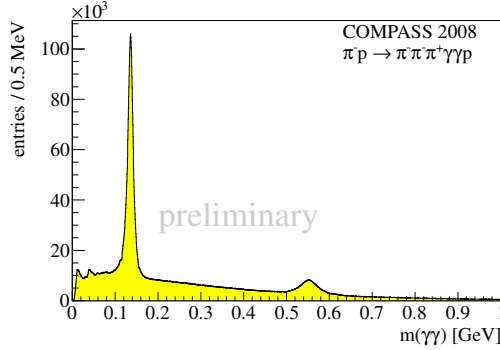


Figure 30: Invariant mass of photon pairs from the reaction  $\pi^- + p \rightarrow \pi^- \pi^- \pi^+ \gamma\gamma + p$  [100].<sup>45</sup>

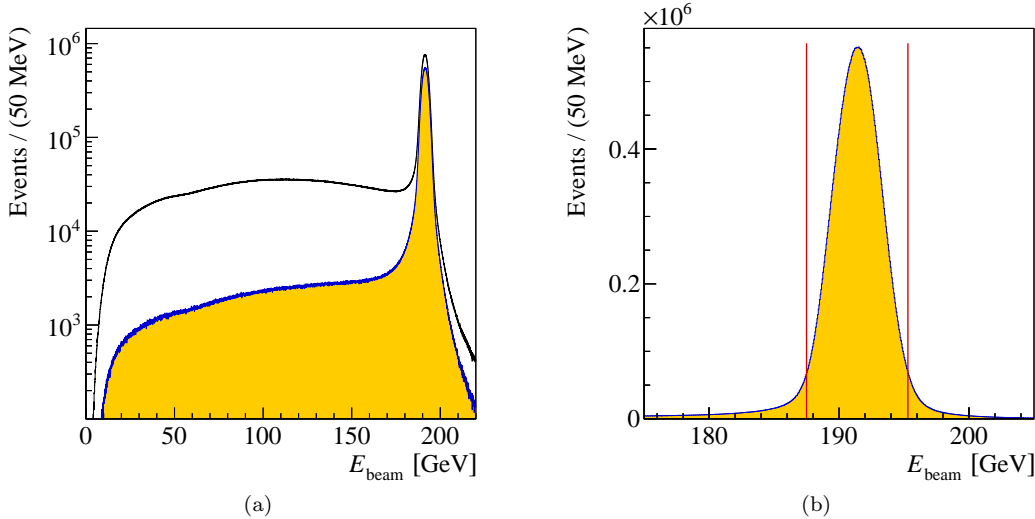


Figure 31: Total energy of all reconstructed final-state particles for the reaction  $\pi^- + p \rightarrow \pi^- \pi^- \pi^+ + p$  [102], (a) full energy range, without (empty histogram) and with coplanarity cut (full histogram), (b) zoomed range with the vertical lines indicating the accepted range around the nominal beam energy.

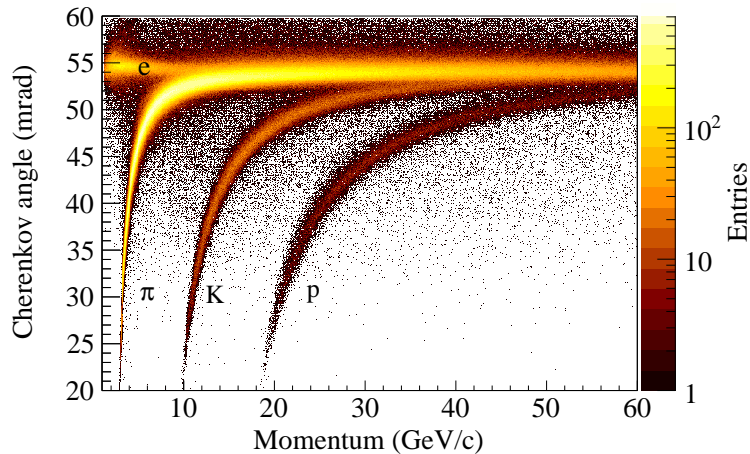


Figure 32: Cherenkov angle for reconstructed rings versus particle momentum for  $\text{C}_4\text{F}_{10}$  radiator gas [95].

## 5. Partial-Wave Analysis Formalism

### 5.1. Analysis Model

#### 5.1.1. Ansatz

As discussed in Section 4.1, we measure at COMPASS single-diffraction dissociation reactions, which are inelastic scattering processes of the form

$$a + b \rightarrow (1 + 2 + \dots + n) + c . \quad (137)$$

In these reactions, a high-energetic beam hadron  $a$  interacts strongly with a target hadron  $b$  thereby producing an  $n$ -body hadronic final state  $(1, 2, \dots, n)$  and a target recoil  $c$ .

Based on Eq. (57) in Section 3.1.3, we construct a model for the cross section of reaction (137) by assuming that the  $n$ -body final state is produced via  $t$ -channel exchange processes and by performing an  $s$ -channel partial-wave expansion of the  $n$ -body system by inserting a complete set of intermediate states  $X$  with well defined quantum numbers. We hence subdivide process (137) into two subprocesses: (i) an inelastic two-body scattering reaction  $a + b \rightarrow X + c$  and (ii) the subsequent decay of state  $X$  into the  $n$ -body final state, i.e.  $X \rightarrow 1 + 2 + \dots + n$ . This is shown in Fig. 33. Subprocess (i) is described in terms of the invariant mass  $m_X$  of the  $n$ -body system and the two Mandelstam variables  $s$  and  $t$ , where  $s$  is the squared center-of-momentum energy of the  $(a, b)$  system (see Eq. (43)) and  $t$  the transferred squared four-momentum (see Eq. (44)). For convenience, we use instead of  $t$  the positive definite reduced squared four-momentum transfer  $t'$  as defined in Eq. (53). For a fixed-target experiment such as COMPASS,  $p_a$  and  $p_b$  are constant and hence the center-of-momentum energy  $\sqrt{s}$  of the scattering reaction is fixed. In this case, the kinematic distribution of the final-state particles depends on  $m_X$ ,  $t'$ , and a set of  $(3n - 4)$  additional phase-space variables (see Section 3.1.1) represented by  $\tau_n$ . These phase-space variables fully describe the  $n$ -body decay and will be defined in Sections 5.1.2 and 5.1.4.

Analogous to subdividing the scattering process, we split the phase space of the  $(n + 1)$  outgoing particles into a two-body phase space for  $X$  and  $c$  (see Eq. (60)) and an  $n$ -body phase space for the decay  $X \rightarrow 1 + 2 + \dots + n$  (see Eq. (41)). For any given choice of the phase-space variables  $\tau_n$ , the Dirac delta function in Eq. (41) that represents four-momentum conservation can be integrated out so that the differential phase-space element can be written as

$$d\Phi_n(m_X, \tau_n) = \rho_n(m_X, \tau_n) d\tau_n , \quad (138)$$

where the phase-space factor  $\rho_n(m_X, \tau_n)$  represents the density of states in the variables  $m_X$  and  $\tau_n$ .<sup>46</sup> A convenient choice for  $\tau_n$  is presented in Appendix A.

<sup>46</sup> For example, the two-body phase-space element can be expressed in terms of the polar and azimuthal angles of one of the two particles in their center-of-momentum frame, i.e.  $\tau_2 = \Omega = (\vartheta, \phi)$ , then using Eq. (60) and  $\sqrt{s} = m_X$  we get

$$d\Phi_2(m_X, \tau_2) = \rho_2(m_X, \tau_2) d\tau_2 \quad \text{with} \quad \rho_2(m_X, \tau_2) = \frac{1}{(4\pi)^2} \frac{q}{m_X} . \quad (139)$$

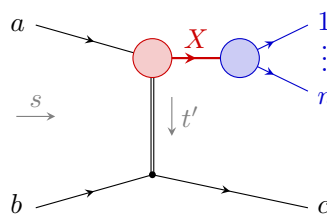


Figure 33: Production of an intermediate state  $X$  by excitation of beam particle  $a$  via  $t$ -channel exchange with target particle  $b$ . The intermediate state decays into an  $n$ -body hadronic final state  $(1, 2, \dots, n)$ .

Splitting the phase space and using Eqs. (53), (57), and (58), we can write the cross section for reaction (137) as

$$\begin{aligned} & d\sigma_{a+b \rightarrow (1+\dots+n)+c} \\ &= \frac{1}{16\pi} \frac{1}{[s - (m_a + m_b)^2][s - (m_a - m_b)^2]} |\mathcal{M}_{fi}|^2 dt' \frac{2m_X}{2\pi} dm_X d\Phi_n(p_X; p_1, p_2, \dots, p_n). \end{aligned} \quad (140)$$

Here, we have expressed the flux factor in terms of  $s$  and we have written the two-body phase space of the  $(X, c)$  system (see Eq. (60)) in terms of  $t'$ . We also have used the fact that for an unpolarized reaction,  $\mathcal{M}_{fi}$  is independent of the azimuthal angle of  $X$  about the beam axis in the center-of-momentum frame of the reaction  $a + b \rightarrow X + c$ . The factor  $2m_X dm_X$  arises due to the splitting of the phase space.

The intensity distribution, i.e. the distribution of the events that are produced in reaction (137), is

$$\mathcal{I}(m_X, t', \tau_n) := \frac{dN}{dm_X dt' d\Phi_n(m_X, \tau_n)} \propto \frac{d\sigma_{a+b \rightarrow (1+\dots+n)+c}}{dm_X dt' d\Phi_n(m_X, \tau_n)} \propto m_X |\mathcal{M}_{fi}(m_X, t', \tau_n)|^2, \quad (141)$$

where  $N$  is the number of produced events and  $d\Phi_n(m_X, \tau_n)$  is given by Eq. (138). On the right-hand side of Eq. (141), all constant factors have been dropped. It is worth noting that  $\mathcal{I}$  is differential in the Lorentz-invariant  $n$ -body phase-space element and is thus independent of the particular choice of the phase-space variables  $\tau_n$  because the phase-space density  $\rho_n(m_X, \tau_n)$  in Eq. (138) contains the corresponding Jacobian. The intensity  $\mathcal{I}$  essentially represents the deviation of the kinematic distribution of the produced final-state particles from a pure phase-space distribution. It is therefore a direct measure for  $|\mathcal{M}_{fi}(m_X, t', \tau_n)|^2$ .

We first construct a model for the amplitude  $\mathcal{M}_{a+b \rightarrow X+c}$  for the hypothetical process, where only a single intermediate state  $X$  is produced and decays into the measured  $n$ -body final state. In Section 5.1.7, we will extend this model to the case of several intermediate resonances. Since production and decay of the intermediate state  $X$  are independent, we can factorize the amplitude into three parts: (i) an amplitude  $\mathcal{P}_{a+b \rightarrow X+c}(m_X, t')$  that describes the production of  $X$ , (ii) a dynamical amplitude  $\mathcal{D}_X(m_X)$  that describes the propagation of  $X$ , and (iii) the decay amplitude  $\tilde{\Psi}_{X \rightarrow \text{FS}}(m_X, \tau_n)$  that describes the decay of  $X$  into the  $n$ -body final state via a particular decay chain. Therefore,

$$\mathcal{M}_{a+b \rightarrow (X \rightarrow \text{FS})+c}(m_X, t', \tau_n) = \mathcal{P}_{a+b \rightarrow X+c}(m_X, t') \mathcal{D}_X(m_X) \tilde{\Psi}_{X \rightarrow \text{FS}}(m_X, \tau_n). \quad (142)$$

### 5.1.2. Decay Amplitude

The decay amplitude  $\tilde{\Psi}_{X \rightarrow \text{FS}}(m_X, \tau_n)$  in Eq. (142) is calculated using the isobar model [103, 104]. In this model, the  $X$  decay is described as a chain of successive two-body decays via additional intermediate resonances, the so-called *isobars*, which appear in the subsystems of the  $n$ -body final state.<sup>47</sup> It is also assumed that the outgoing particles of the two-body decays do not interact with each other, i.e. final-state interactions are neglected.

The fundamental building block for the construction of  $\tilde{\Psi}_{X \rightarrow \text{FS}}$  is the two-body decay amplitude  $\mathcal{A}_r^{J_r M_r}$ . It describes the propagation of a resonance  $r$  with spin  $J_r$  and spin projection  $M_r$  with respect to a chosen quantization axis and the decay of  $r$  into particles 1 and 2. The two-body decay amplitude can be calculated in the  $r$  rest frame using the helicity formalism [47, 106–110]. The two

---

<sup>47</sup>For example, the decay  $X^- \rightarrow \pi^- \pi^- \pi^+$  may proceed via  $\rho(770)^0$  as an intermediate  $\pi^- \pi^+$  resonance, i.e.  $X^- \rightarrow \rho(770)^0 \pi^- \rightarrow \pi^- \pi^- \pi^+$ . The usage of the term isobar for the intermediate states has historical reasons. The isobar model was first introduced by Lindenbaum and Sternheimer in Ref. [105] to describe excited intermediate nucleon resonances, which they called isobars in analogy to nuclear physics.

daughter particles have spins  $J_1$  and  $J_2$  and are described in the helicity basis, where the quantization axes are the directions of the momenta of particles 1 and 2. In the  $r$  rest frame, the momenta of particles 1 and 2 are by definition back to back and have a fixed magnitude  $q$ , which is given by Eqs. (62) and (63). Hence the kinematics of the decay  $r \rightarrow 1 + 2$  is completely defined by the polar angle  $\vartheta_r$  and the azimuthal angle  $\phi_r$  of the momentum of one of the daughter particles.

The daughter particles 1 and 2 are described by the two-particle plane-wave center-of-momentum helicity state  $|\vec{p}_1, \vec{p}_2; \lambda_1, \lambda_2\rangle$ . Here,  $\lambda_1$  and  $\lambda_2$  are the helicities of the two daughter particles and  $\vec{p}_1 = -\vec{p}_2 =: \vec{q}$ . Since  $|\vec{q}|$  as given by Eqs. (62) and (63) is constant, the quantum state can be written as  $|\vartheta_r, \phi_r; \lambda_1, \lambda_2\rangle$ . The amplitude for the propagation and the decay of resonance  $r$  with mass  $m_r$  and spin state  $|J_r, M_r\rangle$  is

$$\mathcal{A}_r^{J_r M_r}(m_r, \vartheta_r, \phi_r) = \mathcal{D}_r(m_r) \sum_{\lambda_1, \lambda_2} \langle \vartheta_r, \phi_r; \lambda_1, \lambda_2 | \hat{T}(m_r) | J_r, M_r \rangle , \quad (143)$$

where  $\mathcal{D}_r(m_r)$  describes the propagation of  $r$  and  $\hat{T}(m_r)$  is the transition operator of the decay  $r \rightarrow 1 + 2$ . The coherent summation over all allowed daughter helicities in Eq. (143) is performed only in the case, where particles 1 and 2 appear as intermediate states in the decay chain of the  $X$ . If one or both daughters are (quasi-stable) final-state particles and their helicity is not measured, the summation over the respective helicities has to be performed incoherently at the intensity level.

We expand the helicity amplitude into partial waves by inserting a complete set of angular-momentum helicity states  $|J, M; \lambda_1, \lambda_2\rangle$ , which describe two-particle states with definite total angular momentum  $J$ .<sup>48</sup> Applying angular-momentum conservation, the helicity amplitude reads

$$\begin{aligned} \mathcal{A}_r^{J_r M_r}(m_r, \vartheta_r, \phi_r) &= \mathcal{D}_r(m_r) \sum_{\lambda_1, \lambda_2} \langle \vartheta_r, \phi_r; \lambda_1, \lambda_2 | J_r, M_r; \lambda_1, \lambda_2 \rangle \langle J_r, M_r; \lambda_1, \lambda_2 | \hat{T}(m_r) | J_r, M_r \rangle . \end{aligned} \quad (145)$$

We expand the helicity amplitude further into states  $|J_r, M_r; L_r, S_r\rangle$ , which describe two-particle states that have definite relative orbital angular momentum  $L_r$  between the two particles and where the spins of the two particles couple to the total intrinsic spin  $S_r$ . This yields

$$\begin{aligned} \mathcal{A}_r^{J_r M_r L_r S_r}(m_r, \vartheta_r, \phi_r) &= \sum_{\lambda_1, \lambda_2} \overbrace{\langle \vartheta_r, \phi_r; \lambda_1, \lambda_2 | J_r, M_r; \lambda_1, \lambda_2 \rangle \langle J_r, M_r; \lambda_1, \lambda_2 | J_r, M_r; L_r, S_r \rangle}^{\text{angular part}} \\ &\quad \times \underbrace{\mathcal{D}_r(m_r) \langle J_r, M_r; L_r, S_r | \hat{T}(m_r) | J_r, M_r \rangle}_{\text{dynamical part}} . \end{aligned} \quad (146)$$

The two-body decay amplitude factorizes into an angular part, which is given by first principles and completely defined by the angular-momentum quantum numbers of the involved particles, and a dynamical part, which describes the dependence of the amplitude on the invariant mass  $m_r$  of the  $(1, 2)$  system and needs to be modeled.<sup>49</sup>

The first scalar product in the angular part of Eq. (146) represents the angular distribution of the daughter particles in the  $r$  rest frame. It is given by [47, 107]

$$\langle J_r, M_r; \lambda_1, \lambda_2 | \vartheta_r, \phi_r; \lambda_1, \lambda_2 \rangle = \sqrt{\frac{2J_r + 1}{4\pi}} D_{M_r \lambda}^{J_r}(\phi_r, \vartheta_r, 0) , \quad (147)$$

---

<sup>48</sup>Completeness means that

$$\sum_{J, M} \sum_{\lambda_1, \lambda_2} |J, M; \lambda_1, \lambda_2\rangle \langle J, M; \lambda_1, \lambda_2| = \mathbb{1} . \quad (144)$$

<sup>49</sup>This is analogous to the case of a two-particle system in a central potential, where the two-body wave function can be factorized into an angular part that is completely determined by the angular-momentum quantum numbers and a radial part that depends on the shape of the potential.

which is derived in Appendix C. The appearing Wigner  $D$ -function  $D_{M' M}^J(\alpha, \beta, \gamma)$  [111, 112] represents the transformation property of a spin state  $|J, M\rangle$  under an arbitrary active rotation  $\hat{\mathcal{R}}$ , which is defined by the three Euler angles  $\alpha$ ,  $\beta$ , and  $\gamma$ . We use the  $y$ - $z$ - $y$  convention for the Euler angles that is defined, for example, in Ref. [113]. Details about the Wigner  $D$ -function can be found in Appendix B. The quantum number  $\lambda$  is discussed below.

The second scalar product in the angular part of Eq. (146) is the so-called recoupling coefficient. It connects the two-particle angular-momentum states in the helicity and the  $L$ - $S$ -coupling representations and is given by [47, 107]

$$\langle J_r, M_r; L_r, S_r | J_r, M_r; \lambda_1, \lambda_2 \rangle = \sqrt{\frac{2L_r + 1}{2J_r + 1}} \underbrace{(J_1, \lambda_1; J_2, -\lambda_2 | S_r, \lambda)}_{\text{spin-spin coupling}} \underbrace{(L_r, 0; S_r, \lambda | J_r, \lambda_r)}_{\text{spin-orbit coupling}}. \quad (148)$$

Here, two Clebsch-Gordan coefficients appear: one for the coupling of the spins of the two daughter particles to the total intrinsic spin  $S_r$  and one for the coupling of  $L_r$  and  $S_r$  to  $J_r$ . The two Clebsch-Gordan coefficients define the spin projection  $\lambda$  of the  $(1, 2)$  system and the spin projection  $\lambda_r$  of  $r$  using, without loss of generality, the direction of particle 1 as the quantization axis:

$$\lambda_r = \lambda = \lambda_1 - \lambda_2. \quad (149)$$

Since the orbital angular momentum  $L_r$  in the decay is by construction perpendicular to the momenta of particles 1 and 2, it has no projection onto the helicity quantization axis.

Inserting Eqs. (147) and (148) into Eq. (146), we get

$$\begin{aligned} \mathcal{A}_r^{J_r M_r L_r S_r}(m_r, \vartheta_r, \phi_r) &= \underbrace{\sqrt{\frac{2L_r + 1}{4\pi}}}_{\text{normalization term}} \underbrace{\mathcal{D}_r(m_r)}_{\text{propagator term}} \underbrace{\alpha_{r \rightarrow 1+2}}_{\text{coupling}} \underbrace{F_{L_r}(m_r)}_{\text{barrier factor}} \underbrace{\text{dynamical part}}_{\text{dynamical part}} \\ &\times \sum_{\lambda_1, \lambda_2} \underbrace{(J_1, \lambda_1; J_2, -\lambda_2 | S_r, \lambda)}_{\text{angular part}} (L_r, 0; S_r, \lambda | J_r, \lambda_r) D_{M_r \lambda_r}^{J_r^*}(\phi_r, \vartheta_r, 0) \\ &\times \underbrace{\mathcal{A}_1^{J_1 \lambda_1 L_1 S_1}(m_1, \vartheta_1, \phi_1)}_{\text{two-body decay amplitude of particle 1}} \underbrace{\mathcal{A}_2^{J_2 \lambda_2 L_2 S_2}(m_2, \vartheta_2, \phi_2)}_{\text{two-body decay amplitude of particle 2}}. \end{aligned} \quad (150)$$

Here, we have modeled the dynamical part in terms of the propagator term  $\mathcal{D}_r(m_r)$ , the complex-valued coupling  $\alpha_{r \rightarrow 1+2}$ , which describes strength and relative phase of the decay mode, and the barrier factor  $F_{L_r}(m_r)$  (see Eq. (97)), which describes the suppression of higher orbital angular momentuma  $L_r$  between the two daughter particles at low  $m_r$ . The propagator term will be discussed in Section 5.1.3. It is worth stressing that we assume the coupling  $\alpha_{r \rightarrow 1+2}$  that appears at the decay vertex to be independent of  $m_r$ . Note that due to the chosen conventions, the complex-conjugate  $D$ -function appears in Eq. (150). Compared to Eq. (146), we added the two-body decay amplitudes  $\mathcal{A}_1^{J_1 \lambda_1 L_1 S_1}$  and  $\mathcal{A}_2^{J_2 \lambda_2 L_2 S_2}$  of particles 1 and 2, which are different from unity only if the respective daughter particle is also unstable and decays into further particles, i.e. when the daughter appears as an isobar in the decay chain. In this case, the decay amplitude of the respective daughter particle has the same form as Eq. (150). To simplify notation, we assume spinless final-state particles in the remaining text, which is true for all final states discussed in this paper.

### 5.1.3. Parameterization of Propagator Terms

As was shown in Section 3.1.4, the propagator terms  $\mathcal{D}_r(m_r)$  of the isobar resonances in Eq. (150) can be approximated by relativistic Breit-Wigner amplitudes with constant width as in Eq. (87), i.e.

$$\mathcal{D}_r^{\text{BW}}(m_r; m_0, \Gamma_0) = \frac{m_0 \Gamma_0}{m_0^2 - m_r^2 - i m_0 \Gamma_0}, \quad (151)$$

where  $m_0$  and  $\Gamma_0$  are nominal mass and total width of the resonance  $r$ .<sup>50</sup>

However, in Section 3.1.4 it was also shown that Eq. (151) is a good approximation only for narrow resonances. For wider resonances, a better approximation is the relativistic Breit-Wigner amplitude with dynamic width as in Eq. (88), i.e.

$$\mathcal{D}_r^{\text{BW}}(m_r; m_0, \Gamma_0) = \frac{m_0 \Gamma_0}{m_0^2 - m_r^2 - i m_0 \Gamma(m_r)} \quad \text{with} \quad \Gamma(m_r) = \sum_j^{\text{decay modes}} \Gamma_j \frac{q_j}{m_r} \frac{m_0}{q_{j,0}} \frac{F_{L_j}^2(q_j)}{F_{L_j}^2(q_{j,0})}, \quad (152)$$

where we have generalized Eq. (95) to the multi-channel case. This parameterization takes into account the opening of the decay phase space for the decay modes  $j$  of resonance  $r$  across the resonance width and the centrifugal barrier due to the orbital angular momenta  $L_j$  in the respective decay modes via the barrier factors  $F_{L_j}$  (see Eq. (97)). Note that compared to Eq. (88) the numerator in  $\mathcal{D}_r^{\text{BW}}$  is constant. The phase space factor from Eq. (88) does not appear because we model the partial-wave amplitude and the barrier factor  $F_{L_j}$  is already taken into account as a separate factor in Eq. (150). It is important to note that the decay amplitude in Eq. (150) is proportional to  $F_{L_j}$  and not to  $F_{L_j}^2$  as is the case for the partial-wave amplitude in Eq. (88). This is because the decay amplitude describes the decay of a resonance, where the barrier factor enters only via the decay vertex, and not a  $2 \rightarrow 2$  scattering process, where the barrier factor enters in addition via the production vertex.

The dynamic total width is given by the sum of the phase-space volumes of all decay modes, weighted by their partial widths  $\Gamma_j$ . In Eq. (152), we assume that all decay modes of  $r$  are two-body decays that are characterized by a relative orbital angular momentum  $L_j$  between the two daughter particles, which are assumed to be stable. The two-body phase-space volume is proportional to  $q_j/m_r$  (see Eq. (60)), where  $q_j(m_r; m_{j,1}, m_{j,2})$  is the magnitude of the two-body breakup momentum in the  $r$  rest frame as given by Eqs. (62) and (63) with  $m_{j,1}$  and  $m_{j,2}$  being the masses of the daughter particles of decay mode  $j$ . Since  $q_{j,0} := q_j(m_0)$ , the dynamic width is normalized such that

$$\Gamma(m_0) = \sum_j^{\text{decay modes}} \Gamma_j. \quad (153)$$

Although we assume in Eq. (152) that the daughter particles of  $r$  are stable, this parameterization is often also applied to cases where at least one of the daughter particles is unstable. Such two-body approximations neglect the effect of the finite width(s) of the unstable daughter particle(s).<sup>51</sup>

The Breit-Wigner parameterizations in Eqs. (151) and (152) do not take into account coupled-channel effects due to multiple decay modes of a resonance. In cases, where the threshold of a decay channel is close to the resonance, the next best approximation beyond the Breit-Wigner amplitude is usually the Flatté parameterization in Eq. (109). More general approaches for the parameterization of propagator terms that respect at least analyticity and two-body unitarity, such as  $K$ -matrix

---

<sup>50</sup>The numerator in Eq. (151) depends on the chosen normalization. The decay amplitudes are independent of this choice because they are normalized separately (see Section 5.2.4).

<sup>51</sup>Note that Eqs. (62), (63), and (152) are not a good approximation anymore if subthreshold contributions are important, i.e. if the decay of  $r$  proceeds via the low-mass tail(s) of the unstable daughter particle(s).

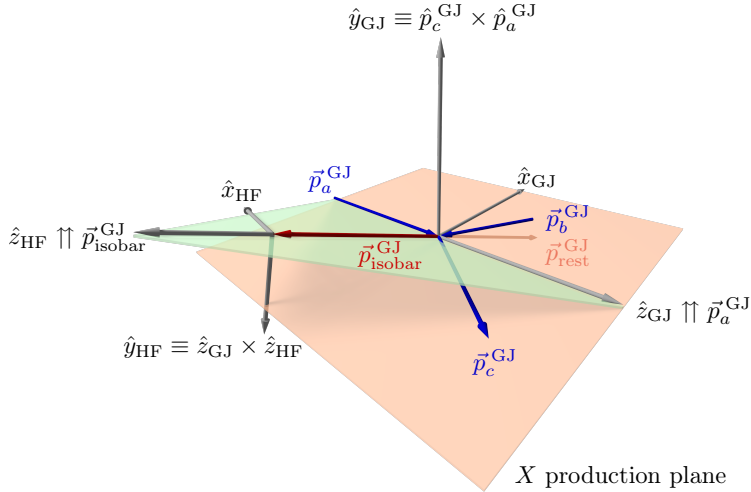


Figure 34: Definition of the Gottfried-Jackson (GJ) and helicity (HF) reference frames for the reaction  $a + b \rightarrow X + c$  with  $X$  decaying into an isobar and a rest, which may be either a final-state particle or again an isobar. Here,  $a$  is the beam,  $b$  the target, and  $c$  the recoil particle. Unit vectors are indicated by circumflexes. (Adapted from Ref. [102])

approaches (see Section 3.1.7) are usually more difficult to employ. One of the difficulties is that these amplitudes typically have unknown parameters that need to be estimated from data. As will be discussed in Section 5.2.5, we cannot allow the decay amplitudes  $\tilde{\Psi}_{X \rightarrow \text{FS}}$  to have any free parameters because otherwise the problem becomes prohibitively expensive in terms of computational resources.

#### 5.1.4. Coordinate Systems

The angles that describe the two-body decays in the  $X$  decay chain and that enter the Wigner  $D$ -function in Eq. (150), are defined in the respective rest frame of the parent particles using right-handed coordinate systems. For high-energy scattering reactions with beam particle  $a$ , target particle  $b$ , which is at rest in the laboratory frame, and target recoil  $c$ , the decay of  $X$  is usually described in the Gottfried-Jackson (GJ) frame. In this reference frame, the direction of the beam particle defines the  $z_{\text{GJ}}$  axis and the  $y_{\text{GJ}}$  axis is given by the normal of the production plane:  $\hat{y}_{\text{GJ}} \propto \hat{p}_a^{\text{lab}} \times \hat{p}_X^{\text{lab}} \propto \hat{p}_c^{\text{GJ}} \times \hat{p}_a^{\text{GJ}}$ , where unit vectors are indicated by circumflexes. Since in the GJ frame  $X$  is at rest, the momenta of its two daughter particles are back to back. Thus the angular distribution is described by the polar angle  $\vartheta_{\text{GJ}}$  and the azimuthal angle  $\phi_{\text{GJ}}$  of one of the daughter particles. The choice of this analyzer is a question of convention, but care has to be taken that the analyzer is chosen consistently for all considered decay chains.

The decays of the isobars are described in the respective helicity reference frames (HF), which are constructed recursively by boosting from the rest frame of the parent particle of the respective isobar into the isobar rest frame. The coordinate system is defined by taking the  $z_{\text{HF}}$  axis along the original direction of motion of the isobar, i.e. opposite to the direction of motion of its parent particle in the isobar rest frame, and  $\hat{y}_{\text{HF}} \propto \hat{z}_{\text{parent}} \times \hat{z}_{\text{HF}}$ , where  $\hat{z}_{\text{parent}}$  is the direction of the  $z$  axis in the parent rest frame. In the helicity frame, the two daughter particles of the isobar are emitted back to back, so that the angular distribution is described by the polar angle  $\vartheta_{\text{HF}}$  and the azimuthal angle  $\phi_{\text{HF}}$  of one of the daughters. Again, the choice of this analyzer is a question of convention but has to be consistent across different decay chains.

Figure 34 illustrates the definition of the Gottfried-Jackson and helicity reference frames for the decay  $X \rightarrow \text{isobar} + \text{bachelor}$  at the beginning of an  $n$ -body decay chain with  $n \geq 3$ . Here, the direction of the isobar is chosen as the analyzer for the  $X$  decay.

### 5.1.5. Examples for Decay Amplitudes

*Decay into Two Spinless Final-State Particles.* The simplest example is the decay of  $X$  into a two-body final state of spinless particles, i.e.  $X \rightarrow 1 + 2$ .<sup>52</sup> In this case, the amplitude  $\tilde{\Psi}_{X \rightarrow 1+2}(m_X, \tau_2)$  for the  $X$  decay is given by Eq. (150) with  $r = X$  and  $\mathcal{A}_1 = \mathcal{A}_2 = 1$ . In addition, we have to take into account that the propagator term  $\mathcal{D}_X(m_X)$  for  $X$  is already accounted for as a factor in Eq. (142). With  $J_1 = J_2 = 0$  and  $\lambda_1 = \lambda_2 = 0$ , the decay amplitude hence reads

$$\begin{aligned} \tilde{\Psi}_{X \rightarrow 1+2}(m_X, \vartheta_{\text{GJ}}, \phi_{\text{GJ}}) &= \sqrt{\frac{2L_X + 1}{4\pi}} \alpha_{X \rightarrow 1+2} F_{L_X}(m_X) \\ &\quad \times (0, 0; 0, 0 | S_X, \lambda) (L_X, 0; S_X, \lambda | J, \lambda_X) D_{M \lambda_X}^{J^*}(\phi_{\text{GJ}}, \vartheta_{\text{GJ}}, 0). \end{aligned} \quad (154)$$

The only non-vanishing Clebsch-Gordan coefficients are the ones, where the total spin  $S_X$  of the  $(1, 2)$  system and its spin projection  $\lambda$  are both zero and as a consequence  $\lambda_X = \lambda = 0$  and  $L_X = J$ . Since  $\lambda_X = 0$ , the Wigner  $D$ -function reduces to the spherical harmonics  $Y_J^M$  according to

$$D_{M 0}^J(\phi_{\text{GJ}}, \vartheta_{\text{GJ}}, 0) = \sqrt{\frac{4\pi}{2J + 1}} Y_J^{M*}(\vartheta_{\text{GJ}}, \phi_{\text{GJ}}). \quad (155)$$

Therefore,

$$\tilde{\Psi}_{X \rightarrow 1+2}(m_X, \vartheta_{\text{GJ}}, \phi_{\text{GJ}}) = \alpha_{X \rightarrow 1+2} F_J(m_X) Y_J^M(\vartheta_{\text{GJ}}, \phi_{\text{GJ}}). \quad (156)$$

*Decay into Three Spinless Final-State Particles.* For  $n$ -body decays of  $X$  with  $n \geq 3$ , the decay amplitude  $\tilde{\Psi}_{X \rightarrow \text{FS}}(m_X, \tau_n)$  is calculated by recursive application of Eq. (150). The simplest example for a three-body decay is the decay  $X \rightarrow r + 3$  with  $r \rightarrow 1 + 2$ , where 1, 2, and 3 are spinless particles. Here, an intermediate isobar resonance  $r$  appears in the  $(1, 2)$  subsystem.<sup>53</sup> Applying Eq. (150) recursively, the amplitude for such a decay reads

$$\begin{aligned} \tilde{\Psi}_{X \rightarrow 1+2+3}(m_X, \vartheta_{\text{GJ}}, \phi_{\text{GJ}}, m_r, \vartheta_{\text{HF}}, \phi_{\text{HF}}) &= \sqrt{\frac{2L_X + 1}{4\pi}} \alpha_{X \rightarrow r+3} F_{L_X}(m_X) \\ &= \delta_{J_r S_X} \delta_{\lambda_r \lambda} \\ &\times \sum_{\lambda_r} \overbrace{(J_r, \lambda_r; 0, 0 | S_X, \lambda)} (L_X, 0; S_X, \lambda | J, \lambda_X) D_{M \lambda_X}^{J^*}(\phi_{\text{GJ}}, \vartheta_{\text{GJ}}, 0) \\ &\quad \times \overbrace{\mathcal{D}_r(m_r) \alpha_{r \rightarrow 1+2} F_{J_r}(m_r) Y_{J_r}^{\lambda_r}(\vartheta_{\text{HF}}, \phi_{\text{HF}})} \\ &= \mathcal{A}_r^{J_r \lambda_r L_r S_r}(m_r, \vartheta_{\text{HF}}, \phi_{\text{HF}}) \text{ as given by Eq. (150)} \end{aligned} \quad (157)$$

The first part of the decay amplitude describes the decay  $X \rightarrow r + 3$  and corresponds to the amplitude  $\mathcal{A}_X^{J_r M L_X S_X}(m_X, \vartheta_{\text{GJ}}, \phi_{\text{GJ}})$  as given by Eq. (150), with the only difference that the propagator term  $\mathcal{D}_X(m_X)$  for  $X$  does not appear here since it is already explicitly contained as a factor in Eq. (142). In Eq. (157),  $\lambda_r$  is the helicity of  $r$  in the Gottfried-Jackson rest frame of  $X$ . Since  $J_3 = 0$  and hence  $\lambda_3 = 0$ , the total spin  $S_X$  of the  $(r, 3)$  system is equal to  $J_r$  and  $\lambda = \lambda_X = \lambda_r$ . The last equality arises because  $L_X$  has no component along the quantization axis in the helicity frame. The second part of Eq. (157) describes the decay  $r \rightarrow 1 + 2$ . Since both final-state particles are spinless, the same arguments apply as for the decay  $X \rightarrow 1 + 2$  discussed in the paragraph above. Equation (157) can

<sup>52</sup>This could be, for example,  $X \rightarrow \eta\pi$  or  $\eta'\pi$ , where  $\eta$ ,  $\eta'$ , and  $\pi$  are considered as quasi-stable particles.

<sup>53</sup>A concrete example would be  $X^- \rightarrow \pi^-\pi^-\pi^+$ , where the two indistinguishable  $\pi^-$  need to be symmetrized as described in Section 5.1.6.

thus be simplified to

$$\begin{aligned}\tilde{\Psi}_{X \rightarrow 1+2+3}(m_X, \vartheta_{\text{GJ}}, \phi_{\text{GJ}}, m_r, \vartheta_{\text{HF}}, \phi_{\text{HF}}) &= \sqrt{\frac{2L_X + 1}{4\pi}} \alpha_{X \rightarrow r+3} F_{L_X}(m_X) \mathcal{D}_r(m_r) \alpha_{r \rightarrow 1+2} F_{J_r}(m_r) \\ &\times \sum_{\lambda_r} (L_X, 0; J_r, \lambda_r | J, \lambda_r) D_M^{J^*}(\phi_{\text{GJ}}, \vartheta_{\text{GJ}}, 0) Y_{J_r}^{\lambda_r}(\vartheta_{\text{HF}}, \phi_{\text{HF}}).\end{aligned}\quad (158)$$

### 5.1.6. Symmetrization of the Decay Amplitudes

If the  $n$ -body final state contains indistinguishable particles, the decay amplitude  $\tilde{\Psi}_{X \rightarrow \text{FS}}$  has to be symmetrized accordingly. For mesonic final states,  $\tilde{\Psi}_{X \rightarrow \text{FS}}$  has to be totally symmetric under exchange of any of the indistinguishable final-state mesons (Bose symmetry). The symmetrized decay amplitude is constructed by summing the amplitudes for all  $N_{\text{perm}}$  permutations of the indistinguishable final-state mesons. For each permutation  $k$  of the final-state four-momenta, the phase-space variables  $\tau_{n,k}$  are calculated and then used to calculate the decay amplitude  $\tilde{\Psi}_{X \rightarrow \text{FS}}^k(m_X, \tau_{n,k})$ . Using these amplitudes, the Bose symmetrized decay amplitude is given by

$$\tilde{\Psi}_{X \rightarrow \text{FS}}^{\text{sym}} = \frac{1}{\sqrt{N_{\text{perm}}}} \sum_{k=1}^{N_{\text{perm}}} \tilde{\Psi}_{X \rightarrow \text{FS}}^k(m_X, \tau_{n,k}).\quad (159)$$

For some final states, the same isobar resonance may appear in different subsystems of the final-state particles. In this case, the relative magnitudes and phases of the corresponding decay amplitudes are fixed by the respective isospin Clebsch-Gordan coefficients.<sup>54</sup> Also if one compares or combines data from decay channels that are related by isospin symmetry, isospin Clebsch-Gordan coefficients need to be taken into account.<sup>55</sup> In addition, the analyzers for the angular distributions have to be chosen consistently for the final states.

To simplify notation, we redefine  $\tilde{\Psi}_{X \rightarrow \text{FS}}(m_X, \tau_n)$  to represent the Bose- and isospin-symmetrized decay amplitude in the remaining text.

### 5.1.7. Extension of the Model to Several Intermediate States

The decay amplitude in Eq. (159) is completely defined by the quantum numbers of  $X$ , the quantum numbers and propagator terms of the isobars, the total intrinsic spins, and the orbital angular momenta in the decay chain. If final-state particles have spin, their helicities appear as additional parameters, which for unpolarized reactions are summed over incoherently, i.e. at the intensity level. In diffractive-dissociation reactions, the possible quantum numbers for  $X$  are limited only by the conservation laws of the strong interaction. As discussed in Section 2.1.1, the quantum numbers of a light meson are defined by isospin  $I$ , spin  $J$ , parity  $P$ , and spin projection  $M$ . If  $X$  is a non-strange meson, also the  $G$  parity is defined; if it is in addition neutral, also the  $C$  parity.<sup>56</sup> In case  $X$  is a strange meson, neither  $G$  nor  $C$  parity are defined and the state is characterized by its strangeness quantum number  $S$ .

For convenience, we introduce an index  $i$  that summarizes all information required to calculate the decay amplitude (except possible helicities of the final-state particles):

$$i := \{I^{(G)} J^P M; \text{isobars, total intrinsic spins, orbital angular momenta}\}.\quad (160)$$

---

<sup>54</sup>For example, in the  $\pi^- \pi^0 \pi^+$  final state, which can be produced in charge-exchange  $\pi^- p$  scattering, the  $\rho(770)$  isobar appears in the  $\pi^- \pi^0$ ,  $\pi^0 \pi^+$ , and  $\pi^- \pi^+$  subsystems. The decay amplitudes for  $X^0 \rightarrow \rho(770)^- \pi^+$ ,  $\rho(770)^+ \pi^-$ , and  $\rho(770)^0 \pi^0$  are related by isospin Clebsch-Gordan coefficients (see e.g. Ref. [114]).

<sup>55</sup>For example, for the  $\pi^- \pi^- \pi^+$  and  $\pi^- \pi^0 \pi^0$  final states different isospin Clebsch-Gordan coefficients appear depending on whether the two-pion isobar resonance is isoscalar or isovector.

<sup>56</sup>By convention, for charged non-strange  $X$  the  $C$  parity of the neutral member of the isospin triplet is quoted instead of the  $G$  parity.

A particular index  $i$  represents a *partial wave* and  $|\tilde{\Psi}_i(m_X, \tau_n)|^2$  represents the  $(3n - 4)$ -dimensional kinematic distribution of the final-state particles for this partial wave for a given value of  $m_X$ .

With the above definitions, the amplitude in Eq. (142), that describes the production of a specific  $X$  and its decay chain which are both defined by  $i$ , reads

$$\mathcal{M}_{a+b \rightarrow (X \rightarrow \text{FS})_i + c}(m_X, t', \tau_n) = \mathcal{P}_{a+b \rightarrow X+c}(m_X, t') \mathcal{D}_X(m_X) \tilde{\Psi}_i(m_X, \tau_n). \quad (161)$$

The decay amplitude  $\tilde{\Psi}_i$  as given by Eqs. (150) and (159) contains for each of the  $N_{\text{vertex}}$  two-body decay vertices a complex-valued coupling  $\alpha_{\text{parent} \rightarrow \text{daughter}_1 + \text{daughter}_2}$ , which is in general unknown. Assuming that these couplings are independent of  $m_X$  or any of the phase-space variables, they can be pulled out of each two-body amplitude  $\mathcal{A}_r^{J_r M_r L_r S_r}$  so that

$$\tilde{\Psi}_i(m_X, \tau_n) := \underbrace{\left[ \prod_{k=1}^{N_{\text{vertex}}} \alpha_k \right]}_{=: \alpha_i} \bar{\Psi}_i(m_X, \tau_n). \quad (162)$$

Here,  $\alpha_k$  is the coupling at the  $k$ th two-body decay vertex in the decay chain. Assuming that we know the propagator terms for all isobars, the decay amplitude  $\bar{\Psi}_i(m_X, \tau_n)$  defined in Eq. (162) is calculable and does not contain any unknown parameters.

Usually, also the amplitude  $\mathcal{P}_{a+b \rightarrow X+c}(m_X, t')$  that describes the production of  $X$  in Eq. (161) is only partly known. As was discussed in Section 3.2, the strong interaction in  $t$ -channel scattering processes can be described as the exchange of Reggeons. At high beam energies, Pomeron exchange becomes dominant (see Section 4.1). Using Regge theory, one can usually construct an approximate amplitude  $\mathcal{P}(m_X, t')$  that at least models the average production probability of an intermediate state with mass  $m_X$  as a function of  $t'$ . The unknown details of the beam-Reggeon vertex are factorized into a so-called *coupling amplitude*  $\mathcal{C}_{X,i}(t')$ , which also absorbs the unknown  $\alpha_k$  from Eq. (162). The coupling amplitude therefore depends not only on the  $X$  quantum numbers but also on the decay chain and hence on  $i$ . With these definitions, the amplitude for the scattering process in Eq. (161) reads

$$\mathcal{M}_{a+b \rightarrow (X \rightarrow \text{FS})_i + c}(m_X, t', \tau_n) = \mathcal{P}(m_X, t') \mathcal{C}_{X,i}(t') \mathcal{D}_X(m_X) \bar{\Psi}_i(m_X, \tau_n). \quad (163)$$

Up to now we considered only the hypothetical case of a single intermediate resonance  $X$  with a single decay chain. However, usually several resonances  $X$  with the same quantum numbers may contribute to the same decay chain, i.e. to the same partial wave  $i$ . Since these resonances appear as intermediate states, they may interfere and the corresponding amplitudes have to be summed coherently. In addition, different partial waves, i.e. resonances with different quantum numbers and different decay chains, may contribute to the intermediate states  $X$ . Since these resonances appear as intermediate states and eventually decay into the same final-state particles, the corresponding partial-wave amplitudes may also interfere and hence have to be added coherently.<sup>57</sup> Therefore, the total amplitude for the production of the  $n$ -body final state taking into account all appearing intermediate resonances  $X$  and all their various decay chains is

$$\mathcal{M}_{fi}(m_X, t', \tau_n) = \mathcal{P}(m_X, t') \sum_i^{N_{\text{waves}}} \left[ \sum_{k \in \mathbb{S}_i} \mathcal{C}_{ki}(t') \mathcal{D}_k(m_X) \right] \bar{\Psi}_i(m_X, \tau_n), \quad (164)$$

where the index  $k$  enumerates the various contributing  $n$ -body resonances  $X$ . The inner sum runs over the subsets  $\mathbb{S}_i$  of the indices of those resonances that contribute to partial wave  $i$ . The same resonance

---

<sup>57</sup>In Section 5.2.2, we will discuss possible sources of incoherence and how to include them in the analysis model. Incoherences also arise in the analysis of data on quasi-real photoproduction via the Primakoff reaction. They will be discussed in Section 7.

may appear in several waves and several resonances may appear in the same wave. Depending on the context, the partial-wave index  $i$  has two meanings. It either represents directly the set of quantum numbers that define a partial-wave amplitude as in Eq. (160) or it enumerates all waves consecutively, i.e.  $i$  is an integer that uniquely identifies a specific wave as in Eq. (164).

Equation (164) is a model for the  $(2 + 3n - 4)$ -dimensional intensity distribution  $\mathcal{I}(m_X, t', \tau_n)$  as defined in Eq. (141). In principle, the best possible approach would be to fit Eq. (164) directly to the data. Such an approach is often called *global fit*. However, in many cases it is impractical or even impossible to perform such a global fit. One of the reasons for this is that the set  $\{k\}$  of resonances that contribute to the intermediate states  $X$  is usually unknown, as are the corresponding resonance parameters. It is the goal of the analysis to determine the resonance content and the resonance parameters from the data. Often, the analysis is guided by information from the kinematic distributions, in particular from the invariant mass distribution of the  $n$ -body final state, and by results from previous experiments. As was discussed in Section 4.1, the identification of resonances in the data is complicated by contributions from non-resonant components that have to be taken into account. This will be discussed further in Section 5.3. Also the values of the coupling amplitudes  $\{\mathcal{C}_{ki}(t')\}$  are in general unknown and have to be inferred from data. Up to now there are no models that are able to describe the details of the  $t'$  dependence of the coupling amplitudes. Finally, even if a realistic model of the form of Eq. (164) could be formulated, it is in most cases computationally too expensive to fit it to the high-dimensional data (see Section 5.2.5).

Given the large data samples of recent experiments, it has proven advantageous to pursue an opposite analysis approach. Instead of formulating the ultimate model of the form of Eq. (164) that has to describe all details of the whole data sample, one tries to reduce the required modeling and hence the model dependence to a minimum. This approach is especially attractive in cases where the analyzed data samples are so large that systematic uncertainties dominate the total uncertainties. Commonly, a two-stage approach is used to separate the decomposition of the data into partial-wave amplitudes with well-defined  $X$  quantum numbers and decay chains, i.e. the modeling of the  $\tau_n$  dependence of  $\mathcal{I}$ , from the extraction of the intermediate  $n$ -body resonances, i.e. the modeling of the  $m_X$  and  $t'$  dependence of  $\mathcal{I}$ . As will be discussed further in Section 5.2.8 below, this two-stage approach circumvents or at least separates many of the issues and limitations that would be encountered in global fits.

In the first analysis stage, which is often called *partial-wave decomposition* or *mass-independent fit*, we make as little assumptions as possible about the intermediate states  $X$ . To this end, we start from Eqs. (141) and (164) and collect all the *a priori* unknown quantities into the so-called *transition amplitudes*  $\overline{\mathcal{T}}_i(m_X, t')$ :

$$\mathcal{I}(m_X, t', \tau_n) = \left| \sum_i^{N_{\text{waves}}} \overbrace{\sqrt{m_X} \mathcal{P}(m_X, t') \left[ \sum_{k \in \mathbb{S}_i} \mathcal{C}_{ki}(t') \mathcal{D}_k(m_X) \right]}^{\overline{\mathcal{T}}_i(m_X, t')} \overline{\Psi}_i(m_X, \tau_n) \right|^2. \quad (165)$$

Here, we have implicitly rescaled the coupling amplitudes  $\mathcal{C}_{ki}(t')$  such that they include the proportionality factor between  $\mathcal{I}$  and the  $m_X |\mathcal{M}_{fi}(m_X, t', \tau_n)|^2$  term in Eq. (141). The goal of the first analysis stage is to determine the set  $\{\overline{\mathcal{T}}_i(m_X, t')\}$  of transition amplitudes from the data. This is possible because we can calculate the decay amplitudes  $\overline{\Psi}_i(m_X, \tau_n)$  for a given value of  $m_X$  assuming that we know the propagator terms of all intermediate isobar resonances that appear in Eq. (165) via Eq. (150) precisely and without any free parameters. In order to avoid modeling of the  $m_X$  and  $t'$  dependence of the transition amplitudes, the partial-wave decomposition is performed in small  $(m_X, t')$  cells. This yields binned approximations to the  $\overline{\mathcal{T}}_i(m_X, t')$  and will be explained in Section 5.2. Because of this binning approach, the first analysis stage makes no assumptions about the resonance content of the partial waves. Based on the isobar model for the  $n$ -body decay of  $X$ , the data are decomposed into partial-wave amplitudes with well-defined quantum numbers that are given by the partial-wave index  $i$  as defined in Eq. (160). One may think of the partial-wave decomposition as

merely a transformation of the data from four-momentum space of the final-state particles into the space of transition amplitudes. This yields a representation of the data in terms of intensities and relative phases of transition amplitudes that allows for a direct interpretation in terms of resonances. As was discussed in Section 4.1, the extracted partial-wave amplitudes also contain contributions from non-resonant processes that have to be taken into account by the resonance model (see discussion below). Since the partial-wave decomposition takes into account the detection and reconstruction efficiency of the experimental setup (see Section 5.2.5) and thanks to the chosen normalization (see Section 5.2.4), the results can be directly compared across experiments. It is important to note that the model in Eq. (165) describes the density of events differential in all phase-space variables. As a consequence, the partial-wave decomposition is able to extract the interference even between waves  $i$  and  $j$  that have different quantum numbers and hence correspond to orthogonal decay amplitudes, for which  $\int d\Phi_n(m_X, \tau_n) \bar{\Psi}_i(m_X, \tau_n) \Psi_j^*(m_X, \tau_n) = 0$ .<sup>58</sup>

In the second analysis stage, which is often called *resonance-model fit* or *mass-dependent fit*, we use the definition of the transition amplitudes in Eq. (165) to construct a model that describes the  $m_X$  and  $t'$  dependence of a selected subset of transition amplitudes in terms of resonant and non-resonant components. This will be explained in Section 5.3. It is important to note that the resonance-model fit does not have to describe *all* transition amplitudes that are extracted from the data, but may focus on selected partial waves. This is in particular important for the analysis of the high-energy scattering reactions considered here, where often sizable non-resonant components contribute to  $X$  (see Section 4.1). These non-resonant contributions project into all transition amplitudes and often dominate the intensity of high-spin waves. Such waves are only important to describe the data but are uninteresting when it comes to extracting resonances. They are therefore not included in resonance-model fits.

## 5.2. Stage I: Partial-Wave Decomposition in Kinematic Cells

The decomposition of the data into partial-wave amplitudes with well-defined quantum numbers and isobar decay chains constitutes the first stage of the analysis. In this stage, the  $m_X$  and  $t'$  dependence of the unknown transition amplitudes  $\bar{\mathcal{T}}_i$ , which are defined in Eq. (165), is extracted from the data by subdividing the data sample into narrow bins in these two kinematic variables. We assume that the  $m_X$  and  $t'$  bins are narrow enough, such that we can in good approximation neglect the  $m_X$  and  $t'$  dependence within the  $(m_X, t')$  cells. Hence within a given  $(m_X, t')$  cell, the intensity distribution in Eq. (165) is a function only of the set of phase-space variables represented by  $\tau_n$ . The other two kinematic variables,  $m_X$  and  $t'$ , appear as constant parameters:

$$\mathcal{I}(\tau_n; m_X, t') = \left| \sum_i^{N_{\text{waves}}} \bar{\mathcal{T}}_i(m_X, t') \bar{\Psi}_i(\tau_n; m_X) \right|^2. \quad (166)$$

Compared to a functional description of the  $m_X$  and  $t'$  dependence of the transition amplitudes, the binned approach does not require a model for the  $n$ -body resonances and the non-resonant contributions. It therefore does not make any assumptions about the resonance content of the transition amplitudes. The only model dependence that enters at this point is the truncation of the partial-wave expansion, i.e. the set of waves used in Eq. (166). This issue will be discussed in Section 5.2.8. In addition, the kinematic cells are statistically independent so that the partial-wave decomposition can be performed in parallel. A caveat of the binning approach is that the method introduces a large number of free parameters—the values of the transition amplitudes in each  $(m_X, t')$  cell—that need to be determined from data. For that reason, this approach is only applicable to sufficiently large data sets.

---

<sup>58</sup>This is in contrast to Dalitz-plot analyses of three-body decays of spinless mesons, where such interferences are inaccessible, because one integrates over the three Euler angles that define the spatial orientation of the three-body system leaving only two of the five phase-space variables.

In order to make the PWA model more realistic, Eq. (166) still needs to be extended in order to take into account (i) possible incoherent background contributions, (ii) incoherences caused by the spin states of the target and recoil particles, and (iii) parity conservation in the strong-interaction scattering process.

### 5.2.1. Incoherent Background Contributions

The analyzed data are usually contaminated by misreconstructed or partially reconstructed events that are similar to the signal process and hence fulfill the event selection criteria. We model this background by a distribution that is isotropic in phase space. Therefore, these events have a constant probability density over all phase-space elements. In order to account for such events, we incoherently add a component to Eq. (166), the so-called *flat wave*. The corresponding decay amplitude  $\bar{\Psi}_{\text{flat}}$  is constant and, without loss of generality, we set  $\bar{\Psi}_{\text{flat}} \equiv 1$  so that

$$\mathcal{I}(\tau_n; m_X, t') = \left| \sum_i^{N_{\text{waves}}} \bar{\mathcal{T}}_i(m_X, t') \bar{\Psi}_i(\tau_n; m_X) \right|^2 + |\bar{\mathcal{T}}_{\text{flat}}(m_X, t')|^2. \quad (167)$$

Since only the intensity of the flat wave enters in Eq. (167), the phase of this wave is immeasurable. Thus  $\bar{\mathcal{T}}_{\text{flat}}$  is chosen to be real-valued.

Background contributions from other processes, e.g. from non-resonant components, for which the final-state particles are correlated and are hence distributed anisotropically in phase space, do not contribute strongly to the flat wave and usually contaminate the transition amplitudes of the other waves in the PWA model (see Section 4.1). These contributions have to be taken into account in the resonance-model fit, which constitutes the second stage of the analysis (see Section 5.3).

### 5.2.2. Spin-Density Matrix and Rank

In order to avoid potential complications from nuclear effects, often protons are used as targets. Since protons have spin 1/2, the absolute value squared  $|\mathcal{M}_{fi}|^2$  of the scattering amplitude in Eq. (140) has to be averaged over the two spin states of the target proton and summed over the spin states of the recoiling proton, assuming an unpolarized target and spinless beam particles. Due to parity conservation and rotational invariance, the scattering amplitude depends only on the relative orientation of the spin states of the target and the recoil proton. Hence the cross section consists of two incoherent parts: one for spin-flip at the target vertex and one for spin-non-flip. Additional incoherent terms may arise if the target proton is excited in the scattering process. Also performing the partial-wave decomposition over wide  $t'$  ranges may lead to effective incoherence, if the transition amplitudes have different dependences on  $t'$ . Depending on the center-of-momentum energy, multiple exchange processes might contribute to the scattering process, which may lead to additional incoherence.

A way to include these incoherences into the analysis model in Eq. (167) is the introduction of an additional index  $r$  for the transition amplitudes that is summed over incoherently:

$$\begin{aligned} \mathcal{I}(\tau_n; m_X, t') &= \sum_{r=1}^{N_r} \left| \sum_i^{N_{\text{waves}}} \bar{\mathcal{T}}_i^r(m_X, t') \bar{\Psi}_i(\tau_n; m_X) \right|^2 + |\bar{\mathcal{T}}_{\text{flat}}(m_X, t')|^2 \\ &= \sum_{i,j}^{N_{\text{waves}}} \bar{\Psi}_i(\tau_n; m_X) \underbrace{\left[ \sum_{r=1}^{N_r} \bar{\mathcal{T}}_i^r(m_X, t') \bar{\mathcal{T}}_j^{r*}(m_X, t') \right]}_{=: \bar{\varrho}_{ij}(m_X, t')} \bar{\Psi}_j^*(\tau_n; m_X) + |\bar{\mathcal{T}}_{\text{flat}}(m_X, t')|^2. \end{aligned} \quad (168)$$

In Eq. (168), we introduce the Hermitian and positive-semidefinite spin-density matrix  $\bar{\varrho}(m_X, t')$  that completely describes the intermediate state  $X$  in terms of combinations of pure quantum states. The elements  $\bar{\varrho}_{ij}(m_X, t')$  of the spin-density matrix represent the actually measurable observables. The

number  $N_r$  of transition amplitudes per partial wave corresponds to the rank of the spin-density matrix. For most reactions,  $N_r$  is significantly smaller than the mathematically allowed maximum, which is given by the dimension of the spin-density matrix, i.e. by  $N_{\text{waves}}$ .<sup>59</sup> We employ the parameterization of Chung and Trueman [115] for the spin-density matrix, which is explained in Appendix E and reduces the number of free real-valued parameters that need to be determined from the data to the minimum, which is  $N_r (2N_{\text{waves}} - N_r)$ .

Assuming a single production mechanism and neglecting other sources of incoherence, the maximum rank  $N_r$  of the spin-density matrix is determined by the spins  $J_a$ ,  $J_b$ , and  $J_c$  of beam, target, and recoil particle, respectively. Together, these particles have

$$N_{\text{mult}} = (2J_a + 1)(2J_b + 1)(2J_c + 1) \quad (169)$$

different unobserved spin states.<sup>60</sup> Taking into account that some of the spin states are related by parity and rotational invariance, the maximum rank is

$$N_r = \begin{cases} \frac{N_{\text{mult}} + 1}{2} & \text{if } N_{\text{mult}} \text{ is odd,} \\ \frac{N_{\text{mult}}}{2} & \text{if } N_{\text{mult}} \text{ is even.} \end{cases} \quad (170)$$

For example, the scattering process  $\pi + p \rightarrow X + p$  is described by a spin-density matrix with maximum rank of  $N_r = 2$ , corresponding to spin-flip and spin-non-flip processes at the target vertex, as discussed above. If, hypothetically, the target proton would be excited into an  $N(1520)$  resonance with spin  $3/2$ , the maximum rank would increase to  $N_r = 4$ . It is worth noting that Eqs. (169) and (170) define only the *maximum* rank of the spin-density matrix. Depending on the scattering process and the data sample, a lower rank might be sufficient to describe the data. For example, diffractive scattering of spinless beam particles off nucleons is dominated by spin-non-flip processes [22, 116]. Hence for these processes, a rank-1 spin-density matrix yields in most cases a satisfactory description of the data, in particular if other sources for incoherence such as target excitations or integration over large  $t'$  intervals are avoided. A different approach that is studied at the VES experiment is to use a spin-density matrix with maximum rank and then to analyze the transition amplitudes that correspond to the largest eigenvalue of the spin-density matrix [117]. The rank considerations for photo- and lepton production are discussed in Ref. [110]. If multiple production mechanisms contribute to the analyzed process, Eqs. (169) and (170) apply separately to each contribution. For incoherent contributions, the total maximum rank is given by the sum of the maximum rank values for each contribution.

### 5.2.3. Parity Conservation and Reflectivity

Although parity violation is not forbidden in strong interactions by any known fundamental principle [118, 119], all experimental results are in agreement with the assumption that the strong interaction conserves parity. A convenient way of incorporating parity conservation into the PWA model in Eq. (168) is to consider the scattering subprocess  $a + b \rightarrow X + c$  in the so-called *reflectivity basis* [115]. We choose the coordinate system that we use to describe the quantum spin states of the particles such that the quantization axis ( $z$  axis) lies in the production plane. A possible choice for such a quantization axis is the beam axis, like it is used in the definition of the Gottfried-Jackson frame in Section 5.1.4. If the process  $a + b \rightarrow X + c$  is parity conserving, the scattering amplitude is invariant under space inversion. Such a parity transformation flips the direction of all particle momenta. Since the four particles lie in the production plane, this can be undone by performing, in addition to the space inversion, a rotation by  $180^\circ$  about the production plane normal, which is taken as the

<sup>59</sup>Since the spin-density matrix is Hermitian and positive-semidefinite, it is diagonalizable and has real-valued eigenvalues. Of these eigenvalues,  $N_r$  are positive and  $N_{\text{wave}} - N_r$  are zero.

<sup>60</sup>We assume here that all particles are massive.

$y$  axis. The combined transformation is represented by the reflectivity operator  $\hat{\Pi}_y$  and corresponds to a reflection through the production plane, which leaves the momenta of those particles that lie in that plane unchanged. A single-particle spin state  $|J^P, M\rangle$  with momentum in the production plane, spin  $J$ , intrinsic parity  $P$ , and spin projection  $M$  transforms under  $\hat{\Pi}_y$  as follows

$$\hat{\Pi}_y |J^P, M\rangle = P(-1)^{J-M} |J^P, -M\rangle. \quad (171)$$

We can therefore construct eigenstates to  $\hat{\Pi}_y$  from linear combinations of canonical states with spin projections of opposite sign:

$$\begin{aligned} |J^P, M^\varepsilon\rangle &:= \mathcal{N}_M \left[ |J^P, M\rangle - \varepsilon \underbrace{P(-1)^{J-M} |J^P, -M\rangle}_{= \hat{\Pi}_y |J^P, M\rangle} \right], \\ &= \hat{\Pi}_y |J^P, M\rangle \end{aligned} \quad (172)$$

where we choose the normalization factor to be

$$\mathcal{N}_M = \begin{cases} 1/\sqrt{2} & \text{for } M > 0, \\ 1/2 & \text{for } M = 0, \\ 0 & \text{for } M < 0. \end{cases} \quad (173)$$

This choice ensures that in the reflectivity basis the multiplicity of the spin state of  $2J+1$  remains unchanged. The reflectivity eigenstate defined in Eq. (172) is characterized by the spin-projection quantum number  $M$  and the eigenvalue  $\varepsilon^*$  of the reflectivity operator, i.e.

$$\hat{\Pi}_y |J^P, M^\varepsilon\rangle = \varepsilon^* |J^P, M^\varepsilon\rangle. \quad (174)$$

The reflectivity  $\varepsilon$  is  $\pm 1$  for bosons.<sup>61</sup> According to Eq. (173), there are no states with  $M < 0$  in the reflectivity basis. States with spin projection  $M = 0$  vanish, if  $\varepsilon = P(-1)^J$ . Hence for given  $J^P$ , there exists only one state with  $\varepsilon = P(-1)^{J+1}$  and  $M = 0$ . For each  $M > 0$ , two states with  $\varepsilon = \pm 1$  exist, so that in total the multiplicity of the spin state is  $2J+1$ , as in the canonical basis.

Using Eq. (172), we can define rotation function for the reflectivity eigenstates:

$$\begin{aligned} {}^\varepsilon D_{M' M}^J(\alpha, \beta, \gamma) &:= \langle J^P, M^\varepsilon | \hat{\mathcal{R}}(\alpha, \beta, \gamma) | J^P, M \rangle \\ &= \mathcal{N}_M \left[ \langle J^P, M | \hat{\mathcal{R}} | J^P, M \rangle - \varepsilon^* P(-1)^{J-M} \langle J^P, -M | \hat{\mathcal{R}} | J^P, M \rangle \right] \\ &= \mathcal{N}_M \left[ D_{M' M}^J(\alpha, \beta, \gamma) - \varepsilon^* P(-1)^{J-M} D_{-M' M}^J(\alpha, \beta, \gamma) \right]. \end{aligned} \quad (175)$$

Although these functions are not a representation of the rotation group, they still have properties similar to those of the fundamental  $D$ -functions (see Appendix B). In particular, the  ${}^\varepsilon D_{M' M}^J$  form an orthogonal function system. In order to calculate the  $X$  decay amplitude in the reflectivity basis, we replace the Wigner  $D$ -function  $D_{M \lambda_X}^J(\phi_{\text{GJ}}, \vartheta_{\text{GJ}}, 0)$  in the two-body decay amplitude for  $X$  by Eq. (175).

Describing the spin state of  $X$  in the reflectivity basis also changes the structure of the spin-density matrix. In order to fully define a wave in the reflectivity basis, we have to specify in addition to the wave index  $i$ , which contains the spin-projection quantum number  $0 \leq M \leq J$  (see Eq. (160)), also the reflectivity quantum number  $\varepsilon = \pm 1$ . Analogous to the definition of the spin-density matrix in Eq. (168), where  $-J \leq M \leq +J$ , we can write the spin-density matrix in the reflectivity basis:

$$\overline{\varrho}_{ij}^{\varepsilon \varepsilon'} = \sum_{r=1}^{N_r} \overline{\mathcal{T}}_i^{r \varepsilon} \overline{\mathcal{T}}_j^{r \varepsilon'^*}. \quad (176)$$

---

<sup>61</sup>For fermions, the reflectivity is  $\pm i$ .

It is important to note that  $\bar{\varrho}_{ij}^{\varepsilon\varepsilon'}$  has the same number of elements as  $\bar{\varrho}_{ij}$  in Eq. (168).

It is shown in Ref. [115] that due to parity conservation and rotational invariance, the spin-density matrix in the reflectivity basis assumes a block-diagonal form with respect to  $\varepsilon$ , i.e.

$$\bar{\varrho}_{ij}^{\varepsilon\varepsilon'} = \begin{pmatrix} \bar{\varrho}_{ij}^{++} & 0 \\ 0 & \bar{\varrho}_{ij}^{--} \end{pmatrix}. \quad (177)$$

This means that all interference terms of transition amplitudes with opposite reflectivity quantum numbers are zero.

In the reflectivity basis, the PWA model in Eq. (168) can therefore be written as

$$\begin{aligned} \mathcal{I}(\tau_n; m_X, t') &= \sum_{\varepsilon=\pm 1} \sum_{r=1}^{N_r} \left| \sum_i^{N_{\text{waves}}} \bar{\mathcal{T}}_i^{r\varepsilon}(m_X, t') \bar{\Psi}_i^\varepsilon(\tau_n; m_X) \right|^2 + |\bar{\mathcal{T}}_{\text{flat}}(m_X, t')|^2 \\ &= \sum_{\varepsilon=\pm 1} \sum_{i,j}^{N_{\text{waves}}} \bar{\Psi}_i^\varepsilon(\tau_n; m_X) \bar{\varrho}_{ij}^\varepsilon(m_X, t') \bar{\Psi}_j^{\varepsilon*}(\tau_n; m_X) + |\bar{\mathcal{T}}_{\text{flat}}(m_X, t')|^2, \end{aligned} \quad (178)$$

where we use the Chung-Trueman parameterization (see Appendix E) for the two submatrices

$$\bar{\varrho}_{ij}^\varepsilon := \bar{\varrho}_{ij}^{\varepsilon\varepsilon} = \sum_{r=1}^{N_r} \bar{\mathcal{T}}_i^{r\varepsilon} \bar{\mathcal{T}}_j^{r\varepsilon*}. \quad (179)$$

In Eq. (178), the  $\bar{\Psi}_i^\varepsilon$  are the decay amplitudes in the reflectivity basis, where the Wigner  $D$ -function for the  $X$  decay is replaced by the function in Eq. (175).

Up to this point, we just transformed from one complete set of states to another. The formulation in the reflectivity basis in Eqs. (177) and (179) is completely equivalent to the formulation in the canonical basis in Eq. (168). An important advantage of the formulation in the reflectivity basis is that the reflectivity quantum number  $\varepsilon$  of  $X$  corresponds to the naturality  $\eta_{\text{ex}}$  (see Eq. (13)) of the exchange particle in the scattering process [120, 121].<sup>62</sup> Depending on the scattering process, amplitudes with certain  $\eta_{\text{ex}}$  values may be suppressed. Since  $\varepsilon \equiv \eta_{\text{ex}}$ , the corresponding partial-wave amplitudes are also suppressed. This is, for example, the case for scattering processes of hadrons at high energies, which are dominated by Pomeron exchange (see Section 4.1). Since the Pomeron has positive naturality,<sup>63</sup> partial-wave amplitudes with  $\varepsilon = -1$  that correspond to unnatural-parity exchange are suppressed. As a consequence, PWA models for these reactions require much less waves with negative than with positive reflectivity in order to describe the data. Therefore, the dimension of  $\bar{\varrho}_{ij}^{\varepsilon=-1}$  is much smaller than that of  $\bar{\varrho}_{ij}^{\varepsilon=+1}$ . This corresponds to a reduced number of free parameters of the PWA model. The different number of waves in the two reflectivity sectors is taken into account by the replacement

$$N_{\text{waves}} \rightarrow N_{\text{waves}}^\varepsilon \quad (180)$$

in Eq. (178).

Since different reflectivity values correspond to different exchange particles and hence different production mechanisms, also the effective rank  $N_r$  of the spin-density matrix may be different for the two values of  $\varepsilon$ . We incorporate this into the PWA model in Eq. (178) by the replacement

$$N_r \rightarrow N_r^\varepsilon. \quad (181)$$

<sup>62</sup>For beam particles with negative intrinsic parity, this is ensured by the minus sign in the linear combination in Eq. (172).

<sup>63</sup>This is also true for the  $f_2$  exchange, which also contributes.

#### 5.2.4. Normalization

An important technical issue is the normalization of the transition and decay amplitudes. A consistent normalization allows us to extract yields of resonances and to compare the transition amplitudes of different waves in a PWA model as well as across different analyses and experiments.

In order to derive a normalization scheme, we go back to the definition of the intensity  $\mathcal{I}$  in Eq. (141) as the number of produced events per unit in  $m_X$ ,  $t'$ , and  $n$ -body phase-space volume. By integrating  $\mathcal{I}$  over the volume of the  $n$ -body phase space of the final-state particles, we get the density of produced events differential in  $m_X$  and  $t'$ :

$$\frac{dN}{dm_X dt'} = \int d\Phi_n(\tau_n; m_X) \mathcal{I}(\tau_n; m_X, t') . \quad (182)$$

Integrating Eq. (182) over the  $(m_X, t')$  cell, in which the partial-wave decomposition is performed, yields the number of events in that cell as predicted by the model:

$$N_{\text{pred}}(m_X, t') = \int_{m_{X,1}}^{m_{X,2}} d\tilde{m}_X \int_{t'_1}^{t'_2} dt' \frac{dN}{d\tilde{m}_X dt'} . \quad (183)$$

Here,  $(m_{X,1}, t'_1)$  and  $(m_{X,2}, t'_2)$  define the borders of the  $(m_X, t')$  cell. In our binned analysis approach, we neglect the  $m_X$  and  $t'$  dependence of  $dN/(dm_X dt')$  within the  $(m_X, t')$  cell, so that the integration in Eq. (183) is trivial and equivalent to multiplying the integrand with the respective bin widths.

We define the normalization of the intensity by demanding<sup>64</sup>

$$\begin{aligned} N_{\text{pred}}(m_X, t') &= \int d\Phi_n(\tau_n; m_X) \mathcal{I}(\tau_n; m_X, t') \\ &= \sum_{\varepsilon=\pm 1} \left\{ \sum_i^{N_{\text{waves}}^{\varepsilon}} \sum_{r=1}^{N_r^{\varepsilon}} |\overline{\mathcal{T}}_i^{r\varepsilon}(m_X, t')|^2 \int d\Phi_n(\tau_n; m_X) |\overline{\Psi}_i^{\varepsilon}(\tau_n; m_X)|^2 \right. \\ &\quad \left. + 2 \sum_{i,j; i < j}^{N_{\text{waves}}^{\varepsilon}} \text{Re} \left[ \sum_{r=1}^{N_r^{\varepsilon}} \overline{\mathcal{T}}_i^{r\varepsilon}(m_X, t') \overline{\mathcal{T}}_j^{r\varepsilon*}(m_X, t') \int d\Phi_n(\tau_n; m_X) \overline{\Psi}_i^{\varepsilon}(\tau_n; m_X) \overline{\Psi}_j^{\varepsilon*}(\tau_n; m_X) \right] \right\} \\ &\quad + |\overline{\mathcal{T}}_{\text{flat}}(m_X, t')|^2 \int d\Phi_n(\tau_n; m_X) . \end{aligned} \quad (184)$$

Here we have absorbed the  $m_X$  and  $t'$  bin widths into the normalization of  $\mathcal{I}$ . We also have used Eqs. (178) and (180) to (182).

Equation (184) fixes the unit of  $\mathcal{I}$  to number of produced events predicted by the model. However, it still leaves room for an arbitrary factor that can be shifted between the transition and decay amplitudes. In order to also fix the unit of the transition amplitudes, we normalize the decay amplitudes to the diagonal elements of the so-called *integral matrix*<sup>65</sup>

$$I_{ij}^{\varepsilon}(m_X) := \int d\Phi_n(\tau_n; m_X) \overline{\Psi}_i^{\varepsilon}(\tau_n; m_X) \overline{\Psi}_j^{\varepsilon*}(\tau_n; m_X) . \quad (185)$$

This is a convenient choice because it makes the normalized decay amplitudes independent of the normalization of the propagator terms that enter the decay amplitudes (see Sections 5.1.2 and 5.1.3).

---

<sup>64</sup>In special cases, where one has to use wide  $m_X$  bins, the integration of the decay amplitudes in Eq. (184) has to be performed also over  $m_X$  (see e.g. Section 7).

<sup>65</sup>See also Appendix G.

The normalized decay amplitudes are defined by<sup>66</sup>

$$\Psi_i^\varepsilon(\tau_n; m_X) := \frac{\bar{\Psi}_i^\varepsilon(\tau_n; m_X)}{\sqrt{I_{ii}^\varepsilon(m_X)}} \quad (188)$$

so that

$$\int d\Phi_n(\tau_n; m_X) \Psi_i^\varepsilon(\tau_n; m_X) \Psi_j^{\varepsilon*}(\tau_n; m_X) = \frac{I_{ij}^\varepsilon(m_X)}{\sqrt{I_{ii}^\varepsilon(m_X) I_{jj}^\varepsilon(m_X)}} \quad (189)$$

and in particular

$$\int d\Phi_n(\tau_n; m_X) |\Psi_i^\varepsilon(\tau_n; m_X)|^2 = 1. \quad (190)$$

In order to leave  $N_{\text{pred}}$  in Eq. (184) unchanged, the transition amplitudes are normalized according to<sup>67</sup>

$$\mathcal{T}_i^{r\varepsilon}(m_X, t') := \bar{\mathcal{T}}_i^{r\varepsilon}(m_X, t') \sqrt{I_{ii}^\varepsilon(m_X)}. \quad (192)$$

Expressing Eq. (184) in terms of the normalized transition and decay amplitudes yields

$$\begin{aligned} N_{\text{pred}}(m_X, t') &= \sum_{\varepsilon=\pm 1} \left\{ \sum_i^{N_{\text{waves}}^\varepsilon} \sum_{r=1}^{N_r^\varepsilon} |\mathcal{T}_i^{r\varepsilon}(m_X, t')|^2 \right. \\ &\quad + 2 \sum_{i,j; i < j}^{N_{\text{waves}}^\varepsilon} \text{Re} \left[ \sum_{r=1}^{N_r^\varepsilon} \mathcal{T}_i^{r\varepsilon}(m_X, t') \mathcal{T}_j^{r\varepsilon*}(m_X, t') \frac{I_{ij}^\varepsilon(m_X)}{\sqrt{I_{ii}^\varepsilon(m_X) I_{jj}^\varepsilon(m_X)}} \right] \left. \right\} \\ &\quad + |\mathcal{T}_{\text{flat}}(m_X, t')|^2 \\ &= \sum_{\varepsilon=\pm 1} \left\{ \underbrace{\sum_i^{N_{\text{waves}}^\varepsilon} \varrho_{ii}^\varepsilon(m_X, t')}_{\text{intensities}} + \underbrace{\sum_{i,j; i < j}^{N_{\text{waves}}^\varepsilon} 2 \text{Re} \left[ \varrho_{ij}^\varepsilon(m_X, t') \frac{I_{ij}^\varepsilon(m_X)}{\sqrt{I_{ii}^\varepsilon(m_X) I_{jj}^\varepsilon(m_X)}} \right]}_{\text{overlaps}} \right\} \\ &\quad + |\mathcal{T}_{\text{flat}}(m_X, t')|^2, \end{aligned} \quad (193)$$

where we have used Eqs. (189) and (190) and we have introduced the normalized spin-density matrix analogous to Eq. (179)

$$\varrho_{ij}^\varepsilon(m_X, t') = \sum_{r=1}^{N_r^\varepsilon} \mathcal{T}_i^{r\varepsilon}(m_X, t') \mathcal{T}_j^{r\varepsilon*}(m_X, t'). \quad (194)$$

Equation (193) provides an interpretation for the normalized spin-density matrix elements. The diagonal elements  $\varrho_{ii}^\varepsilon$  are the *partial-wave intensities*, i.e. the expected number of produced events in

---

<sup>66</sup>Since we set the decay amplitude  $\bar{\Psi}_{\text{flat}}$  of the flat wave to unity, the corresponding normalized decay amplitude is

$$\Psi_{\text{flat}}(\tau_n; m_X) := \frac{1}{\sqrt{I_{\text{flat}}(m_X)}} \quad \text{with} \quad I_{\text{flat}}(m_X) = V_n(m_X), \quad (186)$$

where  $V_n$  is the  $n$ -body phase-space volume:

$$V_n(m_X) := \int d\Phi_n(\tau_n; m_X). \quad (187)$$

<sup>67</sup>In a similar way, the transition amplitude of the flat wave is normalized based on Eqs. (186) and (187) according to

$$\mathcal{T}_{\text{flat}}(m_X, t') := \bar{\mathcal{T}}_{\text{flat}}(m_X, t') \sqrt{V_n(m_X)}. \quad (191)$$

wave  $i$  with reflectivity  $\varepsilon$ .<sup>68</sup> The off-diagonal elements  $\varrho_{ij}^\varepsilon$ , which contain information about the relative phase between waves  $i$  and  $j$ , contribute to the so-called *overlaps*, which are the number of events originating from the interference between waves  $i$  and  $j$  with reflectivity  $\varepsilon$  (see also Section 5.2.6).

Note that the normalizations in Eqs. (186), (188), (191), and (192) only define the *relative* normalization of the transition amplitudes of the various partial waves. In order to fix the *absolute* normalization, the additional normalization condition in Eq. (193) is required. This condition is applied implicitly at the stage of the maximum likelihood fit that will be discussed in Section 5.2.5.

Using the normalized transition and decay amplitudes in Eq. (178), the final formula for the intensity reads

$$\begin{aligned} \mathcal{I}(\tau_n; m_X, t') &= \sum_{\varepsilon=\pm 1} \sum_{r=1}^{N_r^\varepsilon} \left| \sum_i^{N_{\text{waves}}^\varepsilon} \mathcal{T}_i^{r\varepsilon}(m_X, t') \Psi_i^\varepsilon(\tau_n; m_X) \right|^2 + |\mathcal{T}_{\text{flat}}(m_X, t')|^2 \\ &= \sum_{\varepsilon=\pm 1} \sum_{i,j}^{N_{\text{waves}}^\varepsilon} \Psi_i^\varepsilon(\tau_n; m_X) \varrho_{ij}^\varepsilon(m_X, t') \Psi_j^{\varepsilon*}(\tau_n; m_X) + |\mathcal{T}_{\text{flat}}(m_X, t')|^2. \end{aligned} \quad (195)$$

### 5.2.5. Unbinned Extended Maximum Likelihood Fit

The maximum likelihood method is used to estimate unknown parameter values of a statistical model by maximizing the likelihood function  $\mathcal{L}$ , which is the joint probability density of the data set given the parameter values [122]. For a given data set  $\vec{x} := (x_1, \dots, x_N)^T$  of  $N$  independent random variables<sup>69</sup> each following the same probability density function  $f(x; \vec{\theta})$  with  $m$  parameters  $\vec{\theta} := (\theta_1, \dots, \theta_m)^T$  with unknown values, the likelihood function is

$$\mathcal{L}(\vec{\theta}; \vec{x}) = \prod_{k=1}^N f(x_k; \vec{\theta}). \quad (196)$$

The maximum likelihood estimate  $\hat{\vec{\theta}}$  for the parameters is given by those parameter values that maximize the likelihood function, i.e.

$$\hat{\vec{\theta}} = \arg \max_{\vec{\theta}} \mathcal{L}(\vec{\theta}; \vec{x}). \quad (197)$$

In the above equation,  $\mathcal{L}$  is a function of  $\vec{\theta}$  for a given, i.e. fixed,  $\vec{x}$ . It is important to note that  $\mathcal{L}$  is the probability density function of  $\vec{x}$  for given  $\vec{\theta}$ . However,  $\mathcal{L}$  is in general *not* the probability density function of  $\vec{\theta}$  for given  $\vec{x}$ . In other words, maximizing the probability to observe the data with respect to  $\vec{\theta}$ , as expressed in Eq. (197), does not necessarily yield the most probable parameter values. Also,  $\mathcal{L}$  does not need to be normalized with respect to  $\vec{\theta}$ . It can be shown that the maximum likelihood estimate  $\hat{\vec{\theta}}$  in Eq. (197) is consistent, unbiased, and efficient under rather general conditions in the asymptotic limit, where the data-set size  $N \rightarrow \infty$  [123, 124]. Another advantage of the maximum likelihood method is that Eq. (197) does not require any binning of the data. Therefore, the method is applicable also to high-dimensional data, where binned approaches quickly becomes prohibitively expensive in terms of computational resources.<sup>70</sup>

If the number  $N$  of data points is not predetermined but is a result of the measurement and therefore a random variable, the maximum likelihood principle can be extended. In the case of

<sup>68</sup>This number does not include interference effects between the waves. For an experiment with acceptance different from unity, it corresponds to the acceptance-corrected number of events (see Section 5.2.5).

<sup>69</sup>Depending on the measurement, these variables may in turn be vectors in a multi-dimensional data space. In the case of partial-wave analysis, each  $x_k$  corresponds to the measured phase-space variables  $\tau_{n,k}$  of event  $k$ .

<sup>70</sup>This is already the case for the PWA of three-body final states, for which the phase-space in an  $(m_X, t')$  cell is five-dimensional.

counting experiments, events are produced randomly in time with constant average rates and hence the number of produced events follows the Poisson distribution with the expected number of events  $\lambda$ . For this case, the extended likelihood function is

$$\mathcal{L}_{\text{ext}}(\vec{\theta}, \lambda; \vec{x}, N) = \underbrace{\frac{\lambda^N e^{-\lambda}}{N!}}_{\substack{\text{Poisson} \\ \text{distribution}}} \underbrace{\prod_{k=1}^N f(x_k; \vec{\theta})}_{\mathcal{L}(\vec{\theta}; \vec{x})}. \quad (198)$$

This approach was first proposed by Fermi and is discussed in more detail in Refs. [125–127]. In Ref. [127], it is shown that the extended maximum likelihood estimator inherits the desired asymptotic statistical properties of consistency, unbiasedness, and efficiency from the maximum likelihood estimator.

We apply the extended maximum likelihood method to partial-wave analysis in order to estimate the values of the set  $\{\mathcal{T}_i^{r\varepsilon}\}$  of transition amplitudes in our PWA model in Eq. (195). This approach has been pioneered by Ascoli *et al.* [128, 129]. The partial-wave decomposition is performed independently in  $(m_X, t')$  cells and within each cell, we neglect the dependence of the intensity on  $m_X$  and  $t'$ . In order to simplify notation, we from here on consider a specific  $(m_X, t')$  cell and leave off the  $m_X$  and  $t'$  dependence in the formulas below.

Within a given  $(m_X, t')$  cell, our model in Eq. (195) describes the  $(3n - 4)$ -dimensional  $\tau_n$  distribution of the produced events, i.e. the events a hypothetical perfect detector with unit acceptance would measure. In practice, the *acceptance*  $\epsilon$  of the detector setup<sup>71</sup> is smaller than unity and  $\epsilon$  depends on the kinematic variables  $m_X$ ,  $t'$ , and  $\tau_n$ .<sup>72</sup> To obtain a model for the actual intensity distribution measured by the detector, we have to weight Eq. (195) by the detector acceptance. By normalizing this model and using Eq. (138), we get the probability density function of the measured events in the  $\tau_n$  space, i.e.

$$f(\tau_n; \{\mathcal{T}_i^{r\varepsilon}\}) = \frac{\rho_n(\tau_n) \epsilon(\tau_n) \mathcal{I}(\tau_n; \{\mathcal{T}_i^{r\varepsilon}\})}{\int d\tau'_n \rho_n(\tau'_n) \epsilon(\tau'_n) \mathcal{I}(\tau'_n; \{\mathcal{T}_i^{r\varepsilon}\})}, \quad \text{where} \quad \int d\tau_n f(\tau_n; \{\mathcal{T}_i^{r\varepsilon}\}) = 1. \quad (199)$$

The above equation assumes that detector resolution effects that lead to a smearing of the variables  $\tau_n$  are negligible. If this is not the case, the likelihood function has to be constructed from the observed, i.e., smeared probability density function

$$f'(\tau'_n) = \int d\tau_n S(\tau'_n, \tau_n) f(\tau_n), \quad (200)$$

where  $S(\tau'_n, \tau_n)$  is the smearing function of the detector system, for which an analytical form is usually not known. Correcting for smearing requires more elaborate and computationally more expensive methods (see e.g. Ref. [130]).

Using Eq. (199), we can construct the extended likelihood function for our PWA model analogous to Eq. (198):

$$\mathcal{L}_{\text{ext}}(\{\mathcal{T}_i^{r\varepsilon}\}; \{\tau_{n,k}\}, N) = \frac{(N_{\text{pred}}^{\text{meas}})^N e^{-N_{\text{pred}}^{\text{meas}}}}{N!} \prod_{k=1}^N \frac{\rho_n(\tau_{n,k}) \epsilon(\tau_{n,k}) \mathcal{I}(\tau_{n,k}; \{\mathcal{T}_i^{r\varepsilon}\})}{\int d\tau_n \rho_n(\tau_n) \epsilon(\tau_n) \mathcal{I}(\tau_n; \{\mathcal{T}_i^{r\varepsilon}\})}. \quad (201)$$

In order to find the maximum likelihood estimate for the set  $\{\mathcal{T}_i^{r\varepsilon}\}$  of the transition amplitudes, we have to maximize Eq. (201) with respect to these parameters.

<sup>71</sup>The term acceptance is used here in a broad sense and includes all effects that affect the detection efficiency such as the geometry of the detector setup as well as the efficiencies of the detectors in the setup, of the reconstruction, and of the event selection.

<sup>72</sup>Depending on the detector setup, the acceptance might depend on additional kinematic variables. Hence  $\epsilon$  represents the acceptance integrated over all these variables.

Note that the conventional likelihood function,

$$\mathcal{L}(\{\mathcal{T}_i^{r\varepsilon}\}; \{\tau_{n,k}\}) = \prod_{k=1}^N \frac{\rho_n(\tau_{n,k}) \epsilon(\tau_{n,k}) \mathcal{I}(\tau_{n,k}; \{\mathcal{T}_i^{r\varepsilon}\})}{\int d\tau_n \rho_n(\tau_n) \epsilon(\tau_n) \mathcal{I}(\tau_n; \{\mathcal{T}_i^{r\varepsilon}\})}, \quad (202)$$

without the Poisson term is invariant under scaling of all transition amplitudes by a common factor  $C \in \mathbb{R}$ , i.e. under the substitution  $\mathcal{I} \rightarrow C^2 \mathcal{I}$ . The maximization of the additional Poisson term in Eq. (201) enforces

$$N_{\text{pred}}^{\text{meas}}(\{\mathcal{T}_i^{r\varepsilon}\}) = N. \quad (203)$$

In order to normalize the intensity distribution  $\mathcal{I}$  such that it is given in number of produced events, we set

$$N_{\text{pred}}^{\text{meas}}(\{\mathcal{T}_i^{r\varepsilon}\}) = \int d\tau_n \rho_n(\tau_n) \epsilon(\tau_n) \mathcal{I}(\tau_n; \{\mathcal{T}_i^{r\varepsilon}\}). \quad (204)$$

Via Eq. (203), this fixes the arbitrary scaling factor  $C$ , i.e. the absolute normalization of the transition amplitudes (see Section 5.2.4), and ensures also that Eqs. (184) and (193) are fulfilled.<sup>73</sup> Using Eq. (204) the extended likelihood function in Eq. (201) simplifies to

$$\mathcal{L}_{\text{ext}}(\{\mathcal{T}_i^{r\varepsilon}\}; \{\tau_{n,k}\}, N) = \frac{e^{-N_{\text{pred}}^{\text{meas}}}}{N!} \prod_{k=1}^N \rho_n(\tau_{n,k}) \epsilon(\tau_{n,k}) \mathcal{I}(\tau_{n,k}; \{\mathcal{T}_i^{r\varepsilon}\}). \quad (205)$$

Since the actual value of the likelihood function at the maximum is irrelevant for the parameter estimation, we can simplify Eq. (205) further by dropping all constant factors that are independent of the transition amplitudes.<sup>74</sup> It is convenient to consider the logarithm of  $\mathcal{L}_{\text{ext}}$ . Since the logarithm is a strictly monotonous function, it leaves the position of the maximum of  $\mathcal{L}_{\text{ext}}$  in the space of the transition amplitudes unchanged. However, the logarithm converts the product over the measured events into a sum and thus makes the expression numerically easier to treat. Using Eqs. (195) and (204), we arrive at the final expression of the likelihood function that is maximized in order to estimate the transition amplitudes:

$$\begin{aligned} & \ln \mathcal{L}_{\text{ext}}(\{\mathcal{T}_i^{r\varepsilon}\}; \{\tau_{n,k}\}, N) \\ &= \sum_{k=1}^N \ln \mathcal{I}(\tau_{n,k}; \{\mathcal{T}_i^{r\varepsilon}\}) - N_{\text{pred}}^{\text{meas}}(\{\mathcal{T}_i^{r\varepsilon}\}) \\ &= \sum_{k=1}^N \ln \left[ \sum_{\varepsilon=\pm 1} \sum_{r=1}^{N_r^\varepsilon} \sum_{i=1}^{N_{\text{waves}}^\varepsilon} \left| \sum_i \mathcal{T}_i^{r\varepsilon} \Psi_i^\varepsilon(\tau_{n,k}) \right|^2 + |\mathcal{T}_{\text{flat}}|^2 \right] \\ & \quad - \sum_{\varepsilon=\pm 1} \sum_{r=1}^{N_r^\varepsilon} \sum_{i,j}^{N_{\text{waves}}^\varepsilon} \mathcal{T}_i^{r\varepsilon} \mathcal{T}_j^{r\varepsilon*} \underbrace{\int d\tau_n \rho_n(\tau_n) \epsilon(\tau_n) \Psi_i^\varepsilon(\tau_n) \Psi_i^{r\varepsilon*}(\tau_n)}_{=: \text{acc} I_{ij}^\varepsilon} - |\mathcal{T}_{\text{flat}}|^2 \underbrace{\int d\tau_n \rho_n(\tau_n) \epsilon(\tau_n)}_{=: \text{acc} I_{\text{flat}}^\varepsilon}. \end{aligned} \quad (206)$$

<sup>73</sup>An alternative approach, which is often used in Dalitz-plot analyses, is to maximize the conventional likelihood in Eq. (202) while fixing one of the transition amplitudes to  $|\mathcal{T}_i^{r\varepsilon}| = 1$  in order to fix the normalization. However, in this approach one loses the information about absolute yields of resonances.

<sup>74</sup>It is important to note that in particular the factor

$$\prod_{k=1}^N \rho_n(\tau_{n,k}) \epsilon(\tau_{n,k})$$

in Eq. (205) that contains the phase-space and acceptance weights for the measured events is independent of the transition amplitudes and is hence a constant in the maximization procedure.

The maximum likelihood estimate for the transition amplitudes is given by

$$\{\hat{\mathcal{T}}_i^{r\varepsilon}\} = \arg \max_{\{\mathcal{T}_i^{r\varepsilon}\}} \left[ \ln \mathcal{L}_{\text{ext}}(\{\mathcal{T}_i^{r\varepsilon}\}; \{\tau_{n,k}\}, N) \right]. \quad (207)$$

The numerical procedure used to determine the  $\{\hat{\mathcal{T}}_i^{r\varepsilon}\}$  and their uncertainties is discussed in Appendix F.

Since the transition amplitudes are independent of  $\tau_n$ , they can be pulled out of the normalization integral in Eq. (204). In Eq. (206), this leads to an integral matrix  ${}^{\text{acc}}I_{ij}^\varepsilon$  that is similar to the integral matrix  $I_{ij}^\varepsilon$  in Eq. (185). The only differences between the two matrices are that in  ${}^{\text{acc}}I_{ij}^\varepsilon$  the normalized decay amplitudes appear in the integrand (see Eq. (188)) and that the integration is performed over the accepted phase space. As was discussed in Section 5.1, the decay amplitudes do not contain any free parameters. We can therefore calculate the decay amplitudes as well as the integral matrices  $I_{ij}^\varepsilon$  and  ${}^{\text{acc}}I_{ij}^\varepsilon$  using Monte Carlo integration techniques before maximizing the likelihood function. This is described in Appendix G. Since the integral matrices are computationally very expensive, this reduces the time to compute the likelihood function by several orders of magnitude. It is only due to this fact that the maximization procedure becomes actually feasible in terms of computational resources. However, allowing no free parameters in the decay amplitudes is a severe limitation. This means in particular that the dynamical amplitudes of all isobar resonances in the PWA model have to be known. In many analyses, this becomes an important source of systematic uncertainties. This issue will be discussed further in Section 5.2.8. In Section 5.2.9, we will present a novel method that circumvents most of these issues.

### 5.2.6. Observables

The spin-density matrices  $\varrho_{ij}^\varepsilon$  (see Eq. (194)), which are extracted from the data by maximizing the likelihood function in Eq. (206) independently in the  $(m_X, t')$  cells, contain all information obtainable about the intermediate states  $X$ . Based on  $\varrho_{ij}^\varepsilon(m_X, t')$ , we can define a number of observables that are useful to characterize the result of a partial-wave decomposition and to search for resonance signals.

In Eq. (193), we defined the number of produced events  $N_{\text{pred}}(m_X, t')$  that the model predicts for the given  $(m_X, t')$  cell. This number can be expressed in terms of the *partial-wave intensities*,

$$N_i^\varepsilon(m_X, t') := \varrho_{ii}^\varepsilon(m_X, t') = \sum_{r=1}^{N_r^\varepsilon} |\mathcal{T}_i^{r\varepsilon}(m_X, t')|^2, \quad (208)$$

and the *overlaps*,

$$\text{Ovl}_{ij}^\varepsilon(m_X, t') := 2 \text{Re} \left[ \varrho_{ij}^\varepsilon(m_X, t') \frac{I_{ij}^\varepsilon(m_X)}{\sqrt{I_{ii}^\varepsilon(m_X) I_{jj}^\varepsilon(m_X)}} \right], \quad (209)$$

of all pairs of waves, i.e.

$$N_{\text{pred}}(m_X, t') = \sum_{\varepsilon=\pm 1} \left\{ \sum_i^{N_{\text{waves}}^\varepsilon} N_i^\varepsilon(m_X, t') + \sum_{i,j; i < j}^{N_{\text{waves}}^\varepsilon} \text{Ovl}_{ij}^\varepsilon(m_X, t') \right\} + N_{\text{flat}}(m_X, t'). \quad (210)$$

The partial-wave intensities in Eq. (208) correspond to the diagonal elements of the spin-density matrix. Due to the chosen normalization (see Sections 5.2.4 and 5.2.5), the intensities are given in terms of number of produced events in wave  $i$  with reflectivity  $\varepsilon$ . If a resonance is present in a partial wave, the  $m_X$  dependence of the intensity of this wave often exhibits a Breit-Wigner-shaped peak similar to the one shown in Fig. 10a. The overlaps as defined in Eq. (209) are real-valued and represent the interference terms between waves  $i$  and  $j$  with reflectivity  $\varepsilon$ . They are also expressed in terms of number of produced events.<sup>75</sup>

<sup>75</sup>Note that although the overlap is given in units of number of events, it is a signed number. For constructive interference, the overlap is positive; for destructive interference it is negative.

It is often useful to limit the two sums in Eq. (210) to a selected subset  $\mathbb{S}$  of partial waves. In this case, Eq. (210) yields the number of produced events  $N_{\text{pred}}^{\mathbb{S}}$  in these waves in the given  $(m_X, t')$  cell. This number takes into account all mutual interference terms of the waves in  $\mathbb{S}$ . For example, it is often interesting to calculate the number of produced events in subsets of waves that have the same  $J^{PC} M^{\varepsilon}$  quantum numbers but different decay chains. Studying these so-called *spin totals* as a function of  $m_X$  and/or  $t'$  often better reveals possible resonance signals because statistical fluctuations are reduced.

The contribution of an individual partial wave to the data sample is quantified by the *relative intensity*, which is defined as the ratio of the partial-wave intensity  $N_i^{\varepsilon}(m_X, t')$  in Eq. (208) and the total number of produced events  $N_{\text{pred}}(m_X, t')$  in Eq. (210).<sup>76</sup> Often, the relative intensity is calculated by summing  $N_i^{\varepsilon}(m_X, t')$  and  $N_{\text{pred}}(m_X, t')$  over the same  $m_X$  and/or  $t'$  range:

$$\text{Relint}_i^{\varepsilon} := \sum_{m_X \text{ bins}} \sum_{t' \text{ bins}} N_i^{\varepsilon}(m_X, t') / \left[ \sum_{m_X \text{ bins}} \sum_{t' \text{ bins}} N_{\text{pred}}(m_X, t') \right]. \quad (211)$$

Although the relative intensity of a given wave includes—where applicable—the effect of self-interference due to Bose symmetrization (see Section 5.1.6), it does *not* include the overlaps, i.e. the interference effects of this wave with any of the other waves in the PWA model. Consequently, the relative intensities of all waves in the PWA model will in general not sum to unity. The difference of this sum from unity is a measure for the overall strength of the interference in the model.

Another important observable is the relative phase  $\Delta\phi_{ij}^{\varepsilon}(m_X, t')$  between two waves  $i$  and  $j$  with reflectivity  $\varepsilon$ . It is given by the off-diagonal element of the spin-density matrix

$$\Delta\phi_{ij}^{\varepsilon}(m_X, t') := \arg[\varrho_{ij}^{\varepsilon}(m_X, t')], \text{ i.e. } \varrho_{ij}^{\varepsilon}(m_X, t') = |\varrho_{ij}^{\varepsilon}(m_X, t')| e^{i \Delta\phi_{ij}^{\varepsilon}(m_X, t')}. \quad (212)$$

Note that for  $N_r^{\varepsilon} = 1$ , i.e. full coherence of all partial waves,

$$\Delta\phi_{ij}^{\varepsilon}(m_X, t') = \arg[\mathcal{T}_i^{\varepsilon}(m_X, t')] - \arg[\mathcal{T}_j^{\varepsilon}(m_X, t')]. \quad (213)$$

If a resonance is present in a partial wave, the phase relative to a second wave that has no resonance typically grows with rising  $m_X$  by about  $180^{\circ}$  across the resonance, i.e. the partial wave exhibits a *phase motion*.<sup>77</sup> Figure 10c shows, as an example, the phase motion of a Breit-Wigner resonance. The amplitude can also be visualized in the complex plane as shown in Fig. 10b. In these so-called Argand diagrams, a single Breit-Wigner resonance appears as counter-clockwise circular structure.

It is important to note that although the overlap  $\text{Ovl}_{ij}^{\varepsilon}$  between two waves may be zero because of the orthogonality of the decay amplitudes (see Appendix B), the corresponding off-diagonal element  $\varrho_{ij}^{\varepsilon}$  of the spin-density matrix in general does not vanish and hence the two waves still have a well-defined phase, which characterizes their interference. Since the spin-density matrix has a block-diagonal structure with respect to the reflectivity, partial-wave amplitudes with different  $\varepsilon$  do not interfere and therefore relative phases between such waves are undefined.

In Appendix H, we will introduce additional observables that are useful in certain cases.

### 5.2.7. Comparison of Partial-Wave Analysis Model and Data

The goodness of the PWA fit that was described in Section 5.2.5 can be assessed by generating Monte Carlo pseudo data that are distributed according to the acceptance-weighted PWA model using the maximum-likelihood estimates for the transition amplitudes from Eq. (207). Since the intensity distribution  $\mathcal{I}(m_X, t', \tau_n)$  as defined in Eq. (141) describes the distribution of the events relative to

<sup>76</sup>The relative intensities are equivalent to the so-called *fit fractions* often quoted for Dalitz-plot analyses.

<sup>77</sup>If the second wave also contains a resonance, the phase motion might be reduced or even completely compensated if the two resonances have similar masses and widths.

a distribution that is uniform in phase-space, we can generate such a pseudo-data sample in a three-step procedure: (i) We generate Monte Carlo events that are uniformly distributed in the  $n$ -body phase space using, for example, Eq. (A.2) (see Refs. [131, 132] for more details). (ii) These events are processed through the detector simulation, reconstruction, and event selection chain.<sup>78</sup> (iii) The reconstructed and selected phase-space events are weighted by the intensity model in Eq. (195) using the maximum likelihood estimate for the transition amplitudes. The weights from the model intensity are applied using accept-reject sampling (see e.g. Ref. [133]) in order to obtain a pseudo-data sample that consists of events with unit weight.

For a good PWA fit, distributions obtained from these weighted Monte Carlo events are expected to reproduce the real-data distributions. It is in particular mandatory to verify the agreement of the  $\tau_n$  distributions for all  $(m_X, t')$  cells. For an  $n$ -body final state, these distributions are  $(3n - 4)$ -dimensional so that for  $n \geq 3$  usually only one- or two-dimensional projections can be compared in a meaningful way (see e.g. Section IV.E in Ref. [102]). It is important to note that the phase-space events are weighted with the product of the detector acceptance  $\epsilon(m_X, t', \tau_n)$  and the PWA model  $\mathcal{I}(m_X, t', \tau_n)$ . Therefore, observed disagreements between weighted Monte Carlo and real-data distributions can in general be caused by an unrealistic model or by an inaccurate description of the apparatus in the Monte Carlo simulation. One cannot distinguish the two effects based on the weighted Monte Carlo data alone. The detector model used in the Monte Carlo simulation hence needs to be verified using other physics processes. Assuming that the detector description is sufficiently accurate, disagreements e.g. in the invariant mass distributions of the isobars can be a sign that isobars might be missing and/or that some of the employed parameterizations for the isobar amplitudes (see Section 5.1.3) do not agree with the data. Similarly, disagreements in the angular distributions can hint at missing partial waves with certain spin, spin-projection, or orbital angular momentum quantum numbers.

To study properties of the PWA model, one often wants to generate Monte Carlo pseudo-data samples that are distributed according to a PWA model  $\mathcal{I}(m_X, t', \tau_n)$  with known parameters. This can be achieved by slightly modifying the Monte Carlo procedure described above. One starts again with Monte Carlo events that are uniformly distributed in the  $n$ -body phase-space but one skips step (ii), i.e. one does not weight the events with the acceptance. Based on these pseudo data one can perform PWA fits with the same or altered PWA models<sup>79</sup> in order to study, for example, the distinguishability of certain partial-wave amplitudes. If the acceptance is very non-uniform in any of the kinematic variables that enter the PWA model or if detector resolution effects in any of these variables are large, the distinguishability of certain partial-wave amplitudes might be degraded.<sup>80</sup> Such degradations can be studied using a similar procedure as above, where the phase-space events are weighted with the acceptance and the acceptance correction is applied in the likelihood function as for real data.

#### 5.2.8. Discussion of the Partial-Wave Analysis Method

The PWA model presented in Sections 5.1 and 5.2 makes a number of assumptions that have practical consequences. Here, we focus on those aspects that are most relevant for the interpretation of the results that will be presented in Section 6. Further details are discussed e.g. in Ref. [103].

An important practical issue is the truncation of the partial-wave expansion in Eq. (195), i.e. the decision which waves to include in the PWA model and which ones to leave out. Although the quantum numbers of the most dominantly produced intermediate states  $X$  may be known from previous experiments, in situations where the analyzed data set is about an order of magnitude larger

---

<sup>78</sup>To save computation time, one can reuse the Monte Carlo data sample that was generated to calculate the integral matrix  ${}^{\text{acc}}I_{ij}^{\varepsilon}$  in Eq. (G.2).

<sup>79</sup>In these PWA fits, the acceptance is of course unity.

<sup>80</sup>For example, at very low  $t' \lesssim 10^{-3} (\text{GeV}/c)^2$  the resolution of the azimuthal angle  $\phi_{\text{GJ}}$  in the Gottfried-Jackson frame (see Section 5.1.4) becomes so low in the COMPASS data, that waves with opposite reflectivity quantum number cannot be distinguished anymore (see Section 7).

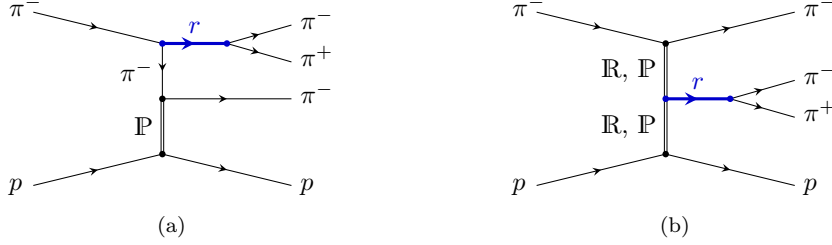


Figure 35: Examples for irreducible non-resonant contributions to diffractive production of  $3\pi$  on a proton target. (a) Process proposed by R. T. Deck [93], where the beam pion dissociates into a  $\pi^-\pi^+$  isobar  $r$  and a bachelor  $\pi^-$ , followed by diffractive scattering of the  $\pi^-$  off the target proton. (b) Process, where the beam and target particles each scatter elastically via exchange of Reggeons, which fuse to produce a  $\pi^-\pi^+$  system.

than any of the existing ones—like it is, for example, the case for the COMPASS  $\pi^-\pi^-\pi^+$  proton-target data (see Section 6.2.3)—this knowledge is usually insufficient to construct a realistic PWA model.

In contrast to formation experiments, where the maximum spin of the intermediate state is limited by the break-up momentum and therefore by the center-of-momentum energy, in formation experiments, the high-energy  $t$ -channel exchange processes may in principle generate arbitrarily high spins. Even though the production of intermediate states is expected to be suppressed with increasing spin, there is no clear cut-off. Also irreducible and interfering contributions from non-resonant processes are often contained in the data. For  $t$ -channel exchange processes, the largest non-resonant contributions come from double-Regge exchange processes (see Section 4.1). Figure 35 shows two examples for such processes in  $\pi^-\pi^-\pi^+$  production. Since in these processes, no  $3\pi$  intermediate states with well-defined quantum numbers appear, the non-resonant contributions typically project into all partial waves. Some high-spin partial waves are even dominated by non-resonant contributions. Such waves are important in order to describe the data but are uninteresting when it comes to extracting resonances. So, in order to estimate the transition amplitudes from the data as was described in Section 5.2.5, one also needs to determine the set  $\{i\}$  of partial waves that enters in Eq. (195) from the data. The analysis problem hence turns into a more difficult model-selection problem, which is complicated by the high dimensionality of the data and the correlations of the partial-wave amplitudes due to their mutual interference.

For  $n$ -body final states with  $n \geq 3$ , another important ingredient of the PWA model that is part of the model-selection problem is the set of isobar resonances. Although signals in the invariant mass distributions of the respective subsystems of the final-state particles help to identify the contributing isobars (see e.g. Fig. 42 in Section 6.2.3), this information is in some cases not enough to unambiguously identify all isobars.<sup>81</sup> As was explained in Section 5.2.5, the decay amplitudes must not have any free parameters because otherwise the computation of the likelihood function becomes very expensive. Thus we do not only have to decide which isobar resonances to include in the PWA model but also which parameterizations and resonance parameters describe them best. The model building hence requires input from other measurements. In most cases, the dynamical amplitudes of the isobar resonances are approximated by Breit-Wigner amplitudes as in Eqs. (151) and (152) and the PDG world averages are used for the resonance parameters. However, for some isobar resonances, the parameters are not precisely known and/or it is unclear which parameterization to use for their dynamical amplitude. For example, the isoscalar resonances with  $J^{PC} = 0^{++}$  quantum numbers, i.e. the  $f_0$  states, that appear in  $\pi\pi$  and  $K\bar{K}$  subsystems are notoriously difficult to describe (see

<sup>81</sup>For example, some isobar resonances have different quantum numbers but similar resonance parameters and therefore may appear as indistinguishable peaks in the invariant mass distribution. In addition, broad isobars and/or isobars that contribute only weakly to the data are difficult to find in the invariant mass distributions.

e.g. Ref. [134]). For high-precision data, the issue is exacerbated by possible effects from final-state interactions, which may distort the effective dynamical amplitudes of the isobar resonances (see e.g. Refs. [61, 135]). The restriction of the conventional PWA approach to parameter-free decay amplitudes makes it difficult to implement and test models that take into account such effects. A crude way of checking, whether the used parameters of the isobar resonances deviate from the data, are so-called likelihood scans. Here, one performs several PWA fits with different values for selected isobar parameters and compares the maximum values of the likelihood function for each parameter set. Using the asymptotic normality of the maximum of the likelihood function in the resonance parameters, one can estimate isobar parameters that better fit the data (see e.g. Ref. [136]). However, with this method one can optimize only a few free parameters simultaneously. A more model-independent approach that is able to extract the amplitudes of subsystems with well-defined quantum numbers from the data will be presented in Section 5.2.9.

Another issue that complicates the wave-set selection is the non-orthogonality of some partial-wave amplitudes. In principle, the orthogonality of the Wigner  $D$ -functions that appear in the decay amplitudes (see Section 5.1.2) also makes the decay amplitudes for waves  $i$  and  $j$  orthogonal, unless the quantum numbers of the two waves that determine the  $D$ -functions are the same (see Appendix B). For orthogonal decay amplitudes, the corresponding off-diagonal elements of the phase-space integral matrix  $I_{ij}^\varepsilon$  in Eq. (185) vanish. Depending on the analyzed final state, the orthogonality of the decay amplitudes may be broken by the Bose symmetrization in Eq. (159). A measure for the (non-)orthogonality are the normalized off-diagonal elements

$${}^{\text{norm}}I_{ij}^\varepsilon(m_X) := \frac{I_{ij}^\varepsilon(m_X)}{\sqrt{I_{ii}^\varepsilon(m_X) I_{jj}^\varepsilon(m_X)}} \quad (214)$$

of the integral matrix in Eq. (185). This matrix is actually a Gram matrix for the scalar product of two partial-wave amplitudes that is represented by the phase space integral in Eq. (185). A modulus of 1 of an off-diagonal element of  ${}^{\text{norm}}I_{ij}^\varepsilon$  would mean that the corresponding partial-wave amplitudes are mathematically indistinguishable, i.e. linearly dependent. A PWA model containing such a pair of waves would be ill-defined and would lead to unphysical fit results for these waves. In practice, due to the finiteness of the measured data set, such distinguishability issues may already arise for waves, for which  $|{}^{\text{norm}}I_{ij}^\varepsilon|$  is close to unity. This is usually the case for wave sets that include in addition to the ground-state isobar resonances also the corresponding radially excited states. At low  $m_X$ , i.e. well below thresholds that correspond to the nominal masses of an isobar and its radial excitation, the dynamical amplitudes of the two isobar resonances are dominated by phase space and are hence very similar. In this case, the elements of  ${}^{\text{norm}}I_{ij}^\varepsilon$  that correspond to waves with the same quantum numbers have large moduli. This is a general problem that always appears when an isobar and its radial excitation are included in the PWA model as separate partial-wave amplitudes. It is a consequence of the binning in  $m_X$ . In order to resolve the arising ambiguities, one usually makes the PWA model discontinuous in  $m_X$ , i.e. one introduces  $m_X$  thresholds, below which certain waves are excluded from the PWA model. In practice, one would hence exclude waves with radially excited isobars at low masses. This means that we have to determine the wave set in principle for each  $m_X$  bin individually.<sup>82</sup> This also takes into account the different size of the data samples in the various  $m_X$  bins.

Up to now, the wave-set selection was performed “by hand”, e.g. by performing the PWA with a large wave set and iteratively removing waves with small intensities. Although this method often yields satisfactory results (as is shown in Section 6), this approach has a number of caveats and limitations. For large data sets that require large wave sets, it is not a well-defined procedure and is hence prone to observer bias and difficult to document and reproduce. It is also often very time

---

<sup>82</sup>In principle, the wave set also depends on  $t'$  because the intensity of a wave is approximately proportional to  $(t')^{|M|}$ , so that waves with spin projection  $M > 0$  are suppressed at low  $t'$  (see Section 5.3.2).

consuming. In addition, systematic uncertainties due to the choice of the wave set are difficult to estimate.

A more systematic approach that is currently under study is the *regularization* of the log-likelihood function in Eq. (206). This means that one adds a regularization term to the log-likelihood function that introduces additional constraints on the fit parameters, i.e.

$$\ln \tilde{\mathcal{L}}(\{\mathcal{T}_i^{r\varepsilon}\}) = \ln \mathcal{L}_{\text{ext}}(\{\mathcal{T}_i^{r\varepsilon}\}) + \ln \mathcal{L}_{\text{reg}}(\{\mathcal{T}_i^{r\varepsilon}\}). \quad (215)$$

The idea is to perform the maximization of the regularized log-likelihood function  $\ln \tilde{\mathcal{L}}(\{\mathcal{T}_i^{r\varepsilon}\})$  using a systematically constructed set of all possible partial waves up to a cut-off criterion and to choose the regularization term  $\ln \mathcal{L}_{\text{reg}}(\{\mathcal{T}_i^{r\varepsilon}\})$  such that partial-wave amplitudes that are statistically consistent with zero are suppressed, while partial-wave amplitudes far away from zero are influenced only negligibly by  $\ln \mathcal{L}_{\text{reg}}$ . This way, one could determine from the data an optimal wave set that describes the data well.

Up to now, several such approaches were studied using Monte Carlo pseudo data with known partial-wave content. The authors of Ref. [137] applied the so-called LASSO method,<sup>83</sup> where  $\mathcal{L}_{\text{reg}}$  has Laplacian form in  $|\mathcal{T}_i^{r\varepsilon}|$ , so that

$$\ln \mathcal{L}_{\text{reg}}(\{\mathcal{T}_i^{r\varepsilon}\}; \lambda) = -\lambda \sum_{\varepsilon=\pm 1} \sum_{r=1}^{N_r^\varepsilon} \sum_i^{N_{\text{waves}}^\varepsilon} |\mathcal{T}_i^{r\varepsilon}|. \quad (216)$$

This effectively suppresses partial waves with small intensities but also potentially biases waves with large intensities. We studied independently the regularization with  $\mathcal{L}_{\text{reg}}$  having a Cauchy form in  $|\mathcal{T}_i^{r\varepsilon}|$  [139–141], i.e.

$$\ln \mathcal{L}_{\text{reg}}(\{\mathcal{T}_i^{r\varepsilon}\}; \Gamma) = - \sum_{\varepsilon=\pm 1} \sum_{r=1}^{N_r^\varepsilon} \sum_i^{N_{\text{waves}}^\varepsilon} \ln \left[ 1 + \frac{|\mathcal{T}_i^{r\varepsilon}|^2}{\Gamma^2} \right]. \quad (217)$$

This term pulls the amplitudes of partial waves with small intensities toward zero, but leaves the waves with large intensities nearly unaffected.

Both regularization approaches yield promising results when applied to Monte Carlo pseudo data. The application to real data is currently under study. A general problem is that the regularization terms have parameters, i.e.  $\lambda$  in Eq. (216) and  $\Gamma$  in Eq. (217), that need to be determined. The authors of Ref. [137] propose to apply information criteria [142, 143] to determine the optimal parameter values, but more studies are needed to verify the applicability of these criteria. Currently, the regularization of the likelihood function seems to be an interesting approach that is worth to be studied in more detail. The method would make the wave-set selection reproducible and the bias that is introduced in form of the regularization term explicit. By applying different regularization terms and parameter values, one could study the wave-set dependence of the PWA result. The method makes it also possible to study, for example, the dependence of the PWA result on the set of isobars, on the parameterizations of the dynamical amplitudes of the isobar resonances, and on the inclusion of partial waves with higher spin. In most cases, such studies are impossible to perform if the waves set is selected by hand.

An additional issue is the choice of the formalism that is employed to calculate the decay amplitudes. As was discussed in Section 5.1.2, we employ the helicity formalism together with simple parameterizations for the propagator terms of the isobar resonances and the orbital angular-momentum barrier factors (see Sections 3.1.4 and 5.1.3). The disadvantage of this approach is that the extracted partial-wave amplitudes have a complicated transformation behavior under Lorentz transformations

---

<sup>83</sup>LASSO stands for “least absolute shrinkage and selection operator” and is a regularization method that was first proposed by R. Tibshirani in Ref. [138].

and—more importantly—do not satisfy all constraints required by analyticity. An alternative approach is to formulate the decay amplitudes in a covariant formalism [144–150], often referred to as *covariant tensor formalism*. In a recent comparison of both approaches, the authors of Ref. [151], however, find that some of the covariant approaches violate crossing symmetry. They also propose improved parameterizations for the dynamical parts of the helicity amplitudes that are more consistent with the relativistic  $S$ -matrix principles (see also Section 5.3.4). Applying these amplitudes to COMPASS data is work in progress.

### 5.2.9. Freed-Isobar Partial-Wave Analysis

As was discussed in Sections 5.2.5 and 5.2.8, in the conventional PWA method the decay amplitudes must not have any free parameters because otherwise the computation of the likelihood function would become too expensive in the minimization procedure. Consequently, the choice of the parameterizations and parameters of the dynamical amplitudes of the isobar resonances induces significant systematic uncertainties that are difficult to estimate. In addition, in the conventional PWA approach it is difficult to take into account decays via ground *and* excited states of isobar resonances. Partial-wave amplitudes that have the same angular quantum numbers but describe decays via isobars with the same  $I^G J^{PC}$  quantum numbers are non-orthogonal because of the non-vanishing overlaps of the dynamic amplitudes of the isobar states. As was discussed in Section 5.2.8, the non-orthogonality may lead to distinguishability issues between these partial-wave amplitudes. Hence yields of resonances can only be measured reliably from the coherent sum of these amplitudes. A notoriously difficult case, where both aspects—not well-known parameterizations and several excited states—come together, is, for example, the sector of isoscalar scalar isobars. Decays via such isobars may involve the  $f_0(500)$ ,  $f_0(980)$ ,  $f_0(1370)$ ,  $f_0(1500)$ , or even higher-lying states. In order to circumvent these limitations and in addition render the analysis less model-dependent, members of the COMPASS analysis group developed the novel so-called *freed-isobar PWA method*. This method is inspired by the so-called model-independent PWA method that was developed by the authors of Ref. [152] in order to study three-body decays of heavy mesons. Here, we briefly sketch the freed-isobar method for the case of three spinless final-state particles as was discussed in Section 5.1.5. More details can be found in Refs. [102, 153, 154]. The extension of the method to final states with more particles is straight forward. Without loss of generality, we assume that the three-body decay proceeds via the two-step process  $X \rightarrow r + 3$  with  $r \rightarrow 1 + 2$ . We assume in addition a rank-1 spin-density matrix.

The conventional PWA model uses fixed parameterizations for the propagator terms  $\mathcal{D}_r(m_r)$  of the isobar resonances in order to calculate the decay amplitude in Eq. (158). To simplify notation, we assume that  $m_X$  is constant and omit all constant and  $m_X$ -dependent factors in the decay amplitude that are fixed by the normalization in Eq. (188). Taking into account Eqs. (160) and (162), we rewrite Eq. (158) as

$$\Psi_i^\varepsilon(\vartheta_{\text{GJ}}, \phi_{\text{GJ}}, m_r, \vartheta_{\text{HF}}, \phi_{\text{HF}}) = \underbrace{F_{L_X}(m_r) \mathcal{D}_r(m_r) F_{J_r}(m_r)}_{=: \tau_3} \mathcal{K}_i^\varepsilon(\Omega_{\text{GJ}}, \Omega_{\text{HF}}). \quad (218)$$

Here, the index  $i$  represents the quantum numbers of the three-body partial wave and those of the isobar resonance  $r$ ,  $\mathcal{D}_r(m_r)$  is the propagator term of the isobar resonance  $r$  (see Section 5.1.3), and  $F_{L_X}(m_r)$  and  $F_{J_r}(m_r)$  are the centrifugal-barrier factors for the  $X \rightarrow r + 3$  and the  $r \rightarrow 1 + 2$  decay, respectively (see Eq. (97)).<sup>84</sup> The amplitude  $\mathcal{K}_i^\varepsilon(\Omega_{\text{GJ}}, \Omega_{\text{HF}})$  collects all terms that depend on the angles  $\Omega_{\text{GJ}} := (\cos \vartheta_{\text{GJ}}, \phi_{\text{GJ}})$  in the Gottfried-Jackson frame and the angles  $\Omega_{\text{HF}} := (\cos \vartheta_{\text{HF}}, \phi_{\text{HF}})$  in the helicity frame (see Section 5.1.4). Taking into account the Bose symmetrization of the final-state

<sup>84</sup>Note that although  $m_X$  is constant, the barrier factor  $F_{L_X}$  still depends on  $m_r$  via the breakup momentum of the  $X \rightarrow r + 3$  decay that appears in Eq. (97).

particles according to Eq. (159), the decay amplitude in a particular  $m_X$  bin is<sup>85</sup>

$$\Psi_i^{\varepsilon, \text{sym}}(\{\tau_{3,k}\}) = \sum_{k=1}^{N_{\text{perm}}} F_{L_X}(m_{r,k}) \mathcal{D}_r(m_{r,k}) F_{J_r}(m_{r,k}) \mathcal{K}_i^{\varepsilon}(\Omega_k^{\text{GJ}}, \Omega_k^{\text{HF}}), \quad (219)$$

where the index  $k$  enumerates the indistinguishable permutations of the final-state particles.<sup>86</sup>

In our novel freed-isobar method, we replace the fixed parameterizations for  $\mathcal{D}_r(m_r)$  by a set of piece-wise constant amplitudes that fully cover the kinematically allowed mass range for  $m_r$ , i.e.

$$\check{\mathcal{D}}_i^{\varepsilon}(m_r) = \sum_l^{m_r \text{ bins}} \mathcal{T}_{i,l}^{\varepsilon} \Pi_{l,r}(m_r). \quad (220)$$

Here, the index  $l$  runs over the  $m_r$  bins. These bins are defined by sets of window functions  $\{\Pi_{l,r}(m_r)\}$  that are non-zero only in a narrow  $m_r$  interval given by the set  $\{m_{r,l}\}$  of bin borders, i.e.

$$\Pi_{l,r}(m_r) = \begin{cases} 1 & \text{if } m_{r,l} \leq m_r < m_{r,l+1}, \\ 0 & \text{otherwise.} \end{cases} \quad (221)$$

In general, the  $m_r$  bins may be non-equidistant so that the bin width  $\delta m_{r,l} = m_{r,l+1} - m_{r,l}$  may depend on the mass region of the  $(1, 2)$  subsystem. The  $\mathcal{T}_{i,l}^{\varepsilon}$  are a set of unknown complex numbers that together determine the freed-isobar amplitude  $\check{\mathcal{D}}_i^{\varepsilon}(m_r)$ . This approach is conceptually similar to the binning in  $m_X$  and  $t'$  in the conventional PWA. Note that the freed-isobar amplitude depends on the partial-wave index  $i$  and the reflectivity  $\varepsilon$ , i.e. the model permits different  $\check{\mathcal{D}}_i^{\varepsilon}(m_r)$  for different intermediate states  $X$ . This is in contrast to the conventional PWA approach, where the *same* isobar parameterization is used for *all* partial-wave amplitudes, where the corresponding isobar resonance appears. Since the analysis is performed independently in  $(m_X, t')$  cells,  $\check{\mathcal{D}}_i^{\varepsilon}(m_r)$  is also allowed to change as a function of  $m_X$  and  $t'$ .

For a given  $(m_X, t')$  cell, the model for the intensity distribution in Eq. (195) contains terms of the form<sup>87</sup>

$$\mathcal{T}_i^{\varepsilon} \Psi_i^{\varepsilon, \text{sym}}(\{\tau_{3,k}\}) = \mathcal{T}_i^{\varepsilon} \sum_{k=1}^{N_{\text{perm}}} \left[ \sum_l^{m_r \text{ bins}} \mathcal{T}_{i,l}^{\varepsilon} \Pi_{l,r}(m_{r,k}) \right] F_{L_X}(m_{r,k}) F_{J_r}(m_{r,k}) \mathcal{K}_i^{\varepsilon}(\Omega_k^{\text{GJ}}, \Omega_k^{\text{HF}}), \quad (222)$$

where we have used Eqs. (219) and (220). We absorb the unknown amplitudes  $\mathcal{T}_{i,l}^{\varepsilon}$  into the transition amplitude  $\mathcal{T}_i^{\varepsilon}$  via the redefinition

$$\check{\mathcal{T}}_{i,l}^{\varepsilon} := \mathcal{T}_i^{\varepsilon} \mathcal{T}_{i,l}^{\varepsilon}. \quad (223)$$

Note that the transition amplitude now also depends on the  $m_r$  bin index  $l$ . Using Eq. (223), we can write the intensity distribution in Eq. (195) as

$$\mathcal{I} = \sum_{\varepsilon=\pm 1} \left| \sum_i^{N_{\text{waves}}^{\varepsilon}} \sum_l^{m_r \text{ bins}} \check{\mathcal{T}}_{i,l}^{\varepsilon} \check{\Psi}_i^{\varepsilon, \text{sym}}(\{\tau_{3,k}\}) \right|^2 + |\mathcal{T}_{\text{flat}}|^2, \quad (224)$$

<sup>85</sup>To simplify notation, we disregard the constant  $1/\sqrt{N_{\text{perm}}}$  factor, which is irrelevant because of the normalization in Eq. (188).

<sup>86</sup>In cases where decay amplitudes are related by isospin symmetry, the symmetrization expression in Eq. (219) becomes more complicated. However, the symmetrized decay amplitude still remains a linear combination of terms of the form of Eq. (218), which is the property relevant for the freed-isobar method.

<sup>87</sup>Since we are considering a rank-1 spin-density matrix, we leave off the rank index  $r$ .

where we have redefined the Bose-symmetrized decay amplitude to include the  $m_r$  window function, i.e.

$$\check{\Psi}_{i,l}^{\varepsilon,\text{sym}}(\{\tau_{3,k}\}) := \sum_{k=1}^{N_{\text{perm}}} \Pi_{l,r}(m_{r,k}) F_{L_X}(m_{r,k}) F_{J_r}(m_{r,k}) \mathcal{K}_i^{\varepsilon}(\Omega_k^{\text{GJ}}, \Omega_k^{\text{HF}}). \quad (225)$$

Note that the decay amplitude now also depends on the  $m_r$  bin index  $l$ .

In Eq. (224), the additional coherent sum over the  $m_r$  bin index  $l$  appears in the same way as the sum over the partial-wave index  $i$ . Therefore, each  $m_r$  mass bin can be treated like an independent partial wave. By defining a new freed-isobar partial-wave index  $\check{i} := \{i, l\}$ , Eq. (224) becomes mathematically equivalent to Eq. (195). This means that exactly the same maximum likelihood fit procedure as was described in Section 5.2.5 can be employed to determine the  $\{\check{\mathcal{T}}_{i,l}^{\varepsilon}\}$ . This also includes the pre-calculation of the integral matrices of the decay amplitudes. It is actually this property of the freed-isobar approach that makes it practically applicable, in contrast to allowing free parameters in the dynamical isobar amplitudes, which is usually prohibitively expensive in terms of computational resources. Another important property of the freed-isobar approach is that not all waves in the PWA model have to be parameterized using the freed-isobar amplitudes in Eq. (220). Depending on the size of the analyzed data sample, one usually employs freed-isobar amplitudes only for a subset of waves while for the remaining waves in the PWA model the conventional fixed parameterizations of the isobar amplitudes are used. Depending on how many decay amplitudes are parameterized using freed-isobar amplitudes and how many  $m_r$  bins are used for the freed-isobar amplitudes, the computation cost for a freed-isobar PWA grows only moderately, typically by about an order of magnitude.

Performing such a freed-isobar PWA in  $(m_X, t')$  cells, yields transition amplitudes  $\check{\mathcal{T}}_i^{\varepsilon}(m_X, t', m_r)$  that now depend not only on  $m_X$  and  $t'$  but also on  $m_r$  (via the  $m_r$  bin index  $l$ ). As is clear from Eq. (223), the freed-isobar transition amplitudes contain information about the intermediate states  $X$  as well as about the respective isobar subsystems. For each freed-isobar wave and each  $(m_X, t')$  cell, the method yields an Argand diagram ranging in  $m_r$  from  $m_1 + m_2$  to  $m_X - m_3$ . It is important to note that by parameterizing the  $m_r$  dependence of the decay amplitude for a wave  $i$  using the freed-isobar amplitude in Eq. (220), we do not make any assumptions about the resonance content of the  $(1, 2)$  subsystem. The freed-isobar PWA determines from the data the total amplitude of all intermediate isobar states with given  $I^G J^{PC}$  quantum numbers in the three-body partial wave defined by  $i$  and  $\varepsilon$ . This amplitude  $\check{\mathcal{T}}_i^{\varepsilon}$  hence includes all isobar resonances, potential non-resonant contributions, as well as possible distortions due to final-state interactions. As a consequence, the method avoids the issue of non-orthogonal partial-wave amplitudes for decays via isobar states with the same  $I^G J^{PC}$  quantum numbers that appear in the conventional PWA as was discussed above. The reduced model dependence of the freed-isobar method and the obtained additional information about the correlation of the dynamic isobar amplitude with the dynamic amplitude of the  $X$  come at the price of a considerably larger number of fit parameters compared to the conventional PWA. Thus even for large data sets, the freed-isobar approach can only be applied to a subset of the partial waves in the PWA model. For the other partial waves, the conventional fixed isobar parameterizations are used.

An additional complication arises if a freed-isobar PWA model contains more than one freed-isobar partial wave with the same three-body  $J^{PC} M^{\varepsilon}$  quantum numbers. In this case, mathematical ambiguities, so-called zero modes, may arise at the amplitude level. How to identify and resolve these ambiguities is described in Refs. [153, 154].

Results from a first freed-isobar PWA of COMPASS  $\pi^- \pi^- \pi^+$  data, that focuses in particular on the  $f_0$  isobars mentioned above, will be discussed in Sections 6.2.3, 6.3.1, 6.3.2, and 6.3.5.

### 5.3. Stage II: Resonance-Model Fit of Spin-Density Matrix

The first analysis stage, i.e. the partial-wave decomposition of the data as described in Section 5.2, yields as a result the spin-density matrices  $\varrho_{ij}^{\varepsilon}$  in the  $(m_X, t')$  cells. This set of spin-density matrices serves as the input for the second analysis stage, where we want to identify  $n$ -body resonances

that contribute to certain partial-wave amplitudes and determine their parameters. To this end, we formulate a model  $\hat{\varrho}_{ij}^\varepsilon(m_X, t')$ <sup>88</sup> that describes the dependence of the spin-density matrix elements on  $m_X$  and  $t'$  in terms of resonant and non-resonant components. The parameters and yields of the resonances included in this model are determined by a fit to the measured spin-density matrices. In this *resonance-model fit*, which is also referred to as *mass-dependent fit*, we exploit that resonances have a characteristic signature. In the simplest case, they appear as Breit-Wigner-shaped peaks in the partial-wave intensities that are accompanied by  $180^\circ$  phase motions relative to non-resonating waves (see e.g. Fig. 10). In reality, this simple picture often does not hold. The behavior of the spin-density matrix elements is usually more complicated because multiple resonances, e.g. a ground state and corresponding radially excited states, may appear in a given partial wave. In general, the resonances overlap and interfere so that resonance peaks might shift, disappear, or—in the case of destructive interference—might even turn into dips in the intensity distribution.<sup>89</sup> In diffractive-dissociation reactions, this interference pattern is further complicated by additional coherent contributions from non-resonant double-Regge exchange processes (see Sections 4.1 and 5.2.8 and Figs. 21c and 21d). The different  $t'$  dependences of these contributions lead to a  $t'$ -dependent interference. Hence in many cases, the information from partial-wave intensities alone is insufficient to extract resonances and their parameters reliably from the data. It is therefore a great advantage that the partial-wave decomposition is performed at the amplitude level. The parameters of the resonances are hence constrained not only by the measured intensities of the partial waves but also by the mutual interference terms of the waves. This greatly improves the sensitivity for potential resonance signals.

As was discussed in Section 5.1.7, an advantage of the two-stage analysis approach is that the resonance model does not need to describe all partial-wave amplitudes that are included in the PWA model. The representation of the data in terms of the spin-density matrix allows us to model only selected matrix elements. Usually, one selects a subset of waves and models all elements of the corresponding spin-density submatrix. The criteria that are used to select the waves that are included in the resonance-model fit depend strongly on the analyzed channel. In general, one tries to select waves with clear signals of known resonances plus a few “interesting” waves, the idea being that the known resonances act as reference amplitudes, against which the resonant amplitudes in the interesting waves can interfere. When searching for resonance signals in the partial-wave amplitudes, one has to take into account that similar to the resonance peaks in the intensity distributions also the phase motions are distorted by the presence of other resonances. If, for example, waves  $i$  and  $j$  with reflectivity  $\varepsilon$  each contain a resonance, the rising motion of their relative phase  $\Delta\phi_{ij}^\varepsilon$  (see Eq. (212)) due to the resonance in wave  $i$  may be compensated by the falling motion due to the other resonance in wave  $j$ . In the extreme case when the two resonances have similar parameters, this cancellation may become nearly complete. It is therefore often difficult to observe undisturbed phase motions of resonances. This effect is particularly pronounced in the high- $m_X$  regions, where broad excited states appear in most or even all waves in the resonance-model fit.

### 5.3.1. Resonance Model

In order to formulate the resonance model, we go back to Eq. (165) in Section 5.1.7, where we defined the transition amplitudes. Using this definition, and taking into account the reflectivity basis (see Section 5.2.3) and possible incoherences in terms of the rank of the spin-density matrix (see Section 5.2.2), we can write the model for the transition amplitudes as

$$\hat{T}_i^{r\varepsilon}(m_X, t') = \sqrt{I_{ii}^\varepsilon(m_X)} \sqrt{m_X} \mathcal{P}^\varepsilon(m_X, t') \sum_{k \in \mathbb{S}_i^\varepsilon} \mathcal{C}_{ki}^{r\varepsilon}(t') \mathcal{D}_k^{r\varepsilon}(m_X, t'; \zeta_k^{r\varepsilon}). \quad (226)$$

---

<sup>88</sup>In the following text, modeled quantities are distinguished from their measured counterparts by a hat (“ $\hat{\cdot}$ ”).

<sup>89</sup>This fact is expressed in a concise way by the common saying: “Not every peak is a resonance and not every resonance is a peak” (see also Ref. [155]).

Here, the factor  $\sqrt{I_{ii}^\varepsilon(m_X)}$  appears due to the chosen normalization of the transition amplitudes in Eq. (192). The amplitude  $\mathcal{P}^\varepsilon(m_X, t')$  models the average production probability of an intermediate state with mass  $m_X$  as a function of  $t'$ . It hence is independent of the wave index  $i$ , but it depends in the most general case on the reflectivity  $\varepsilon$ . This is because different values of  $\varepsilon$  correspond to different exchange particles and hence different production processes. Likewise, the coupling amplitudes  $\mathcal{C}_{ki}^{r\varepsilon}(t')$  depend on  $\varepsilon$ . They depend in addition on the rank index  $r$  in order to model potential incoherences. Together with  $\mathcal{P}^\varepsilon(m_X, t')$ , the coupling amplitudes describe the production of the resonant and non-resonant components that are represented by the dynamical amplitudes  $\mathcal{D}_k^{r\varepsilon}(m_X, t'; \zeta_k^{r\varepsilon})$ . Concerning the latter amplitudes we extended the model with respect to Eq. (165) such that in the most general case also the dynamical amplitudes may depend on  $\varepsilon$  and on  $r$  and that they may have an explicit  $t'$  dependence. The reason for this will become clear in the discussion of the parameterization of the non-resonant components below.

In Eq. (226), we parameterize the transition amplitude of a given partial wave  $i$  as a coherent sum of the amplitudes of so-called *wave components* that can be either resonances or non-resonant components. The wave components are represented by the dynamical amplitudes, which are enumerated by the index  $k$ . The same wave component, e.g. a resonance, may appear in several waves. Hence the sum in Eq. (226) runs over the set  $\mathbb{S}_i^\varepsilon$  of those wave components that we assume to appear in wave  $i$  with reflectivity  $\varepsilon$ . The dynamical amplitudes depend on a set of *shape parameters* that we denote by  $\zeta_k^{r\varepsilon}$ . For example, in the case of a Breit-Wigner resonance, these parameters are mass and width of that resonance. It is important to note that for resonances the dynamical amplitudes and their shape parameters are independent of the partial-wave index  $i$ , the rank index  $r$ , and the reflectivity  $\varepsilon$ . Thus if a resonance component  $\mathcal{D}_k^R$  appears in several partial waves, which e.g. represent different decay chains or  $M^\varepsilon$  states of this resonance, the same shape parameters  $\zeta_k^R$  are used in these waves.

The coupling amplitudes  $\mathcal{C}_{ki}^{r\varepsilon}(t')$  in Eq. (226) collect two kinds of unknowns: (i) the product  $\alpha_i$  of the complex-valued couplings that appear at the two-body decay vertices in the  $n$ -body isobar decay chain of wave  $i$  (see Eq. (162))<sup>90</sup> and (ii) the details of the beam-Reggeon vertex, i.e. the  $t'$  dependence of the production strength and phase of wave component  $k$  in wave  $i$  with reflectivity  $\varepsilon$ . Currently, theoretical models are not detailed enough in order to parameterize these  $t'$  dependences. Therefore, binned approximations of the  $\mathcal{C}_{ki}^{r\varepsilon}(t')$  are extracted from the data by fitting the resonance model to all  $t'$  bins simultaneously and leaving the values of each coupling amplitude in each  $t'$  bin as free parameters to be determined by the fit. The resonance model hence parameterizes mostly the  $m_X$  dependence of the spin-density matrix, but is model-independent with respect to the  $t'$  dependence in the sense that the amplitude of each component in each wave is allowed to have a different  $t'$  dependence. An additional advantage of this binned approach is that the resonant and non-resonant wave components can be better disentangled because their amplitudes have usually different dependences on  $t'$ . The caveat of such a  $t'$ -resolved resonance-model fit is the large number of free parameters.

Assuming factorization of production, propagation, and decay of the intermediate  $n$ -body resonances, the dynamical amplitudes  $\mathcal{D}_k^R(m_X; \zeta_k^R)$  of the resonances should be independent of  $r$ ,  $\varepsilon$ , and  $t'$ . The latter constraint is built into the model by using the same resonance shape parameters  $\zeta_k^R$ , i.e. masses and widths of the resonances, across all  $t'$  bins. Only strength and phase of each resonance component, represented by the coupling amplitudes  $\mathcal{C}_{ki}^{r\varepsilon}(t')$ , can be chosen freely by the fit in each  $t'$  bin. Since the  $t'$  dependence of an amplitude of a resonant component is determined by the production mechanism, factorization of production and decay means that the  $t'$  dependence of the amplitude should be the same in different decay chains of that resonance for a given spin projection  $M^\varepsilon$ . This can be exploited to reduce the number of parameters by fixing the  $t'$  dependence of the amplitude of resonance  $k$  in wave  $j$ , which is represented by  $\mathcal{C}_{kj}^{r\varepsilon}(t')$ , to the  $t'$  dependence of that resonance in

---

<sup>90</sup>The couplings and hence their product are independent of  $t'$ .

wave  $i$ :<sup>91</sup>

$$\mathcal{C}_{kj}^{r\varepsilon}(t') = {}_j\mathcal{B}_{ki}^\varepsilon \mathcal{C}_{ki}^{r\varepsilon}(t'). \quad (227)$$

The  $t'$ -independent complex-valued proportionality factors  ${}_j\mathcal{B}_{ki}^\varepsilon$ , which are determined by the fit, are called *branching amplitudes* and encode the relative strength and phase of the two decay chains  $i$  and  $j$  of resonance  $k$ .

The dynamical amplitudes  $\mathcal{D}_k^R(m_X; \zeta_k^R)$  of the resonance components with the shape parameters  $\zeta_k^R := (m_k, \Gamma_k)$  are often parameterized using Breit-Wigner amplitudes. The parameterization used for the total width depends on how well the decay modes of the resonance are known. If the branching fractions of the resonance are not well-known or even unknown, the constant-width approximation in Eq. (151) is used. If the branching fractions are known sufficiently well, Eq. (152) is employed. This parameterization takes into account the opening of the phase space over the resonance by modeling the decay as an incoherent sum of two-body decays of quasi-stable particles, i.e. by neglecting the width of any isobars that appear in the decays. Equation (152) is only a good approximation in the  $m_X$  range well above the nominal thresholds of the respective decay channels. Close to or below these thresholds, the finite width of the isobar(s) cannot be neglected and more advanced parameterizations have to be used (see e.g. Section IV.A in Ref. [156]).

The dynamical amplitudes of the non-resonant components are in general not well known so that empirical parameterizations are employed, which are often developed in a data-driven approach. In general, we cannot assume factorization of production and decay for the non-resonant components and also Eq. (227) does not hold. Thus one usually includes for each wave a separate non-resonant component with independent shape parameters. Consequently, the dynamical amplitude of a non-resonant component may depend on the reflectivity  $\varepsilon$ . In the most general case, the non-resonant terms may also have incoherent components so that the dynamical amplitude may depend on the rank index  $r$ . A common assumption that is built into the employed parameterizations for these dynamical amplitudes is that their phase is independent of  $m_X$ . Inspired by Ref. [157], in many analyses a Gaussian in the two-body break-up momentum  $q_i$  of the  $X$  decay in wave  $i$  is used, i.e.<sup>92</sup>

$$\begin{aligned} {}^{\text{NR}}\mathcal{D}_k^{r\varepsilon}(m_X; \underbrace{b, c_0}_{=: {}^{\text{NR}}\zeta_k^{r\varepsilon}}) &= \left[ \frac{m_X - m_{\text{thr}}}{m_{\text{norm}}} \right]^b e^{-c_0 q_i^2(m_X)}. \end{aligned} \quad (228)$$

Here, we have added the term in square brackets, which approximates the phase-space opening. The constant  $m_{\text{thr}}$  is set to a value around the kinematical threshold and  $m_{\text{norm}}$  is usually set to  $1 \text{ GeV}/c^2$ . Since for  $m_X$  values close to or below the two-body threshold, Eqs. (62) and (63) are not applicable to calculate  $q_i(m_X)$ , more advanced parameterizations are used, which effectively take into account the width of the isobar resonance that appears in wave  $i$  (see Section IV.A in Ref. [156] for details). In general, the shape of the  $m_X$  distribution of a non-resonant component may change with  $t'$  so that the dynamical amplitude may have an explicit  $t'$  dependence. In such cases, it was found that an extension of Eq. (228) of the form<sup>92</sup>

$$\begin{aligned} {}^{\text{NR}}\mathcal{D}_k^{r\varepsilon}(m_X, t'; \underbrace{b, c_0, c_1, c_2}_{=: {}^{\text{NR}}\zeta_k^{r\varepsilon}}) &= \left[ \frac{m_X - m_{\text{thr}}}{m_{\text{norm}}} \right]^b e^{-\left(c_0 + c_1 t' + c_2 t'^2\right) q_i^2(m_X)} \end{aligned} \quad (229)$$

yields a better description of the data.

For diffractive-dissociation reactions, the average production amplitude  $\mathcal{P}^\varepsilon(m_X, t')$  can be modelled using Regge theory (see Section 3.2). At high energies, these reactions are dominated by  $t$ -channel Pomeron ( $\mathbb{P}$ ) exchange (see Section 4.1). We follow the phenomenological Regge approach

<sup>91</sup>The waves  $i$  and  $j$  must have the same  $J^{PC} M^\varepsilon$  quantum numbers. If more than two waves in the resonance-model fit fulfill this criterion, always the same reference wave  $i$  is used in Eq. (227). Usually, the wave that corresponds to the most dominant decay chain of resonance  $k$  is chosen as the reference wave  $i$ .

<sup>92</sup>To simplify notation, we omit the indices  $k$ ,  $r$ , and  $\varepsilon$  from the shape parameters.

developed in Ref. [158] to describe central-production reactions. The cross section for this reaction is proportional to the so-called *Pomeron flux* factor [159]

$$F_{\mathbb{P}p}(x_{\mathbb{P}}, t') \propto \frac{e^{-b_{\mathbb{P}} t'}}{x_{\mathbb{P}}^{2\alpha_{\mathbb{P}}(t')-1}}, \text{ where } x_{\mathbb{P}} \approx \frac{m_X^2}{s} \quad (230)$$

is the fraction of the longitudinal proton momentum carried by the Pomeron in the center-of-momentum frame of the reaction. Mandelstam  $s$  is the squared center-of-momentum energy of the beam-target system,  $b_{\mathbb{P}}$  is the slope parameter of the  $t'$  dependence of the cross section for Pomeron-exchange reactions, and  $\alpha_{\mathbb{P}}(t')$  is the Regge trajectory of the Pomeron (see Eq. (126)).<sup>93</sup> The Pomeron flux in Eq. (230) can be interpreted as the probability for emission of a Pomeron by the proton. In the limit of  $\alpha_0 = 1$  and  $\alpha' = 0$  ( $\text{GeV}/c$ ) $^{-2}$ , this probability is proportional to  $1/x_{\mathbb{P}}$  and hence proportional to  $1/m_X^2$ . This dependence can be explained, for example, by a Bremsstrahlungs-like mechanism [160, 161]. We assume that the Pomeron flux factor in Eq. (230) is universal and apply it to the single-Pomeron exchange process of diffractive dissociation as it was done e.g. in Ref. [162]. We absorb the normalization and the factor  $e^{-b_{\mathbb{P}} t'}$  into the coupling amplitudes  $\mathcal{C}_{ki}^{r\varepsilon}(t')$  so that the production probability is given by

$$|\mathcal{P}^{\varepsilon}(m_X, t')|^2 = \frac{1}{x_{\mathbb{P}}^{2\alpha_{\mathbb{P}}(t')-1}} \approx \left[ \frac{s}{m_X^2} \right]^{2\alpha_{\mathbb{P}}(t')-1}. \quad (231)$$

### 5.3.2. $t'$ -Dependent Observables

Since the resonance-model fit is performed simultaneously in several  $t'$  bins, we can extract the  $t'$  dependence of production strength and phase for each wave component in the model. This information is contained in the coupling amplitudes  $\mathcal{C}_{ki}^{r\varepsilon}(t')$ .

From the intensity  $N_i^{\varepsilon}$  of partial wave  $i$  with reflectivity  $\varepsilon$  as defined in Eq. (208), we can derive an expression for the intensity of a wave component in this wave for a given  $(m_X, t')$  cell by using the resonance model in Eq. (226):

$$\begin{aligned} N_i^{\varepsilon}(m_X, t') &= \underbrace{\sum_{k \in \mathbb{S}_i^{\varepsilon}} I_{ii}^{\varepsilon}(m_X) m_X |\mathcal{P}^{\varepsilon}(m_X, t')|^2 \sum_{r=1}^{N_r^{\varepsilon}} |\mathcal{C}_{ki}^{r\varepsilon}(t')|^2 |\mathcal{D}_k^{r\varepsilon}(m_X, t'; \zeta_k^{r\varepsilon})|^2}_{\text{intensity of wave component } k} \\ &+ \underbrace{\sum_{\substack{k, l \in \mathbb{S}_i^{\varepsilon} \\ k < l}} I_{ii}^{\varepsilon}(m_X) m_X |\mathcal{P}^{\varepsilon}(m_X, t')|^2 2 \text{Re} \left[ \sum_{r=1}^{N_r^{\varepsilon}} \mathcal{C}_{ki}^{r\varepsilon}(t') \mathcal{C}_{li}^{r\varepsilon*}(t') \mathcal{D}_k^{r\varepsilon}(m_X, t'; \zeta_k^{r\varepsilon}) \mathcal{D}_l^{r\varepsilon*}(m_X, t'; \zeta_l^{r\varepsilon}) \right]}_{\text{overlap of wave components } k \text{ and } l}. \end{aligned} \quad (232)$$

This expression has a structure analogous to Eq. (193) and we can define the intensity  $N_{ki}^{\varepsilon}$  of wave component  $k$  as

$$N_{ki}^{\varepsilon}(m_X, t') := I_{ii}^{\varepsilon}(m_X) m_X |\mathcal{P}^{\varepsilon}(m_X, t')|^2 \sum_{r=1}^{N_r^{\varepsilon}} |\mathcal{C}_{ki}^{r\varepsilon}(t')|^2 |\mathcal{D}_k^{r\varepsilon}(m_X, t'; \zeta_k^{r\varepsilon})|^2. \quad (233)$$

Due to the chosen normalization,  $N_{ki}^{\varepsilon}(m_X, t')$  corresponds to the expected number of produced events in wave component  $k$  in wave  $i$  with reflectivity  $\varepsilon$  in a given  $(m_X, t')$  cell (see Section 5.2.4).

<sup>93</sup>Here, we neglect  $|t|_{\min}$  so that  $t' \approx -t$ . A discussion about the choice of the values for  $\alpha_0$  and  $\alpha'$  can be found in Ref. [102].

By integrating Eq. (233) over the full  $m_X$  range under consideration, we get the  $t'$  spectrum of wave component  $k$ :

$$\begin{aligned} \mathcal{I}_{ki}^\varepsilon(t') &= \frac{dN_{ki}^\varepsilon}{dt'} \\ &= \frac{1}{\Delta t'} \sum_{r=1}^{N_r^\varepsilon} |\mathcal{C}_{ki}^{r\varepsilon}(t')|^2 \int_{m_{\min}}^{m_{\max}} dm_X I_{ii}^\varepsilon(m_X) m_X |\mathcal{P}^\varepsilon(m_X, t')|^2 |\mathcal{D}_k^{r\varepsilon}(m_X, t'; \zeta_k^{r\varepsilon})|^2. \end{aligned} \quad (234)$$

Here, we divide by the  $t'$  bin width  $\Delta t'$  in order to take into account the non-equidistant  $t'$  binning. The  $m_X$  integration range  $[m_{\min}, m_{\max}]$  is usually given by the fit range that is used for the given partial wave.

In diffractive reactions, the  $t'$  spectra of most wave components exhibit an approximately exponential decrease with increasing  $t'$  in the range  $t' \lesssim 1(\text{GeV}/c)^2$ . This behavior can be explained in the framework of Regge theory (see Eq. (132)). The  $t'$  spectra of partial-wave amplitudes with a spin projection of  $M \neq 0$  along the beam direction are modified by an additional factor  $(t')^{|M|}$ . This factor is given by the forward limit of the Wigner  $D$ -functions [53] and suppresses the intensity toward small  $t'$ . Following Eq. (132), we therefore parameterize the  $t'$  spectra by the model

$$\hat{\mathcal{I}}_{ki}^\varepsilon(t'; A_{ki}^\varepsilon, b_{ki}^\varepsilon) = A_{ki}^\varepsilon \cdot (t')^{|M|} \cdot e^{-b_{ki}^\varepsilon t'}. \quad (235)$$

This parameterization has two free real-valued parameters: the magnitude parameter  $A_{ki}^\varepsilon$  and the slope parameter  $b_{ki}^\varepsilon$ . The parameters are estimated by performing a  $\chi^2$  fit, where the model function  $\hat{\mathcal{I}}_{ki}^\varepsilon(t')$  is integrated over each  $t'$  bin and compared to the measured value  $\mathcal{I}_{ki}^\varepsilon(t')$  in Eq. (234).

In addition to the  $t'$  spectrum, we can also extract the relative phase between the coupling amplitudes of wave component  $k$  in wave  $i$  and wave component  $l$  in wave  $j$ ,

$$\Delta\phi_{ki,lj}^\varepsilon(t') := \arg \left[ \sum_{r=1}^{N_r^\varepsilon} \mathcal{C}_{ki}^{r\varepsilon}(t') \mathcal{C}_{lj}^{r\varepsilon*}(t') \right]. \quad (236)$$

This quantity is called *coupling phase* and is conceptually similar to the relative phase in Eq. (212). Note that for a rank-1 spin-density matrix, i.e. full coherence of all partial waves,

$$\Delta\phi_{ki,lj}^\varepsilon(t') = \arg[\mathcal{C}_{ki}^\varepsilon(t')] - \arg[\mathcal{C}_{lj}^\varepsilon(t')]. \quad (237)$$

If the coupling amplitudes of a resonance in different decay chains are constrained via Eq. (227), the corresponding coupling phases are by definition independent of  $t'$  and are given by  $\arg[\mathcal{B}_{ki}^\varepsilon]$ . The interpretation of the values of a coupling phase is complicated by the fact that the coupling amplitude is the product of the actual production amplitude of wave component  $k$  and of the coupling  $\alpha_{ki}$ , which in turn is the product of the complex-valued couplings that appear at each two-body decay vertex in the  $n$ -body isobar decay chain of wave  $i$  (see Eq. (162)). The coupling phases of resonances are expected to be approximately independent of  $t'$ , if a single production mechanism dominates [163, 164]. This is in general not true for non-resonant components, which are produced by different mechanisms. Relative to resonances, the coupling phases of the non-resonant components usually change with  $t'$ . This leads in general to a  $t'$ -dependent interference pattern, which often causes a  $t'$ -dependent shift of resonance peaks, especially for waves with large non-resonant components. So if the shape of the measured  $m_X$  distribution of the intensity of a partial-wave amplitude changes with  $t'$ , it is a sign of contributions from non-resonant components.

### 5.3.3. Fit Method

We construct the model for the spin-density submatrix of those waves that are selected for the resonance-model fit by using Eqs. (194) and (226):

$$\begin{aligned}\widehat{\rho}_{ij}^{\varepsilon}(m_X, t') &= \sum_{r=1}^{N_r^{\varepsilon}} \widehat{T}_i^{r\varepsilon}(m_X, t') \widehat{T}_j^{r\varepsilon*}(m_X, t') \\ &= \sqrt{I_{ii}^{\varepsilon}(m_X) I_{jj}^{\varepsilon}(m_X)} m_X |\mathcal{P}^{\varepsilon}(m_X, t')|^2 \\ &\quad \times \sum_{r=1}^{N_r^{\varepsilon}} \left[ \sum_{k \in \mathbb{S}_i^{\varepsilon}} \mathcal{C}_{ki}^{r\varepsilon}(t') \mathcal{D}_k^{r\varepsilon}(m_X, t'; \zeta_k^{r\varepsilon}) \right] \left[ \sum_{l \in \mathbb{S}_j^{\varepsilon}} \mathcal{C}_{lj}^{r\varepsilon}(t') \mathcal{D}_l^{r\varepsilon}(m_X, t'; \zeta_l^{r\varepsilon}) \right]^*. \end{aligned} \quad (238)$$

The parameters of the resonance model, i.e. the set  $\{\mathcal{C}_{ki}^{r\varepsilon}(t')\}$  of coupling amplitudes and the set  $\{\zeta_k^{r\varepsilon}\}$  of shape parameters, are estimated by fitting the model  $\widehat{\rho}_{ij}^{\varepsilon}(m_X, t')$  to the spin-density matrices that are measured in the  $(m_X, t')$  cells (see Section 5.2). In order to perform this fit, we represent the Hermitian spin-density matrix by a real-valued matrix  $\Lambda_{ij}^{\varepsilon}(m_X, t')$  of the same dimension. The elements of  $\Lambda_{ij}^{\varepsilon}$  are defined by the upper triangular part of the spin-density matrix as follows

$$\Lambda_{ij}^{\varepsilon}(m_X, t') = \begin{cases} \text{Re}[\rho_{ij}^{\varepsilon}(m_X, t')] & \text{for } i < j, \\ \text{Im}[\rho_{ji}^{\varepsilon}(m_X, t')] & \text{for } i > j, \\ \rho_{ii}^{\varepsilon}(m_X, t') & \text{for } i = j. \end{cases} \quad (239)$$

This means that the upper off-diagonal elements of  $\Lambda_{ij}^{\varepsilon}$  are the real parts of the interference terms, the lower off-diagonal elements are the imaginary parts of the interference terms, and the diagonal elements are the partial-wave intensities. In an analogous way, we define  $\widehat{\Lambda}_{ij}^{\varepsilon}(m_X, t')$  for our resonance model in Eq. (238).

In order to quantify the deviation of the resonance model  $\widehat{\Lambda}_{ij}^{\varepsilon}(m_X, t')$  from the measured data  $\Lambda_{ij}^{\varepsilon}(m_X, t')$ , we sum the squared Pearson's residuals [165] of all matrix elements for all  $(m_X, t')$  cells, i.e.

$$\chi^2 = \sum_{\varepsilon=\pm 1} \sum_{i,j}^{N_{\text{waves}}^{\varepsilon}} \sum_{t' \text{ bins}}^{(m_X \text{ bins})_{ij}} \sum \left[ \frac{\Lambda_{ij}^{\varepsilon}(m_X, t') - \widehat{\Lambda}_{ij}^{\varepsilon}(m_X, t')}{\sigma_{ij}^{\varepsilon}(m_X, t')} \right]^2. \quad (240)$$

Here,  $N_{\text{waves}}^{\varepsilon}$  is the number of partial waves with reflectivity  $\varepsilon$  that are included in the fit model and  $\sigma_{ij}^{\varepsilon}(m_X, t')$  is the statistical uncertainty of the matrix element  $\Lambda_{ij}^{\varepsilon}(m_X, t')$  as determined in the partial-wave decomposition stage (see Appendix F). The sum in Eq. (240) runs over all  $t'$  bins and those  $m_X$  bins that lie within the chosen fit ranges. For the off-diagonal interference terms  $\Lambda_{ij}^{\varepsilon}$ , the  $m_X$  range is given by the intersection of the fit ranges for the intensities of waves  $i$  and  $j$ . The best estimate for the model parameters is determined by minimizing the  $\chi^2$  function using the MIGRAD algorithm of the MINUIT package [166, 167].<sup>94</sup>

It is important to note that although we use the notation  $\chi^2$  for the minimized quantity in Eq. (240), the minimum  $\chi^2$  does in general not follow a  $\chi^2$  distribution. This means that the expectation value of the minimum is not the number of degrees of freedom (n.d.f.). Also the deviation of the minimum from the n.d.f. is not directly interpretable as an absolute measure for the goodness of the fit. This is because we assume in Eq. (240) that the elements of  $\Lambda_{ij}^{\varepsilon}(m_X, t')$  are all statistically independent. Although this assumption is true for matrix elements from different  $m_X$

<sup>94</sup>For high-precision data, the resonance model usually is not able to reproduce all details of the data. The residual deviations of the model from the data often induce a multi-modal behavior of the minimization. Reference [156] discusses strategies on how to resolve this multi-modality in order to obtain the best physical solution.

or  $t'$  bins, it is in general not true for matrix elements within a given  $(m_X, t')$  cell. They could be correlated due to statistical correlations of the transition amplitudes in the PWA fit. In principle, these correlations are known because in the partial-wave decomposition that is performed in the first analysis stage also the covariance matrix of the transition amplitudes  $\mathcal{T}_i^{r\varepsilon}(m_X, t')$  is estimated (see Eq. (F.4)). However, the propagation of this information to the covariance matrix of the elements of  $\Lambda_{ij}^\varepsilon$  is not well defined. This is because the spin-density matrix has more free real-valued parameters than the set of transition amplitudes. In an  $(m_X, t')$  cell, the resonance-model fit minimizes the distance of the model to  $([N_{\text{waves}}^{\varepsilon=+1}]^2 + [N_{\text{waves}}^{\varepsilon=-1}]^2)$  data points, which are the elements of  $\Lambda_{ij}^\varepsilon$ . In contrast, the set of transition amplitudes from the partial-wave decomposition represents only  $(N_r^{\varepsilon=+1} [2N_{\text{waves}}^{\varepsilon=+1} - N_r^{\varepsilon=+1}] + N_r^{\varepsilon=-1} [2N_{\text{waves}}^{\varepsilon=-1} - N_r^{\varepsilon=-1}])$  data points (see Section 5.2.2).<sup>95</sup> For a rank-1 spin density matrix, this actually leads to analytical relations among the spin-density matrix elements of waves  $i, j, k$ , and  $l$  of the form

$$\varrho_{ij} \varrho_{kl} = \varrho_{il} \varrho_{kj} , \quad (241)$$

which are also not taken into account by Eq. (240).<sup>96</sup>

The covariance matrix of the fit parameters of the resonance model is estimated from the inverse of the Hessian matrix at the minimum  $\chi^2$ . Due to the not-accounted-for correlations of the elements of the spin-density matrices, this may not be a good approximation. The uncertainty estimates for the fit parameters of the resonance model can be verified, for example, by employing resampling techniques, such as the jackknife [168, 169] or the bootstrap [170–172]. Using these techniques, one generates a set of  $\Lambda_{ij}^\varepsilon$  that is distributed according to the covariance matrix of the transition amplitudes. For each  $\Lambda_{ij}^\varepsilon$  in this set, a resonance-model fit is performed using Eq. (240). This yields a set of fit results, from which the probability distribution of the fit parameters and hence their covariance matrix can then be estimated.

### 5.3.4. Discussion of the Resonance Model

The resonance model that was described in Section 5.3.1 has a number of potential caveats and limitations [52]. In general, the employed Breit-Wigner amplitudes are good approximations only for isolated resonances far above the kinematical thresholds of their decay modes. In addition, using a sum of Breit-Wigner amplitudes to describe the total amplitude of a set of resonances with the same quantum numbers is a good approximation only if the resonances are well-separated so that they have little overlap. Otherwise unitarity, i.e. the conservation of probability, may be violated. For resonances with multiple decay modes, Breit-Wigner parameterizations do also neglect coupled-channel effects caused by unitarity constraints. These effects may become large when the kinematical thresholds of one or more of these decays are in the mass range of the resonance. In practice, the limitations discussed above render Breit-Wigner parameters model- and process-dependent.

Another potential weakness of our model is the decomposition of the partial-wave amplitudes into a sum of resonant and non-resonant components, which is not unique [52] and hence introduces additional process and model dependence of the resonance parameters. In principle, this decomposition would be constrained by unitarity, which is, however, not taken into account here. Due to the absence of realistic models, the parameterizations employed for the non-resonant wave components (see Eqs. (228) and (229)) are only phenomenological. Also, the model assumption that the phase of the non-resonant amplitudes is independent of  $m_X$  may not be well justified especially for cases

---

<sup>95</sup>Only in the case of maximum rank, i.e. for  $N_r^\varepsilon = N_{\text{waves}}^\varepsilon$ , the set of transition amplitudes has the same number of real-valued parameters as  $\Lambda_{ij}^\varepsilon$ .

<sup>96</sup>For the case of a rank-1 spin-density matrix, Appendix C in Ref. [156] provides formulations of the  $\chi^2$  function that correctly take into account all correlations. However, in practice these  $\chi^2$  functions may yield unphysical results due to tensions of the model with the data. The  $\chi^2$  function in Eq. (240) turns out to be more robust against such effects.

where these amplitudes exhibit pronounced peaks in their intensity distribution. Although the parameters of the non-resonant components are in principle nuisance parameters, the choice of their parameterizations turns out to be one of the dominant sources of systematic uncertainty.

A striking advantage of the resonance model employed here is its simplicity, both from a conceptual and computational point of view. The results can also be compared directly to previous analyses of diffractive meson production that employed similar models. Some of the potential issues mentioned above are expected to be mitigated by our approach of simultaneously fitting multiple  $t'$  bins while forcing the resonance parameters to be the same across all  $t'$  bins. This puts strong constraints on the resonant and non-resonant wave components. Additional constraints that help to reduce systematic effects come from including as many decay chains of a resonance as possible into the resonance-model fit and requiring the same resonance parameters in these decay chains. Fitting a large spin-density submatrix with many waves with well-defined resonance signals has a similar effect because the resonance-model fit takes into account the whole spin-density submatrix with all its interference terms. The number of these interference terms grows with the number of selected waves squared. Thus the statistic in Eq. (240) that is employed to estimate the fit parameters effectively gives more weight to the interference terms than to the intensities. In practice, this often helps to stabilize the fit as the model reproduces the phase motions usually more accurately than the intensities.

In order to overcome the caveats and limitations discussed above, improved models that respect the fundamental physical principles and symmetries need to be applied in order to extract process-independent resonance properties, i.e. the resonance poles. This will be described in more detail in Section 5.3.5 below. However, there is an additional aspect that complicates the identification of resonances. An observed intensity peak with an associated phase motion of about  $180^\circ$  does not uniquely define a resonance pole. Under special circumstances, scattering amplitudes may have singularities that exhibit the same experimental signature without being related to resonances. A possible example is the  $a_1(1420)$  signal, which could be the logarithmic singularity of a triangle diagram in a rescattering process of the daughter particles [173, 174]. This will be discussed further in Section 6.3.2.

### 5.3.5. Analytical Unitary Model

In principle, strong-interaction scattering and decay processes are described by the relativistic  $S$ -matrix, which we discussed in Section 3.1.1. As described there, the  $S$ -matrix is constrained by unitarity, crossing symmetry, and analyticity. As shown in Section 3.1.5, the partial-wave amplitudes must be analytic functions in the complex plane of the Mandelstam variable  $s$  up to (i) branch cuts that are caused by the opening of scattering channels with increasing  $s$  and (ii) poles that are caused either by bound states or by resonances. The location of a resonance pole in the complex  $s$ -plane and its residue represent the actual universal resonance properties, which one wants to extract from data. However, the construction of amplitudes that describe multi-body decays of hadrons and that fulfill all  $S$ -matrix constraints is a formidable task and has so far only been achieved in a few cases (see e.g. Refs. [83, 135]). In the past, two-body  $K$ -matrix approaches that respect at least analyticity and two-body unitarity (cf. Section 3.1.7) were applied in some analyses (see e.g. Refs. [164, 175]).

A general framework for a systematic analysis of diffractive meson production at COMPASS using reaction models based on the principles of the relativistic  $S$ -matrix is currently under development in collaboration with the Joint Physics Analysis Center (JPAC) [176–179]. The goal is to extend the Breit-Wigner based fit models discussed in Section 5.3 to analytic models constrained by unitarity, which allows the extraction of resonance pole positions. In this section, we will briefly sketch the model which was successfully applied to the  $\eta\pi$  and  $\eta'\pi$  COMPASS data. The fit results and the extracted pole positions for the  $\pi_1(1600)$ ,  $a_2(1320)$ , and  $a_2(1700)$  [70, 71] will be summarized in Sections 6.3.3 and 6.3.4.

As discussed in Section 4.1, the diffractive production of the  $\eta^{(\prime)}\pi$  final state proceeds dominantly via Pomeron ( $\mathbb{P}$ ) exchange (see Fig. 36a). In Section 3.2, we have shown that the concept of Pomeron exchange emerges from Regge theory and that it allows us to factorize the  $p\text{-}\mathbb{P}$  vertex from the  $\pi\text{-}\mathbb{P}$  vertex. In the model, we then only consider the process  $\pi + \mathbb{P} \rightarrow \eta^{(\prime)}\pi$ , which we describe (cf.

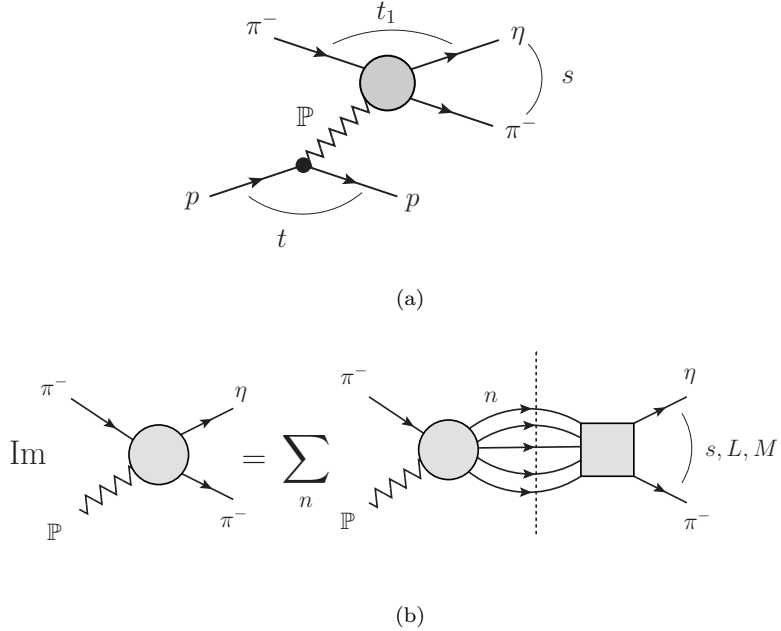


Figure 36: (a) Diffractive-dissociation reaction  $\pi^- + p \rightarrow \eta^{(\prime)}\pi + p$  with  $t$ -channel Pomeron ( $\mathbb{P}$ ) exchange. (b) The  $\pi^- + \mathbb{P} \rightarrow \eta^{(\prime)}\pi$  amplitudes are expanded in partial-wave amplitudes  $a_{i,J}(s)$  in the  $s$ -channel of the  $\eta^{(\prime)}\pi$  system with  $J = L$  and  $i = \{\eta\pi, \eta'\pi\}$ . Unitarity relates the imaginary part of the production partial-wave amplitude  $a_{i,J}(s)$  (grey disc) to final-state interactions that include all kinematically allowed intermediate states  $n$ , described by the scattering partial-wave amplitudes  $t_{ij,J}(s)$  (grey box). From Ref. [70], cf. also Eq. (120).

Section 3.1.10) by  $2 \rightarrow 2$  partial-wave production amplitudes  $a_{i,J}(s)$ , with  $i = \{\eta\pi, \eta'\pi\}$ ,  $J$  the angular momentum of the  $\eta^{(\prime)}\pi$  system, and  $s$  the  $\eta^{(\prime)}\pi$  mass squared. Note that this notation of invariants differs from the one introduced in Section 5.1. In principle, the amplitudes  $a_{i,J}$  also depend on the Pomeron helicity and virtuality  $t$ . Due to the steeply falling  $t'$  spectrum in the analyzed range from 0.1 to 1.0  $(\text{GeV}/c)^2$ , we use an effective value  $t'_{\text{eff}} = 0.1$   $(\text{GeV}/c)^2$ . The Pomeron is modelled as an effective exchange particle with spin 1, in accordance with the dominance of  $M = 1$  partial waves in the data and the approximate constancy of hadron cross sections at high energies (cf. Fig. 5 and Section 3.2).

According to Eq. (118), unitarity relates the production partial-wave amplitudes  $a_{i,J}(s)$  to the scattering partial-wave amplitudes  $t_{ij,J}(s)$  that describe the rescattering of the final-state particles, as displayed graphically in Fig. 36b. Unitarity also constrains the scattering partial-wave amplitudes, as given by Eq. (78), so we have

$$\text{Im } a_{i,J}(s) = \sum_k \rho_k t_{ik,J}^*(s) a_{k,J}(s) \quad \text{and} \quad \text{Im } t_{ij,J}(s) = \sum_k \rho_k t_{ik,J}^*(s) t_{kj,J}(s) . \quad (242)$$

It is known that the barrier factors (cf. Eq. (93)) produce kinematic singularities of the amplitudes [47, 151, 180]. We therefore define the reduced partial-wave amplitudes  $\hat{a}_J$  and  $\hat{t}_J$  by explicitly factoring out the barrier factors:

$$a_{i,J} =: p^{J-1} q_i^J \hat{a}_{i,J} \quad \text{and} \quad t_{ij,J} =: q_i^J q_j^J \hat{t}_{ij,J} , \quad (243)$$

with  $p$  being the momentum of the beam  $\pi$  in the  $\pi\mathbb{P}$  center-of-momentum frame and  $q_i$  the breakup momentum of the  $\eta\pi$  or  $\eta'\pi$  system. In  $a_{i,J}$ , the barrier factor is one unit less for the incoming momentum  $p$  because of the effective vector-nature of the Pomeron. The reduced amplitudes are

parameterized using the  $N$ -over- $D$  method described in Section 3.1.9, Eq. (114):

$$\hat{t}_{ij,J}(s) = \sum_k N_{ik,J}(s) D_{kj,J}^{-1}(s) \quad \text{and} \quad \hat{a}_{i,J}(s) = \sum_k n_{k,J}(s) D_{ki,J}^{-1}(s) . \quad (244)$$

The matrix  $D_J(s)$  has only the right-hand cuts due to unitarity and is assumed to be universal, while  $N_J(s)$  and  $n_J(s)$  have only left-hand cuts, which depend on the exchange processes. They are assumed to be smooth functions of  $s$ . As was shown in Section 3.1.9, unitarity leads to a relation between  $D_J$  and  $N_J$ , i.e.  $\text{Im } D_J(s) = -\rho(s) N_J(s)$ , which can be solved by the once-subtracted dispersion integral Eq. (116):

$$D_{ij,J}(s) = D_{0,ij,J}(s) - \frac{s}{\pi} \int_{s_i}^{\infty} ds' \frac{\rho_{ij}(s') N_{ij,J}(s')}{s'(s'-s)} , \quad (245)$$

with  $s_i$  being the threshold for channel  $i$ . The subtraction constant is parameterized as an inverse  $K$ -matrix ( $K_{ij,J}^{-1}(s)$ ). The numerator functions  $\rho(s) N_J(s)$  and  $n_J(s)$  are parameterized by smooth polynomials with poles to represent the left-hand cuts (see Refs. [70, 71] for details).

Figures 61c to 61f in Section 6.3.3 show the result of a coupled-channel fit employing the unitary model described above to the COMPASS  $\eta\pi$  and  $\eta'\pi$  data. For the  $D$  wave, two poles in the  $K$ -matrix for  $D_{0,ij,J}(s)$  are needed to describe the data. These poles correspond to the  $a_2(1320)$  and the  $a_2(1700)$ . In the  $P$  wave, in contrast, it turns out that both the structure around  $1.4 \text{ GeV}/c^2$  in the  $\eta\pi$  final state and the one around  $1.6 \text{ GeV}/c^2$  in the  $\eta'\pi$  final state can be described by a single pole slightly below  $1.6 \text{ GeV}/c^2$ . The analysis thus confirms the  $\pi_1(1600)$ , while it puts strong doubts on the existence of the  $\pi_1(1400)$ . For a comparison of the result from the pole search with the ones from the Breit-Wigner analyses, see the ideograms in Figs. 62, 66, and 68 in Section 6.3.

## 6. Results from Pion-Diffractive Data

Since the strong interaction conserves isospin and  $G$  parity, intermediate states  $X$  that are produced in diffractive dissociation of pions are restricted to  $I^G = 1^-$  quantum numbers, i.e. only resonances of the  $a_J$  and  $\pi_J$  families with spin  $J$  can be produced. Table I.5 in Appendix I lists the known  $a_J$  and  $\pi_J$  states and their parameters in the mass region below  $2.2 \text{ GeV}/c^2$  according to the PDG [5].

In this section, we will present results of those COMPASS analyses that have been published so far. We will briefly characterize the analyzed data samples in Section 6.1 and describe the models employed for the partial-wave decomposition and the resonance-model fits in Section 6.2. In Section 6.3, we will discuss the results from the analyses organized by the  $J^{PC}$  quantum numbers of the intermediate state  $X$ .

### 6.1. COMPASS Data Samples

The COMPASS collaboration has so far published results from the analysis of four data samples taken with a  $190 \text{ GeV}/c \pi^-$  beam in the kinematic range  $0.1 < t' < 1.0 (\text{GeV}/c)^2$ :  $\eta\pi^-$  and  $\eta'\pi^-$  diffractively produced on a proton target [101] and  $\pi^-\pi^-\pi^+$  diffractively produced on a solid-lead [181] and a proton target [102, 156, 182].

#### 6.1.1. The $\eta\pi^-$ and $\eta'\pi^-$ Data Samples

For the  $\eta\pi^-$  data sample, the  $\eta$  is reconstructed via its decay  $\eta \rightarrow \pi^-\pi^+\pi^0$  with  $\pi^0 \rightarrow \gamma\gamma$ . The  $\eta'$  in the  $\eta'\pi^-$  data sample is reconstructed via its decay  $\eta' \rightarrow \pi^-\pi^+\eta$  with  $\eta \rightarrow \gamma\gamma$ . Therefore, exclusive  $\eta\pi^-$  and  $\eta'\pi^-$  events are both selected from the same final state  $\pi^-\pi^-\pi^+\gamma\gamma$  (see Ref. [101] and Section 4.2.8). A kinematic fit is applied to the  $\gamma\gamma$  system constraining its mass to the nominal mass of  $\pi^0$  and  $\eta$ , respectively. This yields sharp  $\eta$  and  $\eta'$  peaks with widths of 3 to 4  $\text{MeV}/c^2$  in the invariant mass distributions of the  $\pi^-\pi^+\gamma\gamma$  system. Applying cuts of  $\pm 10 \text{ MeV}/c^2$  around the nominal  $\eta$  and  $\eta'$  mass values, we obtain 116 000  $\eta\pi^-$  and 39 000  $\eta'\pi^-$  events in the analyzed range  $0.1 < t' < 1.0 (\text{GeV}/c)^2$ . The  $\eta\pi^-$  and  $\eta'\pi^-$  invariant mass spectra for these events are shown in Fig. 37. The  $m_{\eta\pi}$  spectrum is dominated by a narrow peak at  $1.3 \text{ GeV}/c^2$ , which is the  $a_2(1320)$  (see Section 6.3.4). This peak appears much weaker in the  $m_{\eta'\pi}$  spectrum, which instead is dominated by a broad peak at  $1.7 \text{ GeV}/c^2$  that is related to the  $\pi_1(1600)$  (see Section 6.3.3).

The overall  $t'$  distributions are well described by a simple exponential model of the form (cf. Eqs. (132) and (235))

$$\frac{dN}{dt'} \propto t' e^{-b t'}, \quad (246)$$

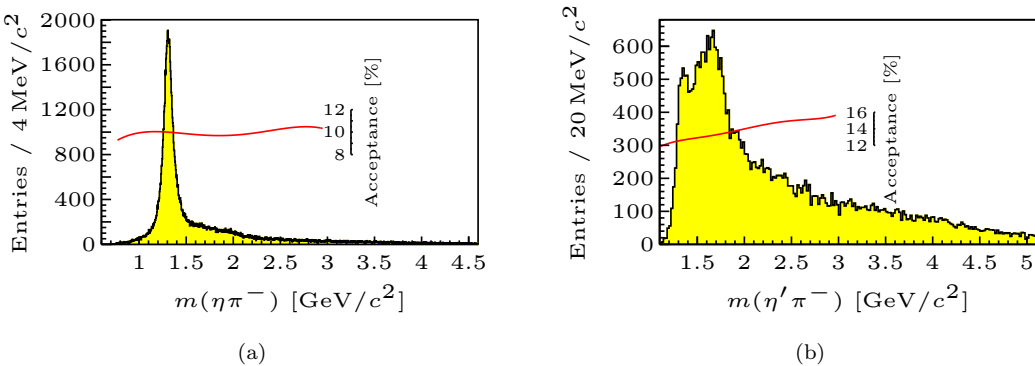


Figure 37: Invariant mass spectra (not acceptance corrected) of diffractively produced (a)  $\eta\pi^-$  and (b)  $\eta'\pi^-$  [101]. The continuous red curves show the acceptances in the analyzed kinematic ranges.

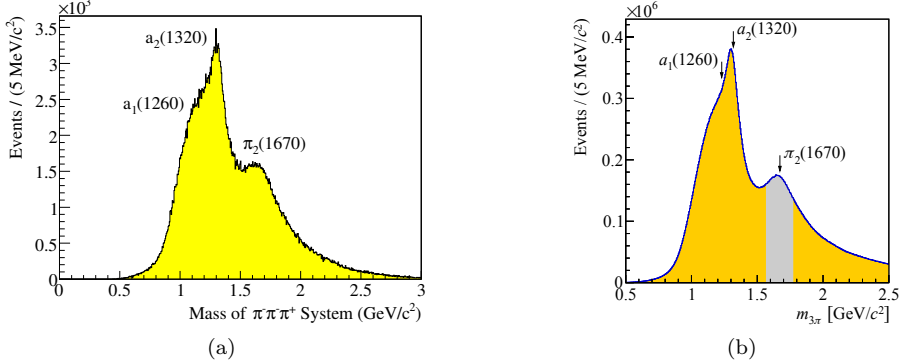


Figure 38: Invariant mass spectra (not acceptance corrected) of diffractively produced  $\pi^- \pi^- \pi^+$  using (a) a solid-lead target [181] and (b) a liquid-hydrogen target [102]. The shaded region in (b) indicates the  $m_{3\pi}$  range used for the Dalitz plot in Fig. 42b.

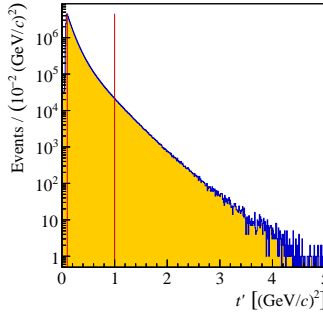


Figure 39: Distribution of the squared four-momentum transfer  $t'$  (not acceptance corrected) of diffractively produced  $\pi^- \pi^- \pi^+$  using a liquid-hydrogen target [102]. The vertical lines indicate the  $t'$  range used in the PWA.

with slope parameters of  $b = 8.45 \text{ (GeV}/c)^{-2}$  for the  $\eta\pi^-$  final state and of  $b = 8.0 \text{ (GeV}/c)^{-2}$  for the  $\eta' \pi^-$  final state. In both cases, we observe only a weak mass dependence of  $b$ .

### 6.1.2. The $\pi^- \pi^- \pi^+$ Data Samples

The  $\pi^- \pi^- \pi^+$  data samples are substantially larger than the  $\eta^{(\prime)}\pi^-$  data samples. After event selection (see Refs. [102, 181] and Section 4.2.8), we obtain 420 000 exclusive events for the solid-lead target and  $46 \cdot 10^6$  exclusive events for the liquid-hydrogen target in the analyzed three-pion mass range  $0.5 < m_{3\pi} < 2.5 \text{ GeV}/c^2$ . For the lead-target data, the target recoil was not measured so that the contribution of non-exclusive backgrounds is larger in this sample. In the analyzed range  $0.1 < t' < 1.0 \text{ (GeV}/c)^2$ , the scattering off the lead nucleus is predominantly of incoherent nature, i.e. the beam pions scatter off individual nucleons within the lead nucleus. Thus the lead-target data are expected to be similar to the proton-target data. Figure 38 shows the  $m_{3\pi}$  distributions for the two data samples. They exhibit pronounced structures that correspond to the well known resonances  $a_1(1260)$ ,  $a_2(1320)$ , and  $\pi_2(1670)$  (see Sections 6.3.2, 6.3.4, and 6.3.5). As shown in Fig. 39, the  $t'$  distribution follows an approximately exponential behavior in the analyzed  $t'$  range.

## 6.2. Analysis Models

All three final states considered here (see Section 6.1) were already studied by previous experiments using similar scattering reactions with lower pion-beam energies. Since some of the COMPASS data

samples, in particular the  $\pi^-\pi^-\pi^+$  proton-target sample, are significantly larger than those obtained by previous experiments, we extend and refine the analysis models used in previous analyses.

### 6.2.1. $\eta^{(\prime)}\pi^-$ Partial-Wave Decomposition

Exclusive diffractive production of  $\eta\pi$  and  $\eta'\pi$  final states was studied by the VES experiment using a  $37\text{ GeV}/c\pi^-$  beam scattering off a solid-beryllium target [183, 184] and by the BNL E852 experiment using an  $18\text{ GeV}/c\pi^-$  beam on a liquid-hydrogen target [185, 186]. At COMPASS, the higher beam energy enables us to access higher invariant masses of the produced final states and higher values of the orbital angular momentum between the two final-state particles.

For final states consisting of two pseudoscalars, the total spin  $J$  of the intermediate state  $X$  is identical to the relative orbital angular momentum  $L$  between the two daughter particles. The parity  $P$  of the state is given by  $(-1)^L$ . Therefore, only states with positive naturality (see Section 2.1.1) are accessible. In diffractive reactions, the isospin  $I$  and the  $C$  parity of  $X$  are given by the isospin and  $C$  parity of the beam particle, i.e.  $I = 1$  and  $C = +1$  for a pion beam. This means that partial waves with odd  $L$  correspond to spin-exotic quantum numbers. In the reflectivity basis (see Section 5.2.3), the combination  $M^\varepsilon = 0^+$  of the spin-projection quantum number  $M$  and the reflectivity  $\varepsilon$  is forbidden for natural-parity states. Thus  $J^{PC} = 0^{++}$  waves, which may contain  $a_0$  resonances, may only appear with  $M^\varepsilon = 0^-$  quantum numbers that correspond to unnatural-parity exchange. At high beam energies, Pomeron exchange dominates and unnatural-parity exchange processes are suppressed. Therefore,  $M^\varepsilon = 1^+$  waves are expected to dominate and  $\varepsilon = -1$  waves should be suppressed. Often, the spectroscopic notation  $LM_\varepsilon$  is used to designate two-pseudoscalar partial waves. E.g., partial waves with  $J^{PC} M^\varepsilon = 0^{++}0^-, 1^{-+}0^-, 1^{-+}1^-, 1^{-+}1^+$ , and  $2^{++}2^+$  quantum numbers correspond to  $S0_-$ ,  $P0_-$ ,  $P1_-$ ,  $P1_+$ , and  $D2_+$ , respectively.

The rough partial-wave structure of the data is already visible in the angular distributions in the Gottfried-Jackson frame, where we use the direction of the  $\eta^{(\prime)}$  as the analyzer (see Section 5.1.4). As already observed by previous experiments [183–186], the  $\phi_{\text{GJ}}$  distributions of both final states follow an approximate  $\sin^2\phi_{\text{GJ}}$  pattern [187, 188] over the full analyzed mass range. This corresponds to the dominance of  $M^\varepsilon = 1^+$  waves (see also discussion below), which is consistent with the fact that the overall  $t'$  spectrum is described by Eq. (246), which includes an explicit  $t'$  factor (cf. also Eqs. (132) and (235)).

The dominant spin content of the data is visible in Fig. 40, which shows the correlation of  $\cos\vartheta_{\text{GJ}}$  of the  $\eta^{(\prime)}$  with the  $\eta^{(\prime)}\pi^-$  invariant mass. In the  $1.3\text{ GeV}/c^2$  mass region of the  $\eta\pi^-$  data, the  $\cos\vartheta_{\text{GJ}}$  distribution exhibits a two-bump structure that is characteristic for a  $D$  wave. This is consistent with the dominant  $a_2(1320)$  signal (see also Fig. 37a). In contrast, the modulation of the angular distribution is weaker in the  $\eta'\pi^-$  data as is the  $a_2(1320)$  signal. In the  $2\text{ GeV}/c^2$  mass region of the  $\eta\pi^-$  data, the  $\cos\vartheta_{\text{GJ}}$  distribution exhibits four bumps, which indicates the presence of a  $G$  wave. This structure is disentangled by the PWA and explained as the  $a_4(2040)$  (see Section 6.3.6). Again, this structure is much weaker in the  $\eta'\pi^-$  data. For masses above  $2\text{ GeV}/c^2$  the character of the  $\cos\vartheta_{\text{GJ}}$  distributions changes drastically. For both final states, the distributions show narrow peaks at  $\cos\vartheta_{\text{GJ}} = \pm 1$ , which correspond to  $\eta^{(\prime)}$  going along the beam direction in the Gottfried-Jackson frame, i.e. forward, or against it, i.e. backward. The peaks become sharper with increasing mass. This behavior corresponds to a rapidity gap that widens with increasing mass and indicates the presence of large contributions from non-resonant processes. Clearly, high-spin partial waves are needed to describe such  $\cos\vartheta_{\text{GJ}}$  distributions. The non-resonant processes are dominated by double-Regge exchanges (see Sections 4.1 and 5.2.8 and Figs. 21c and 21d). Figure 41 shows possible double-Regge exchange diagrams for the  $\eta^{(\prime)}\pi^-$  final state. These processes are similar to the well-known non-resonant Deck process in diffractive  $3\pi$  production [93, 189] and to central production of  $\eta^{(\prime)}$  in  $pp$  collisions as, for example, observed by the WA102 experiment [190]. These irreducible background processes typically have one leading final-state particle. For a two-body final state, this means that the other final-state particle is relatively slow, leading to forward-backward peaks in the  $\cos\vartheta_{\text{GJ}}$  distribution that become sharper with increasing mass of the two-body system.

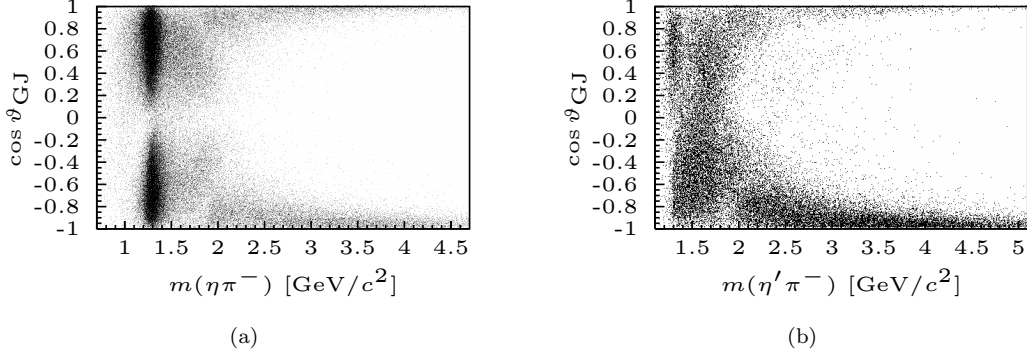


Figure 40: Distribution of the cosine of the polar angle of the  $\eta^{(\prime)}$  in the Gottfried-Jackson frame (not acceptance corrected; see Section 5.1.4) as a function of the invariant mass of (a) the  $\eta\pi^-$  and (b) the  $\eta'\pi^-$  system [101]. Here,  $\cos \vartheta_{\text{GJ}} = 1$  corresponds to  $\eta^{(\prime)}$  emission along the beam direction.

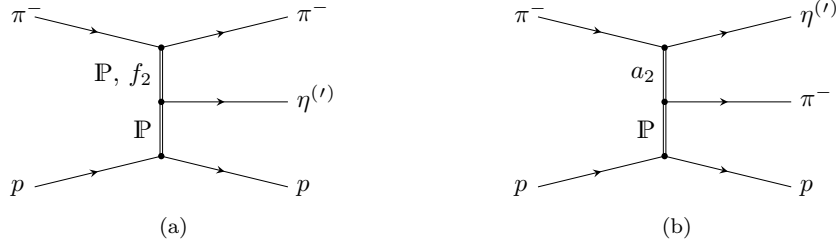


Figure 41: Possible diagrams for non-resonant production of  $\eta^{(\prime)}\pi^-$ . In (a), a backward  $\eta^{(\prime)}$  (opposite to the beam direction in the  $\eta^{(\prime)}\pi$  center-of-momentum frame) is produced by Pomeron or  $f_2$  exchange; in (b), a forward  $\eta^{(\prime)}$  (along the beam direction) is produced by  $a_2$  exchange.

In the high-mass region, the  $\cos \vartheta_{\text{GJ}}$  distributions of both systems show a significant forward-backward asymmetry, i.e. we observe an excess of  $\eta^{(\prime)}$  in the backward direction. This asymmetry is not caused by detector effects. In the  $\eta'\pi^-$  data, the backward excess is more pronounced over the whole mass range. Since even- $L$  waves have only symmetric  $\cos \vartheta_{\text{GJ}}$  distributions, the forward-backward asymmetry indicates the presence of spin-exotic odd- $L$  waves, predominantly those with lowest possible  $L$ , i.e.  $P$  waves. In case of  $\eta'\pi^-$ , contributions of odd- $L$  partial waves that are comparable in strength to those of the even- $L$  partial waves are needed in order to describe the backward enhancement. In the  $\eta\pi^-$  data, the  $\cos \vartheta_{\text{GJ}}$  asymmetry flips from a backward  $\eta$  excess at high masses to a forward excess in the  $a_2(1320)$  mass region. In the  $\eta'\pi^-$  data, this effect is partly masked by the broad enhancement around  $1.6 \text{ GeV}/c^2$  that is caused by the  $P$  wave, which is much stronger in the  $\eta'\pi^-$  channel as compared to  $\eta\pi^-$ .

The PWA model used for the partial-wave decomposition is based on Eq. (195). The two-body decay amplitudes  $\Psi_{LM}^{\varepsilon}(\vartheta_{\text{GJ}}, \phi_{\text{GJ}})$  in the reflectivity basis are given by Eqs. (156), (162), (175), and (188). In order to account for non- $\eta^{(\prime)}$  incoherent backgrounds, we extend the two-body PWA model to a four-body model for the  $\pi^-\pi^-\pi^+(\gamma\gamma)$  system, where the  $(\gamma\gamma)$  subsystem is either a  $\pi^0$  in case of  $\eta\pi^-$  or an  $\eta$  in case of  $\eta'\pi^-$ . Instead of selecting a narrow  $\pi^-\pi^+\gamma\gamma$  mass window around the nominal  $\eta^{(\prime)}$  mass, the analysis is performed requiring at least one  $\pi^-\pi^+\gamma\gamma$  combination inside a wide  $m_{\pi^-\pi^+\gamma\gamma}$  interval of  $\pm 25 \text{ MeV}/c^2$  around the nominal  $\eta^{(\prime)}$  mass. In order to take into account the three-body decay of  $\eta^{(\prime)}$ , we extend the two-body decay amplitudes that are given by the spherical

harmonics by a factor  $f_{\eta^{(\prime)}}$  that describes the measured  $\eta^{(\prime)}$  peak shape and the Dalitz-plot distribution of the three-body  $\eta^{(\prime)}$  decay [191].<sup>97</sup> The  $\eta^{(\prime)}$  peak shape is determined by the detector resolution and is hence assumed to be a Gaussian. The decay amplitudes depend on the four-body phase-space variables  $\tau_4$  and are given by

$$\begin{aligned} \Psi_{LM}^{\varepsilon}(\tau_4; m_{\eta^{(\prime)}\pi}) &= f_{\eta^{(\prime)}}(p_{\pi^-}, p_{\pi^+}, p_{\gamma\gamma}) \underbrace{\left[ Y_L^M(\vartheta_{\text{GJ}}, \phi_{\text{GJ}}) - \varepsilon Y_L^{M*}(\vartheta_{\text{GJ}}, \phi_{\text{GJ}}) \right]}_{\propto P_{LM}(\cos \vartheta_{\text{GJ}}) \times \begin{cases} \sin(M \phi_{\text{GJ}}) & \text{if } \varepsilon = +1, \\ \cos(M \phi_{\text{GJ}}) & \text{if } \varepsilon = -1. \end{cases}}. \end{aligned} \quad (247)$$

Here,  $p_{\pi^{\pm}}$  and  $p_{\gamma\gamma}$  are the four-momenta of the three  $\eta^{(\prime)}$  decay daughters and the  $P_{LM}(\cos \vartheta_{\text{GJ}})$  are the associated Legendre polynomials. From Eq. (247) it is clear, that the above-mentioned observed  $\sin^2 \phi_{\text{GJ}}$  distribution is in agreement with the dominance of  $M^{\varepsilon} = 1^+$  waves.

The decay amplitude  $\Psi_{\text{flat}}(\tau_4)$  of the flat wave (see Section 5.2.1) is isotropic in the  $\pi^- \pi^- \pi^+(\gamma\gamma)$  four-body phase space. It hence absorbs the incoherent non- $\eta^{(\prime)}$  backgrounds. We account for the combinatorial background due to the two possible  $\pi^- \pi^+ \gamma\gamma$  combinations by summing the total intensities that correspond to the two combinations in the PWA model.<sup>98</sup>

Most previous partial-wave analyses used PWA models that contained waves only up to  $L = 2$ , except the one in Ref. [186] where in addition a  $L = 4$  wave was introduced. The PWA model for the COMPASS data contains all positive-reflectivity waves with  $L = 1$  to  $6$  and  $M = 1$ . For the  $\eta\pi$  data, we include in addition a wave with  $L = 2$  and  $M^{\varepsilon} = 2^+$ . We also include the  $L = 0$  wave with  $M^{\varepsilon} = 0^-$  for both channels. Since this is the only negative-reflectivity wave in the model, its amplitude is added incoherently to the intensity. Our four-body PWA approach is able to separate the incoherent non- $\eta^{(\prime)}$  backgrounds, which are absorbed by the flat wave, from the incoherent negative-reflectivity  $\eta^{(\prime)}\pi^-$  contributions. The PWA fits require only a weak  $S$ -wave amplitude with  $\varepsilon = -1$ . This wave contributes 0.5% to the total  $\eta\pi^-$  intensity and 1.1% to the total  $\eta'\pi^-$  intensity and contains mainly incoherent  $\eta^{(\prime)}\pi^-$  background.

One of the crucial assumptions of our PWA model is that it uses a rank-1 spin-density matrix, i.e. we assume full coherence of the partial-wave amplitudes. As was discussed in Section 5.2.2, incoherence of partial waves may arise from contributions with and without proton helicity flip, or from different  $t'$  dependences of the amplitudes over the broad analyzed  $t'$  range. It is known that the spin-density matrix elements may have significantly different  $t'$  dependences as is, for example, the case for the  $\pi^- \pi^- \pi^+$  proton-target data. The  $\eta^{(\prime)}\pi^-$  data are dominated by  $M = 1$  amplitudes with similar  $t'$  dependences [187]. Since waves with  $M = 0$  and  $2$  are strongly suppressed, integration over  $t'$  does not introduce large incoherences.

The PWA of two-pseudoscalar final states may suffer from discrete mathematical ambiguities [192–194], which can be expressed in terms of so-called Barrelet-zeros [195]. For our  $\eta^{(\prime)}\pi^-$  data, the ambiguities are drastically reduced, because we do not observe any significant  $\varepsilon = -1$  contributions except for the  $S$  wave. In the case of  $\eta\pi^-$ , no ambiguities appear because the PWA model contains the  $D$  wave with  $M^{\varepsilon} = 2^+$ . For  $\eta'\pi^-$ , ambiguities occur when we extend the PWA model beyond the dominant  $L = 1, 2$ , and  $4$  waves. We resolve them by requiring continuous behavior of the dominant partial-wave amplitudes and of the Barrelet zeros as a function of  $m_{\eta'\pi^-}$ . From the acceptable solutions, which all agree within statistical uncertainties, we select the one with the smallest  $L = 3$  contribution.

<sup>97</sup>The angular-momentum barrier factor  $F_J(m_{\eta^{(\prime)}\pi})$  in Eq. (156) depends in principle also on the reconstructed  $\eta^{(\prime)}$  mass via the breakup momentum that appears in Eq. (97). However, since the width of the  $\eta^{(\prime)}$  mass peak is given by the detector resolution, the barrier factor is set to a constant for a given  $m_{\eta^{(\prime)}\pi}$  bin and is hence absorbed by the normalization in Eq. (188).

<sup>98</sup>This approach differs from the Bose symmetrization discussed in Section 5.1.6 in that we do not allow for self-interference. We add the intensities because  $\eta$  and  $\eta'$  have very small widths so that the two  $\pi^- \pi^+ \gamma\gamma$  combinations are in principle distinguishable.

We performed the partial-wave decomposition using the model described above in  $40 \text{ MeV}/c^2$  wide bins of the  $\eta^{(\prime)}\pi^-$  mass from threshold up to  $3 \text{ GeV}/c^2$ . The spin-exotic waves with higher orbital angular momenta of  $L = 3$  and  $5$  have small but statistically significant intensities in both final states. This is also true for the  $L = 6$  wave, which has conventional  $J^{PC}$  quantum numbers. These three waves were never included in previous analyses. Each of them contributes less than 1% to the total  $\eta\pi^-$  and  $\eta'\pi^-$  intensities.

The results from our PWA of the  $\eta^{(\prime)}\pi^-$  data show that the relative phases of all partial waves change only little with mass for  $m_{\eta^{(\prime)}\pi} \gtrsim 2.2 \text{ GeV}/c^2$ . In addition, the relative phases between the waves with spin projection  $M = 1$  are compatible with  $0^\circ$  in both final states. This is consistent with the results of the partial-wave decomposition of model amplitudes for double-Regge exchange processes, where the relative phases between the partial waves are found to depend only weakly on the mass of the produced hadronic final state and are often close to  $0^\circ$ .<sup>99</sup>

In order to compare the strengths of the partial waves in the  $\eta\pi^-$  and  $\eta'\pi^-$  final states, we scale the intensities of the  $\eta\pi^-$  waves in each  $m_{\eta\pi}$  bin by the relative kinematic factor

$$c(m_{\eta\pi}; L) = B \cdot \left[ \frac{q(m_{\eta\pi}; m_{\eta'}, m_\pi)}{q(m_{\eta\pi}; m_\eta, m_\pi)} \right]^{2L+1}. \quad (248)$$

Here,  $q$  is the two-body breakup momentum as given by Eqs. (62) and (63) and  $m_{\eta^{(\prime)}}$  and  $m_\pi$  are the nominal masses of  $\eta^{(\prime)}$  and  $\pi^-$ , respectively. The kinematic factor takes into account the different phase-space and angular-momentum barrier factors of the two final states and the branching-fraction ratio of  $B = 0.746$  for  $\eta$  and  $\eta'$  decaying into  $\pi^-\pi^+\gamma\gamma$  [191]. In Eq. (248), we have used the fact that the transition rate for the two-body decay of a point-like particle is expected to be proportional to  $q^{2L+1}$  [196–198].<sup>100</sup>

A feature of our data, which will be discussed further in Sections 6.3.3, 6.3.4, and 6.3.6, is that the intensity distributions of the even- $L$   $\eta\pi^-$  waves with  $L = 2$  and  $4$  that are scaled by Eq. (248) are in astonishing agreement with the corresponding intensity distributions of the  $\eta'\pi^-$  waves (see Sections 6.3.4 and 6.3.6). This means that the apparent differences of the unscaled intensity distributions are of purely kinematical origin. In contrast, a strong enhancement of the  $\eta'\pi^-$  over the scaled  $\eta\pi^-$  partial-wave intensities is observed for the spin-exotic odd- $L$  partial waves, in particular for the  $L = 1$  wave (see Section 6.3.3). Since the amplitudes of the high-spin waves with  $L = 3, 5$ , and  $6$  have large statistical uncertainties, they are not shown here. However, they follow the same trend as the lower-spin even- $L$  and odd- $L$  waves.

### 6.2.2. $\eta^{(\prime)}\pi^-$ Resonance-Model Fits

The spin-density matrices (see Eq. (194)), which have been extracted from the  $\eta\pi^-$  and  $\eta'\pi^-$  data in the partial-wave decomposition stage described in Section 6.2.1, serve as input for the resonance-model fit. As was discussed in Section 5.1.7, for this fit we select a subset of waves. This set includes the  $D$ - and  $G$ -wave amplitudes with  $M^\varepsilon = 1^+$ . For the  $\eta\pi^-$  final state, we include in addition the  $D$ -wave amplitude with  $M^\varepsilon = 2^+$ . These amplitudes exhibit clear resonance signals, i.e. intensity peaks with associated phase motions, of the well-known  $a_2(1320)$  and  $a_4(2040)$ . We include in addition the spin-exotic  $P$ -wave amplitude with  $M^\varepsilon = 1^+$ . The resonance content of this wave is discussed controversially (see Section 6.3.3).

The  $D$ -wave amplitudes are described by a coherent sum of Breit-Wigner amplitudes for the  $a_2(1320)$  and the  $a_2(1700)$ , the  $G$ -wave amplitudes by an  $a_4(2040)$  Breit-Wigner amplitude, and the

---

<sup>99</sup>For multi-body final states such as  $\pi^-\pi^-\pi^+$ , these relative phases may be  $0^\circ$  or  $180^\circ$  depending on the choice of the analyzer in the calculation of the decay amplitudes (see Section 5.1.4).

<sup>100</sup>This corresponds to the simplest possible expression for the centrifugal-barrier factor (see Eq. (93)) and is consistent with the decay amplitude in Eq. (156) being proportional to the barrier factor  $F_J$ . Hence for  $q \rightarrow 0$ , the decay amplitude is proportional to  $q^L$ .

$P$ -wave amplitudes by a  $\pi_1$  Breit-Wigner amplitude. Except for the  $a_2(1320)$ , we use constant-width relativistic Breit-Wigner amplitudes, i.e. Eq. (151). The parameterization of the  $a_2(1320)$  dynamic total width assumes that the total width is saturated by the two dominant decay modes  $\rho(770)\pi$  and  $\eta\pi$  [181, 183] (see also Eq. (25) in Ref. [156]). In addition, we add for each wave a coherent non-resonant amplitude of the form of Eq. (228) with parameter  $b = 0$ .

We fit the resonance model to the real and imaginary parts of the elements of the spin-density submatrices of the selected waves by minimizing the distance measure defined in Eq. (240). Results from separate fits to the  $\eta\pi^-$  and the  $\eta'\pi^-$  data are consistent with each other and with those from a combined fit of both data sets. Statistical uncertainties of the measured  $a_2(1320)$  and  $a_4(2040)$  resonance parameters (see Sections 6.3.4 and 6.3.6) are much smaller than the systematic uncertainties and are hence neglected. The systematic uncertainties are estimated based on several studies. These studies include changing the fit ranges, changing the parameterization of the background components, and excluding the background component in certain waves. In these studies, we find that the resonance parameters of the  $a_2(1700)$  and of the  $\pi_1$  strongly depend on the resonance model and on the fit range. Hence these parameters cannot be reliably extracted from the data. However, the  $\pi_1$  parameters are compatible with previous measurements. In addition, we find that a combined fit of the  $\eta\pi^-$  and  $\eta'\pi^-$  data with the same  $\pi_1$  resonance parameters in both channels also yields a satisfactory description of the data. This point will be discussed again in Section 6.3.3.

Our inability to reliably extract the parameters of the  $a_2(1700)$  and the  $\pi_1$  shows the limitations of our simple sum-of-Breit-Wigner approach. Applying improved analytic and unitary models, which were developed by the JPAC collaboration and were discussed in Section 5.3.5, to the COMPASS  $\eta^{(\prime)}\pi$  data yields well-defined pole positions for  $a_2(1320)$ ,  $a_2(1700)$ , and  $\pi_1(1600)$  that are less model-dependent. These results demonstrate the superiority of this approach. They will be discussed in more detail in Sections 6.3.3 and 6.3.4.

### 6.2.3. $\pi^-\pi^-\pi^+$ Partial-Wave Decomposition

Compared to the PWA of two-body final states (see e.g. Section 6.2.1), the partial-wave decomposition of three-body final states requires considerably more modeling. As was discussed in Section 5.2.8, the development of an optimal PWA model for multi-body decays is a non-trivial and challenging task. This is in particular true for the COMPASS  $\pi^-\pi^-\pi^+$  data sample taken with a liquid-hydrogen target, which is about an order of magnitude larger than any data sample used in previously published analyses (see e.g. Refs. [164, 175, 181, 199, 200]). Hence the employed PWA model has to be significantly more detailed than the models used in previous analyses in order to achieve a good description of the data.

To construct the wave set, we first have to determine the set of two-pion isobar resonances that appear in the data and we have to choose the parameterizations for their propagator terms (see Section 5.1.3). Since there are no known resonances in the  $\pi^-\pi^-$  channel, which has  $I = 2$  and is thus flavor-exotic, we consider only  $\pi^-\pi^+$  isobar resonances. From the  $\pi^-\pi^+$  mass spectrum in Fig. 42a and from Dalitz plots like the one in Fig. 42b, we can already infer that we have to include  $\rho(770)$ ,  $f_0(980)$ , and  $f_2(1270)$  as isobars. The slight enhancement at about  $m_{\pi^-\pi^+} = 1.7 \text{ GeV}/c^2$  in Fig. 42a could be due to  $\rho_3(1690)$ ,  $\rho(1700)$ , or  $f_0(1710)$ . In our PWA model, we include only the  $\rho_3(1690)$ , which is known from previous experiments (see e.g. Ref. [199]) to appear in the  $\pi^-\pi^+$  subsystem of diffractively produced  $3\pi$  final states. Due to ambiguities of the partial-wave amplitudes that may arise when the PWA model contains radially excited isobar resonances (see Section 5.2.8), we include neither the  $\rho(1700)$  nor the  $f_0(1710)$ . We confirm that the  $f_0(1710)$  does not contribute significantly to the data by performing a co-called freed-isobar PWA (see Section 5.2.9), the results of which are described in more detail below. For the proton-target data, we include one wave with the  $f_0(1500)$  isobar in the range  $m_{3\pi} > 1.7 \text{ GeV}/c^2$ . The PWA model for both  $\pi^-\pi^-\pi^+$  data samples contains in addition the  $f_0(500)$ , which is also known as  $\sigma$ . Ignoring possible contributions from excited  $\rho$  and  $f_2$  states and from isobar states with  $J > 3$ , we arrive at sets of 6 and 5 isobars that we include in the PWA models for the proton- and lead-target data, respectively. The  $\rho(770)$ ,  $f_2(1270)$ ,  $f_0(1500)$ , and  $\rho_3(1690)$  are described using relativistic Breit-Wigner amplitudes (see Section 5.1.3

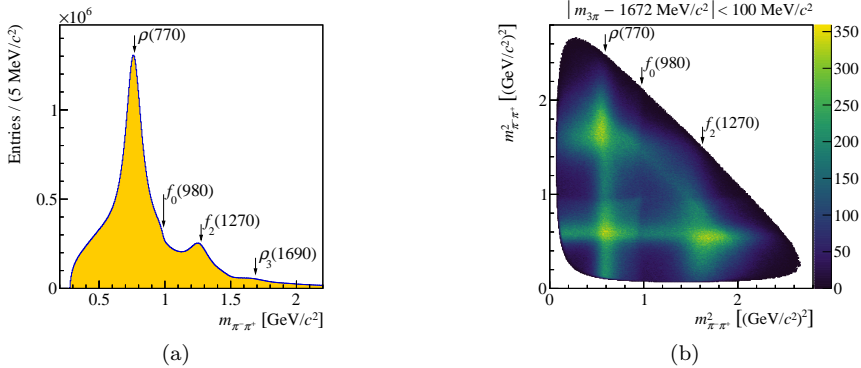


Figure 42: Kinematic distributions for the  $\pi^- \pi^- \pi^+$  proton-target data [102]. (a) Invariant mass distribution of the  $\pi^- \pi^+$  subsystem (two entries per event). The labels indicate the position of  $2\pi$  resonances. (b) Dalitz plot for the  $100 \text{ MeV}/c^2$  wide  $m_{3\pi}$  region around the  $\pi_2(1670)$  as indicated by the shaded region in Fig. 38b. This region exhibits signals for  $\rho(770)\pi$ ,  $f_0(980)\pi$ , and  $f_2(1270)\pi$  decays.

and Section IV.A in Ref. [102] for details). The description of the  $f_0(500)$  and  $f_0(980)$  isobars is more difficult. The distortion of the  $f_0(980)$  line shape due to its closeness to the  $K\bar{K}$  threshold is taken into account by using a Flatté parameterization [66, 201, 202]. The  $f_0(500)$  is extremely broad and is thus not well described by a Breit-Wigner amplitude. We describe this state effectively by a parameterization of the amplitude of the  $S$  wave in  $\pi\pi \rightarrow \pi\pi$  and  $KK$  scattering [203] modified to separate out the  $f_0(980)$  (see Section IV.A in Ref. [102] for details). In the text below, we denote this isobar amplitude by  $[\pi\pi]_S$ .

In our model for the intensity distribution in Eq. (195), the decay amplitudes are given by Eqs. (158) and (159). Since the final-state particles are spinless, the  $3\pi$  partial waves are completely defined by the short-hand notation  $J^{PC} M^\varepsilon r \pi L$ , where  $J^{PC} M^\varepsilon$  are the quantum numbers of the  $X^-$  intermediate state,  $r$  is the isobar resonance with well-defined quantum numbers and propagator term, and  $L$  is the relative orbital angular momentum in the decay  $X^- \rightarrow r + \pi^-$  (cf. Eq. (160)). Based on the set of selected isobar resonances described above, the number of possible partial waves is largely determined by the maximum allowed spin  $J$  of  $X^-$  and the maximum allowed  $L$ . For the proton-target data, we have constructed a set of 128 waves, which—in accordance with Pomeron dominance—includes mainly positive-reflectivity waves with spin  $J \leq 6$ , orbital angular momentum  $L \leq 6$ , and spin projection  $M = 0, 1$ , and 2. From the result of a PWA performed using this wave set, we have derived a smaller wave set by eliminating structureless waves with relative intensities below approximately  $10^{-3}$  in an iterative process [204]. This yields a final set of 88 partial waves, which consists of 80 waves with reflectivity  $\varepsilon = +1$ , seven waves with  $\varepsilon = -1$  and one non-interfering flat wave representing three uncorrelated pions. This is the largest wave set that was used so far in an analysis of diffractively produced  $3\pi$ . In order to avoid ambiguities between partial-wave amplitudes (see Section 5.2.8), we have to exclude 27 waves in the low- $m_{3\pi}$  region. The corresponding  $m_{3\pi}$  thresholds were carefully tuned for each wave and are given in Table IX in Appendix A of Ref. [102]. In order to illustrate the fit result, we show in Fig. 43 the intensities of sums of positive-reflectivity amplitudes that have the same  $J^{PC}$  quantum numbers. Note that the composition of the data in terms of  $J^{PC}$  changes substantially with  $t'$ , in particular for the  $1^{++}$  and  $2^{++}$  waves. For the less precise lead-target data, a smaller PWA model with only 42 waves is used [181], which is a subset of the 88-wave set.

Another important difference between the PWA models for the proton- and the lead-target data is how the  $t'$  dependence is taken into account. Using the 42-wave set, the PWA of the lead-target data was performed independently in 50  $m_{3\pi}$  bins with  $40 \text{ MeV}/c^2$  width integrating over the analyzed  $t'$  range from 0.1 to  $1.0 (\text{GeV}/c)^2$ . In this  $t'$  range, it is assumed that the beam pions scatter off

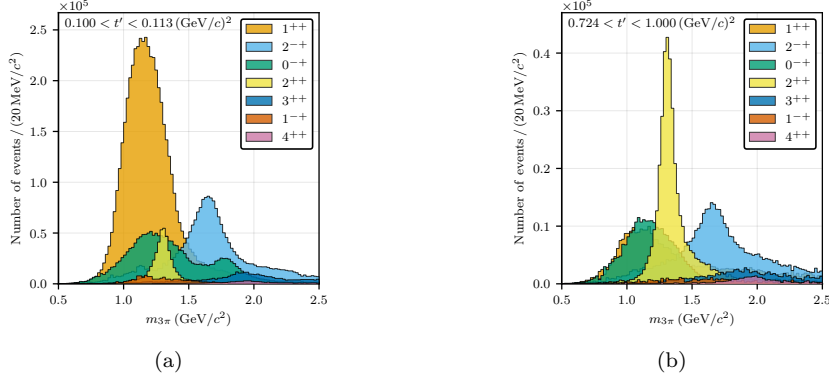


Figure 43: Representation of the fit result from Ref. [102]: intensities of the coherent sums of partial-wave amplitudes with the same  $J^{PC}$  quantum numbers (encoded by different colors) and positive reflectivity as obtained by the 88-wave PWA fit of the  $\pi^- \pi^- \pi^+$  proton-target data (a) for the lowest and (b) for the highest  $t'$  bin.

individual nucleons in the lead nucleus, i.e. that the scattering off the nucleus is incoherent. The results are therefore expected to be similar to the ones obtained from the proton-target data. The  $t'$  dependences of the partial-wave intensities were incorporated into the PWA model in Eq. (195) via the replacement

$$\mathcal{T}_i^{r\varepsilon}(m_X, t') \rightarrow \mathcal{T}_i^{r\varepsilon}(m_X) f_i^\varepsilon(t'), \quad (249)$$

with empirical real-valued functions

$$f_i^\varepsilon(t'; b_i^\varepsilon, A_{i,1}^\varepsilon, A_{i,2}^\varepsilon, A_{i,3}^\varepsilon) = \left[ (t')^{|M|} \left( A_{i,1}^\varepsilon e^{-b_i^\varepsilon t'} + A_{i,2}^\varepsilon e^{-15(\text{GeV}/c)^{-2} t'} + A_{i,3}^\varepsilon e^{-3(\text{GeV}/c)^{-2} t'} \right) \right]^{\frac{1}{2}} \quad (250)$$

that are inspired by Eqs. (132) and (235). For each wave, the values of the four free parameters,  $b_i^\varepsilon$ ,  $A_{i,1}^\varepsilon$ ,  $A_{i,2}^\varepsilon$ , and  $A_{i,3}^\varepsilon$ , were estimated by first performing the PWA in narrow bins of  $t'$  and in three wide  $m_{3\pi}$  ranges and then fitting Eq. (250) to the extracted partial-wave intensities. This approach assumes that the shapes of the  $t'$  spectra of the partial waves are largely independent of  $m_{3\pi}$  and also does not take into account possible  $t'$  dependences of the relative phases between the partial waves. The much larger proton-target data sample allows us to perform the PWA using a two-dimensional binning with 100  $m_{3\pi}$  bins with  $20 \text{ MeV}/c^2$  width and 11 non-equidistant  $t'$  bins, where the  $t'$  bins are chosen to contain approximately equal number of events. For each of the resulting 1100  $(m_{3\pi}, t')$  cells, an independent PWA fit is performed using the 88-wave PWA model (see Section 5.2). Because of the binning in  $t'$ , we do not have to assume any model for the  $t'$  dependences of the partial-wave amplitudes but instead extract this information from the data. This  $t'$ -binned analysis reveals a complicated  $m_{3\pi}$  dependence of the  $t'$  spectra. For many waves, the  $t'$  spectra are not well described by a single exponential and the slope parameters differ significantly between waves and also between different  $m_{3\pi}$  regions in the same wave. Hence the model in Eqs. (249) and (250) that is used in the analysis of the lead-target data may not be sufficient to describe all features of the data.

The different ways how the  $t'$  dependence is taken into account by the PWA models also affect the rank of the spin-density matrix that is required to describe the data. For the  $t'$ -binned analysis of the proton-target data, a rank-1 spin-density submatrix for the 80 waves with  $\varepsilon = +1$  is sufficient to describe the data, i.e.  $N_r^{(\varepsilon=+1)} = 1$  in Eq. (195).<sup>101</sup> In contrast, a rank-2 spin-density matrix is used for the analysis of the lead-target data, i.e.  $N_r^{(\varepsilon=+1)} = N_r^{(\varepsilon=-1)} = 2$ . Most of the additional

<sup>101</sup>This corresponds to full coherence of the partial waves with  $\varepsilon = +1$ . For the seven waves with  $\varepsilon = -1$ , a rank-2 spin-density submatrix is found to describe the data best, i.e.  $N_r^{(\varepsilon=-1)} = 2$  in Eq. (195).

incoherence originates probably from the fact that the PWA is performed integrating over the analyzed  $t'$  range and that the model in Eqs. (249) and (250) does not take into account the  $t'$  dependences of the partial-wave phases as well as contributions from reactions where the beam pion scatters off larger fractions of the nucleus.

As already mentioned above, we also performed a freed-isobar PWA (see Section 5.2.9) for the proton-target data. In the first analysis of this kind, we replace a subset of seven  $3\pi$  partial waves with fixed parameterizations for the  $[\pi\pi]_S$ ,  $f_0(980)$ , and  $f_0(1500)$  isobars and  $J^{PC} M^\varepsilon = 0^{-+} 0^+$ ,  $1^{++} 0^+$ , and  $2^{-+} 0^+$  quantum numbers of the three-body system by the three partial waves  $0^{-+} 0^+ [\pi\pi]_{0^{++}}$ ,  $\pi S, 1^{++} 0^+ [\pi\pi]_{0^{++}} \pi P$ , and  $2^{-+} 0^+ [\pi\pi]_{0^{++}} \pi D$  [102]. These waves use a free parameterization of the dynamical isobar amplitude for the  $J^{PC} = 0^{++}$  isobars according to Eq. (220), which we denote by  $[\pi\pi]_{0^{++}}$ . The freed-isobar amplitudes contain the total  $0^{++}$  isobar amplitudes including all resonant and non-resonant components for the given  $3\pi$  quantum numbers and the analyzed  $(m_{3\pi}, t')$  cell and are model-independent with respect to the parameterizations of the  $0^{++}$  isobars. Due to the much larger number of fit parameters, the freed-isobar PWA is performed using only 50 bins in  $m_{3\pi}$  and 4 bins in  $t'$ . The results of the conventional and the freed-isobar PWA are qualitatively in agreement (see Section VI in Ref. [102]). This validates the fixed parameterizations of the  $0^{++}$  isobars that are employed in the conventional PWA and shows that in the conventional PWA waves decaying into  $[\pi\pi]_S \pi$  and  $f_0(980) \pi$  can be well separated.

#### 6.2.4. $\pi^- \pi^- \pi^+$ Resonance-Model Fits

The goal of the resonance-model fit of the  $\pi^- \pi^- \pi^+$  data is to study isovector resonances of the  $a_J$  and  $\pi_J$  families with masses up to about  $2 \text{ GeV}/c^2$ . In addition to establishing the existence of the resonances, we want to determine their masses and total widths, the relative strengths and phases of their decay modes, and their production parameters, i.e. their  $t'$  spectra and the relative phases between their coupling amplitudes as a function of  $t'$  (see Section 5.3.2). The latter information is not obtainable in the  $t'$ -integrated PWA approach that was used for the lead-target data.

As was discussed in Section 5.1.7, the resonance-model fit is performed on a selected subset of waves that exhibit clear signals of well-known resonances, i.e. resonance peaks that are associated with phase motions. If possible, we include waves that represent different decay modes and different  $M$  states of these resonances. These waves are intended to act as reference amplitudes, against which the resonant amplitudes in more interesting waves can interfere. These latter waves exhibit signals of less well-known excited states or have controversial resonance content such as the spin-exotic  $1^{-+} 1^+ \rho(770) \pi P$  wave.

The input for the resonance-model fit are the spin-density submatrices  $\varrho_{ij}^\varepsilon$  of the selected waves (see Eq. (194)) that have been extracted from the data in the first analysis stage by performing the partial-wave decomposition independently in bins of  $m_{3\pi}$  and for the proton-target data also in bins of  $t'$  (see Section 6.2.3). For the lead-target data, we select a subset of 6 waves out of the 42 waves in the PWA model [181]; for the proton-target data we select 14 out of the 88 waves in the PWA model [156].<sup>102</sup> The latter one is the so far largest wave set that is consistently described in a single resonance-model fit of diffractively produced  $3\pi$ .

The selected sets of 6 and 14 waves contain signals of the well-known  $3\pi$  resonances  $a_1(1260)$ ,  $a_2(1320)$ ,  $\pi_2(1670)$ ,  $\pi(1800)$ , and  $a_4(2040)$ , which appear as peaks in the respective partial-wave intensities and as phase motions in the relative phases of these waves. The 14-wave set includes in addition waves with signals for the well-known  $\pi_2(1880)$ . This set also includes a clear resonance-like signal of the novel  $a_1(1420)$ , which was discovered in an earlier analysis of the same COMPASS proton-target data in Ref. [182]. This earlier analysis used the same 88-wave PWA fit result but the resonance-model fit included only three partial waves. The 14-wave set also contains signals of the less well-known states  $a_1(1640)$  and  $a_2(1700)$ . It turns out that the proton-target data require a third  $\pi_2$  resonance, the  $\pi_2(2005)$ , which according to the PDG requires confirmation [5]. For both

<sup>102</sup>The 6 waves selected for the lead-target data are a subset of the 14 waves selected for the proton-target data.

Table 3: Resonance models used to describe the elements of the spin-density matrix of selected partial waves, which are extracted from the  $\pi^-\pi^-\pi^+$  data, using Eq. (238). For the lead-target data, 6 waves (highlighted in blue) are selected and described using a resonance model containing 6 resonances (highlighted in blue) and a coherent non-resonant component for each wave [181]. For the proton-target data, the listed 14 waves are selected. They are described using a resonance model containing 11 resonances and a coherent non-resonant component for each wave [156].

Partial wave	Resonance(s)
$0^{-+} 0^+ f_0(980) \pi S$	$\pi(1800)$
$1^{++} 0^+ \rho(770) \pi S$	$a_1(1260), a_1(1640)$
$1^{++} 0^+ f_0(980) \pi P$	$a_1(1420)$
$1^{++} 0^+ f_2(1270) \pi P$	$a_1(1260), a_1(1640)$
$1^{-+} 1^+ \rho(770) \pi P$	$\pi_1(1600)$
$2^{++} 1^+ \rho(770) \pi D$	$a_2(1320)$
$2^{++} 2^+ \rho(770) \pi D$	$a_2(1700)$
$2^{++} 1^+ f_2(1270) \pi P$	
$2^{-+} 0^+ \rho(770) \pi F$	
$2^{-+} 0^+ f_2(1270) \pi S$	$\pi_2(1670), \pi_2(1880), \pi_2(2005)$
$2^{-+} 1^+ f_2(1270) \pi S$	
$2^{-+} 0^+ f_2(1270) \pi D$	
$4^{++} 1^+ \rho(770) \pi G$	$a_4(2040)$
$4^{++} 1^+ f_2(1270) \pi F$	

data samples, the waves selected for the resonance-model fit include the spin-exotic  $1^{-+} 1^+ \rho(770) \pi P$  wave. The appearance of a potential  $\pi_1(1600)$  resonance in this wave is disputed [199, 200, 205]. In total, the resonance model in Eq. (238) contains 6 resonances for the 6-wave fit of the lead-target data and 11 resonances for the 14-wave fit of the proton-target data. All resonances are described using Breit-Wigner amplitudes as in Eqs. (151) and (152). For the  $a_1(1260)$  and the  $a_2(1320)$ , we use dynamic widths (see Section IV.A.1 in Ref. [156] for details). For the other resonances, we use constant widths as in Eq. (151). In addition to the resonant components, we include for each wave a separate coherent non-resonant component (see Section 5.3.1). The resonance models for the lead- and proton-target data are summarized in Table 3. For the lead-target data, the resonance model in Eq. (238) has rank 2 to match the rank of the spin-density matrix from the  $t'$ -integrated PWA. The 14-wave resonance-model fit of the proton-target data is performed simultaneously in 11  $t'$  bins using a rank-1 resonance model.<sup>103</sup>

Figure 44 shows the intensities of the resonant and non-resonant wave components from the 14-wave resonance-model fit of the proton-target data as a function of  $m_{3\pi}$  (colored curves) together with the intensity of the coherent sum of the 14 selected partial-wave amplitudes (gray squares) and the total intensity of the PWA model (black points). Integrated over the analyzed  $m_{3\pi}$  range, the coherent sum of the 14 selected partial-wave amplitudes contributes 57.9 % to the total intensity. This value is similar to the intensity sum of the 14 waves, which corresponds to 56.8 % of the total intensity. Thus the net effect of the interferences between the 14 partial-wave amplitudes is slightly constructive. It is worth noting that the intensities of the wave components cover a large dynamic range of more than three orders of magnitude. The largest contributions to the intensity come from the  $a_1(1260)$  and the non-resonant term in the  $1^{++} 0^+ \rho(770) \pi S$  wave (continuous red curves in Figs. 44a and 44c). Since the resonance model contains only waves with positive reflectivity, all wave

<sup>103</sup>This resonance model has 722 real-valued free parameters, which are constrained by 76 505 data points that enter the  $\chi^2$  function in Eq. (240). It is worth noting that only 51 of the 722 fit parameters correspond to shape parameters  $\{\zeta_k^R\}$  of resonant components, i.e. masses and widths. The vast majority of the fit parameters in Eq. (238) are the real and imaginary parts of the coupling amplitudes  $\{\mathcal{C}_{ki}^{re}(t')\}$  in the 11  $t'$  bins.

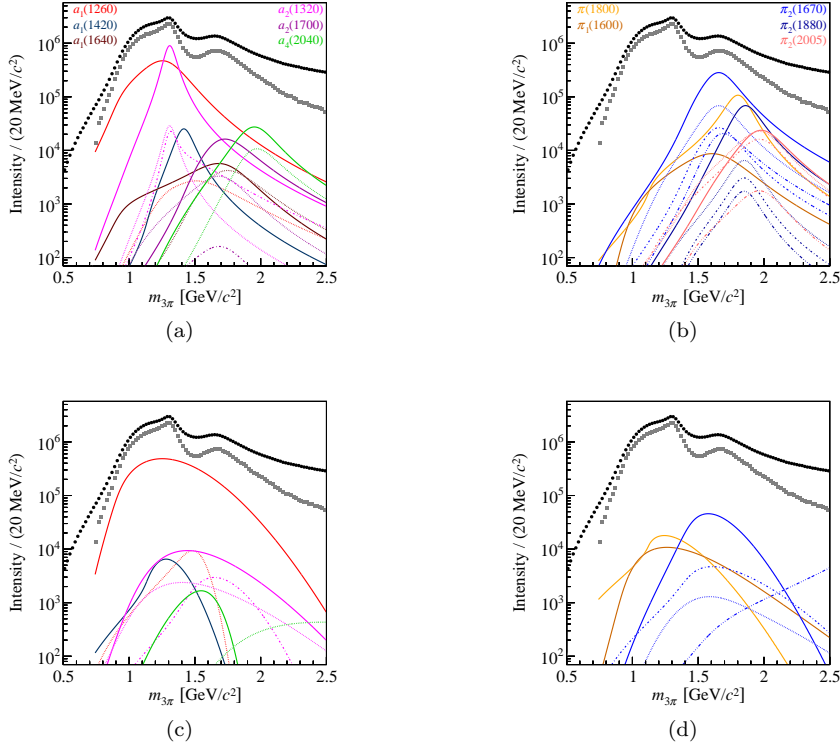


Figure 44: Summary of the result of the 14-wave resonance-model fit of the  $\pi^- \pi^- \pi^+$  proton-target data from Ref. [156]: The intensities of the wave components in the resonance model as a function of  $m_{3\pi}$  (colored curves) are compared to the total intensity of the coherent sum of all 88 partial-wave amplitudes in the PWA model (black points) and to the intensity of the coherent sum of the 14 partial-wave amplitudes selected for the resonance-model fit (gray squares). (Top row) Intensity distributions of the 11 resonances that are included in the resonance model (left:  $a_J$  resonances, right:  $\pi_J$  resonances). Different colors encode different resonances. The same resonance may appear in up to four partial waves that correspond to different decay modes. These different decay modes are encoded by different line styles, which are assigned according to the height of the respective resonance peak. The line shapes of the resonances differ in the various decay modes because of different phase space. (Bottom row) Intensity distributions of the 14 non-resonant components included in the resonance model, one in each wave. Color and line style are defined by the dominant resonance in the respective wave as shown in the top row.

components, in particular the resonant and non-resonant components, do interfere. For waves with larger intensities, this interference is mostly constructive.

Due to the highly precise proton-target data, the uncertainties of the resonance parameters from the 14-wave fit are completely dominated by systematic effects. The corresponding uncertainties are estimated based on extensive systematic studies. The parameters of the various resonances have vastly different systematic uncertainties. This mainly reflects two aspects of our data: (i) the large dynamic range of the intensities of the resonances in the selected waves as is illustrated in Figs. 44a and 44b and (ii) the vastly different strength of the non-resonant components relative to the resonances. As a consequence, we can determine the parameters of  $a_2(1320)$ ,  $a_1(1420)$ ,  $\pi_2(1670)$ ,  $\pi(1800)$ , and  $a_4(2040)$  with high accuracy. In contrast, the parameters of  $a_1(1260)$ ,  $\pi_1(1600)$ ,  $a_1(1640)$ , and  $\pi_2(2005)$  have relatively large systematic uncertainties.

A particularly important systematic effect is caused by the choice of the parameterization of the non-resonant contributions (see Section 5.3.1). The Deck process [93] is a dominant source of non-resonant contributions (see Sections 4.1 and 5.2.8 and Fig. 35a). In order to study the dependence of our fit result on the parameterization of the non-resonant component, we performed a study,

where the shapes of the non-resonant components are determined from a model for the Deck process (see Appendix B in Ref. [156] for details). Based on this model, we generate Monte Carlo pseudo-data and perform a PWA fit like for the real data using the 88-wave PWA model. The empirical parameterizations of the non-resonant components are then replaced by the square root of the intensity distributions as obtained from the partial-wave decomposition of the Deck Monte Carlo data. We will discuss the results from this study in Sections 6.3.2 and 6.3.3 below. More details of the performed systematic studies are discussed in Section V and Appendix D in Ref. [156].

### 6.3. Results

In the following sections, we present selected results from the partial-wave decompositions and the resonance-model fits of the COMPASS  $\eta\pi^-$ ,  $\eta'\pi^-$ , and the two  $\pi^-\pi^-\pi^+$  data samples. These results are ordered by the  $J^{PC}$  quantum numbers of the states. Since the  $\pi^-\pi^-\pi^+$  proton-target data sample is by far the largest one, we discuss results from these data in more detail.

#### 6.3.1. The $J^{PC} = 0^{-+}$ Sector

The PDG lists currently five isovector states with  $J^{PC} = 0^{-+}$  [5]:  $\pi$ ,  $\pi(1300)$ ,  $\pi(1800)$ ,  $\pi(2070)$ , and  $\pi(2360)$  (see also Fig. 3). Although the first three states are considered well established, the parameters of the  $\pi(1300)$  are not well known. The  $\pi(2070)$  and the  $\pi(2360)$  are “further states” and require confirmation.

The  $\pi(1300)$  is considered the first radial excitation of the pion, i.e. the  $2^1S_0$  quark-model state, by the PDG [7] and also the quark model from Ref. [16] that is discussed in Section 2.1.2. The  $\pi(1300)$  was reported in  $\rho(770)\pi$  and  $[\pi\pi]_S\pi$  decay modes, although the latter one is contradicted by a measurement by the Crystal Barrel Collaboration [206]. The  $\pi(1800)$  has a mass that is consistent with the second radial excitation of the pion, i.e. the  $3^1S_0$  quark-model state, but it exhibits a peculiar decay pattern. The  $\pi(1800)$  decays mostly into  $3\pi$  and experiments have reported  $f_0(500)\pi$ ,  $f_0(980)\pi$ , and  $f_0(1370)\pi$  decays, i.e. decays into  $J^{PC} = 0^{++}$  isobars [5]. Surprisingly, the decay into  $\rho(770)\pi$  is not seen [207]. For the  $3\pi$  final state, also the decay into  $f_0(1500)\pi$  is not observed [199], although it is seen in the  $\eta\eta\pi$  final state [208–210]. In the latter final state, however, the  $f_0(1370)\pi$  decay is not observed [210].

The 88-wave PWA model used to analyze the COMPASS  $\pi^-\pi^-\pi^+$  proton-target data contains five waves with  $J^{PC} = 0^{-+}$  that correspond to the five decay modes  $[\pi\pi]_S\pi$ ,  $\rho(770)\pi$ ,  $f_0(980)\pi$ ,  $f_2(1270)\pi$ , and  $f_0(1500)\pi$ . The waves with  $[\pi\pi]_S$ ,  $\rho(770)$ , and  $f_0(980)$  isobars have comparatively large relative intensities of 8.0 %, 3.5 %, and 2.4 %, respectively. In contrast, the waves with  $f_2(1270)$  and  $f_0(1500)$  isobars have relative intensities of only 0.2 %, and 0.1 %, respectively.

We observe broad enhancements in the  $1.3\text{ GeV}/c^2$   $m_{3\pi}$  region in the intensity distributions of the  $\rho(770)\pi$  and  $[\pi\pi]_S\pi$  waves, which may contain the  $\pi(1300)$  (see Figs. 45a and 45b). However, for both waves the shape of the intensity distribution around  $1.3\text{ GeV}/c^2$  changes strongly with  $t'$ . This indicates large non-resonant contributions, which makes the determination of the resonance parameters difficult. This is probably one of the reasons, for the large spread of the  $\pi(1300)$  parameters as measured by previous experiments using similar reactions [5] and the resulting large uncertainty of the PDG estimate (see Table I.5). First attempts to describe the  $\rho(770)\pi$  wave in the COMPASS  $\pi^-\pi^-\pi^+$  proton-target data (see Fig. 45a) by a resonance model failed, because our model is not able to reproduce the observed intensity distribution. Improving the resonance model is the topic of future research.

The results of our analysis of the  $\pi^-\pi^-\pi^+$  proton-target data confirm the small branching of the  $\pi(1800)$  into  $\rho(770)\pi$ . The intensity distribution of the  $0^{-+}0^+\rho(770)\pi P$  wave in Fig. 45a exhibits only a small dip-like structure in the  $1.8\text{ GeV}/c^2$  region, which could be due to the  $\pi(1800)$ , but the spectrum is dominated by a broad peak around  $1.4\text{ GeV}/c^2$ . Consistent with previous experiments, we observe clear  $\pi(1800)$  peaks in the  $[\pi\pi]_S\pi$  and  $f_0(980)\pi$  waves (see Figs. 45b and 46a). However, contrary to the result of Ref. [199], we also observe a  $\pi(1800)$  peak in the  $f_0(1500)\pi$  wave (see Fig. 45c). The signal in this wave is about a factor 25 smaller than the one in the  $f_0(980)\pi$  wave and hence might have been undetectable in previous experiments.

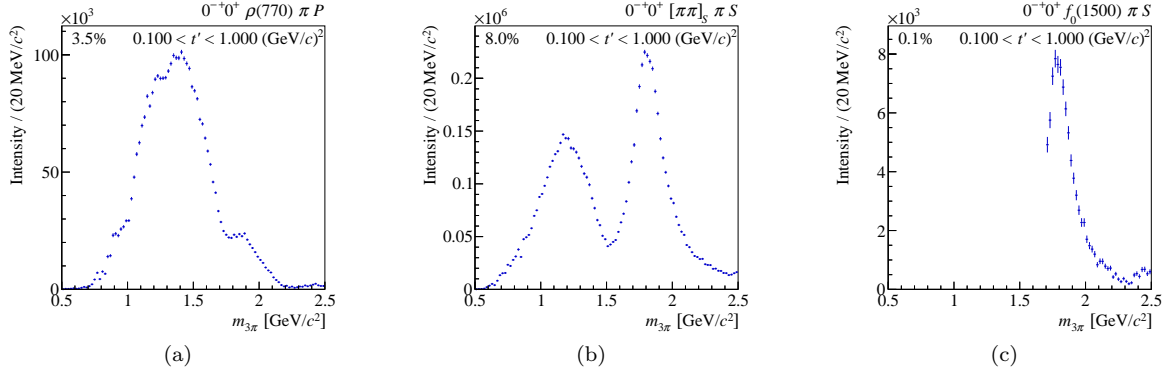


Figure 45: Intensity distributions, summed over the 11  $t'$  bins, for (a) the  $0^{-+} 0^+ \rho(770) \pi P$ , (b) the  $0^{-+} 0^+ [\pi\pi]_S \pi S$ , and (c) the  $0^{-+} 0^+ f_0(1500) \pi S$  wave in the  $\pi^- \pi^- \pi^+$  proton-target data. From Refs. [102, 211].

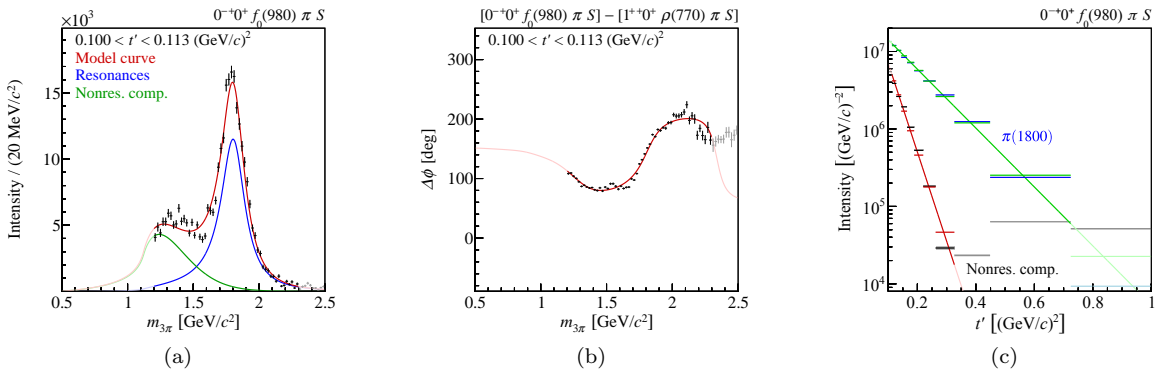


Figure 46: Amplitude of the  $0^{-+} 0^+ f_0(980) \pi S$  wave in the lowest  $t'$  bin of the  $\pi^- \pi^- \pi^+$  proton-target data [156]. (a) Intensity distribution. (b) Phase of this wave with respect to the  $1^{++} 0^+ \rho(770) \pi S$  wave. The data points represent the result of the partial-wave decomposition in the first analysis stage (see Sections 5.2 and 6.2.3). The red curve represents the result of the resonance-model fit (see Sections 5.3 and 6.2.4). The red curve is the coherent sum of the wave components, which are represented by the other curves: (blue curve)  $\pi(1800)$  resonance; (green curve) nonresonant contribution. The extrapolations of the model and the wave components beyond the fitted  $m_{3\pi}$  range are shown in lighter colors. (c)  $t'$  spectra of the two components in the  $0^{-+} 0^+ f_0(980) \pi S$  wave as given by Eq. (234). In each  $t'$  bin, horizontal lines indicate the central value of the yield of the respective model component. The horizontal extent of the lines indicate the width of the  $t'$  bins. The statistical uncertainty of the yield is represented by the height of a shaded box around the central value (for most bins invisibly small). The  $\pi(1800)$  component is shown as blue lines and light blue boxes, and the non-resonant component as black lines and gray boxes. The red and green horizontal lines represent the integrals of the model function over the  $t'$  bins and can be directly compared to the data. The red and green curves represent fits using Eq. (235). Extrapolations of the model beyond the fitted  $t'$  range are shown in lighter colors.

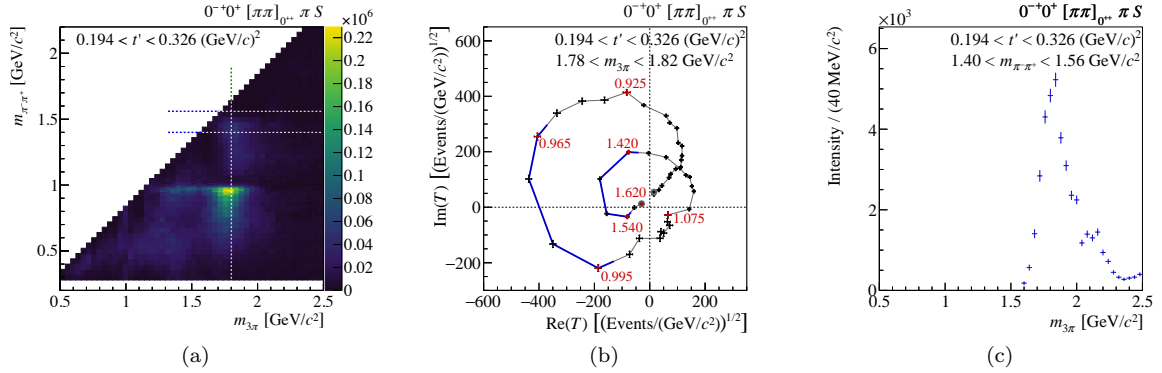


Figure 47: Amplitude of the  $0^{-+} 0^+ [\pi\pi]_{0^{++}} \pi S$  wave with the freed-isobar amplitude  $[\pi\pi]_{0^{++}}$  in an intermediate  $t'$  bin of the  $\pi^- \pi^- \pi^+$  proton-target data [102] (see Sections 5.2.9 and 6.2.3). (a) Two-dimensional representation of the intensity of the  $0^{-+} 0^+ [\pi\pi]_{0^{++}} \pi S$  wave as a function of  $m_{\pi^- \pi^+}$  and  $m_{3\pi}$ . (b) Argand diagram of the  $[\pi\pi]_{0^{++}}$  freed-isobar amplitude as a function of  $m_{\pi^- \pi^+}$  for the  $m_{3\pi}$  bin at the  $\pi(1800)$  mass as indicated by the vertical dashed line in (a). The crosses with error bars are the result of the PWA fit. The numbers in the Argand diagram show the corresponding  $m_{\pi^- \pi^+}$  values. The data points are connected by lines indicating the order of increasing  $m_{\pi^- \pi^+}$ . The line segments highlighted in blue correspond to the  $m_{\pi^- \pi^+}$  ranges around the  $f_0(980)$  from 960 to  $1000 \text{ MeV}/c^2$  and around the  $f_0(1500)$  from 1400 to  $1560 \text{ MeV}/c^2$ . The  $2\pi$  mass is binned in  $10 \text{ MeV}/c^2$  wide intervals around the  $f_0(980)$  and in  $40 \text{ MeV}/c^2$  wide intervals elsewhere. The overall phase of the Argand diagram is fixed by the  $1^{++} 0^+ \rho(770) \pi S$  wave. (c) Intensity as a function of  $m_{3\pi}$  summed over the selected  $m_{\pi^- \pi^+}$  interval around the  $f_0(1500)$  as indicated by the pair of horizontal dashed lines in (a).

The resonant nature of the  $f_0(980)$  and the  $f_0(1500)$  in the  $\pi(1800)$  decay is confirmed by the results of the freed-isobar PWA (see Sections 5.2.9 and 6.2.3). Figure 47a shows the correlation of the  $m_{3\pi}$  intensity distribution of the  $0^{-+} 0^+ [\pi\pi]_{0^{++}} \pi S$  wave with the  $m_{\pi^- \pi^+}$  intensity distribution of the freed-isobar amplitude with  $J^{PC} = 0^{++}$ . The distribution exhibits a clear peak at  $m_{3\pi} \approx 1.8 \text{ GeV}/c^2$  and  $m_{\pi^- \pi^+} \approx 1.0 \text{ GeV}/c^2$ . In the  $\pi(1800)$   $m_{3\pi}$  region, a circular resonance structure appears in the  $f_0(980)$  region (see Fig. 47b). A second circular resonance structure appears in the  $f_0(1500)$  region. The  $m_{3\pi}$  intensity distribution in the  $f_0(1500)$  region, as shown in Fig. 47c, exhibits a clear  $\pi(1800)$  peak and is similar to the corresponding distribution from the conventional PWA with fixed parameterizations for the isobar resonances shown in Fig. 45c. These results show that also in the  $3\pi$  final state the  $\pi(1800)$  decays into  $f_0(1500)\pi$ , as it is expected based on the observation of this decay mode in the  $\eta\eta\pi$  final state.

It is worth noting, that the Argand diagram in Fig. 47b shows no significant signal of a narrow  $f_0(1370)$ ,<sup>104</sup> although  $f_0(1370)\pi$  was claimed as a  $3\pi$  decay mode of the  $\pi(1800)$  by previous experiments [175, 207]. In addition, the VES experiment measured the branching-fraction ratio  $\text{BF}[\pi(1800) \rightarrow f_0(980)\pi]/\text{BF}[\pi(1800) \rightarrow f_0(1370)\pi] = 1.7 \pm 1.3$  [175]. A reason for this discrepancy could be the strong dependence of  $f_0(500)\pi$  and  $f_0(1370)\pi$  branching fractions on the PWA model, in particular on the parameterizations employed for the dynamical amplitudes of the overlapping  $0^{++}$  isobars. Also in other  $m_{3\pi}$  slices and for other  $J^{PC}$  quantum numbers of the  $3\pi$  system (see e.g. Figs. 54e and 71e and Section VI in Ref. [102]), we do not observe significant signals of a narrow  $f_0(1370)$  in the extracted isobar amplitudes. Our results from the freed-isobar PWA hence call into question the existence of the  $f_0(1370)$  as a narrow  $\pi\pi$  resonance.

We find the cleanest  $\pi(1800)$  signal in the  $f_0(980)\pi$  wave, which is the only  $0^{-+}$  wave included in the resonance-model fit. Figure 46a shows the intensity distribution of the  $0^{-+} 0^+ f_0(980) \pi S$  wave in the lowest  $t'$  bin. It exhibits a pronounced peak at  $1.8 \text{ GeV}/c^2$  that is accompanied by a

<sup>104</sup>The PDG estimates only a range for the Breit-Wigner width of the  $f_0(1370)$  of  $200$  to  $500 \text{ MeV}/c^2$  [5].

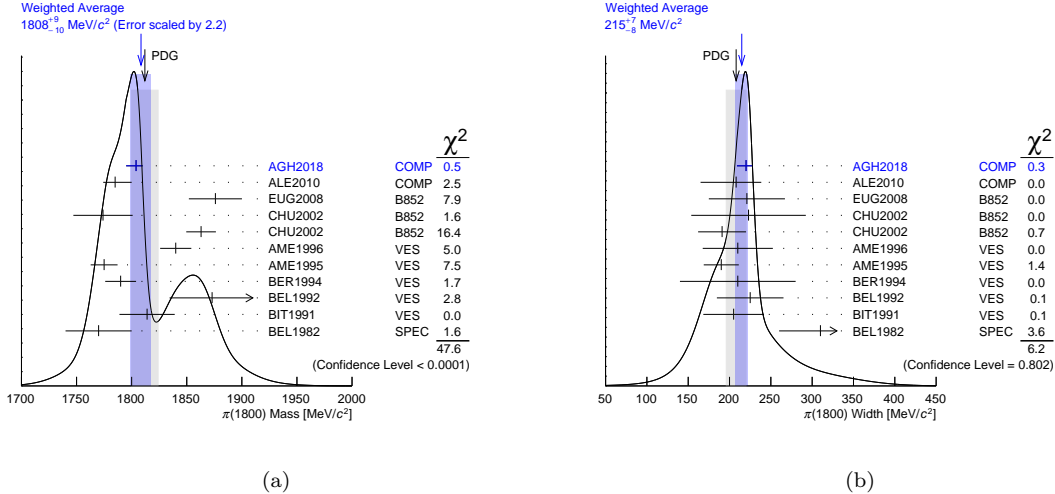


Figure 48: Ideograms for (a) the mass and (b) the width of the  $\pi(1800)$  as defined by the Particle Data Group (see Section 5.2.2 in Ref. [5]). The Breit-Wigner parameters obtained from fits of the COMPASS  $\pi^-\pi^-\pi^+$  proton-target (AGH2018, [156]) and lead-target data (ALE2010, [181]) are compared to previous measurements. Values that are based on COMPASS data and that are not yet included in the present PDG averages [5] are shown in blue. The weighted averages of all data points (blue arrows and blue-shaded bands) are compared to the present PDG averages (black arrows and gray-shaded bands).

rapid phase motion (see Fig. 46b). Although all final-state particles in the  $f_0(980)\pi$  wave are in relative  $S$  waves, the amplitude of this wave is reliably extracted from the data and is found to be robust against changes of the PWA model. The resonance model (red curve) contains one resonance term for the  $\pi(1800)$  (blue curve) and one non-resonant term (green curve). From the fit, we obtain the Breit-Wigner parameters  $m_{\pi(1800)} = 1804^{+6}_{-9} \text{ MeV}/c^2$  and  $\Gamma_{\pi(1800)} = 220^{+8}_{-11} \text{ MeV}/c^2$  [156]. Our measurement of the  $\pi(1800)$  parameters is the so far most accurate and in good agreement with the PDG world average [5] as well as with our result of  $m_{\pi(1800)} = 1785 \pm 9 \text{ (stat.)}^{+12}_{-6} \text{ (sys.)} \text{ MeV}/c^2$  and  $\Gamma_{\pi(1800)} = 208 \pm 22 \text{ (stat.)}^{+21}_{-37} \text{ (sys.)} \text{ MeV}/c^2$  from the analysis of the  $\pi^-\pi^-\pi^+$  lead-target data [181]. The ideograms in Fig. 48 show that the measured  $\pi(1800)$  width values are in good agreement, whereas the mass values have a large spread and fall into two clusters centered at about  $1780 \text{ MeV}/c^2$  and  $1860 \text{ MeV}/c^2$ . Our new value from the analysis of the  $\pi^-\pi^-\pi^+$  proton-target data (top point in Fig. 48a) falls inbetween these two clusters. It is interesting to note that the measurement that has the largest discrepancy with respect to the weighted average of the  $\pi(1800)$  mass in Fig. 48a was obtained from a resonance-model fit of the  $1.8 \text{ GeV}/c^2$  region of the  $0^{-+}0^+\sigma\pi S$  amplitude in an analysis of BNL E852 data on diffractively produced  $\pi^-\pi^-\pi^+$  [199]. Although this wave exhibits a clear  $\pi(1800)$  signal also in our data (see Fig. 45b), it contains an additional broad enhancement at about  $1.3 \text{ GeV}/c^2$ , which may contain the  $\pi(1300)$ . However, the strong  $t'$  dependence of the shape of the intensity distribution in this mass range suggests large non-resonant components. In order to reliably measure the  $\pi(1800)$  resonance parameters in this wave, the interference of the  $\pi(1800)$  with the other wave components that dominate the  $1.3 \text{ GeV}/c^2$  region would need to be taken into account, like in our fit of the  $\pi(1800)$  in the  $0^{-+}0^+f_0(980)\pi S$  wave. This, however, was not done in the analysis in Ref. [199].

The low-mass shoulder in Fig. 46a is well described by the non-resonant component. We do not find evidence for a possible  $\pi(1300)$  component in the  $0^{-+}0^+f_0(980)\pi S$  wave (see Section VI.A.2 in Ref. [156] for details). Interestingly, the non-resonant component (black lines in Fig. 46c) has an extremely large slope parameter value of  $26^{+6}_{-5} (\text{GeV}/c)^{-2}$  and its  $t'$  spectrum exhibits a dip at  $t' \approx 0.3 (\text{GeV}/c)^2$ . This behavior is strikingly different from that of all other resonant components in

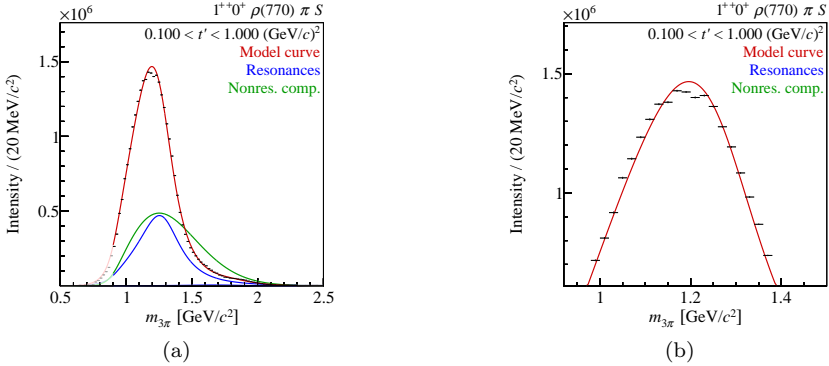


Figure 49: Intensity distribution of the  $1^{++} 0^+ \rho(770) \pi S$  wave in the  $\pi^- \pi^- \pi^+$  proton-target data summed over the 11  $t'$  bins [156]. The curves represent the result of the resonance-model fit. The model and the wave components are represented as in Fig. 46. The dominant resonant component is the  $a_1(1260)$ ; the  $a_1(1640)$  is barely visible. (b) shows a zoomed view of (a).

our model and is in agreement with the absence of a significant  $\pi(1300)$  component in the  $f_0(980)\pi$  wave. Similar dip-like  $t'$  spectra were observed in other inelastic diffraction-dissociation reactions, for example in the reaction  $n + p \rightarrow p\pi^- + p$  [212, 213], and were explained by a cancellation of double-Regge exchange processes and direct resonance production (see e.g. Refs. [214–216]). In contrast, the  $t'$  spectrum of the  $\pi(1800)$ , which is shown as blue lines in Fig. 46c, has an approximately exponential behavior with a slope parameter value of  $8.8^{+0.7}_{-0.3} (\text{GeV}/c)^{-2}$ , which is consistent with a resonance.

### 6.3.2. The $J^{PC} = 1^{++}$ Sector

Currently, six  $a_1$  states are known [5] (see also Fig. 3). However, only the  $a_1(1260)$  ground state is considered an established state by the PDG. The  $a_1(1420)$  and  $a_1(1640)$  are omitted from the summary table. The  $a_1(1930)$ , the  $a_1(2095)$ , and the  $a_1(2270)$  are listed as “further states”.

Although the existence of the  $a_1(1260)$  as the isovector  $J^{PC} = 1^{++}$  ground state, i.e. the  $1^3P_1$  quark-model state, is well established, the parameters of the  $a_1(1260)$  are not well known. Depending on the analyzed process and the employed parameterizations, the measured values of the  $a_1(1260)$  parameters differ substantially [217]. The reported values for the  $a_1(1260)$  mass cover a wide range from  $1041 \pm 13 \text{ MeV}/c^2$  [218] to  $1331 \pm 10 \text{ (stat.)} \pm 3 \text{ (sys.)} \text{ MeV}/c^2$  [219]; the values for the  $a_1(1260)$  width range from  $230 \pm 50 \text{ MeV}/c^2$  [218] to  $814 \pm 36 \text{ (stat.)} \pm 13 \text{ (sys.)} \text{ MeV}/c^2$  [219]. Due to the large spread of the measured parameter values, the PDG does not perform an average but only gives estimates of  $m_{a_1(1260)} = 1230 \pm 40 \text{ MeV}/c^2$  and  $\Gamma_{a_1(1260)} = 250 \text{ to } 600 \text{ MeV}/c^2$  [5].

The  $a_1(1260)$  decays mainly to  $3\pi$ . The  $\rho(770)\pi$   $S$ -wave decay mode is the most dominant one with a branching fraction of 60.19 % [219]. The branching fractions into  $\sigma\pi$  and  $f_0(1370)\pi$  are also large, whereas those into the  $\rho(770)\pi$   $D$  wave and  $f_2(1270)\pi$  are small. This is consistent with our  $\pi^- \pi^- \pi^+$  lead- and proton-target data, where the  $a_1(1260)$  in the  $1^{++} 0^+ \rho(770) \pi S$  wave is the by far largest resonance signal (see Figs. 43 and 49a). Hence the  $1^{++} 0^+ \rho(770) \pi S$  wave plays a special role in the resonance-model fits. In the highly precise proton-target data, the statistical uncertainties of the  $1^{++} 0^+ \rho(770) \pi S$  amplitude are extremely small, so that the resonance model has difficulties to describe all details of the data. This applies in particular to the peak region in the intensity distribution of this wave as shown in Fig. 49b. Hence the  $1^{++} 0^+ \rho(770) \pi S$  amplitude has a large contribution of about 25 % to the minimum value of the  $\chi^2$  function of the fit model (see Eq. (240)). The deviations of the model from the data induce a multi-modal behavior of the minimization procedure and comparatively large systematic uncertainties of the resonance parameters of the  $a_1(1260)$  and of other resonances (see Sections IV.B and V in Ref. [156] for details).

One of the challenges in describing the  $1^{++} 0^+ \rho(770) \pi S$  intensity distribution is that the peak

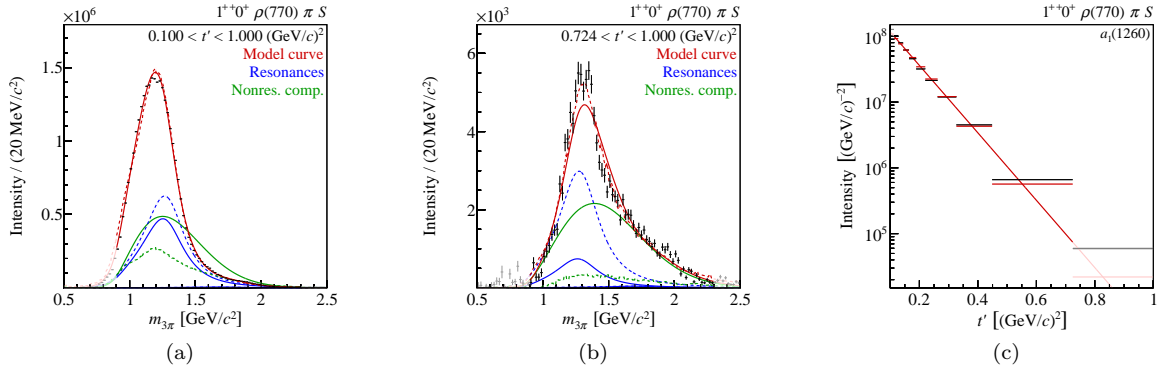


Figure 50: Intensity distribution of the  $1^{++} 0^+ \rho(770) \pi S$  wave (a) in the lowest and (b) in the highest  $t'$  bin of the  $\pi^- \pi^- \pi^+$  proton-target data [156]. The curves represent the result of two resonance-model fits. The model and the wave components are represented as in Fig. 46. The dominant resonant component is the  $a_1(1260)$ ; the  $a_1(1640)$  is barely visible. The result of the main resonance-model fit is represented by the continuous curves. The dashed curves represent the result of a fit, where the empirical parameterizations of the non-resonant components are replaced by the square root of the intensity distributions of the partial-wave decomposition of Deck Monte Carlo data. (c) Similar to Fig. 46c, but showing the  $t'$  spectrum of the  $a_1(1260)$  in the  $1^{++} 0^+ \rho(770) \pi S$  wave.

in the  $a_1(1260)$  region changes its position and shape as a function of  $t'$ . This behavior is illustrated in Figs. 50a and 50b. At low  $t'$ , the peak is located at about  $1.15 \text{ GeV}/c^2$  and shifts toward higher masses with increasing  $t'$ , up to about  $1.30 \text{ GeV}/c^2$  in the highest  $t'$  bin. In addition, the peak narrows significantly. This demonstrates the necessity to perform a  $t'$ -resolved analysis. It is also a sign that contributions from non-resonant processes to this partial-wave amplitude are large. Indeed, the resonance-model fit finds a non-resonant component that is comparable in strength to the  $a_1(1260)$  in the low and intermediate  $t'$  range and that is even dominant at high  $t'$ . The  $t'$  spectrum of the  $a_1(1260)$  in the  $1^{++} 0^+ \rho(770) \pi S$  wave exhibits an approximately exponential dependence on  $t'$  (see Fig. 50c). However, the slope parameter has a value of  $11.8^{+0.9}_{-4.2} (\text{GeV}/c)^{-2}$ , which is larger than what one would expect for a resonance. The slope parameter value is similar to the one of the non-resonant component in this wave. This might be a hint that our resonance model is not able to completely separate the  $a_1(1260)$  from the non-resonant component.

Since the  $1^{++} 0^+ \rho(770) \pi S$  wave has a large contribution from non-resonant processes, the fit result depends strongly on the parameterization employed for the non-resonant component. We study this model dependence by performing a resonance-model fit, where the empirical parameterizations of the non-resonant components (see Eqs. (228) and (229)) are replaced by the square root of the intensity distributions obtained from the partial-wave decomposition of Deck Monte Carlo data (see Section 6.2.4). The result of this fit is shown as dashed curves in Figs. 50a and 50b. The model describes the  $1^{++} 0^+ \rho(770) \pi S$  intensity distributions well. At high  $t'$ , the peak is described even better than in the main fit (see Fig. 50b), where we used the empirical parameterization in Eq. (229) for the non-resonant component. The shapes of the non-resonant component from the Deck Monte Carlo are for all  $t'$  bins similar to those found in the main fit, but the yields are considerably smaller. In turn, the  $a_1(1260)$  yields are significantly larger, in particular at high  $t'$ .

From the 14-wave resonance-model fit to the  $\pi^- \pi^- \pi^+$  proton-target data, we extract the Breit-Wigner parameters  $m_{a_1(1260)} = 1299^{+12}_{-28} \text{ MeV}/c^2$  and  $\Gamma_{a_1(1260)} = 380 \pm 80 \text{ MeV}/c^2$  [156]. The large systematic uncertainties are mostly due to the issues discussed above. From the 6-wave fit to the  $\pi^- \pi^- \pi^+$  lead-target data, we obtain  $m_{a_1(1260)} = 1255 \pm 6 \text{ (stat.)}^{+7}_{-17} \text{ (sys.)} \text{ MeV}/c^2$  and  $\Gamma_{a_1(1260)} = 367 \pm 9 \text{ (stat.)}^{+28}_{-25} \text{ (sys.)} \text{ MeV}/c^2$  [181]. In both analyses, the  $a_1(1260)$  is described by a Breit-Wigner amplitude as in Eq. (152) with a parameterization of the dynamic width that takes into account the variation of the  $\rho(770)\pi$  decay phase space across the resonance width [220] (see also Eq. (24) in Ref. [156]). Our mass values are compatible with the PDG estimate and our width values lie close to

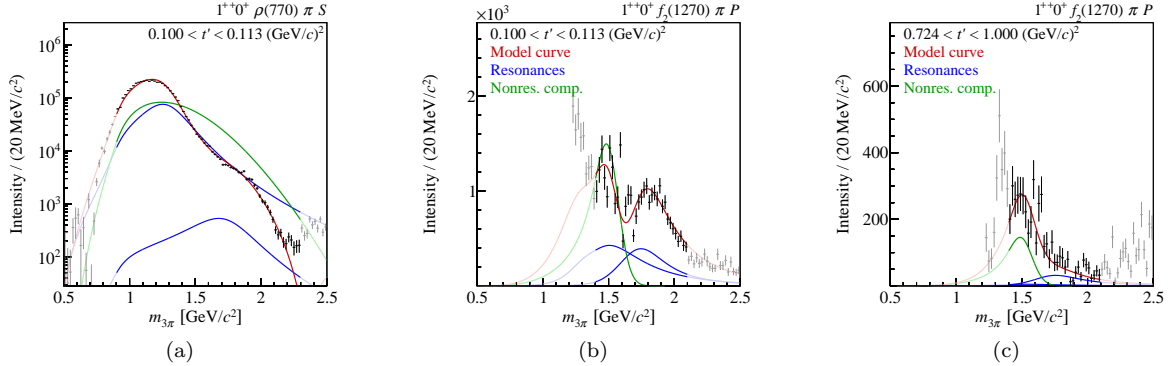


Figure 51: Signals of the  $a_1(1640)$  in the  $\pi^- \pi^- \pi^+$  proton-target data [156]. (a) Intensity distribution of the  $1^{++} 0^+ \rho(770) \pi S$  wave in the lowest  $t'$  bin (same as Fig. 50a but in logarithmic scale). (b) and (c): Intensity distributions of the  $1^{++} 0^+ f_2(1270) \pi P$  wave in the lowest and highest  $t'$  bin, respectively. The curves represent the result of the resonance-model fit. The model and the wave components are represented as in Fig. 46.

the center of the range estimated by the PDG [5].

A good candidate for the first radial excitation of the  $a_1(1260)$ , i.e. for the  $2^3P_1$  quark-model state, is the  $a_1(1640)$ . In the  $\pi^- \pi^- \pi^+$  data, most of the  $1^{++}$  waves are dominated by the ground-state  $a_1(1260)$  signal. This is true in particular for the  $1^{++} 0^+ \rho(770) \pi S$  wave. In this wave, the  $a_1(1640)$  signal is about two orders of magnitude smaller than the  $a_1(1260)$  signal (see Fig. 51a and cf. Fig. 50a). Since the  $\rho(770) \pi S$  wave is the only  $1^{++}$  wave in the 6-wave resonance-model fit of the  $\pi^- \pi^- \pi^+$  lead-target data, no  $a_1(1640)$  component was included. The  $a_1(1260)$  signal is suppressed in waves with heavier isobars, e.g. in  $f_2(1270) \pi$  and  $\rho_3(1690) \pi$  waves. In the  $\pi^- \pi^- \pi^+$  proton-target data, we observe an  $a_1(1640)$  signal in the  $1^{++} 0^+ f_2(1270) \pi P$  wave, which was included in the 14-wave resonance-model fit (see Figs. 51b and 51c). We obtain  $a_1(1640)$  Breit-Wigner parameters with large uncertainties:  $m_{a_1(1640)} = 1700^{+35}_{-130} \text{ MeV}/c^2$  and  $\Gamma_{a_1(1640)} = 510^{+170}_{-90} \text{ MeV}/c^2$  [156]. In Fig. 52, we compare these values to the measurements that are included in the PDG average [5]. Our mass value is in agreement with previous measurements. However, our width value is higher. This discrepancy might be at least in part due to the limitations of our analysis model.

In addition to the known states discussed above, we have discovered a surprising resonance-like signal, the  $a_1(1420)$ , in the  $1^{++} 0^+ f_0(980) \pi P$  wave in the COMPASS  $\pi^- \pi^- \pi^+$  proton-target data [182]. The observed  $f_0(980) \pi$  decay mode is peculiar. Only few light mesons are known to decay into  $f_0(980)$ , among them only two isovector mesons, the  $\pi(1800)$  [102, 156, 175, 199] and the  $\pi_2(1880)$  [102] (see Sections 6.3.2 and 6.3.5). Hence the 88-wave PWA model for the proton-target data includes only four waves with an  $f_0(980)$  isobar (see Table IX in Appendix A of Ref. [102]), two of which, the  $0^{-+} 0^+$  and the  $1^{++} 0^+$  wave, are included in the 14-wave resonance-model fit. The coherent sum of the four  $f_0(980)$  waves, which have all positive reflectivity, contributes only 3.3% to the total intensity. Most of this intensity is due to the  $0^{-+} 0^+ f_0(980) \pi S$  wave (see Section 6.3.1). The  $1^{++} 0^+ f_0(980) \pi P$  wave contributes only 0.3% to the total intensity. This small relative intensity is the main reason why previous experiments were not able to observe the  $a_1(1420)$  signal. As shown in Fig. 53a, the intensity distribution of the  $1^{++} 0^+ f_0(980) \pi P$  wave exhibits a narrow peak at about  $1.4 \text{ GeV}/c^2$  that is associated by a rapid phase motion of about  $180^\circ$  with respect to other waves, in particular with respect to the dominant  $1^{++} 0^+ \rho(770) \pi S$  wave as shown in Fig. 53b. Both features are robust against changes of the PWA model and other systematic effects (see Section IV.F and Appendix B in Ref. [102]).

The  $a_1(1420)$  signal also appears in the freed-isobar PWA (see Sections 5.2.9 and 6.2.3) in the  $1^{++} 0^+ [\pi\pi]_{0^{++}} \pi P$  wave. Figure 54a shows the correlation of the  $m_{3\pi}$  intensity distribution of this wave with the  $m_{\pi^- \pi^+}$  intensity distribution of the freed-isobar amplitude with  $J^{PC} = 0^{++}$ . A clear

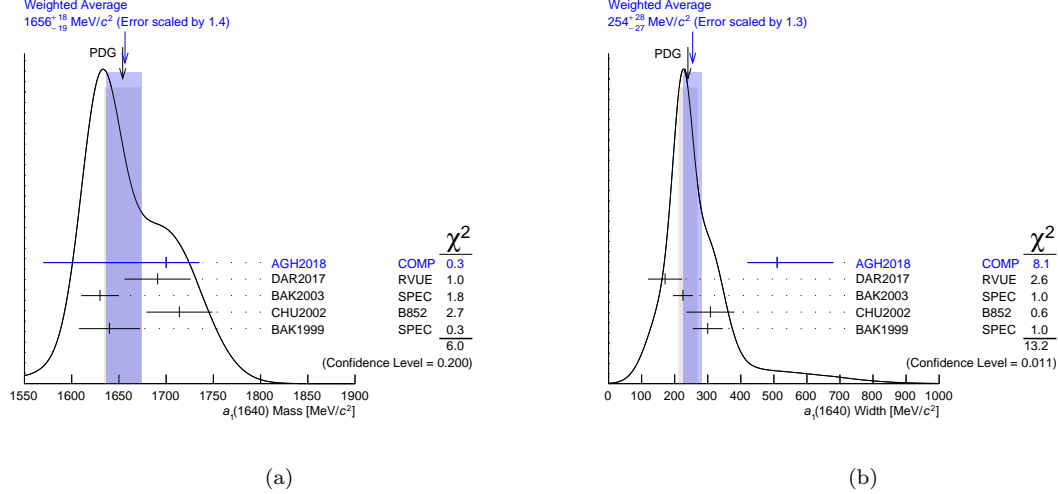


Figure 52: Ideograms similar to the ones in Fig. 48 but for (a) the mass and (b) the width of the  $a_1(1640)$ . The Breit-Wigner parameters obtained from a fit of the COMPASS  $\pi^-\pi^-\pi^+$  proton-target data (AGH2018, [156]) are compared to previous measurements [5].

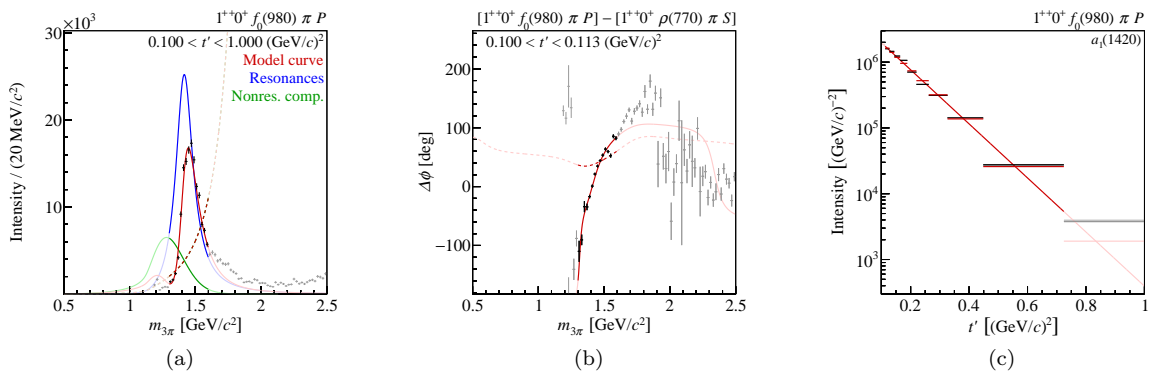


Figure 53: (a) Intensity distribution of the  $1^{++} 0^+ f_0(980) \pi P$  wave in the  $\pi^-\pi^-\pi^+$  proton-target data summed over the 11  $t'$  bins [156]. (b) Phase of this wave with respect to the  $1^{++} 0^+ \rho(770) \pi S$  wave in the lowest  $t'$  bin. The curves represent the result of two resonance-model fits. The model and the wave components are represented as in Fig. 46 except that the blue curve represents the  $a_1(1420)$ . The result of the main resonance-model fit is represented by the continuous curves. The dashed curves represent the result of a fit, where the  $a_1(1420)$  component is removed from the resonance model, i.e. where we try to model the data using only a non-resonant component. (c) Similar to Fig. 46c, but showing the  $t'$  spectrum of the  $a_1(1420)$  in the  $1^{++} 0^+ f_0(980) \pi P$  wave.

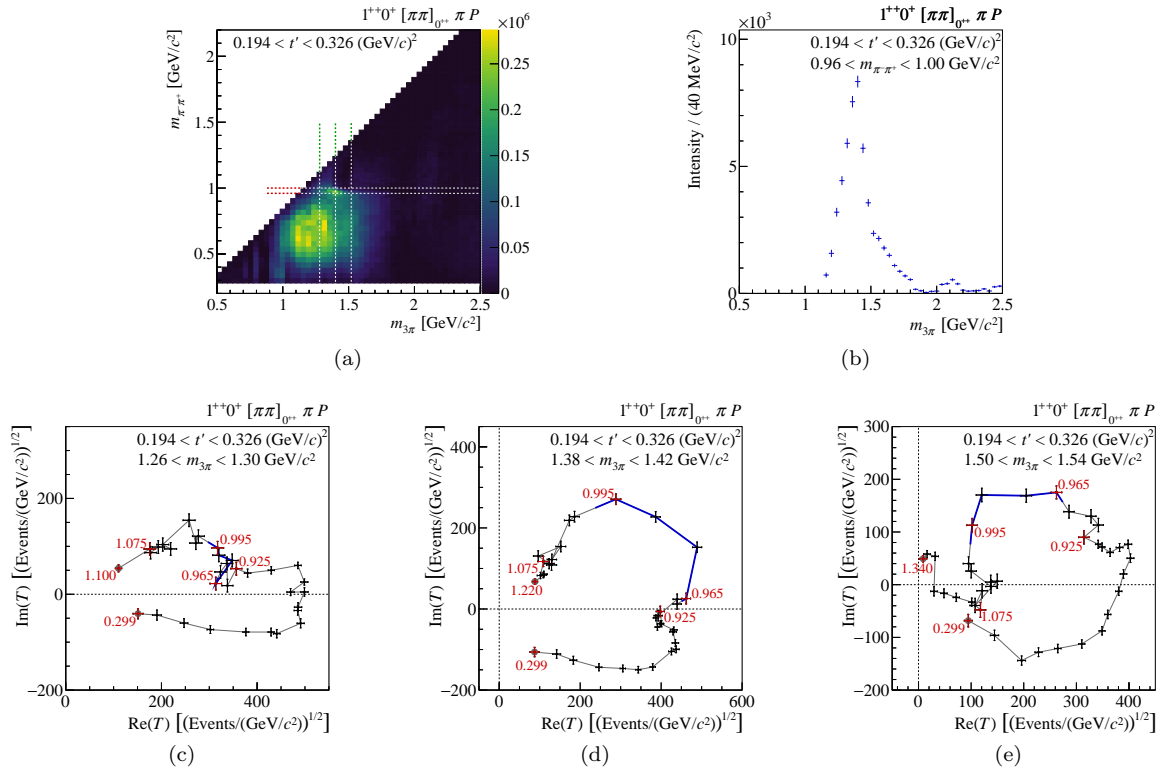


Figure 54: Similar to Fig. 47 but for the  $1^{++} 0^+ [\pi\pi]_{0^{++}} \pi P$  wave with the freed-isobar amplitude  $[\pi\pi]_{0^{++}}$  in an intermediate  $t'$  bin of the  $\pi^-\pi^-\pi^+$  proton-target data [102]. (a) Intensity of the  $1^{++} 0^+ [\pi\pi]_{0^{++}} \pi P$  wave as a function of  $m_{\pi^-\pi^+}$  and  $m_{3\pi}$ . (b) Intensity as a function of  $m_{3\pi}$  summed over the selected  $m_{\pi^-\pi^+}$  interval around the  $f_0(980)$  as indicated by the pair of horizontal dashed lines in (a). (c), (d), and (e): Argand diagrams of the  $[\pi\pi]_{0^{++}}$  freed-isobar amplitude for  $m_{3\pi}$  bins below, at, and above the  $a_1(1420)$  mass, respectively, as indicated by the vertical dashed lines in (a).

peak is found at  $m_{3\pi} \approx 1.4 \text{ GeV}/c^2$  and  $m_{\pi^-\pi^+} \approx 1.0 \text{ GeV}/c^2$ . The  $m_{3\pi}$  intensity distribution in the  $f_0(980)$  region, as shown in Fig. 54b, exhibits a clear  $a_1(1420)$  peak that is similar to the one in the conventional PWA (cf. Fig. 53a). The resonant nature of the  $\pi^-\pi^+$  subsystem at the  $a_1(1420)$  mass is proven by the Argand diagram in Fig. 54d, which exhibits a clear circular resonance structure in the highlighted  $f_0(980)$  region. We observe a continuous evolution of the Argand diagrams with  $m_{3\pi}$ , where the circular  $f_0(980)$  structure rotates counterclockwise with respect to its center due to the phase motion caused by the  $a_1(1420)$  signal thereby confirming its resonance-like nature. As an example, we show in Figs. 54c to 54e the Argand diagrams measured with respect to the  $1^{++} 0^+ \rho(770)$   $\pi S$  wave for three  $m_{3\pi}$  bins. The results from the freed-isobar PWA therefore confirm the  $a_1(1420)$  signal and prove in particular that it is not an artificial structure caused by the parameterizations that are used for the  $J^{PC} = 0^{++}$  isobars in the conventional 88-wave PWA fit.

The resonance features of the  $a_1(1420)$  signal were first established in a much simpler resonance-model fit that was based on the same 88-wave PWA result but included only three waves [182]. The estimated Breit-Wigner parameters  $m_{a_1(1420)} = 1414^{+15}_{-13} \text{ MeV}/c^2$  and  $\Gamma_{a_1(1420)} = 153^{+8}_{-23} \text{ MeV}/c^2$  from this 3-wave fit are consistent with the parameters  $m_{a_1(1420)} = 1411^{+4}_{-5} \text{ MeV}/c^2$  and  $\Gamma_{a_1(1420)} = 161^{+11}_{-14} \text{ MeV}/c^2$  that are obtained in the 14-wave fit [156]. In both analyses, a Breit-Wigner amplitude describes the  $a_1(1420)$  peak well. This is also true for the observed phase motions of the  $1^{++}$   $0^+ f_0(980) \pi P$  wave (see e.g. Fig. 53b). Another feature of the data that supports the resonance

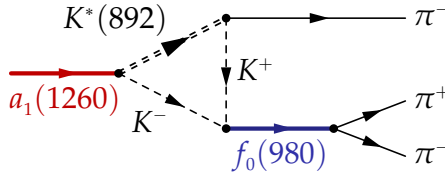


Figure 55: Rescattering diagram proposed in Refs. [173, 174] to explain the  $a_1(1420)$  signal.

interpretation of the  $a_1(1420)$  signal is the approximately exponential behavior of its  $t'$  spectrum (see Fig. 53c) with a slope parameter of  $9.5^{+0.6}_{-1.0} (\text{GeV}/c)^{-2}$ , which is a value in the range that is expected for resonances.

The interpretation of the  $a_1(1420)$  signal is still unclear. It is too close in mass and too narrow in order to be the radial excitation of the ground-state  $a_1(1260)$ , i.e. the  $2^3P_1$  quark-model state. Also the low intensity of the  $a_1(1420)$  signal, which is about 20 times smaller than the one of the  $a_1(1260)$  in the  $1^{++} 0^+ \rho(770) \pi S$  wave speaks against a  $|q\bar{q}\rangle$  interpretation. It is peculiar that we find the  $a_1(1420)$  signal only in the  $f_0(980)\pi$  decay mode. The  $f_0(980)$  is known to have a large  $s\bar{s}$  component and is interpreted by some models as a tetraquark, a molecular state, or a mixture of both [134, 221]. Another interesting aspect of the  $a_1(1420)$  is that its mass is suspiciously close to the  $K\bar{K}^*(892)$  threshold.

Several interpretations were proposed for the  $a_1(1420)$ . Based on its mass, it could be the isospin partner of the  $f_1(1420)$ . The much smaller width of the  $f_1(1420)$  of only  $54.9 \pm 2.6 \text{ MeV}/c^2$  [5] could be explained by its strong coupling to  $K\bar{K}^*(892)$ , which has a much smaller phase space than the decay  $a_1(1420) \rightarrow f_0(980)\pi$ . The molecular model for the  $f_1(1420)$  proposed in Ref. [222] could possibly be extended to the isovector case. The  $a_1(1420)$  signal was also described as a mixed state of a  $q\bar{q}$  and a tetraquark component [223] and as a tetraquark with mixed flavor symmetry [224]. In addition, calculations based on the AdS/QCD correspondence find isovector tetraquarks with masses similar to that of the  $a_1(1420)$  [225, 226]. The authors of Ref. [227] studied the two-body decay rates for the modes  $a_1(1420) \rightarrow f_0(980)\pi$  and  $a_1(1420) \rightarrow K\bar{K}^*(892)$  for four-quark configurations using the covariant confined quark model. They found that a molecular configuration is preferred over a compact diquark-antidiquark state.

In addition to the resonance interpretations discussed above, other explanations do not require an additional  $a_1$  resonance. Basdevant and Berger proposed resonant rescattering corrections in the Deck process as an explanation [228, 229], whereas the authors of Ref. [173] suggested an anomalous triangle singularity in the rescattering diagram for  $a_1(1260) \rightarrow K\bar{K}^*(892) \rightarrow K\bar{K}\pi \rightarrow f_0(980)\pi$ , which is shown in Fig. 55. The results of the latter calculation were confirmed in Ref. [174]. In order to study how well the amplitude of the triangle diagram describes the data in comparison to the Breit-Wigner amplitude, we have performed two resonance-model fits with a reduced wave set of only three waves:  $1^{++} 0^+ \rho(770) \pi S$ ,  $1^{++} 0^+ f_0(980) \pi P$ , and  $2^{++} 1^+ \rho(770) \pi D$ . In the first fit (dashed curves in Fig. 56), we use a Breit-Wigner amplitude for the  $a_1(1420)$  (blue dashed curve), like in the 14-wave fit discussed above. In the second fit (continuous curves in Fig. 56), the Breit-Wigner amplitude is replaced by the amplitude of the triangle diagram (continuous blue curve). From these fits, we find that the amplitude of the triangle diagram describes the data equally well as the Breit-Wigner model. In the case of a triangle singularity, the production rate of the  $a_1(1420)$  would be completely determined by that of the  $a_1(1260)$ . Therefore, the slope parameters of the two wave components would be equal. Unfortunately, in our analysis the systematic uncertainties of the slope parameters are too large in order to draw a conclusion. Hence more detailed studies are still needed in order to distinguish between the different models for the  $a_1(1420)$ .

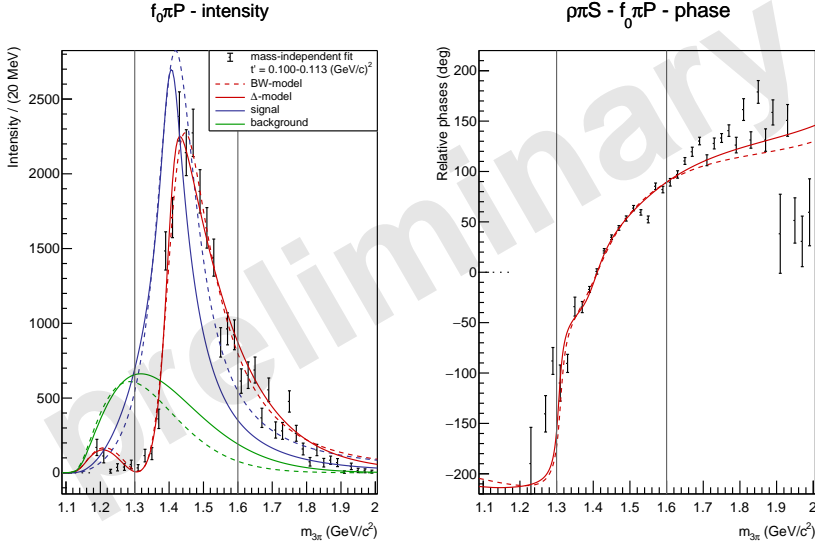


Figure 56: Intensity distribution of the  $1^{++} 0^+ f_0(980) \pi P$  wave (left) and phase of this wave with respect to the  $1^{++} 0^+ \rho(770) \pi S$  wave (right), both in the lowest  $t'$  bin of the  $\pi^- \pi^- \pi^+$  proton-target data (black points with error bars; same as in Fig. 53b). The curves represent the result of two 3-wave resonance-model fits (see text).<sup>105</sup> The vertical lines indicate the fit range. The model and the wave components are represented as in Fig. 46. The dashed curves represent the result of a fit, where the  $a_1(1420)$  is described by a Breit-Wigner amplitude (blue dashed curve) as in the 14-wave resonance-model fit shown in Fig. 53. The continuous curves represent a fit, where we use the amplitude of the triangle rescattering diagram shown in Fig. 55 (blue continuous curve) instead of the Breit-Wigner amplitude.

### 6.3.3. The $J^{PC} = 1^{-+}$ Sector

The PDG lists three light-meson states with spin-exotic quantum numbers [5]:  $\pi_1(1400)$ ,  $\pi_1(1600)$ , and  $\pi_1(2015)$ , which are all isovector states with  $J^{PC} = 1^{-+}$  quantum numbers (see also Fig. 3). The  $\pi_1(1400)$  has so far been observed only in the  $\eta\pi$  final state [185, 230–235] with the exception of the Obelix experiment, which claims the observation of the  $\pi_1(1400)$  in the  $\rho(770)\pi$  decay mode [236]. The  $\pi_1(2015)$  is listed by the PDG as a “Further State” and has been observed only by the BNL E852 experiment in the  $b_1(1235)\pi$  and  $f_1(1285)\pi$  final states [237, 238]. The  $\pi_1(1600)$  is the best established of the three known spin-exotic light-meson candidates. It has been observed by several experiments in various decay modes. The COMPASS, E852, and VES experiments have studied high-energy inelastic scattering reactions of pion beams on nuclear targets and have reported  $\pi_1(1600)$  signals in the  $\rho(770)\pi$  [156, 181, 199, 205],  $\eta'(958)\pi$  [186, 239],  $b_1(1235)\pi$  [238, 239], and  $f_1(1285)\pi$  [237, 239] decay modes. In an analysis of Crystal Barrel data on the reaction  $p\bar{p} \rightarrow \omega\pi^+\pi^-\pi^0$ , the authors of Ref. [240] reported evidence for the  $\pi_1(1600)$  in the  $b_1(1235)\pi$  decay mode. The CLEO-c experiment has studied the decays of the charmonium state  $\chi_{c1}$  to  $\eta\pi^+\pi^-$  and  $\eta'\pi^+\pi^-$  [241]. They found evidence for an exotic signal in the  $\eta'\pi$  subsystem consistent with the  $\pi_1(1600)$  signal seen in other production mechanisms. A recent summary of all measurements can be found in Ref. [24].

Although significant intensity was observed by previous experiments in the  $\eta\pi$  and  $\eta'\pi$   $P$  waves with  $M^\varepsilon = 1^+$ , surprisingly the resonance content of the two  $P$  waves seems to be different: the  $\pi_1(1400)$  is seen only in  $\eta\pi$ , whereas the  $\pi_1(1600)$  is seen only in  $\eta'\pi$ . In addition, the VES group observed a significant suppression of the squared matrix element, i.e. the intensity divided by the two-body phase-space volume  $q_{\eta^{(\prime)}\pi}/m_{\eta^{(\prime)}\pi}$  (cf. Eq. (248)), of the  $P$  wave with  $M^\varepsilon = 1^+$  in  $\eta\pi$  compared to  $\eta'\pi$  [183]. This favors a possible hybrid ( $q\bar{q}g$ ) or four-quark interpretation of the  $\pi_1(1600)$  and disfavors a hybrid interpretation of the  $\pi_1(1400)$  [242–245]. The  $\pi_1(1600)$  is consistent with the lightest hybrid

<sup>105</sup>Publication in preparation.

state predicted by lattice QCD (see Section 2.4) and models (see e.g. Ref. [24]). In contrast, the  $\pi_1(1400)$  is too light for a hybrid state. Four-quark interpretations of the  $\pi_1(1400)$  (e.g. the one in Ref. [245]) suffer from the fact that they predict additional  $SU(3)_{\text{flavor}}$  partner states that have not been observed so far. It should also be noted that resonance-like signals were observed mostly in  $\eta^{(\prime)}\pi^-$  systems that have the same charge as the beam particle. Such final states are produced predominantly via the exchange of Pomerons, which have vacuum quantum numbers and are commonly expected to have largely gluonic content. In contrast, in charge-exchange reactions no spin-exotic resonance signal was found in the  $\eta'\pi^0$  final state by the VES experiment [246], while analyses of  $\eta\pi^0$  data from the BNL E852 experiment yielded contradictory results [235, 247]. A coupled-channel analysis of the  $\eta\pi^-$  and  $\eta'\pi^-$  data from the BNL E852 experiment found no evidence for the  $\pi_1(1400)$  [248].

Although  $\pi_1(1600)$  signals were claimed in various final states measured by several experiments, in most of these analyses the resonance interpretation of the  $\pi_1(1600)$  relies on model assumptions and alternative explanations could not be ruled out completely. Hence the experimental situation is actually rather unclear. Particularly controversial is the  $\pi_1(1600)$  signal in the  $\rho(770)\pi$  channel. The BNL E852 experiment used an  $18\text{ GeV}/c$  pion beam incident on a proton target and was the first to claim a signal for  $\pi_1(1600) \rightarrow \rho(770)\pi$  based on a PWA performed in the kinematic range  $0.1 < t' < 1.0\text{ (GeV}/c)^2$  [199, 205]. The VES experiment used a  $37\text{ GeV}/c$  pion beam on a solid-beryllium target and performed the PWA in the kinematic range  $0.03 < t' < 1.0\text{ (GeV}/c)^2$ . They also observed significant intensity in the  $1^{-+} 1^+ \rho(770)\pi P$  wave (see Fig. 57a). However, they found that the intensity distribution in this wave depends significantly on the PWA model and hence concluded that the wave is contaminated by intensity that leaks from the dominant  $1^{++}$  waves into the  $1^{-+}$  wave [249]. They neither excluded nor claimed the existence of the  $\pi_1(1600)$ . A later analysis of a BNL E852 data sample that was about an order or magnitude larger than the one used in Refs. [199, 205] came to the conclusion that there is no  $\pi_1(1600)$  signal in the  $\rho(770)\pi$  channel [200]. The authors of Ref. [200] performed systematic studies to find the optimal wave set and found that in the original BNL E852 analysis in Refs. [199, 205] a number of important waves were missing in the PWA model. When they included these waves in the PWA model, the peak at about  $1.6\text{ GeV}/c^2$  in the  $1^{-+} 1^+ \rho(770)\pi P$  wave disappeared. However, the slow phase motions with respect to other waves remained. This is shown in Fig. 57c for the kinematic range  $0.18 < t' < 0.23\text{ (GeV}/c)^2$ , where the “low wave” points are the result of a PWA fit performed with the smaller wave set from Refs. [199, 205] and the “high wave” points are the result of a PWA fit performed with the larger wave set from Ref. [200]. Based on this observation, the authors of Ref. [200] concluded that there is no evidence for a  $\pi_1(1600)$  in this wave. For the discussion below it is important to note that this conclusion was based on a PWA performed in the range  $t' < 0.53\text{ (GeV}/c)^2$ . In contrast to the analysis in Ref. [200], the analysis of the  $\pi^-\pi^-\pi^+$  data from the COMPASS experiment using a solid-lead target showed again evidence for a  $\pi_1(1600)$  signal [181] (see Fig. 57e) although the PWA model contained even more partial waves than the one used in Ref. [200].

The 88-wave set used to analyze the COMPASS  $\pi^-\pi^-\pi^+$  proton-target data also includes the  $1^{-+} 1^+ \rho(770)\pi P$  wave, which has a relative intensity of 0.8 %. As shown in Figs. 58a and 58b, the shape of the intensity distribution of this wave has a surprisingly strong dependence on  $t'$ . At low  $t'$ , the intensity distribution exhibits a broad structure with a maximum at about  $1.2\text{ GeV}/c^2$  (see Fig. 58a). This structure becomes narrower with increasing  $t'$  and the maximum moves to higher masses, such that a peak emerges at about  $1.6\text{ GeV}/c^2$  in the two highest  $t'$  bins (see e.g. Fig. 58b). This  $t'$  dependence of the intensity distribution illustrates the necessity for performing the analysis in narrow  $t'$  bins. It also indicates that, in addition to potential resonant components, this wave contains large contributions from non-resonant processes. This is consistent with the fact that we do not observe large phase motions with respect to other waves in the  $1.6\text{ GeV}/c^2$  region (see e.g. Fig. 58c).

The strong modulation of the shape of the  $1^{-+}$  intensity distribution with  $t'$  is successfully repro-

---

<sup>106</sup>Publication in preparation.

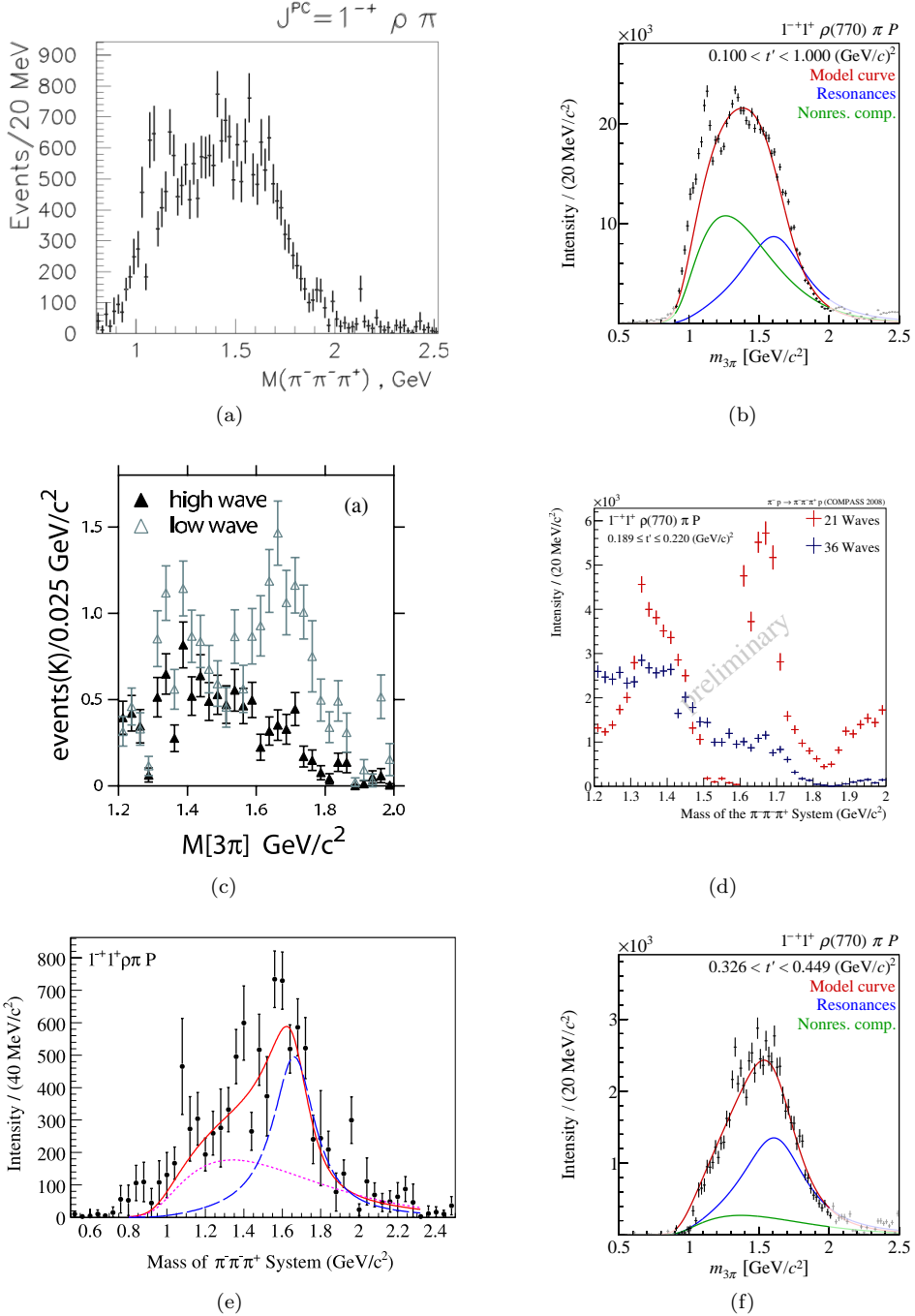


Figure 57: Comparison of intensity distributions of the  $1^{-+} 1^+ \rho(770) \pi P$  wave obtained by different experiments measuring the diffractive dissociation of pion beams into  $\pi^- \pi^- \pi^+$ . Note the different  $m_{3\pi}$  ranges. (a) Result of an analysis of VES data [249]. (b) Result of the analysis of COMPASS proton-target data [156]. The intensity is summed over the analyzed 11  $t'$  bins. (c) Results of an analysis of BNL E852 data using two different PWA models [200] (see text). (d) Result of an analysis of the COMPASS proton-target data using the same two PWA models as in (c).<sup>106</sup> The 21-wave set corresponds to “low wave” in (c), the 36-wave set to “high wave”. (e) and (f): Results of analyses of COMPASS data: (e) using a solid-lead target and integrating over  $0.1 < t' < 1.0 (\text{GeV}/c)^2$  [181] and (f) using a proton target and selecting the kinematic range  $0.326 < t' < 0.449 (\text{GeV}/c)^2$  [156].

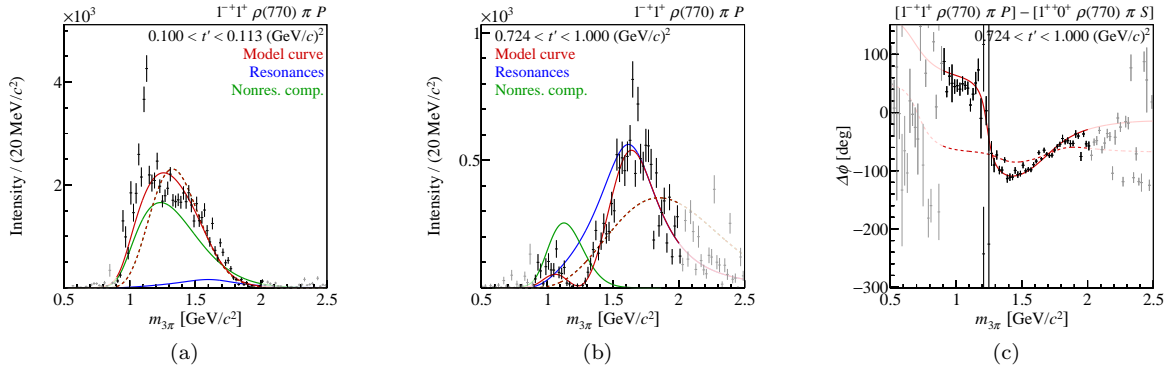


Figure 58: (a) and (b): Intensity distributions of the  $1^{-+} 1^+ \rho(770) \pi P$  wave in the COMPASS  $\pi^- \pi^- \pi^+$  proton-target data in the lowest and highest  $t'$  bin, respectively [156]. (c) Phase of this wave relative to the  $1^{++} 0^+ \rho(770) \pi S$  wave in the highest  $t'$  bin. The curves represent the result of two resonance-model fits. The model and the wave components are represented as in Fig. 46 except that the blue curves represent the  $\pi_1(1600)$ . The result of the main resonance-model fit is represented by the continuous curves. The dashed curves represent the result of a fit, where the  $\pi_1(1600)$  component is removed from the resonance model, i.e. where we try to model the data using only a non-resonant component.

duced by the resonance model as a  $t'$ -dependent interference of a  $\pi_1(1600)$  Breit-Wigner amplitude as in Eq. (151) and a non-resonant component parameterized using Eq. (229). The dashed curves in Fig. 58 represent the result of a fit, where the  $\pi_1(1600)$  resonance component is omitted from the model so that only the non-resonant component remains in this wave. Although at low  $t'$ , the intensity distribution is still reproduced roughly by the model (see Fig. 58a), it fails to reproduce the phases (see e.g. Fig. 58c) and the intensity distributions at higher  $t'$  (see Fig. 58b). This demonstrates that the COMPASS  $\pi^- \pi^- \pi^+$  proton-target data require a resonant component in the  $1^{-+}$  wave. The resonance interpretation is supported by the fact that the coupling phases of the  $\pi_1(1600)$  component relative to the other resonances in the model (see Eq. (236)) depend only weakly on  $t'$ . In contrast, the coupling phase of the  $1^{-+}$  non-resonant component with respect to the  $\pi_1(1600)$  changes strongly with  $t'$ , as does the shape of the non-resonant component (see Section VII in Ref. [156] for more details).

Due to the large contribution of the non-resonant component to the  $1^{-+}$  intensity, especially at low  $t'$ , the fit result depends strongly on the parameterization used for the non-resonant component. This model dependence is studied by replacing the empirical parameterizations of the non-resonant components (see Eqs. (228) and (229)) by the square root of the intensity distributions obtained from the partial-wave decomposition of Deck Monte Carlo data (see Section 6.2.4). The result of this study is represented by the dashed curves in Fig. 59. Compared to the main fit that employs the empirical parameterizations of the non-resonant components, the description of the  $1^{-+}$  amplitude is only slightly worse. The non-resonant component has a qualitatively similar dependence on  $t'$  and has shapes similar to those in the main fit. Only in the highest  $t'$  bin, the non-resonant component has a different, actually more plausible shape than the one found in the main fit. In the Deck study, the yield of the non-resonant component is significantly lower than in the main fit, whereas the yield of the  $\pi_1(1600)$  is significantly higher without affecting the resonance parameters too much. This shows that in our resonance model, the  $\pi_1(1600)$  yield has a large systematic uncertainty.

The  $t'$  spectrum of the non-resonant component (black lines in Fig. 60a) falls steeply with  $t'$  and has an exceptionally large slope parameter value of  $19.1^{+1.4}_{-4.7} (\text{GeV}/c)^{-2}$ . Hence the non-resonant component dominates the  $1^{-+}$  intensity at low  $t'$ . Only for  $t' \gtrsim 0.3 (\text{GeV}/c)^2$ , the intensity of the  $\pi_1(1600)$  component (blue lines in Fig. 60a) becomes larger than that of the non-resonant component. The simple exponential model in Eq. (235) is not able to reproduce the downturn of the  $\pi_1(1600)$   $t'$  spectrum toward low  $t'$ . However, this might be an artificial effect caused by an inappropriate

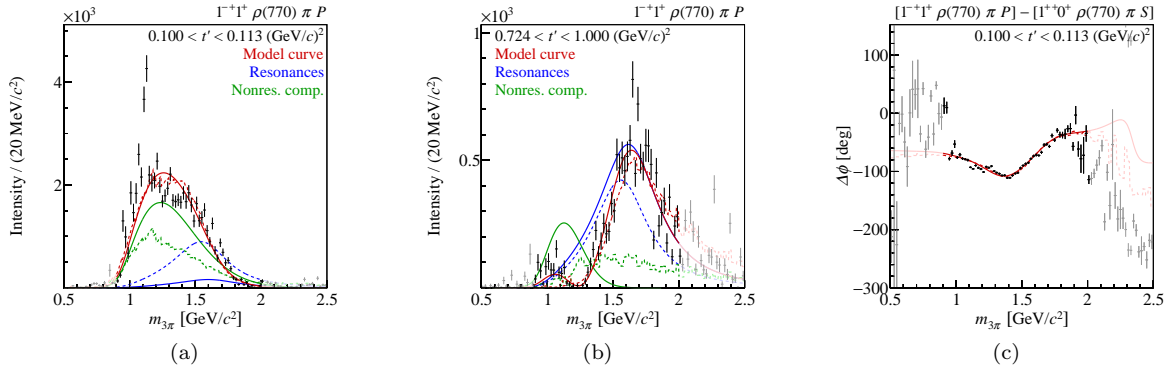


Figure 59: Similar to Fig. 58, except that the phase is shown for the lowest  $t'$  bin [156]. Here, the dashed curves represent the result of a resonance-model fit, where the empirical parameterizations of the non-resonant components are replaced by the square root of the intensity distributions of the partial-wave decomposition of Deck Monte Carlo data.

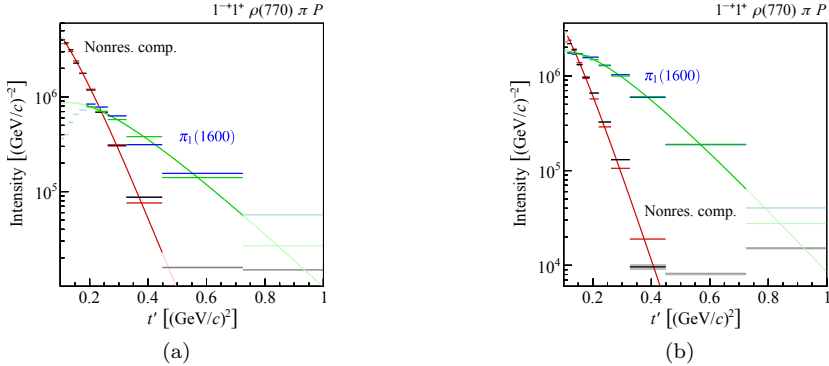


Figure 60: Similar to Fig. 46c, but showing the  $t'$  spectra of the two components in the  $1^{-+} 1^+ \rho(770) \pi P$  wave [156]. The  $\pi_1(1600)$  component is shown as blue lines and light blue boxes, and the non-resonant component as black lines and gray boxes. (a) Result of the main fit. (b) Result of a fit, in which the empirical parameterizations of the non-resonant components are replaced by the square root of the intensity distributions of the partial-wave decomposition of Deck Monte Carlo data.

description of the non-resonant component by our parameterizations. It seems that the fit is not able to completely separate the  $\pi_1(1600)$  from the non-resonant component, which dominates at low  $t'$ . This hypothesis is supported by the study discussed above, where the shape of the non-resonant component is determined from a model of the Deck process (see Fig. 60b). In this study, the  $\pi_1(1600)$  has a larger yield at low  $t'$  so that the resulting  $t'$  spectrum of the  $\pi_1(1600)$  is well described by the exponential model in Eq. (235) and has a slope parameter of  $7.3 (\text{GeV}/c)^{-2}$ , which lies in the range expected for resonances.

The results from our  $t'$ -resolved analysis of the  $\pi^- \pi^- \pi^+$  proton-target data explain the seemingly contradictory experimental findings of the BNL E852, VES, and COMPASS experiments concerning the existence of a  $\pi_1(1600)$  resonance in the  $\rho(770)\pi P$  wave. Figure 57b shows that our intensity distribution of the  $1^{-+} 1^+ \rho(770) \pi P$  wave summed over the 11  $t'$  bins is very similar to the one found in the VES analysis [249] (cf. Fig. 57a). In Fig. 57d, we show the intensity of the  $1^{-+} 1^+ \rho(770) \pi P$  wave in the range  $0.18 < t' < 0.23 (\text{GeV}/c)^2$  that is obtained if we perform the PWA using the same two wave sets as in Ref. [200]. The similarity of the results with Fig. 57c confirms that the  $\pi_1(1600)$  intensity peak in the original BNL E852 analysis in Refs. [199, 205] was mostly an artificial structure

caused by leakage of intensity from the  $2^{-+} 1^+ \rho(770) \pi P$ ,  $2^{-+} 0^+ \rho(770) \pi F$ , and  $2^{-+} 1^+ \rho(770) \pi F$  waves that were missing in the PWA model. We also confirm the finding of Ref. [200] that in the region  $t' \lesssim 0.5 \text{ (GeV}/c^2\text{)}^2$  there is only weak evidence for the  $\pi_1(1600)$ . However, our data show that a resonance-like signal is required to describe the data in the region  $t' \gtrsim 0.5 \text{ (GeV}/c^2\text{)}^2$  (see Figs. 58b and 58c). This  $t'$  region was excluded from the analysis in Ref. [200]. In the COMPASS  $\pi^- \pi^- \pi^+$  data taken with a solid-lead target, the contribution of the non-resonant component is much smaller than in the proton-target data. The  $t'$ -integrated lead-target data actually resemble the high- $t'$  region of the proton-target data (compare Figs. 57e and 57f). So far, no explanation has been found for this effect.

The intensity distributions of the  $P$  wave with  $M^\varepsilon = 1^+$  in the COMPASS  $\eta\pi^-$  and  $\eta'\pi^-$  data (black dots in Figs. 61a and 61b) are similar to previous observations. The  $\eta\pi^-$   $P$ -wave intensity shows a broad peak of about  $400 \text{ MeV}/c^2$  width, centered at a mass of  $1.4 \text{ GeV}/c^2$ . For  $m_{\eta\pi} > 1.8 \text{ GeV}/c^2$ , the intensity nearly vanishes. The  $\eta\pi^-$   $P$ -wave intensity is about a factor of 20 smaller than the dominant  $D$ -wave intensity. Hence the detector acceptance has to be simulated accurately in order to resolve the small  $P$ -wave contribution. In the  $\eta'\pi^-$  data,  $P$  and  $D$  waves have comparable intensities. The  $P$ -wave intensity distribution also shows a broad peak but the peak position is shifted to about  $1.65 \text{ GeV}/c^2$ . Similar to  $\eta\pi^-$ , the intensity is small in the high-mass region  $m_{\eta'\pi} > 2 \text{ GeV}/c^2$ . The differences in the shape of the  $P$ -wave intensity distributions in  $\eta\pi^-$  and  $\eta'\pi^-$  remain after scaling the  $\eta\pi^-$  intensity distribution by the kinematic factor in Eq. (248) (see Fig. 61b). In addition, we observe an enhancement of about a factor of 10 of the  $\eta'\pi^-$   $P$ -wave intensity with respect to the scaled  $\eta\pi^-$   $P$ -wave intensity. This is in stark contrast to the striking similarity of the  $\eta'\pi^-$  and the scaled  $\eta\pi^-$  intensity distributions observed for the  $D$  and  $G$  waves (see Figs. 65a and 77b). The relative phases exhibit a pattern similar to the one of the intensity distributions. While the phases of the  $P$  wave relative to the  $D$  wave are significantly different in  $\eta\pi^-$  and  $\eta'\pi^-$  for masses above  $1.4 \text{ GeV}/c^2$  (see Figs. 61e and 61f), the phases between the  $D$  and  $G$  waves are nearly identical (see Fig. 77c). Naively, one could interpret this as different resonance content of the  $P$  wave in the  $\eta\pi^-$  and  $\eta'\pi^-$  final states consistent with the observations of the  $\pi_1(1400)$  and the  $\pi_1(1600)$  by previous experiments.

Fitting the COMPASS  $\eta^{(\prime)}\pi^-$  data using simple Breit-Wigner resonance-models, similar to the ones employed in previous analyses, yields  $\pi_1(1400)$  resonance parameters from the  $\eta\pi^-$  data and  $\pi_1(1600)$  resonance parameters from the  $\eta'\pi^-$  data that are consistent with previous results [184–186]. However, the results for the  $\pi_1$  resonances depend strongly on whether we include a coherent non-resonant component in the  $P$  waves and on how we describe the high-mass shoulder in the  $D$  waves (see Section 6.3.4). A more stable result can be achieved by performing an  $\eta\pi-\eta'\pi$  coupled-channel fit to the  $P$ - and  $D$ -wave data using the unitary analytic model described in Section 5.3.5 (see green curves in Fig. 61). Compared to sum-of-Breit-Wigner models, this model improves, among other things, the description of the interference of the various resonances and the non-resonant components. The data are described well by the model. An important and astonishing finding of this analysis is that only a single  $\pi_1$  resonance pole is extracted from the data with parameters that are compatible with those of the  $\pi_1(1600)$  (see below). This result puts strong doubts on the existence of a separate  $\pi_1(1400)$  state in  $\eta\pi$  and thereby resolves a long-standing puzzle.

Although the COMPASS  $\pi^- \pi^- \pi^+$  proton-target data are the most precise so far, the 14-wave resonance-model fit results in  $\pi_1(1600)$  Breit-Wigner parameters of  $m_{\pi_1(1600)} = 1600^{+110}_{-60} \text{ MeV}/c^2$  and  $\Gamma_{\pi_1(1600)} = 580^{+100}_{-230} \text{ MeV}/c^2$  that have large systematic uncertainties [156]. This mainly reflects the limitations of our current analysis model. These values are in good agreement with the pole parameters  $m_{\pi_1(1600)} = 1564 \pm 24 \text{ (stat.)} \pm 86 \text{ (sys.)} \text{ MeV}/c^2$  and  $\Gamma_{\pi_1(1600)} = 492 \pm 54 \text{ (stat.)} \pm 102 \text{ (sys.)} \text{ MeV}/c^2$  from the  $\eta\pi-\eta'\pi$  coupled-channel analysis performed by JPAC [71]. From the  $\pi^- \pi^- \pi^+$  lead-target data, we obtain Breit-Wigner parameters of  $m_{\pi_1(1600)} = 1660 \pm 10 \text{ (stat.)}^{+0}_{-64} \text{ (sys.)} \text{ MeV}/c^2$  and  $\Gamma_{\pi_1(1600)} = 269 \pm 21 \text{ (stat.)}^{+42}_{-64} \text{ (sys.)} \text{ MeV}/c^2$  [181]. While the mass values are compatible with previous measurements (see Fig. 62a), the widths from the  $\pi^- \pi^- \pi^+$  proton-target data and the  $\eta^{(\prime)}\pi^-$  data are larger than the PDG average of  $241 \pm 40 \text{ MeV}/c^2$  [5]. As shown in Fig. 62b, the width values

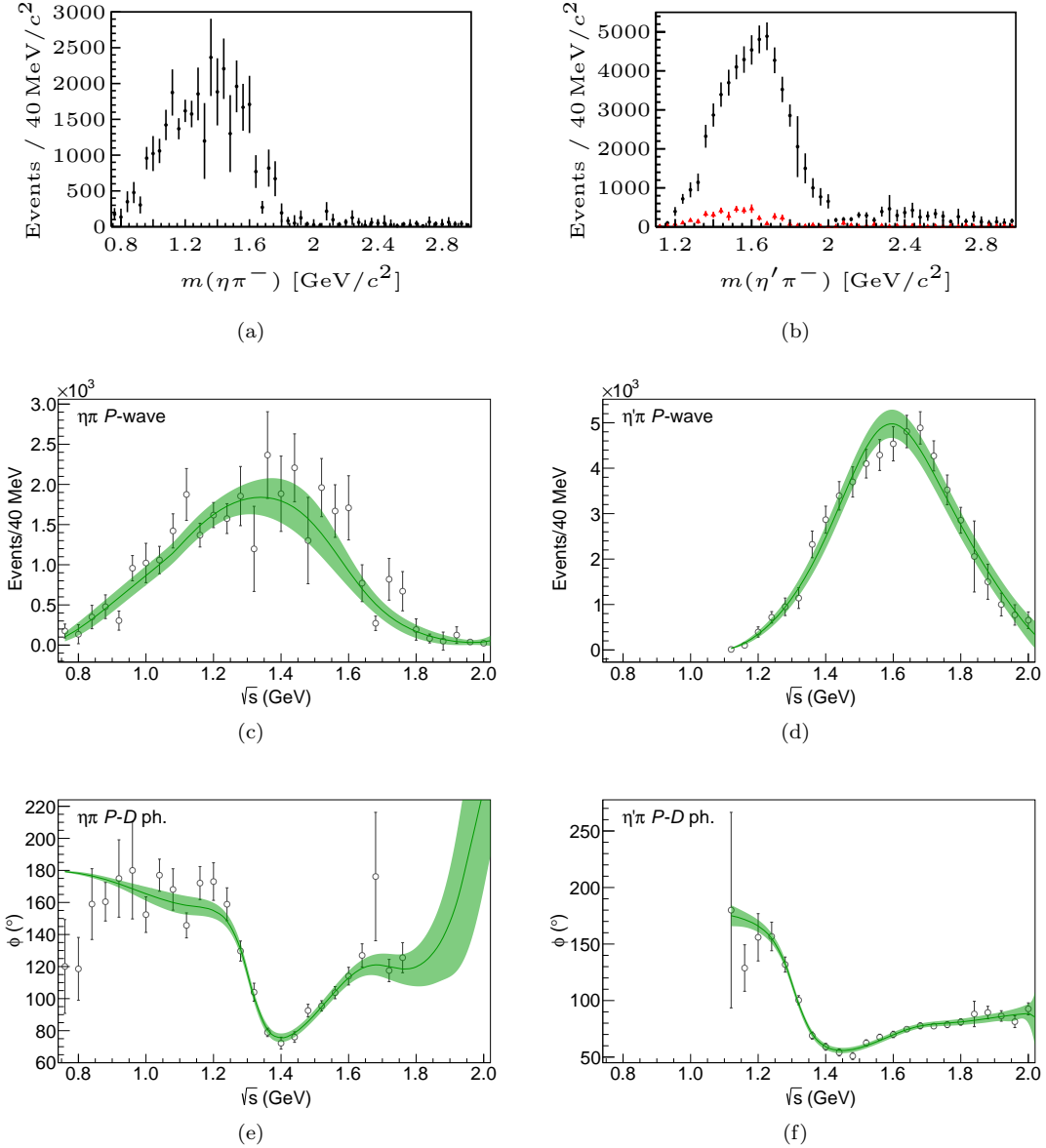


Figure 61: Intensities of the  $P$  wave with  $M^\varepsilon = 1^+$  (a) in the  $\eta\pi^-$  and (b) in the  $\eta'\pi^-$  COMPASS data (black dots) [101]. The red triangles in (b) show the  $\eta\pi^-$  intensity from (a) scaled by the kinematic factor in Eq. (248). (c) and (d): Same data as in (a) and (b) overlaid with the result of a fit of the unitary model (green curves) described in Section 5.3.5 [71]. The shaded bands represent the two-standard-deviation confidence interval. Note the different mass range. (e) and (f): Phases of the  $P$  wave relative to the  $D$  wave both with  $M^\varepsilon = 1^+$  [71]. The phase drop around  $1.3 \text{ GeV}/c^2$  is due to the  $a_2(1320)$  (see Section 6.3.4). Data and model curve as in (a) and (b).

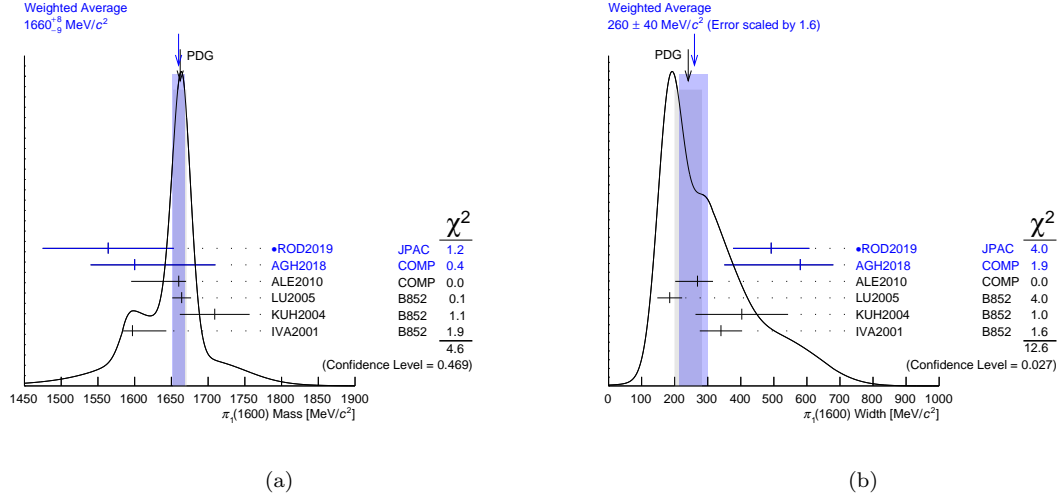


Figure 62: Ideograms similar to the ones in Fig. 48 but for (a) the mass and (b) the width of the  $\pi_1(1600)$ . The pole parameters obtained from a coupled-channel fit of the COMPASS  $\eta^{(\prime)}\pi^-$  data by the JPAC collaboration (ROD2019, [71], marked by  $\bullet$ ) and the Breit-Wigner parameters obtained from fits of the COMPASS  $\pi^-\pi^-\pi^+$  proton-target (AGH2018, [156]) and lead-target data (ALE2010, [181]) are compared to previous measurements [5].

are mainly at variance with the extremely small width value reported by the BNL E852 experiment in the  $b_1(1235)\pi$  decay mode [238].

A remaining mystery is that the production of the  $\pi_1(1600)$  in photon-induced reactions seems to be much less prominent than expected. The CLAS experiment did not observe a  $\pi_1(1600)$  signal in the charge-exchange reaction  $\gamma + p \rightarrow \pi^+\pi^-\pi^+ + (n)_{\text{miss}}$  [250, 251] (see Fig. 63a). This finding is supported by an analysis of COMPASS data of the reaction  $\pi^- + \text{Pb} \rightarrow \pi^-\pi^-\pi^+ + \text{Pb}$  in the range  $t' < 10^{-3} (\text{GeV}/c)^2$ , where photon exchange is dominant [252] (see Fig. 63b; more details of this analysis will be discussed in Section 7). In both processes, the dominant underlying reaction is  $\gamma + \pi^\pm \rightarrow \pi^\pm\pi^-\pi^+$ . Since we observe the  $\pi_1(1600)$  to decay into  $\rho(770)\pi$ , it should couple to  $\gamma\pi$  via vector-meson dominance. This is because the photon fluctuates into quark-antiquark pairs with  $J_{q\bar{q}}^{PC} = 1^{--}$  quantum numbers. In addition, the  $\pi_1(1600)$  is a hybrid candidate and is compatible with the lightest  $1^{-+}$  hybrid state predicted by lattice QCD (see Section 2.3 and Fig. 7). Lattice QCD and also many models predict that the lowest excitation of the gluon field in a hybrid meson has  $J_g^{PC} = 1^{+-}$  quantum numbers. Hence the  $q\bar{q}$  pair from the photon and the gluonic excitation can directly couple to spin-exotic  $J^{PC} = 1^{-+}$  quantum numbers, which is not the case for pion-induced reactions. Thus the production of hybrids is expected to be enhanced in photon-induced reactions [253, 254], which seems to be contradicted by the nearly vanishing intensities that are observed in the  $1.6 \text{ GeV}/c^2$  mass region. This, however, could be due to destructive interference of a  $\pi_1(1600)$  with a non-resonant component. This hypothesis could be verified by performing resonance-model fits on the existing data. In the future, much more precise photoproduction data from the GlueX experiment at JLab will help to clarify the situation.

#### 6.3.4. The $J^{PC} = 2^{++}$ Sector

Currently, the PDG lists seven isovector states with  $J^{PC} = 2^{++}$  [5]:  $a_2(1320)$ ,  $a_2(1700)$ ,  $a_2(1950)$ ,  $a_2(1990)$ ,  $a_2(2030)$ ,  $a_2(2175)$ , and  $a_2(2255)$  (see also Fig. 3). The  $a_2(1320)$  is the  $2^{++}$  ground state, i.e. the  $1^3P_2$  quark-model state. It is the best known  $3\pi$  resonance and is the dominant resonance in the

<sup>107</sup>Figure 63b is the result of an analysis of COMPASS data taken 2004. The analysis of a larger lead-target data sample taken 2009 is work in progress.

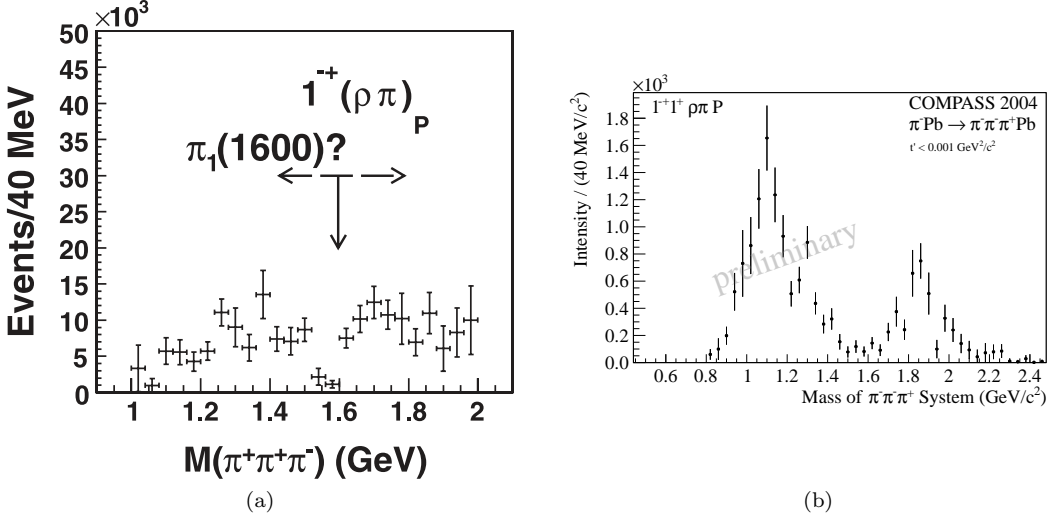


Figure 63: Intensities of the  $1^{-+} 1^+ \rho(770) \pi P$  wave produced in  $\gamma + \pi^\pm \rightarrow \pi^\pm \pi^- \pi^+$  reactions. (a) Result from the CLAS experiment [250], where the process is embedded into  $\gamma + p \rightarrow \pi^+ \pi^- \pi^+ + (n)_{\text{miss}}$ . (b) Result from the COMPASS experiment [23, 252], where the process is embedded into  $\pi^- + \text{Pb} \rightarrow \pi^- \pi^- \pi^+ + \text{Pb}$ .<sup>107</sup> The PWA model includes a leading-order  $\chi$ PT amplitude for  $m_{3\pi} < 1.24 \text{ GeV}/c^2$ , which is discussed in Section 7.5.

$\eta\pi$  channel. The  $a_2(1700)$  is omitted from the PDG summary table and hence not well known. It is a good candidate for the first radial excitation, i.e. the  $2^3P_2$  quark-model state. The five higher-lying states are listed as “further states” by the PDG and require confirmation.

The  $a_2(1320)$  has a large branching fraction into  $3\pi$  of  $70.1 \pm 2.7\%$  [5]. The second most probable decay mode is  $\eta\pi$  with a branching fraction of  $14.5 \pm 1.2\%$ . In contrast, the decay into  $\eta'\pi$  has only a small branching fraction of  $(5.5 \pm 0.9) \cdot 10^{-3}$  and was first observed by the VES experiment [183]. The  $a_2(1320)$  is the narrowest  $3\pi$  resonance and appears in the  $3\pi$  channel predominantly in the  $\rho(770)\pi D$  waves with  $M = 1$  and 2 with very low background (see e.g. Fig. 64a). The  $a_2(1320)$  peak is also associated with rapid phase motions with respect to other waves (see e.g. Fig. 64b). This makes the  $a_2(1320)$  the cleanest resonance signal in our  $\pi^- \pi^- \pi^+$  data. The  $\eta\pi^-$  data are dominated by the  $D$  wave with  $M^\varepsilon = 1^+$  with a prominent  $a_2(1320)$  peak (see Fig. 65c). In the  $\eta\pi^-$  data, we observe in addition a  $D$  wave with  $M^\varepsilon = 2^+$  and an intensity at the 5% level with respect to the  $D$  wave with  $M^\varepsilon = 1^+$  (see Fig. 65b). Also the  $D$  wave with  $M^\varepsilon = 2^+$  contains a clear  $a_2(1320)$  signal. As expected, the  $a_2(1320)$  signal is much weaker in the  $\eta'\pi^-$  data (see Fig. 65d). As shown in Fig. 65a, the observed differences in the intensity distributions of the  $\eta\pi^-$  and  $\eta'\pi^-$   $D$  waves with  $M^\varepsilon = 1^+$  are nearly completely explained by the kinematic factor in Eq. (248).

The  $a_2(1320)$  peaks in the  $\eta^{(\prime)}\pi^-$  and  $\pi^- \pi^- \pi^+$  data are well described by the employed Breit-Wigner amplitude. In the 14-wave resonance-model fit of the  $\pi^- \pi^- \pi^+$  proton-target data, the  $a_2(1320)$  resonance parameters have the smallest uncertainties of all resonances in this fit. From this fit, we extract Breit-Wigner parameters of  $m_{a_2(1320)} = 1314.5^{+4}_{-3.3} \text{ MeV}/c^2$  and  $\Gamma_{a_2(1320)} = 106.6^{+3.4}_{-7.0} \text{ MeV}/c^2$  [156]. These values are consistent with the Breit-Wigner parameters  $m_{a_2(1320)} = 1321 \pm 1 \text{ (stat.)}^{+0}_{-7} \text{ (sys.)} \text{ MeV}/c^2$  and  $\Gamma_{a_2(1320)} = 110 \pm 2 \text{ (stat.)}^{+2}_{-15} \text{ (sys.)} \text{ MeV}/c^2$  obtained from the 6-wave resonance-model fit of the  $\pi^- \pi^- \pi^+$  lead-target data [181] and with the Breit-Wigner parameters  $m_{a_2(1320)} = 1315 \pm 12 \text{ MeV}/c^2$  and  $\Gamma_{a_2(1320)} = 119 \pm 14 \text{ MeV}/c^2$  obtained from the combined fit of the  $\eta\pi^-$  and  $\eta'\pi^-$  data [101]. Pole positions of the  $a_2(1320)$  are extracted from fits of more advanced analytical models that were developed by the JPAC collaboration and are based on the principles of the relativistic  $S$ -matrix (see Section 5.3.5). From a fit to the intensity distribution of the  $\eta\pi^- D$  wave with

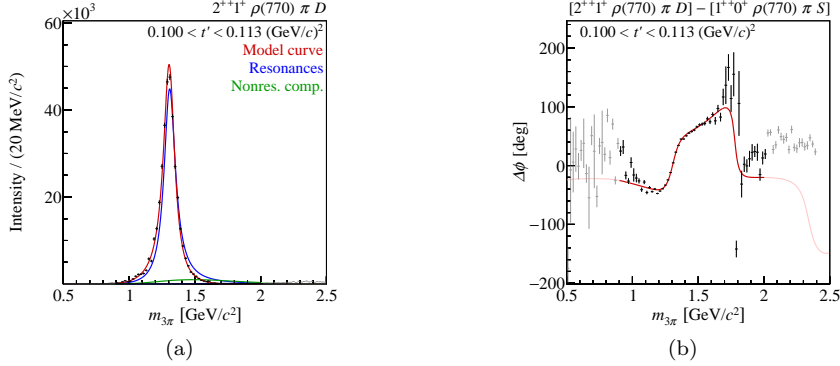


Figure 64: (a) Intensity distribution of the  $2^{++} 1^+ \rho(770) \pi D$  wave and (b) phase of this wave with respect to the  $1^{++} 0^+ \rho(770) \pi S$  wave, both in the lowest  $t'$  bin of the  $\pi^- \pi^- \pi^+$  proton-target data [156]. The curves represent the result of the resonance-model fit. The model and the wave components are represented as in Fig. 46. The dominant resonant component is the  $a_2(1320)$ ; the  $a_2(1700)$  is barely visible (see Fig. 67a for a log-scale version of (a)).

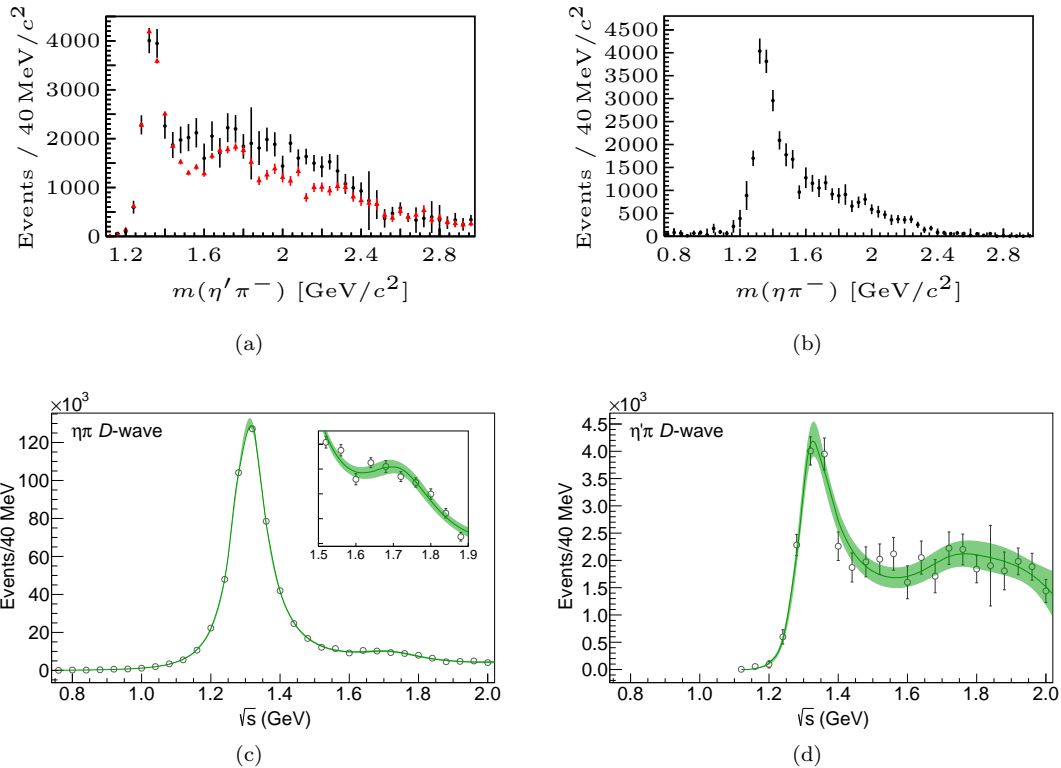
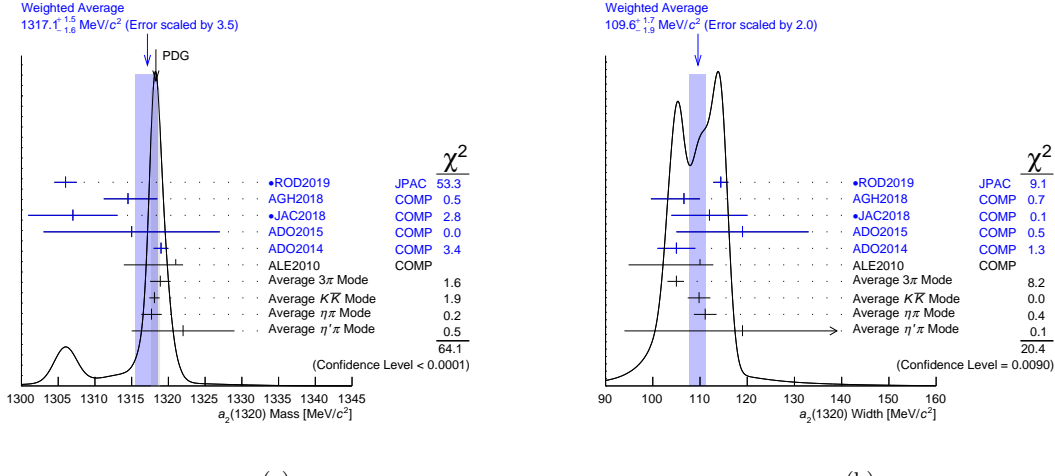


Figure 65: (a) Intensity distribution of the  $D$  waves with  $M^\epsilon = 1^+$  in the COMPASS  $\eta' \pi^-$  data (black dots) overlaid with the intensity distribution of the same wave in the COMPASS  $\eta \pi^-$  data (red triangles), scaled by the kinematic factor in Eq. (248) [101]. (b) Intensity distribution of the  $\eta \pi^- D$  wave with  $M^\epsilon = 2^+$  [101]. (c) and (d): Intensity distributions of the  $D$  waves with  $M^\epsilon = 1^+$  in the COMPASS  $\eta \pi^-$  and  $\eta' \pi^-$  data [71]. The points in (d) are the same as in (a). Note the different mass range. The green curves show the result of a fit of the unitary model from Ref. [71] that was described in Section 5.3.5. The shaded bands represent the two-standard-deviation confidence interval.



(a)

(b)

Figure 66: Ideograms similar to the ones in Fig. 48 but for (a) the mass and (b) the width of the  $a_2(1320)$ . The pole parameters obtained from a coupled-channel fit of the COMPASS  $\eta^{(\prime)}\pi^-$  data by the JPAC collaboration (ROD2019, [71]) and from a fit of the  $D$ -wave intensity distribution in the COMPASS  $\eta\pi^-$  data (JAC2018, [70]) are marked by  $\bullet$ . These values and the Breit-Wigner parameters obtained from fits of the COMPASS diffractive  $\pi^-\pi^-\pi^+$  proton-target data (AGH2018, [156]), the diffractive  $\eta^{(\prime)}\pi^-$  data (ADO2015, [101]), the photo-production  $\pi^-\pi^-\pi^+$  data (ADO2014, [255]) (uncertainties are statistical only; see Section 7), and of the diffractive  $\pi^-\pi^-\pi^+$  lead-target data (ALE2010, [181]) are compared with previous measurements. Note that the values from the COMPASS  $\pi^-\pi^-\pi^+$  lead-target data (ALE2010, [181]) are already included in the present PDG averages for the  $3\pi$  decay mode. For the  $a_2(1320)$  width in (b), the PDG provides only an estimate, which is not shown.

$M^\varepsilon = 1^+$ , we obtain the pole parameters  $m_{a_2(1320)} = 1307 \pm 1$  (stat.)  $\pm 6$  (sys.) MeV/c<sup>2</sup> and  $\Gamma_{a_2(1320)} = 111 \pm 1$  (stat.)  $\pm 8$  (sys.) MeV/c<sup>2</sup> [70]. A coupled-channel fit of the  $\eta\pi^-$  and  $\eta'\pi^-$   $P$ - and  $D$ -wave amplitudes with  $M^\varepsilon = 1^+$  yields the pole parameters  $m_{a_2(1320)} = 1306.0 \pm 0.8$  (stat.)  $\pm 1.3$  (sys.) MeV/c<sup>2</sup> and  $\Gamma_{a_2(1320)} = 114.4 \pm 1.6$  (stat.)  $\pm 0.0$  (sys.) MeV/c<sup>2</sup> [71] (see curves in Figs. 65c and 65d). As shown in Fig. 66, the results of the Breit-Wigner fits are in good agreement with the PDG averages. The  $a_2(1320)$  mass values from the pole positions are smaller than the Breit-Wigner masses. The result from Ref. [71] also prefers a larger width compared to the Breit-Wigner parameters.

Based on the Breit-Wigner resonance-model fit to the  $\eta^{(\prime)}\pi^-$  data, we measure the branching-fraction ratio of the  $a_2(1320)$  decays into  $\eta\pi$  and  $\eta'\pi$  [101]:

$$B_{\eta'\pi, \eta\pi}^{a_2} = \frac{\text{BF}[a_2(1320) \rightarrow \eta'\pi]}{\text{BF}[a_2(1320) \rightarrow \eta\pi]} = 0.05 \pm 0.02. \quad (251)$$

This value is consistent with previous measurements [5]. As shown in Fig. 67b, we observe for the first time the decay of the  $a_2(1320)$  into  $f_2(1270)\pi$ , which is a sub-threshold decay and hence suppressed by phase space. The branching-fraction ratio for the decays of the  $a_2(1320)$  into the  $\rho(770)\pi$   $D$  and  $f_2(1270)\pi$   $P$  decay modes with  $M = 1$  is

$$B_{\rho\pi D, f_2\pi P}^{a_2, \text{corr}} = \frac{\text{BF}[a_2(1320)^- \rightarrow \rho(770)\pi]}{\text{BF}[a_2(1320)^- \rightarrow f_2(1270)\pi]} = 16.5^{+1.2}_{-2.4}. \quad (252)$$

This number takes into account the unobserved decays into  $\pi^-\pi^0\pi^0$  via isospin symmetry, the branching fraction of the  $f_2(1270)$  to  $2\pi$  and the effect of the different Bose symmetrizations in the  $\pi^-\pi^-\pi^+$  and  $\pi^-\pi^0\pi^0$  final states (see Section VI.C.2 in Ref. [156] for details).

In the  $\pi^-\pi^-\pi^+$  data, the signal of the first radially excited  $2^{++}$  state, i.e. the  $a_2(1700)$ , is approximately two orders of magnitude smaller than the one of the ground state, i.e. the  $a_2(1320)$ . This is similar to the situation in the  $1^{++}$  sector (see Section 6.3.2). As a consequence, the  $a_2(1700)$  is only included in the resonance-model fit of the much larger proton-target data set. In the  $2^{++}1^+\rho(770)\pi D$  intensity distribution, the  $a_2(1700)$  appears in the lowest  $t'$  bin as a dip at about  $1.7\text{ GeV}/c^2$  due to destructive interference (see Fig. 67a and cf. Fig. 64a). The interference pattern changes with  $t'$  such that the dip disappears with increasing  $t'$  and turns into a subtle shoulder. As shown in Fig. 67b, the  $a_2(1700)$  signal is clearer in the  $2^{++}1^+f_2(1270)\pi P$  intensity distribution, where it appears as a high-mass shoulder of the suppressed  $a_2(1320)$  peak. If the  $a_2(1700)$  component is removed from the fit model, the shoulder cannot be described (see dashed curves in Fig. 67b). Figure 67c shows that the  $t'$  spectrum of the  $a_2(1700)$  is well described by the simple exponential model in Eq. (235) and has a slope parameter of  $7.3^{+2.4}_{-0.9}(\text{GeV}/c)^{-2}$  in the  $\rho(770)\pi$  wave, which is similar to the value of  $7.9 \pm 0.5(\text{GeV}/c)^{-2}$  for the  $a_2(1320)$ .<sup>108</sup> This supports the resonance interpretation of the  $a_2(1700)$  signal. From the 14-wave resonance-model fit, we obtain Breit-Wigner parameters of  $m_{a_2(1700)} = 1681^{+22}_{-35}\text{ MeV}/c^2$  and  $\Gamma_{a_2(1700)} = 436^{+20}_{-16}\text{ MeV}/c^2$  [156]. Whereas our mass value is consistent with the PDG average, our width value is considerably larger and incompatible with the other measurements included in the PDG average (see Fig. 68). This could in part be due to our simplifying model assumptions, which may lead to an overestimation of the  $a_2(1700)$  width. This hypothesis is supported by the results of the resonance-model fits of the  $\eta^{(\prime)}\pi^-$  data using the more advanced analytical models developed by the JPAC collaboration (see Section 5.3.5). In the  $\eta^{(\prime)}\pi^-$  data, the  $a_2(1700)$  appears as a broad high-mass shoulder in the  $D$ -wave intensity distribution. This shoulder is more pronounced in  $\eta'\pi^-$  (see Figs. 65c and 65d). From a fit to the intensity distribution of the  $\eta\pi^- D$  wave with  $M^\varepsilon = 1^+$ , we obtain the pole parameters  $m_{a_2(1700)} = 1720 \pm 10(\text{stat.}) \pm 60(\text{sys.})\text{ MeV}/c^2$  and  $\Gamma_{a_2(1700)} = 280 \pm 10(\text{stat.}) \pm 70(\text{sys.})\text{ MeV}/c^2$  [70]. A coupled-channel fit of the  $\eta\pi^-$  and  $\eta'\pi^- P$ - and  $D$ -wave amplitudes with  $M^\varepsilon = 1^+$  yields the pole parameters  $m_{a_2(1700)} = 1722 \pm 15(\text{stat.}) \pm 67(\text{sys.})\text{ MeV}/c^2$  and  $\Gamma_{a_2(1700)} = 247 \pm 17(\text{stat.}) \pm 63(\text{sys.})\text{ MeV}/c^2$  [71] (see curves in Figs. 65c and 65d). Both pole positions are in agreement with the PDG average.

In the  $\pi^-\pi^-\pi^+$  proton-target data, we observe that the  $a_2(1700)$  decays more often into  $f_2(1270)\pi$  than into  $\rho(770)\pi$ . This is at odds with the result of the L3 experiment, which observed a dominance of the  $\rho(770)\pi$  over the  $f_2(1270)\pi$  decay mode in an analysis of the  $\pi^+\pi^-\pi^0$  final state produced in two-photon collisions [256]. At the moment, we do not have an explanation for this discrepancy and more studies are needed.

### 6.3.5. The $J^{PC} = 2^{-+}$ Sector

The PDG lists currently five isovector states with  $J^{PC} = 2^{-+}$  [5]:  $\pi_2(1670)$ ,  $\pi_2(1880)$ ,  $\pi_2(2005)$ ,  $\pi_2(2100)$ , and  $\pi_2(2285)$  (see also Fig. 3). The latter three states require confirmation: the  $\pi_2(2100)$  is omitted from the summary table, the  $\pi_2(2005)$  and  $\pi_2(2285)$  are listed as “further states”. The  $\pi_2(1670)$  is the  $2^{-+}$  ground state, i.e. the  $1^1D_2$  quark-model state. The  $\pi_2(1880)$  is an established state but its mass is too close to that of the  $\pi_2(1670)$  ground state in order to be the radial excitation of the latter, i.e. the  $2^1D_2$  state. The  $\pi_2(2005)$  or the  $\pi_2(2100)$  would be more plausible candidates for the  $2^1D_2$  quark-model state.

The  $\pi_2(1670)$  decays nearly exclusively into  $3\pi$  with a branching fraction of  $95.8 \pm 1.4\%$  [5]. The dominant  $3\pi$  decay modes are  $f_2(1270)\pi$  with a branching fraction of  $56.3 \pm 3.2\%$  and  $\rho(770)\pi$  with  $31 \pm 4\%$ . Decays into  $[\pi\pi]_S\pi$  have also been observed using different models for the  $\pi\pi$   $S$ -wave [164, 199, 257]. In the  $\pi^-\pi^-\pi^+$  proton-target data, we see clear peaks of the  $\pi_2(1670)$  in three of the four  $2^{-+}$  waves that are included in the 14-wave resonance-model fit, namely in the  $\rho(770)\pi F$  wave and the  $f_2(1270)\pi S$  waves with  $M = 0$  and  $1$  (see Fig. 69). The measured  $\pi_2(1670)$  Breit-Wigner parameters of  $m_{\pi_2(1670)} = 1642^{+12}_{-1}\text{ MeV}/c^2$  and  $\Gamma_{\pi_2(1670)} = 311^{+12}_{-23}\text{ MeV}/c^2$  have comparatively small

<sup>108</sup>Since the  $t'$  dependences of the  $\rho(770)\pi$  and  $f_2(1270)\pi$  amplitudes are constrained by Eq. (227), the slope parameters of  $a_2(1320)$  and  $a_2(1700)$  in the  $f_2(1270)\pi$  wave have nearly identical values.

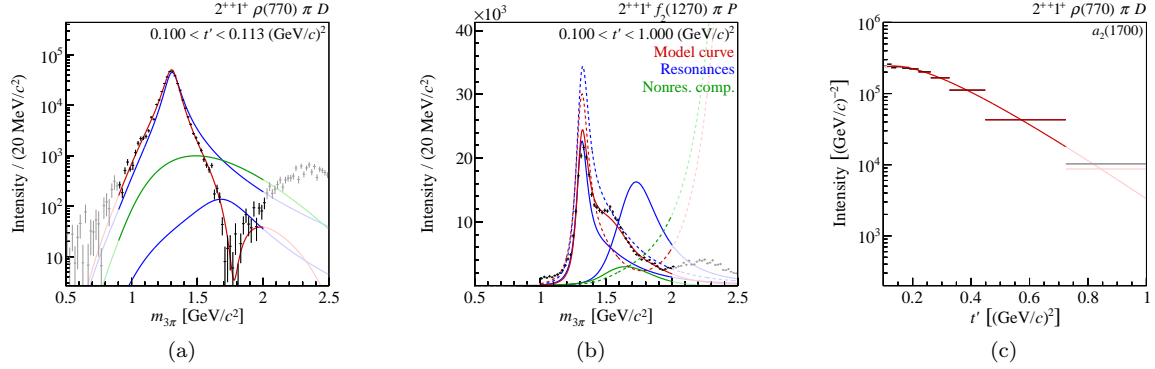


Figure 67: The  $a_2(1700)$  signal in the  $\pi^- \pi^- \pi^+$  proton-target data [156]. (a) Intensity distribution of the  $2^{++} 1^+ \rho(770) \pi D$  wave in the lowest  $t'$  bin (same as Fig. 64a but in log scale). (b) Intensity distribution of the  $2^{++} 1^+ f_2(1270) \pi P$  wave summed over the 11  $t'$  bins. The curves represent the result of the resonance-model fit. The model and the wave components are represented as in Fig. 46 except that the blue curves represent the  $a_2(1320)$  and the  $a_2(1700)$ . In addition to the continuous curves that represent the main resonance-model fit as in (a), the dashed curves in (b) represent the result of a fit, where the  $a_2(1700)$  component is removed from the resonance model. (c) Similar to Fig. 46c, but showing the  $t'$  spectrum of the  $a_2(1700)$  in the  $2^{++} 1^+ \rho(770) \pi D$  wave.

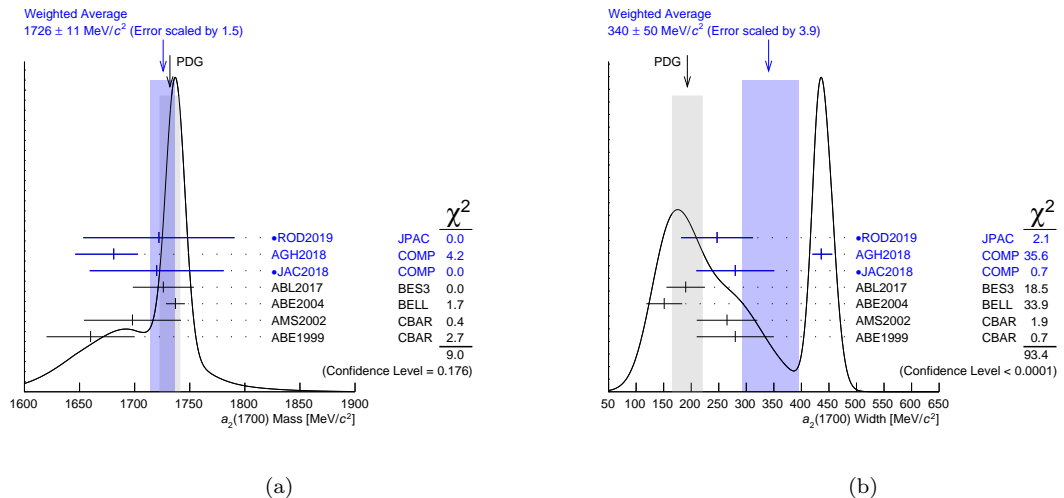


Figure 68: Ideograms similar to the ones in Fig. 48 but for (a) the mass and (b) the width of the  $a_2(1700)$ . The pole parameters obtained from a coupled-channel fit of the COMPASS  $\eta^{(\prime)} \pi^-$  data by the JPAC collaboration (ROD2019, [71]) and from a fit of the  $D$ -wave intensity distribution in the COMPASS  $\eta \pi^-$  data (JAC2018, [70]) are marked by  $\bullet$ . These values and the Breit-Wigner parameters obtained from a fit of the COMPASS  $\pi^- \pi^- \pi^+$  proton-target data (AGH2018, [156]) are compared with previous measurements [5].

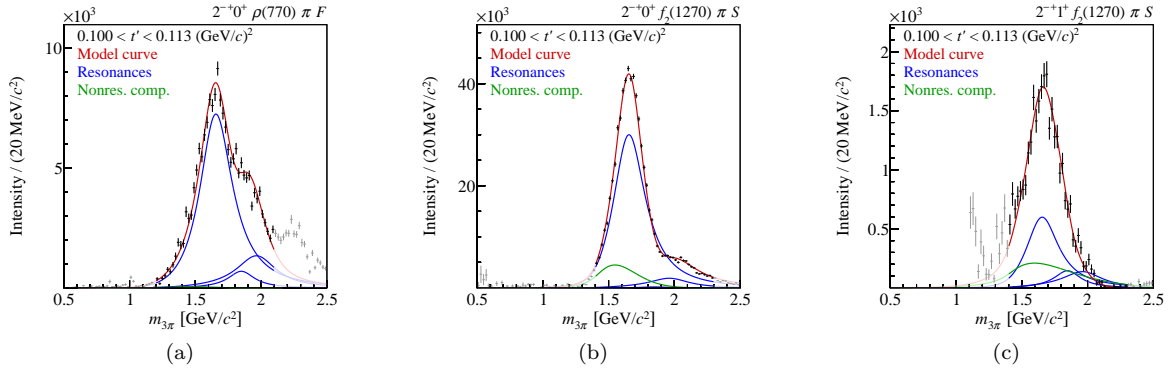


Figure 69: Intensity distributions of (a) the  $2^{-+} 0^+ \rho(770) \pi F$ , (b) the  $2^{-+} 0^+ f_2(1270) \pi S$ , and (c) the  $2^{-+} 1^+ f_2(1270) \pi S$  wave, all in the lowest  $t'$  bin of the  $\pi^- \pi^- \pi^+$  proton-target data [156]. The curves represent the result of the resonance-model fit. The model and the wave components are represented as in Fig. 46, except that the blue curves represent the  $\pi_2(1670)$ ,  $\pi_2(1880)$ , and  $\pi_2(2005)$ . At low  $t'$ , the  $\pi_2(1670)$  is the dominant resonant component in all three waves.

uncertainties [156]. These values are consistent with the Breit-Wigner parameters  $m_{\pi_2(1670)} = 1658 \pm 3$  (stat.)  $\pm 24$  (sys.)  $\text{MeV}/c^2$  and  $\Gamma_{\pi_2(1670)} = 271 \pm 9$  (stat.)  $\pm 24$  (sys.)  $\text{MeV}/c^2$  obtained from the  $\pi^- \pi^- \pi^+$  lead-target data [181]. In the latter analysis, only the  $2^{-+} 0^+ f_2(1270) \pi S$  wave was included in the 6-wave resonance-model fit. As shown in Fig. 70, the  $\pi_2(1670)$  parameters from the lead-target data are in good agreement with the PDG average. Those from the proton-target data are in fair agreement: the mass is somewhat lower, while the width is somewhat larger.

As already mentioned above, the  $\pi_2(1880)$  is peculiar. Not only is its mass too low in order to be the radial excitation of the  $\pi_2(1670)$  ground state, but it also exhibits an unexpected decay pattern. The PDG does not list any  $3\pi$  decay modes and in particular no  $\rho(770)\pi$  decay mode [5]. However, the  $\pi_2(1880)$  is expected to decay into  $3\pi$  because it has been observed in  $f_0(1500)\pi \rightarrow \eta\eta\pi$  [209]. We have studied the  $\pi_2(1880)$  decay modes into  $f_0$  isobars using the freed-isobar PWA method (see Sections 5.2.9 and 6.2.3). Figure 71a shows the correlation of the  $m_{3\pi}$  intensity distribution of the  $2^{-+} 0^+ [\pi\pi]_{0++} \pi D$  wave with the  $m_{\pi^- \pi^+}$  intensity distribution of the freed-isobar amplitude with  $J^{PC} = 0^{++}$ . We observe a clear peak slightly below  $m_{3\pi} = 1.9 \text{ GeV}/c^2$  and at  $m_{\pi^- \pi^+} \approx 1.0 \text{ GeV}/c^2$ . This  $\pi_2(1880)$  peak is also clearly visible in the  $m_{3\pi}$  intensity distribution in the  $f_0(980)$  region that is shown in Fig. 71b. The  $m_{\pi^- \pi^+}$  intensity distribution at the  $\pi_2(1880)$  peak position is shown in Fig. 71d and exhibits a narrow peak of the  $f_0(980)$ . The resonant nature of this peak is confirmed by the corresponding highlighted circular structure in the Argand diagram in Fig. 71e. The Argand diagram exhibits an additional smaller circular structure in the highlighted  $f_0(1500)$  region. This structure corresponds to a small peak at about  $1.5 \text{ GeV}/c^2$  in the  $m_{\pi^- \pi^+}$  intensity distribution shown in Fig. 71d and to a  $\pi_2(1880)$  peak in the  $m_{3\pi}$  intensity distribution shown in Fig. 71c. Our freed-isobar PWA result hence establishes two  $3\pi$  decay modes of the  $\pi_2(1880)$ , namely  $f_0(980)\pi$  and  $f_0(1500)\pi$ .<sup>109</sup> The latter one is consistent with the  $f_0(1500)\pi$  decay mode seen in the  $\eta\eta\pi$  final state [209].

In the 14-wave resonance-model fit, we observe a strong  $\pi_2(1880)$  signal only in the  $2^{-+} 0^+ f_2(1270) \pi D$  wave. In the  $\rho(770)\pi F$  wave and the two  $f_2(1270)\pi S$  waves with  $M = 0$  and  $1$ , the  $\pi_2(1880)$  component is small. The intensity distribution of the  $f_2(1270)\pi D$  wave as shown in Fig. 72a exhibits a peak at about  $1.8 \text{ GeV}/c^2$  that is described mostly by the  $\pi_2(1880)$  component. The non-resonant contribution is small. There is, however, considerable destructive interference of the  $\pi_2(1880)$

<sup>109</sup>Since in the conventional PWA the intensities of the  $2^{-+}$  waves with  $J^{PC} = 0^{++}$  isobars depend on the particular parameterizations chosen for the isobar amplitudes, these waves are not included in the 14-wave resonance-model fit (see also Section VI.D.2 in Ref. [156]).

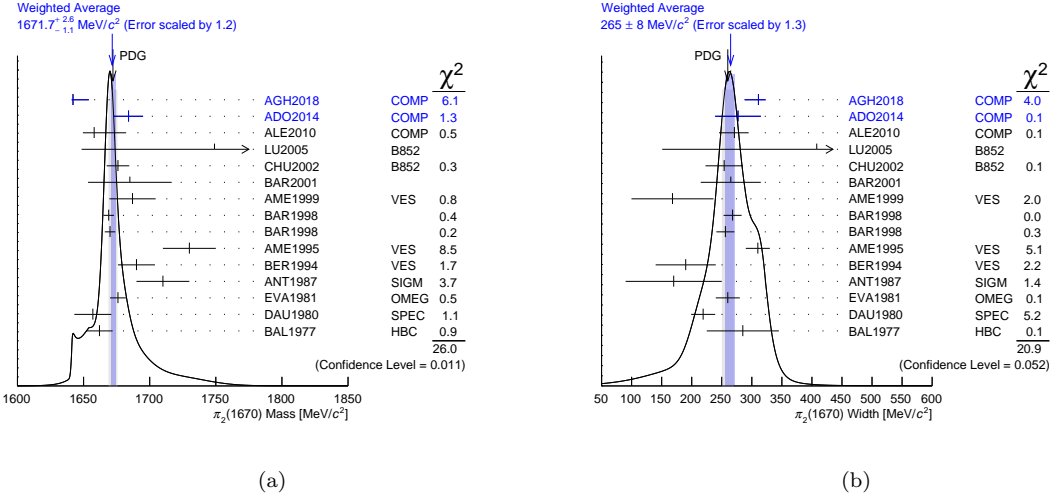


Figure 70: Ideograms similar to the ones in Fig. 48 but for (a) the mass and (b) the width of the  $\pi_2(1670)$ . The Breit-Wigner parameters obtained from fits of the COMPASS diffractive  $\pi^- \pi^- \pi^+$  proton-target (AGH2018, [156]), the photo-production  $\pi^- \pi^- \pi^+$  data (ADO2014, [255]) (uncertainties are statistical only; see Section 7), and diffractive lead-target data (ALE2010, [181]) are compared to previous measurements [5].

with the  $\pi_2(1670)$  and the  $\pi_2(2005)$ . As is shown in Fig. 72b, the peak is associated with a rapid phase motion. In our resonance model, the coupling amplitudes of the  $\pi_2(1880)$  in the three  $2^{-+}$  waves with  $M = 0$  are constrained by Eq. (227). Therefore, the  $t'$  spectra of the  $\pi_2(1880)$  are very similar in these three waves. As an example, Fig. 72c shows the  $t'$  spectrum of the  $\pi_2(1880)$  in the  $2^{-+} 0^+$   $f_2(1270)\pi S$  wave. The distribution is approximately exponential and has a slope parameter value of  $7.8^{+0.5}_{-0.9} (\text{GeV}/c)^{-2}$ , which is typical for resonances. We find  $\pi_2(1880)$  Breit-Wigner parameters of  $m_{\pi_2(1880)} = 1847^{+20}_{-3} \text{ MeV}/c^2$  and  $\Gamma_{\pi_2(1880)} = 246^{+33}_{-28} \text{ MeV}/c^2$  [156]. As is shown in Fig. 73, our values are compatible with the PDG world average [5].

The peculiar properties of the  $\pi_2(1880)$  and the fact that it does not appear in quark-model calculations (see e.g. Fig. 3) suggest that the  $\pi_2(1880)$  could be a supernumerary state. The authors of Refs. [258, 259] propose it as a hybrid candidate. This would be also consistent with the predictions from lattice QCD calculations (see Fig. 7). The authors of Ref. [260] predict for a hybrid meson that the  $f_2(1270)\pi D$ -wave decay would be strongly suppressed with respect to the  $f_2(1270)\pi S$ -wave decay. It is therefore interesting to compare the  $\pi_2(1880)$  signals in the  $2^{-+} 0^+$   $f_2(1270)\pi S$  and  $2^{-+} 0^+$   $f_2(1270)\pi D$  waves. Although the interference of the model components in the  $f_2(1270)\pi D$  wave is strongly model-dependent and hence the  $\pi_2(1880)$  yield not well determined, we can still conclude that the  $\pi_2(1880)$  signal in the  $f_2(1270)\pi D$  wave is enhanced with respect to the one in the  $S$  wave by about an order of magnitude (cf. Figs. 69b and 72a). The decay pattern that we observe in the  $\pi^- \pi^- \pi^+$  final state is hence exactly opposite to the one predicted in Ref. [260] for a hybrid state and challenges the hybrid interpretation of the  $\pi_2(1880)$ .

The  $\pi_2(2005)$  appears as high-mass shoulders in the  $2^{-+} 0^+ \rho(770)\pi F$ ,  $2^{-+} 0^+ f_2(1270)\pi S$ , and  $2^{-+} 0^+ f_2(1270)\pi D$  waves, however, in the latter wave only at high  $t'$  (see Figs. 69a, 69b, and 72a). We also observe phase motions in the  $2 \text{ GeV}/c^2$  mass region (see e.g. Fig. 72b). In the  $\rho(770)\pi F$  and the  $f_2(1270)\pi S$  waves the  $\pi_2(2005)$  component is significantly larger than the  $\pi_2(1880)$  component.

The  $t'$  spectra of the  $\pi_2(2005)$  in the three  $2^{-+}$  waves with  $M = 0$  are constrained by Eq. (227) and hence very similar. We show, as an example, in Fig. 74a the  $t'$  spectrum of the  $\pi_2(2005)$  in the  $2^{-+} 0^+ f_2(1270)\pi S$  wave. It is described well by the exponential model in Eq. (234) with a slope parameter value of  $6.7^{+0.4}_{-1.3} (\text{GeV}/c)^{-2}$  that is in the range typical for resonances. Due to the slightly shallower  $t'$  slope of the  $\pi_2(2005)$  in comparison of the other  $2^{-+}$  wave components, its signal

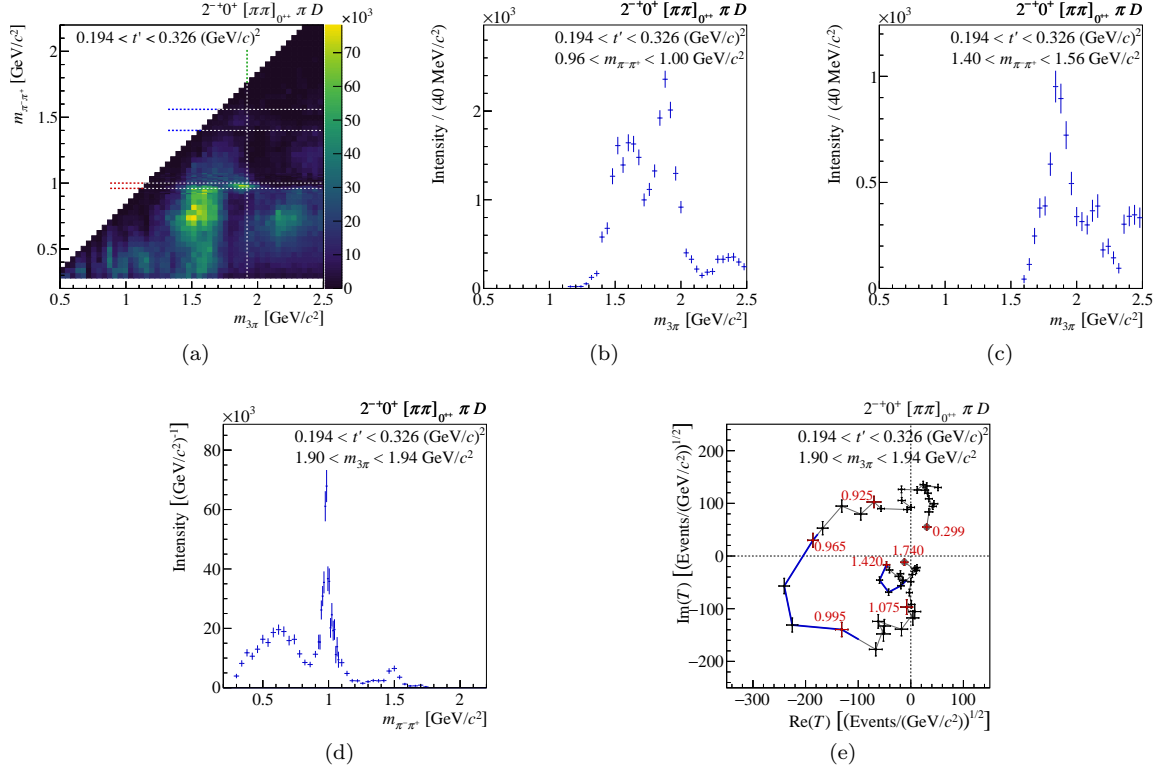


Figure 71: Similar to Fig. 47 but for the  $2^{-+} 0^+ [\pi\pi]_{0++} \pi D$  wave with the freed-isobar amplitude  $[\pi\pi]_{0++}$  in an intermediate  $t'$  bin of the  $\pi^-\pi^-\pi^+$  proton-target data [102]. (a) Intensity of the  $2^{-+} 0^+ [\pi\pi]_{0++} \pi D$  wave as a function of  $m_{\pi^-\pi^+}$  and  $m_{3\pi}$ . (b) and (c): Intensity as a function of  $m_{3\pi}$  summed over the selected  $m_{\pi^-\pi^+}$  intervals around (b) the  $f_0(980)$  and (c) the  $f_0(1500)$  as indicated by the pairs of horizontal dashed lines in (a). (d) and (e): The  $[\pi\pi]_{0++}$  freed-isobar amplitude for the  $m_{3\pi}$  bin at the  $\pi_2(1880)$  mass as indicated by the vertical dashed line in (a). (d) Intensity as a function of  $m_{\pi^-\pi^+}$ . (e) Argand diagram.

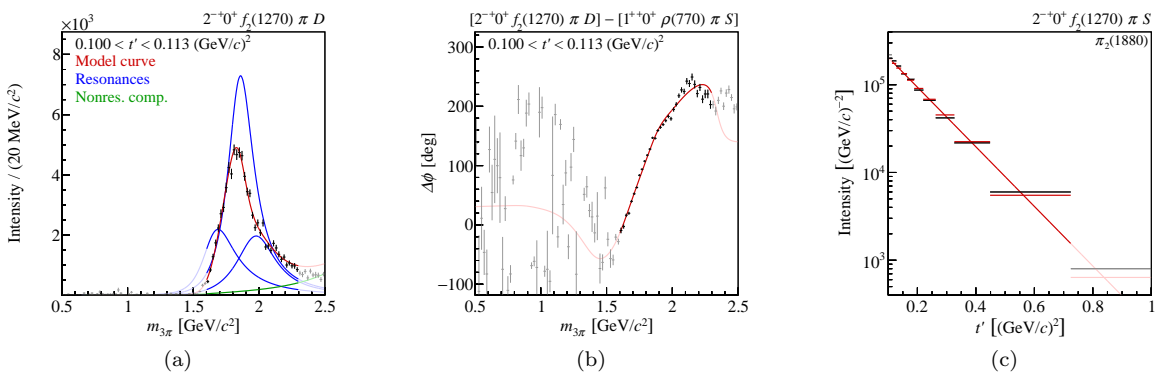


Figure 72: (a) Intensity distribution of the  $2^{-+} 0^+ f_2(1270) \pi D$  wave and (b) phase of this wave with respect to the  $1^{++} 0^+ \rho(770) \pi S$  wave, both in the lowest  $t'$  bin of the  $\pi^-\pi^-\pi^+$  proton-target data [156]. The curves represent the result of the resonance-model fit. The model and the wave components are represented as in Fig. 46 except that the blue curves represent the  $\pi_2(1670)$ ,  $\pi_2(1880)$ , and  $\pi_2(2005)$ . (c) Similar to Fig. 46c, but showing the  $t'$  spectrum of the  $\pi_2(1880)$  in the  $2^{-+} 0^+ f_2(1270) \pi S$  wave.

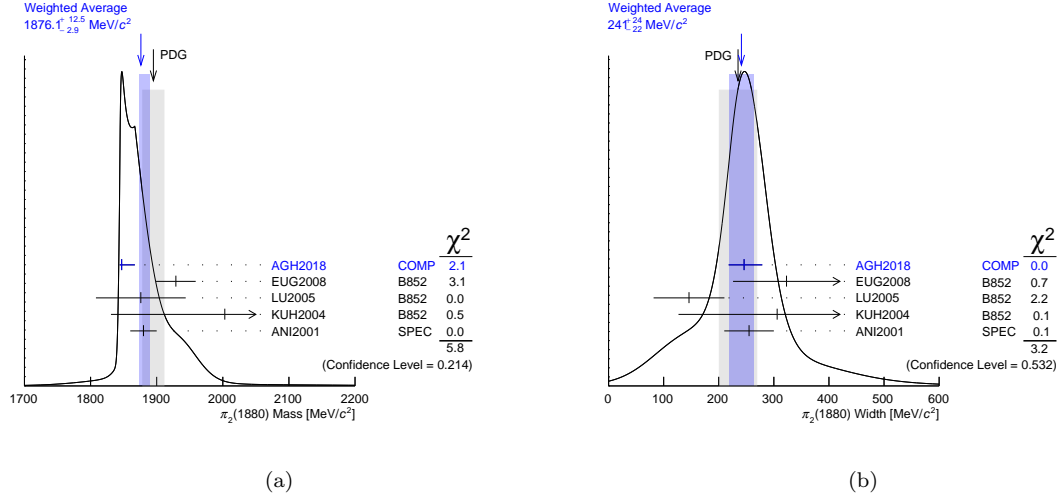


Figure 73: Ideograms similar to the ones in Fig. 48 but for (a) the mass and (b) the width of the  $\pi_2(1880)$ . The Breit-Wigner parameters obtained from a fit of the COMPASS  $\pi^-\pi^-\pi^+$  proton-target data (AGH2018, [156]) are compared to previous measurements [5].

is more pronounced at high  $t'$ . The  $2^{-+} 1^+ f_2(1270) \pi S$  wave is the only  $2^{-+}$  wave in the 14-wave resonance-model fit with  $M = 1$ . Hence in this wave, the  $\pi_2(2005)$  amplitude is not constrained by Eq. (227). Nevertheless, the corresponding  $t'$  spectrum is well described by Eq. (234) with a slope parameter value of  $7.1 \pm 3.5$  (GeV/c)<sup>-2</sup> that is consistent with the ones in the other  $2^{-+}$  waves. The measured  $t'$  spectra hence support the resonance interpretation of the  $\pi_2(2005)$  signal. That the data require a resonance in the 2 GeV/c<sup>2</sup> mass region is verified by comparing the main resonance-model fit with a fit without the  $\pi_2(2005)$  component. In the latter fit, the model describes the intensity distributions and interference terms of the  $2^{-+}$  waves less well, in particular for the  $2^{-+} 0^+ f_2(1270) \pi S$  and  $2^{-+} 0^+ f_2(1270) \pi D$  waves. Figure 74c shows, for example, that the high mass-shoulder in the  $2^{-+} 0^+ f_2(1270) \pi S$  intensity distributions is not reproduced well. In addition the  $\pi_2(1880)$  becomes 20 MeV/c<sup>2</sup> lighter and 100 MeV/c<sup>2</sup> wider, which would be in tension with previous measurements.

We find  $\pi_2(2005)$  Breit-Wigner parameters of  $m_{\pi_2(2005)} = 1962 \pm 17$  MeV/c<sup>2</sup> and  $\Gamma_{\pi_2(2005)} = 371 \pm 16$  MeV/c<sup>2</sup> [156] that are consistent with the results of previous measurements [238, 261, 262]. Our  $\pi_2(2005)$  signal could be related to the  $\pi_2(2100)$  that has a similar mass but a larger width of  $625 \pm 50$  MeV/c<sup>2</sup> [5]. The  $\pi_2(2100)$  PDG entry is based on two observations in diffractively produced  $\pi^-\pi^-\pi^+$  reported by the ACCMOR [164] and the VES experiments [175]. For both analyses, the set of  $2^{-+}$  waves that were included in the resonance-model fit differs from our choice. In addition, the resonance model was based on a  $K$ -matrix approach.<sup>110</sup> A potential caveat of our resonance model that might affect our measurement of the  $\pi_2$  resonance parameters is that the three  $\pi_2$  resonances have considerable overlap. As a consequence, our sum-of-Breit-Wigner ansatz might not be a good approximation anymore. Applying more advanced models is the topic of future research [177, 178, 263]. However, first studies also find three  $\pi_2$  resonance poles in the analyzed mass region and seem to confirm the findings from our Breit-Wigner analysis at least qualitatively.

### 6.3.6. The $J^{PC} = 4^{++}$ Sector

The  $a_4(2040)$  and the  $a_4(2255)$  are the only isovector states with  $J^{PC} = 4^{++}$  that are listed by the PDG [5] (see also Fig. 3). The latter is listed as a “further state” and requires confirmation. The

<sup>110</sup>A more detailed comparison of the ACCMOR and VES analyses with our approach can be found in Ref. [156].

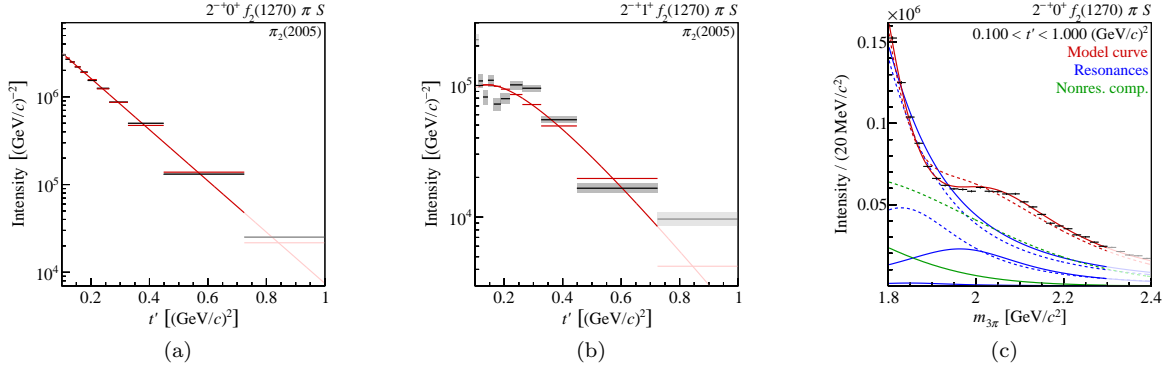


Figure 74: (a) and (b): Similar to Fig. 46c, but showing the  $t'$  spectra of the  $\pi_2(2005)$  in the  $2^{-+} 0^+ f_2(1270) \pi S$  and  $2^{-+} 1^+ f_2(1270) \pi S$  waves. (c) Zoomed view of the intensity distribution of the  $2^{-+} 0^+ f_2(1270) \pi S$  wave summed over the analyzed  $t'$  range. The curves represent the result of two resonance-model fits. The model and the wave components are represented as in Fig. 46 except that the blue curves represent the  $\pi_2(1670)$ ,  $\pi_2(1880)$ , and  $\pi_2(2005)$ . The result of the main resonance-model fit is represented by the continuous curves. The dashed curves represent the result of a fit, where the  $\pi_2(2005)$  component is removed from the resonance model. From Ref. [156].

$a_4(2040)$  is known to decay into all final states considered here, i.e. into  $\eta^{(\prime)}\pi$  and  $3\pi$ . However, the branching fractions for these decay modes are still unknown.

In the  $\pi^-\pi^-\pi^+$  proton-target data, we observe clear signals of the  $a_4(2040)$  in the  $4^{++} 1^+ \rho(770) \pi G$  and  $4^{++} 1^+ f_2(1270) \pi F$  waves, which are well described by the resonance model (see Figs. 75a and 75b). Figure 75c shows the  $t'$  spectrum of the  $a_4(2040)$  in the  $f_2(1270)\pi$  wave. The simple exponential model in Eq. (235) is in fair agreement with the data and yields a slope parameter value of  $9.2^{+0.8}_{-0.5} (\text{GeV}/c)^{-2}$ , which is larger than for most of the other resonances in the fit. Due to the constraint in Eq. (227), the  $t'$  spectrum of the  $a_4(2040)$  in the  $\rho(770)\pi$  wave is practically identical. We obtain Breit-Wigner parameters of  $m_{a_4(2040)} = 1935^{+11}_{-13} \text{ MeV}/c^2$  and  $\Gamma_{a_4(2040)} = 333^{+16}_{-21} \text{ MeV}/c^2$  [156]. This is the most precise measurement of the  $a_4(2040)$  parameters so far. As shown in Fig. 76, this result is in agreement with the Breit-Wigner parameters  $m_{a_4(2040)} = 1885 \pm 11 \text{ (stat.)}^{+50}_{-2} \text{ (sys.)} \text{ MeV}/c^2$  and  $\Gamma_{a_4(2040)} = 294 \pm 25 \text{ (stat.)}^{+46}_{-19} \text{ (sys.)} \text{ MeV}/c^2$  from our 6-wave resonance-model fit of the  $\pi^-\pi^-\pi^+$  lead-target data, where only the  $\rho(770)\pi$  wave was included in the fit.

In the  $\eta\pi^-$  data, the  $a_4(2040)$  appears in the intensity distribution of the  $G$  wave with  $M^\varepsilon = 1^+$  as a broad peak below  $2 \text{ GeV}/c^2$  (see Fig. 77a). In addition, the data exhibit a broad high-mass shoulder. The  $G$ -wave intensity distribution is contaminated by leakage of the order of 3% from the dominant  $a_2(1320)$  in the  $D$  wave (gray data points in Fig. 77a). This contamination is, however, well separated from the  $a_4(2040)$  region. The intensity distribution of the  $\eta'\pi^-$   $G$  wave with  $M^\varepsilon = 1^+$  is qualitatively similar to that of the  $\eta\pi^-$   $G$  wave (see black dots in Fig. 77b). It exhibits a peak consistent with the  $a_4(2040)$  that is, however, a bit broader and shifted toward higher masses. The high-mass shoulder is more pronounced. Figure 77b shows that after scaling of the  $\eta\pi^-$  intensity distribution with the kinematic factor in Eq. (248) (red triangles), the two  $G$ -wave intensity distributions become nearly identical. In particular the leakage from the  $a_2(1320)$  is completely suppressed by the angular-momentum barrier factor in Eq. (248). Also the phases between the  $D$ - and  $G$ -wave amplitudes exhibit a striking similarity in  $\eta\pi^-$  and  $\eta'\pi^-$ , as shown in Fig. 77c. For both final states, the  $a_4(2040)$  resonance produces a slow rise of the phase around  $2.0 \text{ GeV}/c^2$ . A combined resonance-model fit of the  $\eta\pi^-$  and  $\eta'\pi^-$  data yields Breit-Wigner parameters of  $m_{a_4(2040)} = 1900^{+80}_{-20} \text{ MeV}/c^2$  and  $\Gamma_{a_4(2040)} = 300^{+80}_{-100} \text{ MeV}/c^2$  [101], which are consistent with the parameters obtained from the COMPASS  $\pi^-\pi^-\pi^+$  data.

Figure 76 shows that, compared to the PDG average, the COMPASS data prefer a lighter and wider  $a_4(2040)$ . This is particularly apparent for the parameter values from the  $\pi^-\pi^-\pi^+$  proton-

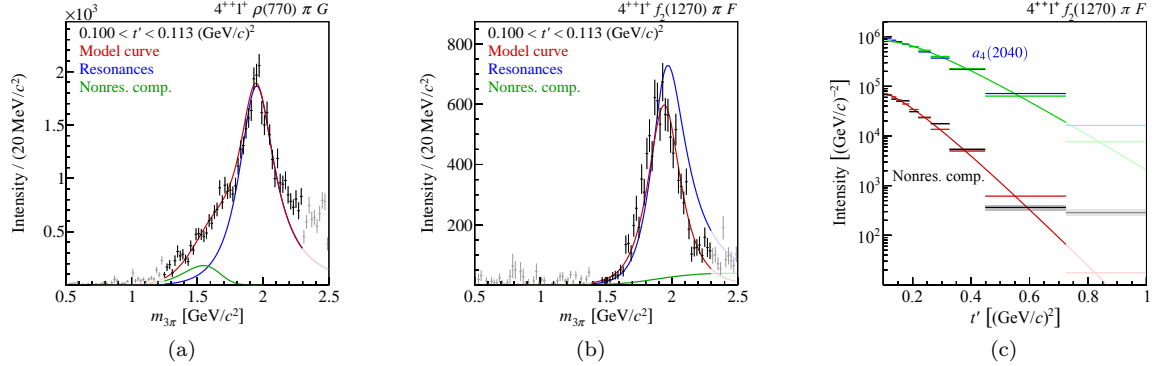


Figure 75: Intensity distributions of (a) the  $4^{++} 1^+ \rho(770) \pi G$  and (b) the  $4^{++} 1^+ f_2(1270) \pi F$  waves in the lowest  $t'$  bin of the  $\pi^- \pi^- \pi^+$  proton-target data [156]. The curves represent the result of the resonance-model fit. The model and the wave components are represented as in Fig. 46 except that the blue curve represents the  $a_4(2040)$ . (c) Similar to Fig. 46c, but showing the  $t'$  spectrum of the  $a_4(2040)$  (blue lines and light blue boxes) and the non-resonant component (black lines and gray boxes) in the  $4^{++} 1^+ f_2(1270) \pi F$  wave.

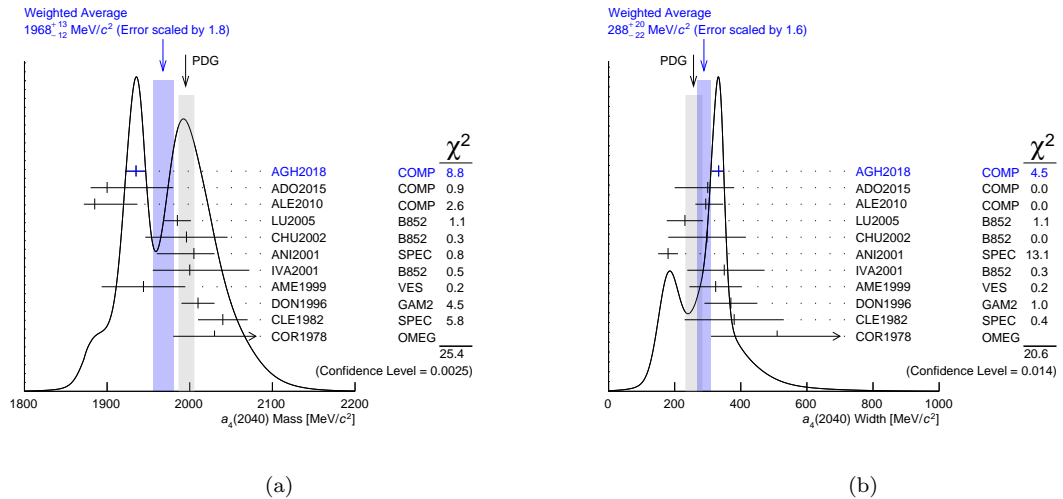


Figure 76: Ideograms similar to the ones in Fig. 48 but for (a) the mass and (b) the width of the  $a_4(2040)$ . The Breit-Wigner parameters obtained from fits of the COMPASS  $\pi^- \pi^- \pi^+$  proton-target data (AGH2018, [156]), the  $\eta^{(\prime)} \pi^-$  data (ADO2015, [101]), and the  $\pi^- \pi^- \pi^+$  lead-target data (ALE2010, [181]) are compared to previous measurements [5].

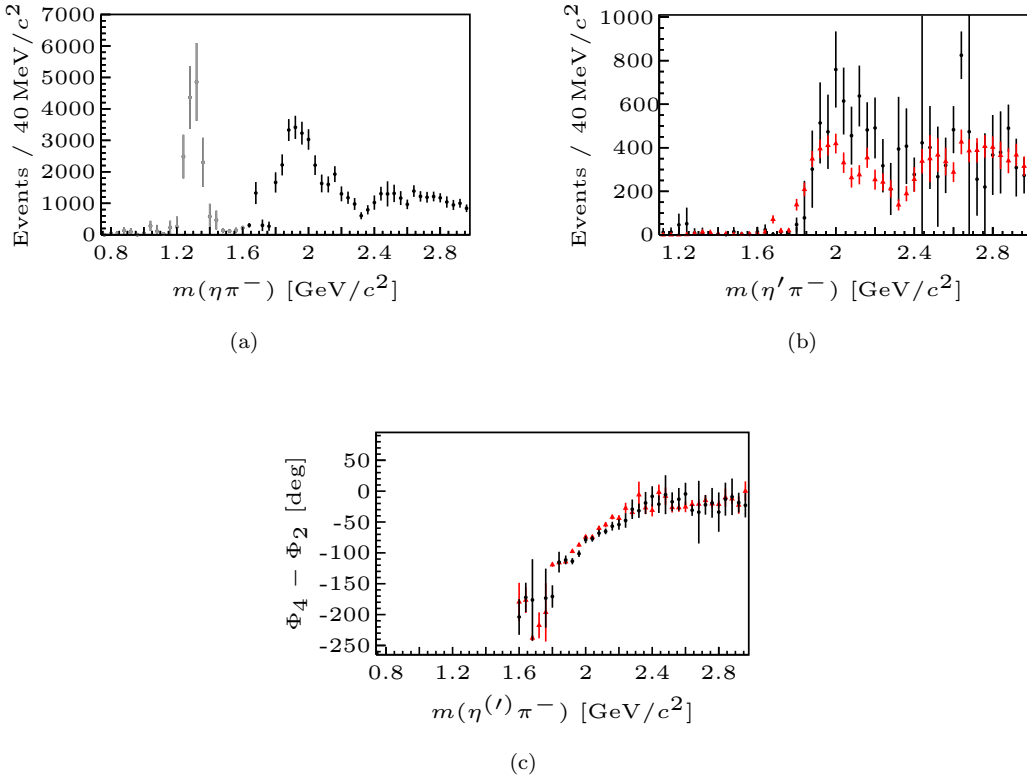


Figure 77: Intensities of the  $G$  wave with  $M^\varepsilon = 1^+$  (a) in the  $\eta\pi^-$  and (b) in the  $\eta'\pi^-$  COMPASS data (black dots) [101]. The gray data points for  $m_{\eta\pi^-} \leq 1.6 \text{ GeV}/c^2$  in (a) indicate leakage from the  $\eta\pi^-$   $D$  wave with  $M^\varepsilon = 1^+$  (cf. Fig. 65c). The red triangles in (b) show the  $\eta\pi^-$  intensity from (a) scaled by the kinematic factor in Eq. (248). (c) Phases of the  $G$  wave relative to the  $M^\varepsilon = 1^+$   $D$  wave in  $\eta\pi^-$  (red triangles) and  $\eta'\pi^-$  (black dots).

target data, where we find the  $a_4(2040)$  mass to be  $60\text{ MeV}/c^2$  smaller and the width  $76\text{ MeV}/c^2$  larger. The latter is in tension only with the extremely low width value of  $180 \pm 30\text{ MeV}/c^2$  reported by the authors of Ref. [262], our mass values, however, are lower than any of the other mass values included in the PDG average.

Based on the Breit-Wigner resonance-model fit to the  $\eta^{(\prime)}\pi^-$  data, we measure the branching-fraction ratio of the  $a_4(2040)$  decays into  $\eta\pi$  and  $\eta'\pi$  [101]:

$$B_{\eta'\pi, \eta\pi}^{a_4} = \frac{\text{BF}[a_4(2040) \rightarrow \eta'\pi]}{\text{BF}[a_4(2040) \rightarrow \eta\pi]} = 0.23 \pm 0.07. \quad (253)$$

This constitutes the first measurement of this quantity. From the  $\pi^-\pi^-\pi^+$  proton-target data, we obtain a branching-fraction ratio for the decays of the  $a_4(2040)$  into the  $\rho(770)\pi$   $G$  and  $f_2(1270)\pi$   $F$  modes with  $M = 1$ :

$$B_{\rho\pi G, f_2\pi F}^{a_4, \text{corr}} = \frac{\text{BF}[a_4(2040)^- \rightarrow \rho(770)\pi]}{\text{BF}[a_4(2040)^- \rightarrow f_2(1270)\pi]} = 2.9^{+0.6}_{-0.4}. \quad (254)$$

This number takes into account the unobserved decays into  $\pi^-\pi^0\pi^0$  via isospin symmetry, the branching fraction of the  $f_2(1270)$  to  $2\pi$  and the effect of the different Bose symmetrizations in the  $\pi^-\pi^-\pi^+$  and  $\pi^-\pi^0\pi^0$  final states (see Section VI.B.2 in Ref. [156] for details). Our value is in good agreement with the value of 3.3 predicted by the  ${}^3P_0$  decay model [259]. This model describes the decay of  $q\bar{q}$  states into  $(q\bar{q}')(q'\bar{q})$  meson pairs via production of a  $q'\bar{q}'$  pair with vacuum quantum numbers, i.e.  $J^{PC} = 0^{++}$ .

## 7. Primakoff Production of $\pi^-\pi^-\pi^+$

As was discussed in Section 4.1, high-energy scattering reactions such as

$$\pi + A \rightarrow 3\pi + A , \quad (255)$$

where a beam pion interacts coherently with a target nucleus with mass number  $A$  and dissociates into  $3\pi$ , are dominated by diffraction, i.e. Pomeron exchange, at low reduced four-momentum transfer squared  $t'$ . The differential cross section  $d\sigma/dt'$  follows approximately an exponential distribution  $e^{-bt'}$  (see Eq. (132)), which corresponds to a dominant contribution from spin projection  $M = 0$ . For heavy nuclei, the slope parameter  $b$  is related to the geometrical size of the nucleus, i.e.  $b \propto R^2$ , where  $R \propto A^{1/3}$  is the nuclear radius. The cross section integrated over  $t'$  from 0 to the first diffractive minimum is approximately proportional to  $A^{2/3}$ , i.e. to the surface of the nucleus. The features of diffractive-dissociation reactions described above were, for example, studied by the FNAL E272 experiment with a 200 GeV/c pion beam impinging on C, Al, Cu, and Pb targets [264].

In addition to diffractive production, i.e. Pomeron exchange between the incoming beam particle and the target nucleus, also photon exchange is possible (see Fig. 78 in Section 4.1). Such a reaction is called Coulomb or Primakoff production. Primakoff production is described theoretically using the Weizsäcker-Williams equivalent-photon approximation, which assumes that ultra-relativistic, i.e. quasi-stable, beam pions scatter off quasi-real photons of the electromagnetic field of the heavy target nucleus [265, 266]. The equivalent-photon approximation relates the cross section  $\sigma_{\pi A}$  for the experimentally observed process (255) to the cross section  $\sigma_{\pi\gamma}$  for the process  $\pi + \gamma \rightarrow 3\pi$  [267–269]:

$$\frac{d\sigma_{\pi A}}{dm_{3\pi}^2 dt' d\Phi_3} = \frac{\alpha_{\text{em}} Z^2}{\pi} \frac{1}{m_{3\pi}^2 - m_\pi^2} \frac{t'}{(t' + |t|_{\min})^2} |F_{\text{eff}}(t', |t|_{\min})|^2 \frac{d\sigma_{\pi\gamma}(m_{3\pi})}{d\Phi_3} . \quad (256)$$

Here,  $m_{3\pi}$  is the invariant mass of the  $3\pi$  system, which is equal to the center-of-momentum energy of the pion-photon system,  $d\Phi_3$  is the differential phase-space element of the  $3\pi$  final state as defined in Eq. (41),  $t'$  and  $|t|_{\min}$  are defined by Eqs. (52) and (53). The fine-structure constant is denoted by  $\alpha_{\text{em}}$ ,  $Z$  is the charge number of the nucleus, and  $F_{\text{eff}}(t', |t|_{\min})$  is the electromagnetic nuclear form factor specific to  $\pi^-$ - $A$  scattering. This form factor accounts not only for the charge distribution in the nucleus but also for the distortion of the pion wave function in the Coulomb field and depends on  $t'$  and  $|t|_{\min}$  [255, 270, 271].

The cross section for Primakoff processes grows with the charge number as  $Z^2$ , while the diffractive cross section grows with the mass number as  $A^{2/3}$ . As a consequence, Primakoff processes are enhanced on heavy target nuclei. The different  $A$  and  $Z$  dependence of the Primakoff and the diffractive cross sections also provides a handle to separate the two mechanisms.

The FNAL E272 experiment first observed Primakoff production of  $3\pi$  final states off heavy nuclear targets [264]. The signature was a sharp peak in the  $t'$  spectrum toward  $t' = 0$  on top of an exponential distribution from coherent diffraction events. Later, a partial-wave analysis was performed to study the Primakoff production of  $a_2(1320)$  and  $a_1(1260)$  [272]. A much larger data sample of  $3\pi$  events was acquired by the FNAL E781 (SELEX) experiment using a 600 GeV/c pion beam on Cu and

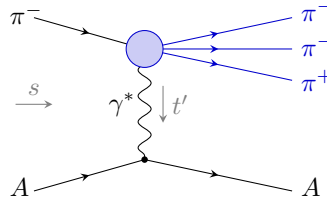


Figure 78: Diagram for pion-induced  $3\pi$  production on a target nucleus via photon exchange.

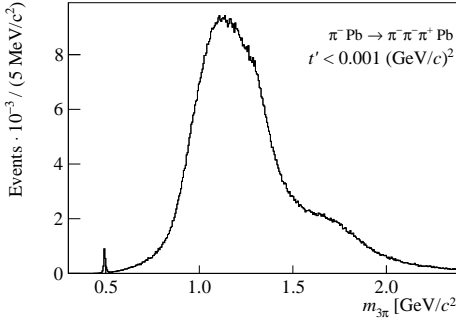


Figure 79: Invariant mass spectrum (not acceptance corrected) of  $\pi^- \pi^- \pi^+$  events produced in the reaction  $\pi^- + \text{Pb} \rightarrow \pi^- \pi^- \pi^+ + \text{Pb}$  with  $t' < 10^{-3} (\text{GeV}/c)^2$  [255]. The sharp peak below  $0.5 \text{ GeV}/c^2$  originates from in-flight decays of beam kaons into  $\pi^- \pi^- \pi^+$ .

Pb targets [273]. They measured the radiative width  $\Gamma[a_2(1320) \rightarrow \pi\gamma]$ . To separate Primakoff production of  $a_2(1320)$  from diffractive production, a statistical subtraction method was applied.

The COMPASS experiment has collected a data sample of about  $10^6$  events for the reaction  $\pi^- + \text{Pb} \rightarrow \pi^- \pi^- \pi^+ + \text{Pb}$  in the kinematic region  $t' < 10^{-3} (\text{GeV}/c)^2$ , i.e. in the Primakoff region [255]. The  $\pi^- \pi^- \pi^+$  invariant mass spectrum of these events is shown in Fig. 79, where the main contributions from diffractive production of the  $a_1(1260)$  and  $\pi_2(1670)$  resonances are visible.

### 7.1. Extraction of Primakoff Process via $t'$ Spectrum

The  $t'$  spectrum of diffractively produced  $3\pi$  states with spin projection  $M$  is given by (cf. Eqs. (132) and (235))

$$\frac{dN_{\text{diff}}}{dt'} \propto (t')^{|M|} e^{-b_{\text{diff}}(m_{3\pi}) t'} . \quad (257)$$

Due to the  $(t')^{|M|}$  factor, diffractive production of states with  $|M| > 0$  becomes negligible at sufficiently low  $t'$  so that only states with  $M = 0$  remain. This is in contrast to quasi-real photoproduction, where only states with  $|M| = 1$  are produced because for quasi-real photons the state with helicity 0 is suppressed due to the very small virtuality (see e.g. Ref. [274]).

Figure 80a shows the  $t'$  spectrum in the analyzed range  $0.42 < m_{3\pi} < 2.50 \text{ GeV}/c^2$  and provides first insights into the Primakoff production of  $\pi^- \pi^- \pi^+$  states. Two production mechanisms, diffraction and Primakoff production, are assumed to be present at low  $t'$ . In the region  $t' < 6 \cdot 10^{-3} (\text{GeV}/c)^2$ , the  $t'$  spectrum can be fitted well by a sum of two exponentials, i.e.

$$\frac{dN_{\pi A}}{dt'} = \frac{dN_{\text{diff}}}{dt'} + \frac{dN_{\text{Prim}}}{dt'} \quad \text{with} \quad \frac{dN_{\text{diff}}}{dt'} \propto e^{-b_{\text{diff}}(m_{3\pi}) t'} \quad \text{and} \quad \frac{dN_{\text{Prim}}}{dt'} \propto e^{-b_{\text{Prim}}(m_{3\pi}) t'} , \quad (258)$$

which is shown as the black curve in Fig. 80a. The shallower slope of  $b_{\text{diff}} \approx 400 (\text{GeV}/c)^{-2}$  corresponds to coherent diffractive production (red points in Fig. 80a), while the much steeper slope of  $b_{\text{Prim}} \approx 1500 (\text{GeV}/c)^{-2}$  corresponds to Primakoff production.

According to Eq. (256) the theoretical  $t'$  spectrum for Primakoff production peaks at  $|t|_{\min}$  and vanishes at  $t' = 0$ . The measured  $t'$  spectrum is, however, modified significantly by experimental resolution. To obtain parameterizations of the smeared Primakoff  $t'$  spectrum, we performed dedicated Monte Carlo (MC) simulations. In the Primakoff region  $t' < 10^{-3} (\text{GeV}/c)^2$ , the reconstructed Primakoff MC events approximately follow an exponential distribution, i.e.  $dN_{\text{Prim, MC}}/dt' \propto e^{-b_{\text{Prim, MC}}(m_{3\pi}) t'}$ . This indicates that the dip at  $t' = 0$  is fully smeared out due to resolution effects.

<sup>111</sup>Figures 80a and 80b are unpublished auxiliary plots from the analysis presented in Ref. [255].

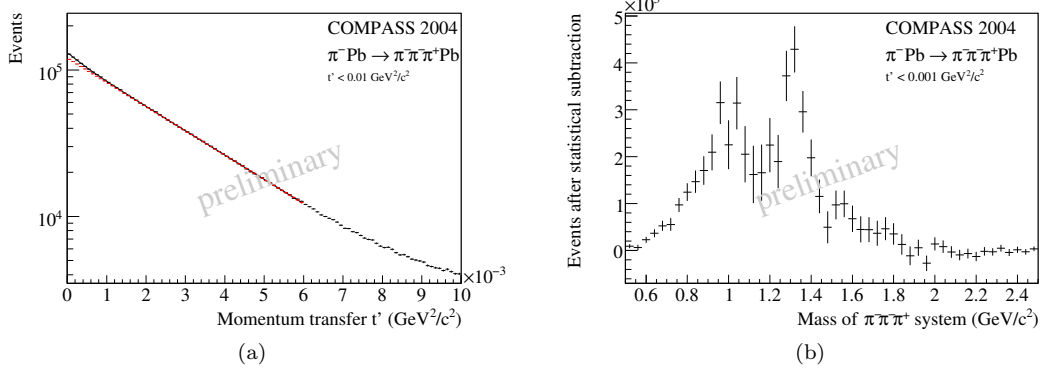


Figure 80: (a) Measured  $t'$  spectrum for the reaction  $\pi^- + \text{Pb} \rightarrow \pi^- \pi^- \pi^+ + \text{Pb}$  in the analyzed range  $0.42 < m_{3\pi} < 2.50 \text{ GeV}/c^2$  (black points) [252]. The black curve represents the result of a fit of Eq. (258). The red points represent the diffractive component in the fit model. (b)  $m_{3\pi}$  distribution of the Primakoff component (not acceptance corrected) obtained by fitting the  $t'$  spectrum in each  $40 \text{ MeV}/c^2$  wide  $m_{3\pi}$  bin with Eqs. (258) and (260) (see text) [275, 276].<sup>111</sup>

The slope parameter changes with  $m_{3\pi}$  from  $b_{\text{Prim, MC}}(m_{3\pi} = 0.5 \text{ GeV}/c^2) \approx 1500 (\text{GeV}/c)^{-2}$  to  $b_{\text{Prim, MC}}(m_{3\pi} = 2.5 \text{ GeV}/c^2) \approx 700 (\text{GeV}/c)^{-2}$ . The flattening of the reconstructed MC  $t'$  spectrum with increasing  $m_{3\pi}$  is mainly due to the increase of  $|t|_{\min}$  with  $m_{3\pi}$ . The  $m_{3\pi}$  dependence of the Primakoff slope parameter is parameterized by

$$b_{\text{Prim, MC}}(m_{3\pi}) = 2108.0 (\text{GeV}/c)^{-2} - 812.1 \text{ GeV}^{-3}/c^{-4} m_{3\pi} + 46.4 \text{ GeV}^{-4}/c^{-6} m_{3\pi}^2. \quad (259)$$

In order to separate the small Primakoff contribution from the dominant diffractive background, a fitting range of  $t' < 6 \cdot 10^{-3} (\text{GeV}/c)^2$  is needed, which extends beyond the Primakoff region. It turns out that in this extended  $t'$  range the reconstructed Primakoff MC  $t'$  spectrum cannot be well described anymore by an exponential distribution. Instead, the empirical formula

$$\frac{dN_{\text{Prim, MC}}}{dt'} \propto \frac{A(m_{3\pi})}{[t' + P(m_{3\pi})]^{3.9}} \quad (260)$$

is used, where  $A(m_{3\pi})$  is a normalization parameter and  $P(m_{3\pi})$  is a fifth-order polynomial.

We fit a modified version of Eq. (258) to the measured  $t'$  spectra in  $40 \text{ MeV}/c^2$  wide  $m_{3\pi}$  bins, where we replace the exponential distribution for the Primakoff component with Eq. (260) with the parameters fixed to the values from the Primakoff MC. These fits of the measured data yield the contributions of diffractive and Primakoff production and the slope parameter  $b_{\text{diff}}$  of the diffractive component as functions of  $m_{3\pi}$ . A significant variation of the diffractive slope parameter is observed. It falls monotonically from  $b_{\text{diff}}(m_{3\pi} = 0.5 \text{ GeV}/c^2) \approx 400 (\text{GeV}/c)^{-2}$  to  $b_{\text{diff}}(m_{3\pi} = 2.5 \text{ GeV}/c^2) \approx 300 (\text{GeV}/c)^{-2}$ . The explicit  $m_{3\pi}$  dependence is parameterized by

$$b_{\text{diff}}(m_{3\pi}) = 456 (\text{GeV}/c)^{-2} - 72 \text{ GeV}^{-3}/c^{-4} m_{3\pi} + 6 \text{ GeV}^{-4}/c^{-6} m_{3\pi}^2. \quad (261)$$

The extracted Primakoff intensity integrated over  $t' < 10^{-3} (\text{GeV}/c)^2$  is shown as a function of  $m_{3\pi}$  in Fig. 80b. The intensity distribution shows a clear peak at  $1.3 \text{ GeV}/c^2$ , stemming from Primakoff-produced  $a_2(1320)$ . We do not observe clear signals of  $a_1(1260)$  or  $\pi_2(1670)$ . The intensity from  $3\pi$  threshold to about  $1.1 \text{ GeV}/c^2$  is dominated by non-resonant low-energy processes. These processes are calculable in the framework of Chiral Perturbation Theory (see Section 3.4) and will be discussed in Section 7.5.

## 7.2. Model for Partial-Wave Decomposition in the Primakoff Kinematical Region

Compared to the statistical subtraction method based on the  $t'$  spectrum (see Section 7.1), partial-wave analysis techniques are a much more powerful tool to separate Primakoff and diffractive contributions because they exploit the full information contained in the multi-dimensional distribution of the  $3\pi$  phase-space variables. A number of special features of photoproduction and of the analyzed Primakoff region  $t' < 10^{-3} (\text{GeV}/c)^2$  require modifications of the PWA model that was derived in Sections 5.1, 5.2, and 6.2.3. Both Pomeron and photon have positive naturality (see Section 2.1.1). A PWA of diffractive  $\pi^-\pi^-\pi^+$  production on a lead target in the range  $10^{-3} < t' < 10^{-2} (\text{GeV}/c)^2$  [277], showed that contributions from unnatural exchanges have negligibly small contributions, which is consistent with the expected Pomeron dominance at high energies (see Section 4.1). We therefore include only waves with positive reflectivity (see Section 5.2.3) in the PWA model. As was discussed in Section 7.1, in the analyzed  $t'$  range the spin-projection quantum number of diffractively produced states is limited to  $M = 0$ , while states produced by quasi-real photon exchange have  $M = 1$ .<sup>112</sup> For both production processes, the scattering is coherent, i.e. the beam pion interacts with the target nucleus as a whole. Therefore, the total amplitude for reaction (255) is the coherent sum of the amplitudes for the two production processes and hence a rank-1 spin-density matrix (see Section 5.2.2) is used. Based on the model for the intensity distribution in Eq. (195), our ansatz for the Primakoff PWA model is<sup>113</sup>

$$\mathcal{I}(\tau_3; m_{3\pi}, t') = \left| \sum_i^{N_{\text{waves}}} \mathcal{T}_i(m_{3\pi}, t') \Psi_i(\tau_3; m_{3\pi}) \right|^2 + |\mathcal{T}_{\text{flat}}(m_{3\pi}, t')|^2. \quad (262)$$

At low  $t'$ , detector resolution effects play an important role. They significantly affect the measured  $t'$  spectra (see Section 7.1) and also the production plane defined by the incoming pion and the intermediate state  $X$  is only poorly reconstructed because of the very small scattering angle of  $X$ . As was explained in Section 5.2.5, we construct from the model in Eq. (262) the probability density function in Eq. (199) that describes the  $\tau_3$  distribution for given values of  $m_{3\pi}$  and  $t'$ . This function takes into account the acceptance of the detector but neglects smearing of the phase-space variables  $\tau_3$  due to detector resolution. Taking resolution effects into account would require to convolve the theoretical model with a smearing function as in Eq. (200), where this function describes the experimental resolution in the whole phase space. Such a convolution approach is computationally very expensive. We thus use a different approach, where we modify the PWA model such that we take into account resolution effects in an effective way.

Due to the significant smearing of  $t'$  and the limited size of the data sample, we do not perform the PWA in narrow  $m_{3\pi}$  and  $t'$  bins as was described in Section 5.2. Instead, we model the explicit  $t'$  dependence of the transition amplitudes  $\mathcal{T}_i(m_{3\pi}, t')$  in Eq. (262) in the analyzed  $t'$  range using the same approach as for the analysis of  $\pi^-\pi^-\pi^+$  diffractive production on a lead target that was discussed in Section 6.2.3. Following Eq. (249), we factorize the  $m_{3\pi}$  and the  $t'$  dependence of the transition amplitudes by introducing real-valued functions  $f_i(t')$ . For diffractively produced waves, which all have  $M = 0$ , the  $t'$  dependence of the transition amplitudes is parameterized by

$$f_{\text{diff}}^{M=0}(t') = e^{-\frac{1}{2} b_{\text{diff}}(m_{3\pi}) t'}. \quad (263)$$

Here, we use the  $m_{3\pi}$  dependence of the slope parameter in Eq. (261) that was extracted from the experimental data. For Primakoff-produced waves, which all have  $M = 1$ , the theoretically expected  $t'$  dependence as given by Eq. (256) is

$$f_{\text{Prim, theo}}^{M=1}(t') = F_{\text{eff}}(t', |t|_{\min}) \frac{\sqrt{t'}}{t' + |t|_{\min}}. \quad (264)$$

<sup>112</sup>Note that we use the reflectivity basis, where  $M \geq 0$  (see Section 5.2.3).

<sup>113</sup>We omit the sums over reflectivity and rank index because  $\varepsilon = +1$  and  $N_r = 1$ .

As was discussed in Section 7.1, this  $t'$  dependence is significantly modified by resolution effects. Thus Eqs. (249) and (264) is used in the PWA model in Eq. (262) only for Monte Carlo simulation. To analyze real data, we employ the same parameterization as in Eq. (258) for the Primakoff component, i.e.

$$f_{\text{Prim}}^{M=1}(t') = e^{-\frac{1}{2} b_{\text{Prim}}(m_{3\pi}) t'}, \quad (265)$$

where we use the  $m_{3\pi}$  dependence of the slope parameter in Eq. (259) that was extracted from simulated Primakoff events.

Smearing of the  $3\pi$  phase-space variables, in particular of the azimuthal angle  $\phi_{\text{GJ}}$  in the Gottfried-Jackson frame (see Section 5.1.4), causes two specific features that we observe in the PWA results: (i) contrary to expectation, negative-reflectivity waves with  $M = 1$  are significant and (ii) the amplitudes of waves with  $M^\varepsilon = 0^+$  and  $1^+$  quantum numbers are not fully coherent. We hence have to modify the PWA model in Eq. (262) in order to take into account these effects. The most economical PWA model in terms of fit parameters, that provides a satisfactory description of the data, is obtained by (i) including negative-reflectivity waves with  $M = 1$  in the PWA model and (ii) introducing an additional real-valued parameter  $r_{M=0,M=1}$  that quantifies the degree of coherence between the  $M^\varepsilon = 0^+$  and  $1^+$  waves:

$$\begin{aligned} \mathcal{I}(\tau_3; m_{3\pi}, t') = & \left| \sum_k^{N_{\text{waves}}^{M=0}} \mathcal{T}_k^{(\varepsilon=+1)} \Psi_k^{(\varepsilon=+1)} \right|^2 + \left| \sum_l^{N_{\text{waves}}^{M=1}} \mathcal{T}_l^{(\varepsilon=+1)} \Psi_l^{(\varepsilon=+1)} \right|^2 + \left| \sum_l^{N_{\text{waves}}^{M=1}} \mathcal{T}_l^{(\varepsilon=-1)} \Psi_l^{(\varepsilon=-1)} \right|^2 \\ & + r_{M=0,M=1} 2 \text{Re} \left[ \sum_k^{N_{\text{waves}}^{M=0}} \mathcal{T}_k^{(\varepsilon=+1)} \Psi_k^{(\varepsilon=+1)} \sum_l^{N_{\text{waves}}^{M=1}} \mathcal{T}_l^{(\varepsilon=+1)*} \Psi_l^{(\varepsilon=+1)*} \right] + |\mathcal{T}_{\text{flat}}(m_{3\pi}, t')|^2. \end{aligned} \quad (266)$$

Here, index  $k$  runs over all  $M = 0$  waves, whereas index  $l$  runs over all  $M = 1$  waves. For the latter, we use the same wave set for  $\varepsilon = +1$  and  $-1$ . The PWA model contains 17 waves with  $J \leq 3$  and  $M^\varepsilon = 0^+$  attributed to diffractive dissociation and 8 waves with  $J \leq 2$  and  $M = 1$  attributed to Primakoff production. Each of the  $M = 1$  waves appears with both reflectivities. For  $m_{3\pi} < 1.56 \text{ GeV}/c^2$ , the model contains in addition a  $\chi\text{PT}$  amplitude with  $\varepsilon = \pm 1$  (see Section 7.5). We also include an amplitude that takes into account the  $K^- \rightarrow \pi^- \pi^- \pi^+$  events close to threshold. In total, the wave set consists of 37 waves including the flat wave (see Tab. 4 in Ref. [255] for a complete list). In order to define waves, we use the same short-hand notation  $J^{PC} M^\varepsilon r \pi L$  that we already introduced for diffractively produced  $\pi^- \pi^- \pi^+$  in Section 6.2.3.

It is important to note that the modifications in Eq. (266) compared to Eq. (262) do not reflect any physical feature of the scattering process. The modifications are applied only to effectively take into account effects of experimental resolution. To demonstrate this, we performed a dedicated Monte Carlo study, which is based on the result from a fit of the PWA model in Eq. (266) to the measured data.<sup>114</sup> From the set of transition amplitudes that we obtain in each  $m_{3\pi}$  bin, we then construct a PWA model according to Eq. (262) that we use to generate MC data.<sup>115</sup> In order to construct this MC PWA model, we scale each  $M^\varepsilon = 1^+$  transition amplitude in Eq. (262) such that the corresponding intensity is equal to the sum of the  $M^\varepsilon = 1^+$  and  $1^-$  intensities of this wave in the PWA model in Eq. (266). The full Monte Carlo and reconstruction chain, which includes a detailed simulation of the detector resolution effects, is applied to the simulated events. The reconstructed Monte Carlo events are then fit using the same PWA model in Eq. (266) that we use for the measured data. The fit result exhibits the same two features that we already observed in the PWA of the measured data: (i) for each  $M^\varepsilon = 1^+$  wave in the simulated PWA model in Eq. (262), we find significant  $M^\varepsilon = 1^+$  and  $1^-$  components of this wave in the PWA result of the reconstructed MC data, with their intensity sum

<sup>114</sup>Note that in PWA fits to measured data, we use the smeared  $t'$  dependence for the  $M = 1$  waves, i.e. Eq. (265) with Eq. (259).

<sup>115</sup>Note that for generating MC data, we use the unsmeared  $t'$  dependence from Eq. (264) for the  $M^\varepsilon = 1^+$  waves.

being close to the intensity of the simulated  $M^\varepsilon = 1^+$  wave, and (ii) we observe reduced coherence between the  $M^\varepsilon = 0^+$  and  $1^+$  amplitudes. This study hence points to the necessity of summing up the intensities of the  $M^\varepsilon = 1^+$  and  $1^-$  components of each wave in each  $m_{3\pi}$  bin to get the proper intensities of the Primakoff-produced waves. In Appendix J, we show that the effects discussed above can be explained by a substantial smearing of the  $\phi_{GJ}$  angle.

In order to study the production mechanisms for states with spin projections  $M = 0$  and  $1$  in detail, we perform a dedicated PWA in  $t'$  bins. This analysis is performed in the region  $t' < 10^{-2} (\text{GeV}/c)^2$  using 31 narrow non-equidistant  $t'$  bins in order to resolve the  $t'$  spectra of Primakoff and diffractive production. Due to the limited size of the experimental data sample, we perform this PWA in two broad mass ranges: (i)  $1.26 < m_{3\pi} < 1.38 \text{ GeV}/c^2$ , which we use to study the  $a_2(1320)$  signal, and (ii)  $1.50 < m_{3\pi} < 1.80 \text{ GeV}/c^2$ , which we use to study the  $\pi_2(1670)$  signal. Since the PWA is performed in narrow  $t'$  bins, the transition amplitudes are assumed to be independent of  $t'$  in each bin, i.e. the functions  $f_i^\varepsilon(t')$  in the PWA model in Eq. (266) that model these  $t'$  dependences are set to 1.

As the transition amplitudes vary significantly over the analyzed broad  $m_{3\pi}$  ranges, we have to model this  $m_{3\pi}$  dependence. We use the same ansatz in Eq. (226) that we use for the resonance-model fits.<sup>116</sup> This means that we model the transition amplitudes as a sum of dynamical amplitudes  $\mathcal{D}_k(m_{3\pi})$  for the wave components  $k$ , which are, in the case of resonances, Breit-Wigner amplitudes. The main difference with respect to a resonance-model fit is that here the dynamical amplitudes have no free parameters. Due to this restriction, the standard PWA fit procedure (see Section 5.2.5), including the pre-calculation of the integral matrices, can be applied. The coupling amplitudes  $\mathcal{C}_{ki}^\varepsilon(t')$ , which are free parameters that are determined independently in each  $t'$  bin, contain information about the  $t'$  dependence of production strength and phase of component  $k$  in wave  $i$  with reflectivity  $\varepsilon$  (see Section 5.1.7). Since we perform the PWA fits in broad  $m_{3\pi}$  ranges that fully contain the peak of the studied  $3\pi$  resonance  $k$ , we effectively integrate over the analyzed  $m_{3\pi}$  range so that  $|\mathcal{C}_{ki}^\varepsilon(t')|^2$  corresponds to the total intensity of resonance  $k$  in the given  $t'$  bin. Dividing by the  $t'$  bin width, we hence obtain the  $t'$  spectrum  $dN_{ki}^\varepsilon/dt'$  of the resonance (cf. Eq. (234)). We also measure the coupling phases  $\Delta\phi_{ki,lj}^\varepsilon$  defined in Eq. (237) as a function of  $t'$ . These are the phase differences between component  $k$  in wave  $i$  and component  $l$  in wave  $j$ , which contain information about the production phases of the wave components. The  $t'$  dependence of these phases allows us to study the production mechanism of resonances.

For the  $a_2(1320)$  mass range, the  $m_{3\pi}$  dependence of the transition amplitudes of the  $1^{++} 0^+$   $\rho(770)\pi S$  and  $2^{++} 1^\pm \rho(770)\pi D$  waves are modeled by Breit-Wigner amplitudes for  $a_1(1260)$  and  $a_2(1320)$ , respectively. The  $a_2(1320)$  parameters are fixed to the PDG values [278]; for the  $a_1(1260)$ , we use the parameters  $m_{a_1(1260)} = 1220 \text{ MeV}/c^2$  and  $\Gamma_{a_1(1260)} = 370 \text{ MeV}/c^2$ . For the dynamic widths of the two resonances, we use the same parameterizations as for the resonance-model fit of the diffractive  $\pi^-\pi^-\pi^+$  proton-target data (see Section 6.2.4 and Section IV.A.1 in Ref. [156] for details). All the other transition amplitudes in the PWA model are assumed to be independent of  $m_{3\pi}$ . For the broader  $\pi_2(1670)$  mass range, all transition amplitudes depend on  $m_{3\pi}$ . The  $m_{3\pi}$  dependence of the  $J^{PC} = 2^{-+}$  transition amplitudes of the  $f_2(1270)\pi S$  and the  $\rho(770)\pi P$  and  $F$  waves with  $M = 0$  and 1 is modelled by a constant-width Breit-Wigner amplitude (Eqs. (87) and (151)) with mass and width fixed to the PDG parameters of the  $\pi_2(1670)$  [278]. In addition, the transition amplitudes of the  $2^{-+} 0^+$   $f_2(1270)\pi D$  wave and of selected  $M = 0$  waves with  $J^{PC} = 0^{-+}$  and  $1^{++}$  are modeled by a coherent sum of a Breit-Wigner amplitude and a non-resonant component (see Appendix A.5 and Table 5 in Ref. [255] for details). The  $m_{3\pi}$  dependence of the remaining transition amplitudes is modeled by the square root of polynomials that were obtained by fitting the intensity distributions of the respective waves, as obtained from the PWA in  $m_{3\pi}$  bins, in the analyzed  $m_{3\pi}$  range.

---

<sup>116</sup>Here, the amplitude  $\mathcal{P}(m_{3\pi}, t')$  that models the average production probability is set to 1.

### 7.3. Results for $a_2(1320)$ and $\pi_2(1670)$ from Partial-Wave Decomposition

In Fig. 81, we summarize the PWA results for Primakoff production of  $a_2(1320)$  and  $\pi_2(1670)$ . The points with error bars represent the result of the partial-wave decomposition in  $m_{3\pi}$  and  $t'$  bins, respectively, using the PWA models that were discussed in Section 7.2. The PWA in the Primakoff region  $t' < 10^{-3} (\text{GeV}/c)^2$  is performed in 40  $\text{MeV}/c^2$  wide  $m_{3\pi}$  bins. In addition, we perform partial-wave analyses in 31 narrow non-equidistant  $t'$  bins in the extended range  $t' < 10^{-2} (\text{GeV}/c)^2$  for two broad mass regions around  $a_2(1320)$  and  $\pi_2(1670)$ .

Figure 81a shows the intensity sum of the  $2^{++} 1 \rho(770) \pi D$  waves with  $\varepsilon = +1$  and  $-1$  with a clear  $a_2(1320)$  signal. The curve represents the result of a fit with a resonance model that will be discussed in Section 7.4. Figure 81b shows the corresponding intensity sum of the  $2^{-+} 1 f_2(1270) \pi S$  waves with a clear  $\pi_2(1670)$  peak.

In Figs. 81c to 81f, we show the results of the PWA performed in 31 non-equidistant  $t'$  bins in broad mass ranges around the  $a_2(1320)$  and  $\pi_2(1670)$ . As was discussed in Section 7.2, in the employed PWA model the  $2^{++} 1 \rho(770) \pi D$  amplitudes are described by a Breit-Wigner amplitude for the  $a_2(1320)$ . The  $t'$  spectrum in Fig. 81c hence represents the  $a_2(1320)$  intensity, where we again sum the intensities of the  $\varepsilon = +1$  and  $-1$  contributions. The  $t'$  spectrum is fitted well by an incoherent sum of two exponentials similar to Eq. (258):

$$\frac{dN_{a_2(1320)}}{dt'} = \frac{dN_{a_2(1320)}^{\text{diff}}}{dt'} + \frac{dN_{a_2(1320)}^{\text{Prim}}}{dt'} \quad \text{with} \quad \frac{dN_{a_2(1320)}^{\text{diff}}}{dt'} \propto t' e^{-b_{a_2(1320)}^{\text{diff}} t'} \quad \text{and} \quad \frac{dN_{a_2(1320)}^{\text{Prim}}}{dt'} \propto e^{-b_{a_2(1320)}^{\text{Prim}} t'}. \quad (267)$$

We obtain slope parameters of  $b_{a_2(1320)}^{\text{diff}} = 374 \pm 25 (\text{GeV}/c)^{-2}$  and  $b_{a_2(1320)}^{\text{Prim}} = 1292 \pm 53 (\text{GeV}/c)^{-2}$ . The latter value is in fair agreement with the one obtained in the Primakoff MC study that was described in Section 7.1 (cf. Eq. (259)). The fit of the  $t'$  spectrum also provides an estimate of the diffractive background. For the  $a_2(1320)$ , it amounts to approximately 3% of the total intensity in the Primakoff region. Applying the model in Eq. (267) to the  $t'$  spectrum of the  $\pi_2(1670)$  (see Fig. 81d), which is obtained by summing the intensities of the  $\varepsilon = +1$  and  $-1$  contributions, we find that the relative contribution of the diffractive background is significantly larger than for the  $a_2(1320)$ . In the Primakoff region, it amounts to about 14%. This makes the separation of the contributions from Primakoff and diffractive production more difficult. As a consequence, additional constraints are needed to stabilize the fit (see Section 3.2 in Ref. [255] for details).

As explained in Section 7.3, the PWA in  $t'$  bins also allows us to extract the relative phases between resonances, i.e. the coupling phases  $\Delta\phi_{k_i, l_j}^{\varepsilon}$ , as a function of  $t'$ . Figure 81e shows the relative phase of the  $a_2(1320)$  with  $M^{\varepsilon} = 1^+$  and the  $a_1(1260)$  with  $M^{\varepsilon} = 0^+$ . For  $t' < 6 \cdot 10^{-3} (\text{GeV}/c)^2$ , this phase rises monotonically with  $t'$  and levels off for larger  $t'$  reaching a plateau at about  $0^\circ$ . This reflects the continuous evolution from nearly pure Primakoff production of the  $a_2(1320)$  at low  $t'$  to nearly pure diffractive production at higher  $t'$ . In the Primakoff region  $t' < 10^{-3} (\text{GeV}/c)^2$ , the relative phase is given by the phase difference of the Primakoff production amplitude for the  $a_2(1320)$ , which is approximately purely real, and the diffractive production amplitude of the  $a_1(1260)$ , which is approximately purely imaginary. This results in  $\Delta\phi_{a_2(1320), a_1(1260)}^{(\varepsilon=+1)} \approx -90^\circ$ . Assuming that the phase of the diffractive production amplitude of the  $a_2(1320)$  has a  $t'$  dependence similar to that of the  $a_1(1260)$ , interference effects between diffractive and Primakoff production of the  $a_2(1320)$  are expected to be small. Hence the sum of two non-interfering contributions in Eq. (267) is a good approximation to describe the  $t'$  spectrum. At higher values of  $t'$ , both  $a_2(1320)$  and  $a_1(1260)$  are diffractively produced so that  $\Delta\phi_{a_2(1320), a_1(1260)}^{(\varepsilon=+1)}(t')$  flattens and reaches approximately  $0^\circ$ . Like for the  $a_2(1320)$ , we observe for the  $\pi_2(1670)$  a phase difference of roughly  $-90^\circ$  between the  $M^{\varepsilon} = 1^+$  (Primakoff-produced) and  $0^+$  (diffractively produced) states in the  $f_2(1270)\pi S$  decay mode (see Fig. 81f). However, at larger values of  $t'$  the phase difference does not approach  $0^\circ$  but levels off already at approximately  $-50^\circ$ . This behavior is not yet understood.

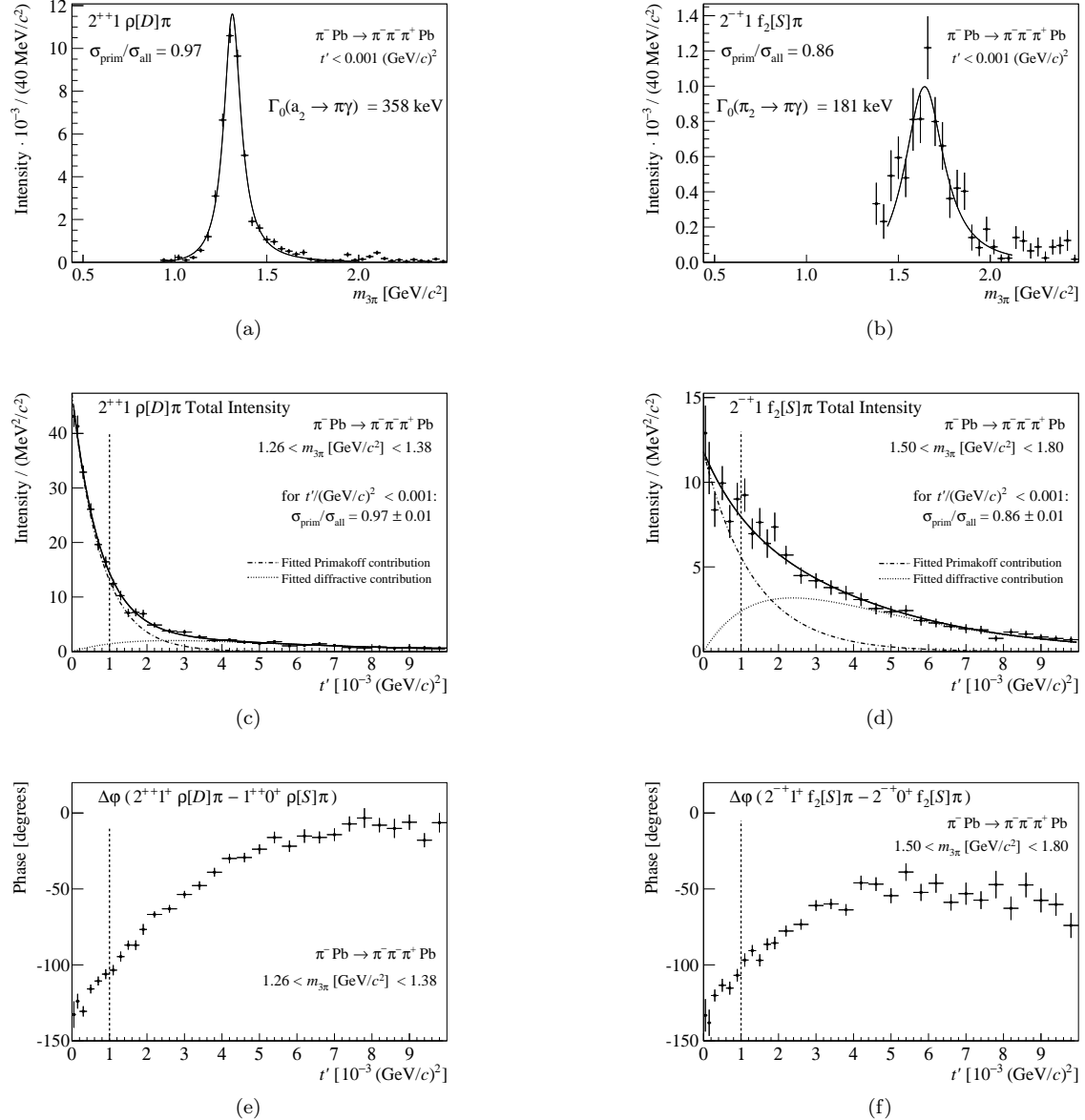


Figure 81: (a) and (c): Intensity sum of the  $2^{++} 1 \rho(770) \pi D$  waves with  $\varepsilon = +1$  and  $-1$ , (a) as a function of  $m_{3\pi}$  for  $t' < 10^{-3} (\text{GeV}/c)^2$  and (c) as a function of  $t'$  for a broad  $m_{3\pi}$  range around the  $a_2(1320)$ . The curve in (a) represents the result of a fit with Eq. (268) integrated over  $t' < 10^{-3} (\text{GeV}/c)^2$ . The continuous curve in (c) represents the result of a fit with Eq. (267). The dotted curve represents the contribution from diffractive production, the dashed-dotted curve the one from Primakoff production. (b) and (d): Similar to (a) and (c) but for the  $2^{-+} 1^\pm f_2(1270) \pi S$  waves and the  $m_{3\pi}$  range around the  $\pi_2(1670)$ . (e) Relative phase between the  $a_2(1320)$  in the  $2^{++} 1^+ \rho(770) \pi D$  wave and the  $a_1(1260)$  in the  $1^{++} 0^+ \rho(770) \pi S$  wave as a function of  $t'$ . (f) Relative phase between the  $\pi_2(1670)$  in the  $2^{-+} f_2(1270) \pi S$  waves with  $M^\varepsilon = 1^+$  and  $0^+$  as a function of  $t'$ . In (c) and (e), the  $m_{3\pi}$  dependence of the  $2^{++} 1^\pm \rho(770) \pi D$  amplitudes is modeled by a Breit-Wigner for the  $a_2(1320)$ . In (d) and (f), the  $m_{3\pi}$  dependence of the  $2^{-+} 1^\pm f_2(1270) \pi S$  amplitudes is modeled by a Breit-Wigner for the  $\pi_2(1670)$ .

#### 7.4. Radiative Widths of $a_2(1320)$ and $\pi_2(1670)$

Electromagnetic decays of mesons are important to understand their internal structure. Like in atomic and nuclear physics, the multipolarities of the electromagnetic transitions, probe different aspects of the meson wave function. Several phenomenological models have been developed to describe electromagnetic decays of mesons, for example, the relativized quark model [15], the covariant oscillator quark model [279–281], and the vector-meson dominance model (see e.g. Ref. [282]). The latter model assumes that any soft interaction of photons with hadrons proceeds via intermediate vector-meson states, predominantly via the lightest ones, i.e.  $\rho(770)$ ,  $\omega(782)$ , and  $\phi(1020)$ . Some electromagnetic decays such as  $\pi^0 \rightarrow \gamma\gamma$  are also calculable in the framework of  $\chi$ PT. The latest experimental result for  $\Gamma[\pi^0 \rightarrow \gamma\gamma]$  in Ref. [283] is in excellent agreement with the theoretical prediction from Ref. [284].

For most light mesons, the direct observation of their radiative decays is impossible because the corresponding partial decay widths are usually only  $10^{-4}$  to  $10^{-3}$  of the total decay width. Hence backgrounds originating from  $\pi^0 \rightarrow \gamma\gamma$ , where one photon is not detected, obscure the signal. However, there has been a lot of progress in the development of experimental approaches to measure these radiative decays nevertheless. The Primakoff approach is widely employed to measure the  $\pi^\pm\gamma$  and  $K^\pm\gamma$  partial decay widths of various pseudoscalar, (pseudo)vector or (pseudo)tensor mesons  $X$  by measuring the cross section of reactions of the form  $h^\pm + A \rightarrow X^\pm + A$  on a target nucleus  $A$ , where  $h^\pm$  stands for  $\pi^\pm$  or  $K^\pm$  beam particles. The Primakoff approach was used to measure  $\Gamma[\rho(770) \rightarrow \pi\gamma]$  [285–287],  $\Gamma[K^*(892) \rightarrow K\gamma]$  [288, 289],  $\Gamma[a_1(1260) \rightarrow \pi\gamma]$  [290],  $\Gamma[b_1(1235) \rightarrow \pi\gamma]$  [291],  $\Gamma[a_2(1320) \rightarrow \pi\gamma]$  [255, 273, 292, 293], and  $\Gamma[\pi_2(1670) \rightarrow \pi\gamma]$  [255].

The cross section for pion-induced Primakoff production of a broad resonance  $X$  with spin  $J$ , nominal mass  $m_0$ , and nominal total width  $\Gamma_0$  that is measured in the  $\pi^-\pi^-\pi^+$  partial wave with index  $i$  is given by integrating Eq. (256) over the  $\pi^-\pi^-\pi^+$  phase space  $\Phi_3$  [268, 269]. This yields

$$\frac{d\sigma_{\pi+A \rightarrow X+A}}{dm_{3\pi} dt'} = \underbrace{\frac{\alpha_{\text{em}} Z^2}{\pi} \frac{2m_{3\pi}}{m_{3\pi}^2 - m_\pi^2} \frac{t'}{(t' + |t|_{\min})^2} |F_{\text{eff}}(t', |t|_{\min})|^2 \sigma_{\pi+\gamma \rightarrow X \rightarrow i}(m_{3\pi})}_{=: \mathcal{F}(m_{3\pi}, t')} , \quad (268)$$

where

$$\sigma_{\pi+\gamma \rightarrow X \rightarrow i}(m_{3\pi}) = 8\pi (2J+1) \left[ \frac{m_{3\pi}}{m_{3\pi}^2 - m_\pi^2} \right]^2 \frac{m_0 \Gamma_{\pi\gamma}(m_{3\pi}) m_0 \Gamma_i(m_{3\pi})}{(m_{3\pi}^2 - m_0^2)^2 + m_0^2 \Gamma^2(m_{3\pi})} . \quad (269)$$

Here, we have used  $dm_{3\pi}^2 = 2m_{3\pi} dm_{3\pi}$  and we have parameterized the resonance propagator by a relativistic Breit-Wigner amplitude with the dynamic total width  $\Gamma(m_{3\pi})$  (see Eq. (152)). The dynamic partial width of the decay  $X \rightarrow \pi + \gamma$ , i.e. the radiative width of  $X$ , is denoted by  $\Gamma_{\pi\gamma}(m_{3\pi})$ ; the dynamic partial width for the decay of  $X$  into  $\pi^-\pi^-\pi^+$  via the partial wave  $i$  by  $\Gamma_i(m_{3\pi})$ .

We parameterize the radiative width  $\Gamma_{\pi\gamma}(m_{3\pi})$  following Eq. (152) but omitting the term  $m_0/m_{3\pi}$  [294], i.e.

$$\Gamma_{\pi\gamma}(m_{3\pi}) = \Gamma_{\pi\gamma,0} \frac{q}{q_0} \frac{F_L^2(q)}{F_L^2(q_0)} , \quad (270)$$

where  $\Gamma_{\pi\gamma,0}$  is the nominal radiative width that we want to measure. For the  $\pi\gamma$  decay of the  $a_2(1320)$  we use  $L = 2$ , i.e.  $D$  wave, and for that of the  $\pi_2(1670)$  we use  $L = 1$ , i.e.  $P$  wave.

For an accurate description of the resonance line shape, the dynamic partial decay width  $\Gamma_i(m_{3\pi})$  must take into account the width of the  $2\pi$  isobar and self-interference effects due to Bose symmetrization (see Section 5.1.6). This is achieved by parameterizing the  $m_{3\pi}$  dependence of the partial width for the decay chain represented by the wave index  $i$  by  $\int d\Phi_3(\tau_3) |\Psi_i(m_{3\pi}, \tau_3)|^2$ , where  $\Psi_i$  is Bose-symmetrized according to Eq. (159). Normalizing to the nominal partial decay width  $\Gamma_{i,0}$ , we

obtain:

$$\Gamma_i(m_{3\pi}) = \Gamma_{i,0} \frac{\int d\Phi_3(\tau_3) |\Psi_i(m_{3\pi}, \tau_3)|^2}{\int d\Phi_3(\tau_3) |\Psi_i(m_0, \tau_3)|^2}. \quad (271)$$

We measure the  $a_2(1320)$  and  $\pi_2(1670)$  in their dominant  $3\pi$  decay channels, i.e.  $a_2(1320) \rightarrow \rho(770)\pi D$  and  $\pi_2(1670) \rightarrow f_2(1270)\pi S$ . The values of the nominal partial widths are taken from the PDG [278]. For  $a_2(1320) \rightarrow \rho(770)\pi D$ , we assume that this decay mode saturates the branching fraction  $\text{BF}[a_2(1320) \rightarrow 3\pi] = \Gamma_{a_2(1320) \rightarrow 3\pi,0}/\Gamma_{a_2(1320),0} = 70.1 \pm 2.7\%$  and we apply an isospin factor of 1/2 to correct for the unobserved  $a_2(1320)^- \rightarrow \rho(770)^-\pi^0 \rightarrow \pi^-\pi^0\pi^0$  decay mode. For  $\pi_2(1670) \rightarrow f_2(1270)\pi S$ , we assume that this decay saturates the branching fraction  $\text{BF}[\pi_2(1670) \rightarrow f_2(1270)\pi] = \Gamma_{\pi_2(1670) \rightarrow f_2(1270)\pi,0}/\Gamma_{\pi_2(1670),0} = 56.3 \pm 3.2\%$  and we apply an isospin factor of 2/3 to correct for the unobserved  $\pi_2(1670)^- \rightarrow f_2(1270)\pi^- \rightarrow \pi^-\pi^0\pi^0$  decay mode.

The employed parameterization for the total width of the  $a_2(1320)$  is similar to the one used in the resonance-model fit of the diffractive  $\pi^-\pi^-\pi^+$  proton-target data (see Section 6.2.4 and Section IV.A.1 in Ref. [156] for details). We also assume that the  $a_2(1320)$  decays only into  $\rho(770)\pi D$  (82%) and  $\eta\pi D$  (18%), i.e. we neglect all other decay modes. We use Eq. (271) for  $\Gamma_{a_2(1320) \rightarrow \rho(770)\pi D}(m_{3\pi})$  and Eq. (152) for  $\Gamma_{a_2(1320) \rightarrow \eta\pi D}(m_{3\pi})$ . For the  $\pi_2(1670)$ , the situation is more complicated. The  $\pi_2(1670)$  decays nearly exclusively, i.e. with a branching fraction of  $95.8 \pm 1.4\%$ , into  $3\pi$ , which includes the decays into  $f_2(1270)\pi$  ( $56.3 \pm 3.2\%$ ),  $\rho(770)\pi$  ( $31 \pm 4\%$ ),  $\sigma\pi$  ( $10.9 \pm 3.4\%$ ), and  $[\pi\pi]_S\pi$  ( $8.7 \pm 3.4\%$ ) [5]. In the analysis of the diffractive  $\pi^-\pi^-\pi^+$  data (see Section 6.3.5), we observe sizable interference of different  $3\pi$  decay chains of the  $\pi_2(1670)$ . Therefore, the branching fraction information in the PDG is insufficient to construct a realistic  $3\pi$  decay model that takes into account these interferences. However, for our analysis the details of the parameterization of  $\Gamma(m_{3\pi})$  are not very important. They have only a subtle influence on the peak shape, which mostly affects the estimates for  $m_0$  and  $\Gamma_0$ , whereas the resonance yield that we are mainly interested in (see below) is basically unaffected by the choice of parameterization. Considering in addition the limited precision of our data in Fig. 81b, we choose a simple parameterization for the total width of the  $\pi_2(1670)$ , where we assume that the  $f_2(1270)\pi S$  decay mode saturates the total width and use Eq. (271).

With the above definitions, only three unknowns remain in Eqs. (268) and (269): the nominal radiative width  $\Gamma_{\pi\gamma,0}$ , which defines the height of the resonance peak, the nominal mass  $m_0$ , and the nominal total width  $\Gamma_0$  of the resonance, which both determine the shape of the resonance peak. In order to measure  $\Gamma_{\pi\gamma,0}$ , we use the fact that  $d\sigma_{\pi+A \rightarrow X+A}/(dm_{3\pi} dt') \propto \Gamma_{\pi\gamma,0}$  and perform the analysis in three steps.

In the first step, we integrate Eq. (268) over  $t' < 10^{-3}(\text{GeV}/c)^2$  and fit the resulting function of  $m_{3\pi}$  to the  $2^{++} 1 \rho(770)\pi D$  and  $2^{-+} 1 f_2(1270)\pi S$  intensity distributions. The results are represented by the curves in Figs. 81a and 81b. In the  $\chi^2$  function that is used in the fit, we convolve the model with the  $m_{3\pi}$  resolution obtained from MC simulations and compare the integral of the model function over each  $m_{3\pi}$  bin with the measured intensity in this bin. As a result, we determine  $m_0$ ,  $\Gamma_0$ , and an overall normalization factor that contains  $\Gamma_{\pi\gamma,0}$ . For the  $a_2(1320)$ , we obtain the Breit-Wigner parameters  $m_{a_2(1320)} = 1319 \pm 1 \text{ MeV}/c^2$  and  $\Gamma_{a_2(1320)} = 105 \pm 4 \text{ MeV}/c^2$ , and for the  $\pi_2(1670)$ ,  $m_{\pi_2(1670)} = 1684 \pm 11 \text{ MeV}/c^2$  and  $\Gamma_{\pi_2(1670)} = 277 \pm 38 \text{ MeV}/c^2$ . Here, the uncertainties are statistical only. For both resonances, the measured parameter values are in good agreement with the PDG averages and with the PWA results from the COMPASS diffractive data (see Figs. 66 and 70).

In the second step, we obtain the acceptance-corrected yields of  $a_2(1320)$  and  $\pi_2(1670)$  in terms of number of events by integrating the curves in Figs. 81a and 81b over the  $m_{3\pi}$  fit range. The yields are corrected for the contributions from diffractive background, which are estimated by fitting Eq. (267) to the  $t'$  spectra in Figs. 81c and 81d as obtained from the PWA in  $t'$  bins (see Section 7.3). A second correction factor is applied to account for the migration of events from above and below the Primakoff limit at  $t' = 10^{-3}(\text{GeV}/c)^2$ , which is caused by the limited  $t'$  resolution. The correction

Table 4: Comparison of the COMPASS values for the radiative widths of  $a_2(1320)$  and  $\pi_2(1670)$  with the ones from previous measurements and theoretical calculations.

	$\Gamma[a_2(1320) \rightarrow \pi\gamma]$	$\Gamma[\pi_2(1670) \rightarrow \pi\gamma]$
<b>Experiments</b>		
COMPASS [255]	$358 \pm 6 \pm 42 \text{ keV}/c^2$	$181 \pm 11 \pm 27 \text{ keV}/c^2$
FNAL E781 (SELEX) [273]	$284 \pm 25 \pm 25 \text{ keV}/c^2$	
FNAL E272 [292]	$295 \pm 60 \text{ keV}/c^2$	
E. N. May <i>et al.</i> [293]	$0.46 \pm 0.11 \text{ MeV}/c^2$	
<b>Theory</b>		
Vector-meson dominance model [295]	$375 \pm 50 \text{ keV}/c^2$	
Relativistic quark model [296]	$324 \text{ keV}/c^2$	
Covariant oscillator quark model [280]	$235 \text{ keV}/c^2$	
Covariant oscillator quark model [281]	$237 \text{ keV}/c^2$	2 values: $335 \text{ keV}/c^2$ and $521 \text{ keV}/c^2$

factor is estimated by simulating Primakoff events and calculating the ratio of the number of generated events in the region  $t'_{\text{gen}} < 10^{-3} (\text{GeV}/c)^2$  and the number of reconstructed events in the region  $t'_{\text{rec}} < 10^{-3} (\text{GeV}/c)^2$ .<sup>117</sup> For the  $a_2(1320)$ , this ratio is 1.348; for the  $\pi_2(1670)$  it is 1.359.

In the third step, we use the corrected yield  $N_X$  from above to calculate the Primakoff production cross section  $\sigma_{\text{Prim},X}$  for resonance  $X$ . For this, we need the integrated luminosity  $\mathcal{L}$ , for which we need in turn the total integrated  $\pi^-$  beam flux. The effective beam flux is determined using  $\pi^-\pi^-\pi^+$  decays of beam kaons that are observed outside the target. Based on the known  $K^-$  fraction of 2.4% in the beam, the branching fraction  $\text{BF}[K^- \rightarrow \pi^-\pi^-\pi^+] = 5.54\%$  [278], the acceptance for  $K^- \rightarrow \pi^-\pi^-\pi^+$  of 45.9%, which was estimated by a dedicated Monte Carlo simulation, the limited decay volume, and the thickness of the Pb target of 3 mm, we obtain an integrated effective luminosity of  $\mathcal{L} = 208 \text{ pb}^{-1}$ . Using the numbers from Ref. [255], we calculate the Primakoff cross sections  $\sigma_{\text{Prim},a_2(1320)} = 280 \text{ pb}$  and  $\sigma_{\text{Prim},\pi_2(1670)} = 39.2 \text{ pb}$ . These values correspond to the integral of Eq. (268) over  $t' < 10^{-3} (\text{GeV}/c)^2$  and the  $m_{3\pi}$  fit range.<sup>118</sup> Since the radiative width is a multiplicative parameter in Eq. (268) that is independent of  $t'$  and  $m_{3\pi}$ , we can write this integral as

$$\sigma_{\text{Prim},X} = \int_0^{t'_{\text{max}}} dt' \int_{m_{3\pi,\text{min}}}^{m_{3\pi,\text{max}}} dm_{3\pi} \frac{d\sigma_{\pi+A \rightarrow X+A}}{dm_{3\pi} dt'} = \Gamma_{\pi\gamma,0} I_X , \quad (272)$$

where  $I_X$  represents the integral of Eq. (268) with  $\Gamma_{\pi\gamma,0}$  taken out. The constant  $I_X$  is calculable using the resonance parameters of  $X$  and the parameterizations of the partial and total widths discussed above.

The results for the radiative widths of  $a_2(1320)$  and  $\pi_2(1670)$  are listed in Table 4 together with the results of previous measurements and theoretical calculations using various models. The values for the  $a_2(1320)$  are compatible with previous measurements and with calculations using a vector-meson dominance model [295] and a relativistic quark model [296]. The values obtained using a covariant oscillator quark model [280, 281] lie below the experimental values. For the  $\pi_2(1670)$ , we performed the first measurement of its radiative width. The predictions from the covariant oscillator quark model from Ref. [281] are both significantly higher than our value.

When comparing the experimental values in Table 4, it is important to note that the value of  $\Gamma_{\pi\gamma,0}$  depends on the choice of the parameterization of the form factor  $F_{\text{eff}}$  in Eq. (268). We use the

<sup>117</sup>Since the contribution of diffractive events with  $M = 1$  is negligible (see below), the migration of these events is not considered.

<sup>118</sup>For  $a_2(1320)$ , the fit range is  $0.92 < m_{3\pi} < 2.00 \text{ GeV}/c^2$ ; for  $\pi_2(1670)$ , it is  $1.44 < m_{3\pi} < 2.12 \text{ GeV}/c^2$ .

form factor from Ref. [270] that includes corrections, which take into account the distortion of the pion wave function in the Coulomb field. These Coulomb corrections were neglected in the previous measurements of the  $a_2(1320)$  radiative width that used the Primakoff technique. However, as noted by the authors of Ref. [270], the Coulomb corrections can significantly reduce the Primakoff cross section and hence increase the estimate for the radiative width. This may explain that the COMPASS value for the  $a_2(1320)$  radiative width lies above the values from the FNAL SELEX [273] and E272 experiments [292]. For COMPASS kinematics, accounting for the Coulomb corrections increases both radiative widths by 24 %. For SELEX kinematics, the increase is 15 %. The latter value is at variance with the conclusion of the authors of Ref. [273], who report that taking into account the Coulomb corrections had only a “minor impact” on their result.

### 7.5. Test of Chiral Perturbation Theory

In addition to Primakoff production of resonances also non-resonant processes contribute to the reaction  $\pi^- \gamma \rightarrow \pi^- \pi^- \pi^+$  and may interfere with the resonant production. In the case of quasi-real photon exchange and in the region of low  $m_{3\pi}$ , the non-resonant processes can be calculated using  $\chi$ PT (see Section 3.4). The leading-order (LO) calculation was performed by Kaiser and Friedrich in Ref. [297]. The next-to-leading-order (NLO)  $\chi$ PT calculations include contributions from loops [298] and from the  $\rho(770)$  [299]. They are expected to describe the non-resonant physics also at higher  $m_{3\pi}$ .

We take into account the non-resonant processes described above in the PWA by including a dedicated non-isobaric decay amplitude, called  $\chi$ PT amplitude. Since we perform the analysis in the range  $m_{3\pi} < 0.72 \text{ GeV}/c^2$  below the  $\rho(770)\pi$  threshold,  $\rho(770)$  contribution are expected to be negligible. It was shown in Ref. [298] that at low  $m_{3\pi}$  also the contributions from NLO diagrams with loops are negligible for the  $\pi^- \pi^- \pi^+$  final state.<sup>119</sup> We thus use for the PWA in the low- $m_{3\pi}$  region the LO  $\chi$ PT amplitude. This amplitude decomposes into  $3\pi$  partial waves with  $M^\varepsilon = 1^+$  and various  $J^{PC}$  quantum numbers. Due to the resolution effects that were discussed in Section 7.2, the  $\chi$ PT amplitude has to be included with  $\varepsilon = \pm 1$  into the PWA model in Eq. (266).

We performed a detailed study of the process  $\pi^- + A \rightarrow \pi^- \pi^- \pi^+ + A$  in the Primakoff region  $t' < 10^{-3} (\text{GeV}/c)^2$  and in the low-mass range  $0.44 < m_{3\pi} < 0.72 \text{ GeV}/c^2$  [300], where  $\chi$ PT is applicable. The PWA model in Eq. (266) is used with a wave set that consists of the LO  $\chi$ PT amplitude with  $M^\varepsilon = 1^\pm$  that describes the quasi-real photoproduction plus a set of 5 isobaric amplitudes with  $M^\varepsilon = 0^+$  and  $J \leq 2$  that describe the diffractive production. We also include a wave that represents the  $K^- \rightarrow \pi^- \pi^- \pi^+$  events close to threshold. We verified that the  $\chi$ PT amplitude can indeed replace the isobaric amplitudes with  $M = 1$  by performing a PWA, where we included 6 isobaric waves with  $M = 1$  instead of the  $\chi$ PT amplitude. The intensity of the  $\chi$ PT amplitude is found to be similar to the intensity of the coherent sum of the  $M = 1$  isobaric waves [300] (see also Ref. [252] for details).

The total  $\chi$ PT intensity is obtained by performing the PWA in seven  $40 \text{ MeV}/c^2$  wide  $m_{3\pi}$  bins and by summing up the intensities of the two  $\chi$ PT amplitudes with  $\varepsilon = \pm 1$ . The such obtained numbers of events are corrected for migration of events into and out of the Primakoff region using the same MC technique as for the radiative-width measurement (see Section 7.4). We do not correct for the diffractive background since it was found to be negligibly small (see discussion of  $t'$  spectra below). For each  $m_{3\pi}$  bin, the corrected number of events is converted into a cross-section value for the process  $\pi^- + A \rightarrow \pi^- \pi^- \pi^+ + A$  using the same value for the integrated luminosity as for the radiative-width measurements (see Section 7.4). Finally, by integrating Eq. (268) over each  $m_{3\pi}$  bin and over  $t' < 10^{-3} (\text{GeV}/c)^2$  and by dividing out the quasi-real photon flux factor  $\mathcal{F}(m_{3\pi}, t')$ , we obtain  $\sigma_{\pi^- + \gamma \rightarrow \pi^- \pi^- \pi^+}(m_{3\pi})$  at each  $m_{3\pi}$  bin center.<sup>120</sup> The resulting cross-section values are shown in Fig. 82a. The total systematic uncertainty is about 20 %, where the dominant contributions come from varying the fitting model and from the determination of the luminosity. The short-dashed

<sup>119</sup>The loop corrections are significantly larger for the  $\pi^- \pi^0 \pi^0$  final state.

<sup>120</sup>Here, we assume  $\sigma_{\pi^- + \gamma \rightarrow \pi^- \pi^- \pi^+}(m_{3\pi})$  to be a constant in each  $m_{3\pi}$  bin.

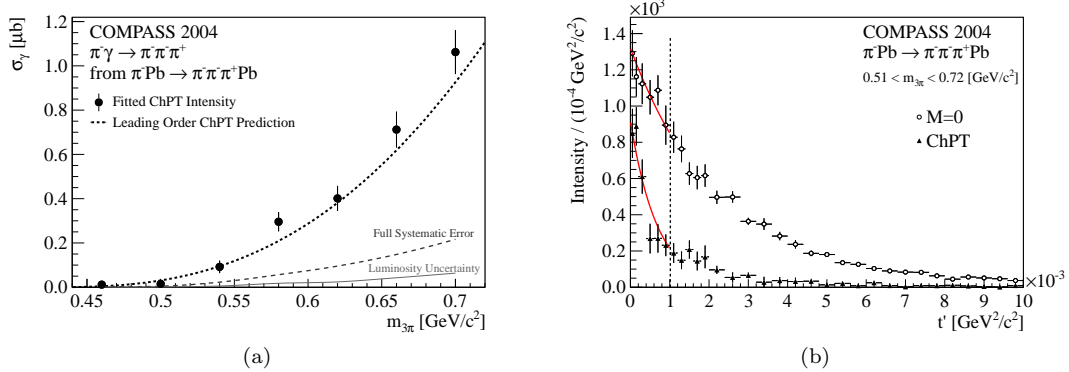


Figure 82: (a) Cross section of the  $\chi$ PT process  $\pi + \gamma \rightarrow \pi^- \pi^- \pi^+$  as a function of  $m_{3\pi}$ . The points with error bars are calculated from the total intensity of the  $\chi$ PT amplitude as obtained from the PWA; error bars are statistical only. The short-dashed curve shows the leading-order  $\chi$ PT prediction from Ref. [297]. The long-dashed curve represents the total systematic uncertainty, the continuous curve the contribution from the luminosity uncertainty. (b) The  $t'$  spectra of the total  $M = 0$  intensity (open circles) and the total  $\chi$ PT intensity (triangles). The curves represent the results of single-exponential fits of the form  $e^{-b t'}$ .

curve shows the LO  $\chi$ PT prediction from Ref. [297], which is in good agreement with the measured cross-section values.

To study the details of the production mechanisms, we performed another PWA in 31 narrow non-equidistant  $t'$  bins, using now the broad mass region  $0.51 < m_{3\pi} < 0.72 \text{ GeV}/c^2$ , where the lower mass limit is chosen to exclude  $K^- \rightarrow \pi^- \pi^- \pi^+$  events. In the PWA model, all transition amplitudes have  $m_{3\pi}$  dependences that are modelled using polynomials. The parameters of these polynomials are determined by fitting the  $m_{3\pi}$  intensity distribution of each partial wave as determined by the PWA in  $m_{3\pi}$  bins described above. Figure 82b shows the  $t'$  dependence of the intensity of the coherent sum of all  $M = 0$  waves and of the total  $\chi$ PT intensity. The dominant  $M = 0$  intensity shows the typical shape for diffraction on a Pb nucleus, while the  $\chi$ PT intensity forms a sharper peak toward  $t' = 0$ . A single-exponential fit to the latter results in a slope parameter of  $b_{\chi\text{PT}} = 1447 \pm 196 \text{ (GeV}/c)^{-2}$ . This value is consistent with  $b_{\chi\text{PT, MC}} = 1600 \text{ (GeV}/c)^{-2}$  that is obtained from MC simulation of quasi-real photon exchange. Since no isobaric waves with  $M = 1$  are included in the PWA model, the  $\chi$ PT amplitude may wrongly absorb diffractive  $M = 1$  contributions at higher  $t'$ . However, at  $t' \approx 3 \cdot 10^{-3} \text{ (GeV}/c)^2$ , where for Pb we expect the maximum of the diffractive  $M = 1$  contributions, the  $\chi$ PT intensity nearly vanishes. Fitting the  $\chi$ PT  $t'$  spectrum over a broader  $t'$  range and adding a diffractive contribution of the form  $t' e^{-b_{\text{diff}} t'}$ , we estimate that the diffractive background is well below 5 % for  $t' < 10^{-3} \text{ (GeV}/c)^2$ .

The results of our analysis confirm the LO  $\chi$ PT prediction for the process  $\pi + \gamma \rightarrow \pi^- \pi^- \pi^+$  for  $m_{3\pi} < 0.72 \text{ GeV}/c^2$  and  $t' < 10^{-3} \text{ (GeV}/c)^2$ . The  $\chi$ PT prediction is confirmed on two levels of the analysis: (i) We demonstrated that the  $\chi$ PT amplitude describes the data similarly well than a PWA model with 6 isobaric  $M = 1$  waves. This confirms that at low  $m_{3\pi}$  and low  $t'$  the  $3\pi$  phase-space distribution of the physical process is consistent with the  $\chi$ PT prediction. (ii) The cross section  $\sigma_{\pi+\gamma \rightarrow \pi^- \pi^- \pi^+}(m_{3\pi})$  that is calculated from the total intensity of the  $\chi$ PT amplitude as obtained by the PWA fit, agrees well with the LO  $\chi$ PT prediction. In addition, we find that the  $t'$  spectrum of the  $\chi$ PT amplitude shows a sharp peak at  $t' = 0$  with a shape that is consistent with Primakoff production, convolved with the experimental resolution. The  $\chi$ PT intensity nearly vanishes for  $t' > 3 \cdot 10^{-3} \text{ (GeV}/c)^2$ , which demonstrates that possible diffractive  $M = 1$  background is negligibly small.

## 8. Conclusions and Outlook

The COMPASS experiment has collected world-leading data samples on the scattering of a 190 GeV/c pion beam on proton and nuclear targets to perform a high-precision measurement of the excitation spectrum of isovector mesons. Based on these data, COMPASS has performed the so far most comprehensive and most detailed partial-wave analyses of  $\eta\pi$ ,  $\eta'\pi$ , and  $\pi^-\pi^-\pi^+$  final states from diffractive production in the squared four-momentum transfer range  $0.1 < t' < 1.0$  (GeV/c)<sup>2</sup> and of the  $\pi^-\pi^-\pi^+$  final state from quasi-real photoproduction in the range  $t' < 10^{-3}$  (GeV/c)<sup>2</sup>. At the used beam energy, diffractive production is dominated by Pomeron exchange.

The PWA of 116 000  $\eta\pi$  and 39 000  $\eta'\pi$  diffractive events of the reaction  $\pi^- + p \rightarrow \eta^{(\prime)}\pi + p$  was performed using a PWA model, which includes waves with relative orbital angular momentum  $L$  between the two final-state particles ranging from 1 to 6. This analysis revealed a striking pattern in the partial-wave amplitudes. On the one hand, even partial waves with  $L = 2, 4$ , and  $6$  exhibit a close similarity of their intensities and phases as a function of the  $\eta^{(\prime)}\pi$  mass after the intensities have been scaled by a kinematic factor that accounts for the different phase-space and angular-momentum barrier factors in the two final states. On the other hand, applying the same scaling, odd partial waves with  $L = 1, 3$ , and  $5$ , which carry spin-exotic, i.e. non- $q\bar{q}$ ,  $J^{PC}$  quantum numbers, are suppressed in  $\eta\pi$  with respect to  $\eta'\pi$ .

COMPASS also studied diffractive production of  $\pi^-\pi^-\pi^+$  using proton and Pb targets. The Pb target data sample consists of 420 000 events, whereas the proton-target data sample is much larger and consists of  $46 \cdot 10^6$  events. For the latter data, a PWA model with 88 partial waves is used, which is the largest wave set used so far in a PWA of  $3\pi$  final states. It consists of 80 waves with positive reflectivity, 7 with negative reflectivity, and one incoherent wave that is isotropic in the phase space and represents uncorrelated three pions. Due to the large size of the  $\pi^-\pi^-\pi^+$  proton-target data sample, a  $t'$ -resolved PWA is performed by subdividing the analyzed range  $0.1 < t' < 1.0$  (GeV/c)<sup>2</sup> into 11 non-equidistant bins.

For the  $\pi^-\pi^-\pi^+$  proton-target data, we developed the novel freed-isobar PWA method to extract the dynamical amplitudes of  $\pi^-\pi^+$  subsystems with well-defined  $I^G J^{PC}$  quantum numbers in selected  $\pi^-\pi^-\pi^+$  partial waves as a function of two-pion mass, three-pion mass, and squared four-momentum transfer. This approach not only reduces the model dependence of the PWA but in addition allows us to study  $\pi^-\pi^+$  isobar resonances and possible distortions of their amplitudes due to final-state interactions. We applied this method to the  $\pi^-\pi^-\pi^+$  proton-target data in order to study the isoscalar  $J^{PC} = 0^{++}$   $\pi^-\pi^+$  isobars, i.e.  $f_0$  states. Comparing the result of the freed-isobar PWA with the one of the conventional PWA, we find that the parameterizations employed in the conventional PWA do not cause artificial resonance-like structures in the extracted partial-wave amplitudes and that partial waves with  $[\pi\pi]_S$  and  $f_0(980)$  isobars can be well separated. Using the freed-isobar PWA method, we establish, for the first time, the  $3\pi$  decay modes  $\pi(1800) \rightarrow f_0(1500)\pi$ ,  $\pi_2(1880) \rightarrow f_0(980)\pi$ , and  $\pi_2(1880) \rightarrow f_0(1500)\pi$  in a model-independent way.

We performed resonance-model fits for all analyzed data samples using different models. Due to the high precision of the  $\pi^-\pi^-\pi^+$  proton-target data, the resonance model employed for this data sample is the most comprehensive one. Out of the 88 waves, a subset of 14 partial waves with  $J^{PC} = 0^{-+}$ ,  $1^{++}$ ,  $2^{++}$ ,  $2^{-+}$ ,  $4^{++}$ , and spin-exotic  $1^{-+}$  quantum numbers was selected for the resonance-model fit. Compared to previous analyses of the  $3\pi$  final state, this is by far the largest wave set that is consistently described in a single resonance-model fit. The amplitudes of the 14 waves including all of their mutual interference terms are described simultaneously using 11 resonances. The resonance models for the other data samples contain only subsets of these resonances. For the  $\pi^-\pi^-\pi^+$  proton-target data, we performed, for the first time, a simultaneous resonance-model fit in all 11  $t'$  bins. Using this novel  $t'$ -resolved approach, we extracted the  $t'$  dependences of the amplitudes of the resonant and non-resonant wave components in individual partial waves from the data in a model-independent way. This allows us to study the production mechanism of resonances in terms of their  $t'$  spectra and of the  $t'$  dependences of their relative phases with respect to other wave components. Most resonances are produced with a phase that is approximately independent of  $t'$ , which is expected if a

single production mechanism contributes over the analyzed  $t'$  range. With the  $t'$ -resolved approach, we also take into account the change of the shape of the  $m_{3\pi}$  intensity distributions of the partial waves with  $t'$ , which for some waves is very pronounced. Hence our approach avoids a potential broadening of resonance peaks and artificial incoherences between waves and wave components that may have led to dilutions and distortions of resonance signals in previous analyses. In addition, the  $t'$ -resolved approach exploits the generally different  $t'$  dependences of the resonant and non-resonant wave components in order to better disentangle the two.

We have measured the Breit-Wigner masses and widths of the  $a_J$ -like resonances:  $a_1(1260)$ ,  $a_1(1640)$ ,  $a_2(1320)$ ,  $a_2(1700)$ ,  $a_4(2040)$ , and the novel resonance-like  $a_1(1420)$ ; and those of the  $\pi_J$ -like resonances:  $\pi(1800)$ ,  $\pi_2(1670)$ ,  $\pi_2(1880)$ ,  $\pi_2(2005)$ , and the spin-exotic  $\pi_1(1600)$ . The parameters of  $a_2(1320)$ ,  $a_4(2040)$ ,  $\pi(1800)$ , and  $\pi_2(1670)$  are reliably extracted with comparatively small uncertainties. The values from the  $\pi^-\pi^-\pi^+$  proton- and Pb-target data are in good agreement. The  $a_2(1320)$  and  $a_4(2040)$  parameters from the  $\eta^{(\prime)}\pi$  data also agree with the  $\pi^-\pi^-\pi^+$  results. The  $a_2(1320)$  and  $\pi(1800)$  parameter values are consistent with the ones from previous experiments. Our values for the  $a_4(2040)$  mass and width are the most accurate so far. We find a lower  $a_4(2040)$  mass and a larger width than some of the previous experiments. The  $\pi_2(1880)$  is found to decay into  $f_2(1270)\pi D$ ,  $f_0(980)\pi D$ , and  $f_0(1500)\pi D$ . Its coupling to the  $\rho(770)\pi F$  and  $f_2(1270)\pi S$  decay modes is found to be small. This decay pattern contradicts model predictions that assume a hybrid interpretation of the  $\pi_2(1880)$ . The measured  $\pi_2(1880)$  width is consistent with the world average, its mass is found to be smaller. The  $\pi^-\pi^-\pi^+$  proton-target data require a third  $J^{PC} = 2^{-+}$  resonance, the  $\pi_2(2005)$ , which has so far been reported by only two previous experiments. The  $a_1(1260)$  parameters have large systematic uncertainties mainly because of large backgrounds from non-resonant components. Due to the dominant  $a_1(1260)$  and  $a_2(1320)$  signals, the parameters of their radial excitations,  $a_1(1640)$  and  $a_2(1700)$ , are difficult to measure, which leads to large systematic uncertainties of the respective resonance parameters in the analysis of the  $\pi^-\pi^-\pi^+$  proton-target data. Resonance-model fits of the  $\eta^{(\prime)}\pi$  data using Breit-Wigner amplitudes were inconclusive concerning the  $a_2(1700)$  parameter values. This shows the limitations of our simple sum-of-Breit-Wigner approach. Together with the JPAC collaboration, we performed a resonance-model fit of the  $\eta\pi$   $D$ -wave intensity distribution using a more advanced model that adheres to the principles of the relativistic  $S$ -matrix, in particular analyticity and unitarity. This analysis yielded pole positions for  $a_2(1320)$  and  $a_2(1700)$  and showcases the superiority of this approach.

The  $\pi^-\pi^-\pi^+$  proton- and Pb-target data require a spin-exotic resonance, the  $\pi_1(1600)$ , in the  $1^{-+} 1^+ \rho(770)\pi P$  wave. The  $t'$ -resolved analysis allows us to establish, for the first time, that for a proton target a significant  $\pi_1(1600)$  signal appears only for  $t' \gtrsim 0.5 \text{ (GeV}/c)^2$ , whereas at low  $t'$  the intensity of the spin-exotic wave is saturated by Deck-like non-resonant contributions. This finding reconciles the seemingly contradictory results from previous experiments that led to a controversy about the existence of the  $\pi_1(1600)$ . Our values for the  $\pi_1(1600)$  Breit-Wigner parameters have large uncertainties, which are mainly due to the large background contributions from non-resonant processes. The width measured in the  $\pi^-\pi^-\pi^+$  proton-target data is larger than the values reported by previous experiments including our own result from the  $\pi^-\pi^-\pi^+$  Pb-target data. Resonance-model fits of the  $\eta^{(\prime)}\pi$  data using Breit-Wigner amplitudes were inconclusive concerning the parameters of the  $\pi_1$  in the spin-exotic  $P$ -waves. However, an  $\eta\pi$ - $\eta'\pi$  coupled-channel analysis performed by the JPAC collaboration using an analytic and unitary model based on  $S$ -matrix principles shows that the COMPASS data can be described consistently by only a single  $\pi_1(1600)$  resonance pole. Breit-Wigner-based analyses of previous experiments required an additional  $\pi_1(1400)$  resonance in order to explain the  $\eta\pi$  data. However, compared to predictions from models and lattice QCD a  $\pi_1(1400)$  would be too light and too close to the  $\pi_1(1600)$ . The JPAC result shows that no extra  $\pi_1(1400)$  is required and that the  $\pi_1(1400)$  signals found in previous analyses are probably due to the  $\pi_1(1600)$ .

The highly precise  $\pi^-\pi^-\pi^+$  proton-target data also revealed an unexpected novel resonance-like signal, the  $a_1(1420)$ , which is observed only in the  $f_0(980)\pi$  decay channel and is well-described by a Breit-Wigner amplitude. The  $a_1(1420) \rightarrow f_0(980)\pi$  signal was confirmed by the freed-isobar PWA,

without separating the data into non-orthogonal waves with  $I^G J^{PC} = 0^+ 0^{++}$  isobar resonances. If interpreted as a genuine resonance, the  $a_1(1420)$  would be a supernumerary state and a candidate for a four-quark state. However, the peculiar properties of the  $a_1(1420)$  signal indicate that it might not be due to a resonance but a triangle singularity, which is related to the  $a_1(1260)$  ground state. Preliminary studies show that the latter hypothesis fits the data equally well as the Breit-Wigner amplitude.

In addition to diffractive production, COMPASS has studied the pion-induced production of  $\pi^- \pi^- \pi^+$  in the Coulomb field of a Pb target nucleus, i.e. by quasi-real photon exchange. This process is strongly enhanced at very low squared four-momentum transfer  $t' < 10^{-3} (\text{GeV}/c)^2$ . In this kinematic region, photoproduced states have spin-projection quantum numbers of  $M = \pm 1$  with respect to the beam axis because of the transverse nature of the photon, whereas diffractively produced states have  $M = 0$ . We separated these contributions by means of a partial-wave analysis. Using the equivalent-photon approach, we determined the partial widths for  $a_2(1320) \rightarrow \pi\gamma$  and, for the first time, the one for  $\pi_2(1670) \rightarrow \pi\gamma$  from the measured production cross sections of the resonances. In this analysis, we take into account sizable corrections from the distortion of the pion wave function in the Coulomb field of the nucleus, which have been neglected in previous measurements. The subprocess  $\pi^- + \gamma \rightarrow \pi^- \pi^- \pi^+$  that is embedded in the measured scattering reaction also allows us to test predictions from chiral perturbation theory at low three-pion mass. COMPASS has measured the cross section for  $\pi^- \pi^- \pi^+$  Coulomb production in the range  $m_{3\pi} < 5m_\pi$  using PWA techniques and confirms the leading-order predictions from chiral perturbation theory.

A focus of current research is the improvement of the analysis models, in particular for the analysis of the high-precision  $\pi^- \pi^- \pi^+$  proton-target data, which is dominated by systematic uncertainties. We pursue two strategies in order to reduce these uncertainties: (i) by reducing the model dependence, e.g. by extending the freed-isobar PWA to more freed waves, and (ii) by employing more advanced models that incorporate more physical constraints, similar to what was done for  $\eta^{(\prime)}\pi$ . For the latter, in particular a better understanding of the non-resonant contributions from double-Regge exchange processes, such as the Deck effect, is essential.

COMPASS data could also settle the claims by previous experiments of  $\pi_1$  signals in  $\pi^- \pi^0 \pi^0$ ,  $\pi^- \pi^0 \omega$ , and  $\pi^- f_1(1285)$  from pion diffraction, which is another focus of future work. An additional line of research is the study of kaon diffraction into various final states by using the  $K^-$  component in the beam. Since kaons are not eigenstates of  $G$  parity, nearly all kaon states can be produced in kaon diffraction. A first analysis of the diffractive process  $K^- + p \rightarrow K^- \pi^- \pi^+ + p$  on a subset of the available data showed promising results [301, 302].

The exploration of the light-meson spectrum is a global effort with several experiments focusing on different parts of the spectrum. In addition to COMPASS, the VES experiment at IHEP (Russia) studies diffractive-dissociation reactions. Using a  $29 \text{ GeV}/c$  pion beam on a Be target, the VES experiment collected data samples of  $87 \cdot 10^6 \pi^- \pi^- \pi^+$  and  $32 \cdot 10^6 \pi^- \pi^0 \pi^0$  events that are even larger than the COMPASS data samples of  $46 \cdot 10^6 \pi^- \pi^- \pi^+$  and  $3.5 \cdot 10^6 \pi^- \pi^0 \pi^0$  events [117, 303–307]. Despite the lower beam energy and the different target, the PWA results from VES are in good agreement with the COMPASS results [307]. In particular, the VES experiment also observes a narrow peak in the  $1^{++} 0^+ f_0(980) \pi P$  wave of the  $3\pi$  data that is consistent with the  $a_1(1420)$  signal observed by COMPASS. Two experiments at JLab are dedicated to the study of the light-meson spectrum: GlueX and MesonEx. The GlueX experiment [308–313] uses a high-intensity beam of linearly polarized photons that is produced from the primary  $12 \text{ GeV}$  electron beam of the CEBAF accelerator using coherent Bremsstrahlung from a thin diamond radiator. The produced photons have a most probable energy of about  $9 \text{ GeV}$  and a polarization of about  $40\%$ . The MesonEx experiment at CLAS12 [314, 315] studies electroproduction of mesons using an  $11 \text{ GeV}$  high-intensity electron beam from CEBAF. The quasi-real photons exchanged with the target have energies from  $6.5$  to  $10.5 \text{ GeV}$ . Both experiments study photoproduction of mesons on proton targets at intermediate energies. Due to the—compared to COMPASS—lower center-of-momentum energies, the photons may interact via various exchange processes with the target proton and also target excitations can be studied. This has

the advantage that in contrast to high-energy pion diffraction, where the produced states are limited to isovector states with negative  $G$  parity, states with a wide variety of  $I^G J^{PC}$  quantum numbers are accessible. In particular, both experiments will search for the spin-exotic  $\eta_1$ , which would be the isoscalar partner of the  $\pi_1(1600)$ . The  $\eta_1$  is expected to decay, for example, into  $\eta f_2(1270)$  and  $a_2(1320)\pi$ , which can be measured e.g. in the  $\eta\pi\pi$  final state. But also spin-exotic states with  $J^{PC} = 0^{+-}$  and  $2^{+-}$  quantum numbers (i.e.  $b_0$ ,  $h_0$ ,  $h'_0$ , and  $b_2$ ,  $h_2$ ,  $h'_2$ ) that cannot be produced in pion diffraction are in principle accessible. As was discussed in Section 6.3.3, photoproduction of hybrid mesons is expected to be enhanced with respect to pion-induced reactions. In contrast, currently available data on  $3\pi$  photoproduction seem to suggest that the production rate of the hybrid candidate  $\pi_1(1600)$  is suppressed although it is observed to decay into  $\rho(770)\pi$ . The data from the JLab experiments will help to solve this puzzle. A complication caused by the lower beam energies is the fact that particles emitted from the beam and the target vertex of the scattering reaction, i.e. beam and target fragmentation, are less clearly kinematically separated than in high-energy diffraction, making it necessary to take into account baryon excitations in the analysis of excited mesons. Light mesons are also studied at  $e^+e^-$  machines using two-photon processes, processes with initial-state radiation, and multi-body decays of tau leptons or heavy-quark mesons. The CMD-3 [316] and SND [317, 318] experiments at BINP perform high-precision exclusive measurements of  $e^+e^- \rightarrow$  hadrons cross sections up to center-of-momentum energies of 2 GeV. These data allow detailed studies of the properties of the light vector mesons  $\rho$ ,  $\omega$ ,  $\phi$  and of their excited states in a large variety of final states. The BESIII experiment [319] at IHEP (China) also studies the light-meson spectrum, for example, by high-precision measurements of radiative  $J/\psi$  decays. These decays are a rich source of light mesons and allow e.g. the study of  $f_0$  and  $f_2$  states up to high masses. Also the  $B$ -factories, i.e. the *BABAR* [320], *Belle* [320], *Belle II* [321], and *LHCb* experiments [322], have studied and are studying light mesons, although this research is not their main goal.

In the future, the PANDA experiment at GSI [323] will measure proton-antiproton annihilations in flight and will continue the successful meson-spectroscopy programs carried out by the Crystal Barrel experiment [324] at LEAR and by the E760 [325–327] and E835 experiments [328] at Fermilab. In addition to a broad heavy-meson spectroscopy program, which will in particular focus on the illusive  $X$ ,  $Y$ ,  $Z$  states, PANDA will also study light mesons. Proton-antiproton annihilations provide a gluon-rich environment, which should enhance the production of glueballs or hybrid states [329]. For example, isoscalar scalar mesons, i.e.  $f_0$  states, can be studied in reactions like  $p\bar{p} \rightarrow 3\pi^0$ ,  $\eta\eta\pi^0$ ,  $\eta\eta'\pi^0$ ,  $K\bar{K}\pi^0$ , and  $5\pi^0$  [330–333], for which PANDA is expected to record high-precision data samples. At CERN, there are plans for a new fixed-target experiment covering a wide range of QCD-related research topics [334]. One of these topics is the high-precision study of the kaon excitation spectrum by measuring high-energy kaon-diffraction reactions. Compared to the non-strange light mesons, the kaon spectrum is not very well known [5]. From the spectroscopy point of view, it is of most importance to complete the light-meson  $SU(3)_{\text{flavor}}$  nonets and to search for the  $SU(3)_{\text{flavor}}$  partners of exotic states. A better knowledge of the kaon spectrum will also help to improve the analyses that search for  $CP$  violation in multi-body hadronic decays of  $D$  and  $B$  mesons, where kaon resonances appear in the subsystems of various final states. Using RF-separation techniques [335–337], the kaon fraction of the high-intensity hadron beam in the SPS M2 beam line could be dramatically enhanced so that data samples of much higher precision than any previous experiment could be obtained. For example, for the  $K^-\pi^-\pi^+$  final state, data samples of the order of  $10^7$  events could be collected.

## Acknowledgments

We are greatly indebted to our COMPASS collaborators and colleagues, especially to S. U. Chung, W. Dünnweber, M. Faessler, J. M. Friedrich, and S. Paul for many enlightening discussions. We thank in particular the students A. Austregesilo, K. A. Bicker, S. Grabmüller, F. Haas, S. Huber, P. K. Jasinski, F. M. Kaspar, M. C. Krämer, F. M. Krinner, M. Mikhasenko, T. Nagel, S. Neubert, T. Schlüter, S. Schmeing, S. Uhl, M. Wagner, S. Wallner, and Q. Weitzel, who played an important role in collecting and analyzing the data discussed here. We also gratefully acknowledge the support of the CERN management and staff as well as the skills and efforts of the technicians of the collaborating institutions.

We are especially indebted to the members of the JPAC collaboration, in particular to M. Pennington and A. Szczepaniak, for many useful discussions and for a fruitful collaboration on the analysis of COMPASS spectroscopy data. We also would like to thank E. L. Berger, C. Hanhart, N. Kaiser, E. Klemp, B. Kubis, W. Ochs, J. Pelaez, A. Sarantsev, A. M. Zaitsev, and Q. Zhao for important theory input and discussions. We have in addition profited greatly from conversations and discussions during a series of PWA workshops: a joint COMPASS-JLab-GSI Workshop on Physics and Methods in Meson Spectroscopy (Garching/2008), Workshops on Spectroscopy at COMPASS held 2009 and 2011 in Garching, and in the context of the (PWA)ATHOS workshop series (Camogli/2012, Kloster Seeon/2013, Ashburn/2015, Bad Honnef/2017, and Beijing/2018). We thank J. Beringer for allowing us to use the PDG computer code to create the ideograms. D. R. would like to thank the Excellence Cluster “Universe” for supporting many visits to Munich during the past years.

We acknowledge the support by the German Bundesministerium für Bildung und Forschung (BMBF), the DFG cluster of excellence “Origin and Structure of the Universe”, the DFG Collaborative Research Centre/Transregio 110, and the computing facilities of the Computational Center for Particle and Astrophysics (C2PAP).

## Appendix A. *n*-Body Phase-Space Element

A convenient parameterization for the  $n$ -body differential phase-space element for  $n > 2$  is obtained by applying the phase-space recurrence relation [49, 131] such that the  $n$ -body phase space is expressed as a product of  $(n - 1)$  two-body differential phase-space elements.

For the decay of a parent state with mass  $m$  into two daughter particles with masses  $m_1$  and  $m_2$ , the two-body differential phase-space element is given by Eq. (60):

$$d\Phi_2(m, \underbrace{\vartheta, \phi}_{=: \Omega}; m_1, m_2) = \frac{1}{(4\pi)^2} \frac{q(m; m_1, m_2)}{m} \underbrace{d\cos \vartheta \, d\phi}_{=: d\Omega}. \quad (\text{A.1})$$

Here,  $q(m; m_1, m_2)$  is the magnitude of the two-body breakup momentum in the parent rest frame as given by Eqs. (62) and (63). The polar angle  $\vartheta$  and the azimuthal angle  $\phi$  in Eq. (A.1) describe the direction of daughter 1 in the parent rest frame.<sup>121</sup>

The decomposition of the  $n$ -body decay  $X \rightarrow 1 + 2 + \dots + n$  into a chain of  $(n - 1)$  successive two-body decays is not unique, but all decompositions are mathematically equivalent. Using Eq. (A.1), the  $n$ -body phase-space element can be written as [107, 131]

$$\begin{aligned} d\Phi_n(m_{s_1}, \underbrace{m_{s_2}, \dots, m_{s_{n-1}}, \Omega_{s_1}, \Omega_{s_2}, \dots, \Omega_{s_{n-1}}}_{=: \tau_n}) \\ = \frac{1}{(4\pi)^2} \frac{q_{s_1}}{m_{s_1}} d\Omega_{s_1} \prod_{i=2}^{n-1} \frac{2m_{s_i}}{2\pi} \frac{dm_{s_i}}{(4\pi)^2} \frac{1}{m_{s_i}} \frac{q_{s_i}}{m_{s_i}} d\Omega_{s_i}. \end{aligned} \quad (\text{A.2})$$

The  $m_{s_i}$  are the parent masses of the  $n - 1$  two-body systems  $s_i$ , where  $m_{s_1} = m_X$ . The  $\Omega_{s_i}$  are the angles and the  $q_{s_i}$  the breakup momenta of the two-body systems. The  $(3n - 4)$  phase-space variables that define the kinematics of the  $n$  final-state particles are represented by  $\tau_n$ .

## Appendix B. Wigner *D*-Function

The Wigner *D*-function  $D_{M' M}^J(\alpha, \beta, \gamma)$  [111, 112] represents the transformation property of a spin state  $|J, M\rangle$  under an arbitrary active rotation  $\hat{\mathcal{R}}$  defined by the three Euler angles  $\alpha$ ,  $\beta$ , and  $\gamma$ . Since the  $|J, M\rangle$  basis is complete, the rotated state can be expressed as a linear combination of the basis states:

$$\begin{aligned} \hat{\mathcal{R}}(\alpha, \beta, \gamma) |J, M\rangle &= \underbrace{\sum_{M'=-J}^{+J} |J, M'\rangle \langle J, M'|}_{=: \mathbb{1}} \underbrace{\hat{\mathcal{R}}(\alpha, \beta, \gamma) |J, M\rangle}_{=: D_{M' M}^J(\alpha, \beta, \gamma)} \\ &= \sum_{M'=-J}^{+J} D_{M' M}^J(\alpha, \beta, \gamma) |J, M'\rangle. \end{aligned} \quad (\text{B.1})$$

We use the *y*-*z*-*y* convention from Ref. [113], where

$$\hat{\mathcal{R}}(\alpha, \beta, \gamma) = e^{-i\alpha \hat{J}_z} e^{-i\beta \hat{J}_y} e^{-i\gamma \hat{J}_z}. \quad (\text{B.2})$$

---

<sup>121</sup>Since in the parent rest frame the two daughter particles are emitted back to back, the choice of daughter particle 1 is a matter of convention.

Here,  $\hat{J}_y$  and  $\hat{J}_z$  are the  $y$  and  $z$  components of the angular momentum operator  $\hat{J}$ , respectively. Hence

$$\begin{aligned} D_{M' M}^J(\alpha, \beta, \gamma) &= \langle J, M' | e^{-i\alpha \hat{J}_z} e^{-i\beta \hat{J}_y} e^{-i\gamma \hat{J}_z} | J, M \rangle \\ &= e^{-iM' \alpha} \underbrace{\langle J, M' | e^{-i\beta \hat{J}_y} | J, M \rangle}_{=: d_{M' M}^J(\beta)} e^{-iM \gamma} \end{aligned} \quad (\text{B.3})$$

with the Wigner (small)  $d$ -function (see e.g. Ref. [338] and Eq. (3) in Section 4.3.1 of Ref. [339])

$$\begin{aligned} d_{M' M}^J(\beta) &= (-1)^{J+M'} \sqrt{(J+M')! (J-M')! (J+M)! (J-M)!} \\ &\times \sum_k \left[ \frac{(-1)^k}{k! (J+M'-k)! (J+M-k)! (k-M'-M)!} \left( \cos \frac{\beta}{2} \right)^{2k-M'-M} \left( \sin \frac{\beta}{2} \right)^{2J+M'+M-2k} \right]. \end{aligned} \quad (\text{B.4})$$

The sum in Eq. (B.4) runs over all values of  $k$ , for which the factorials are non-negative.

The Wigner  $D$ -functions are orthogonal, i.e.

$$\int_0^{2\pi} d\alpha \int_{-1}^1 d\cos \beta \int_0^{2\pi} d\gamma D_M^J(\alpha, \beta, \gamma) D_{M' K'}^{J'*}(\alpha, \beta, \gamma) = \frac{8\pi^2}{2J+1} \delta_{JJ'} \delta_{MM'} \delta_{KK'} . \quad (\text{B.5})$$

Since the decay amplitudes  $\Psi_i^\varepsilon(\tau_n; m_X)$  in our PWA model in Eq. (195) are constructed by recursive application of Eq. (150), they are linear combinations of products of Wigner  $D$ -functions and hence inherit the orthogonality property in Eq. (B.5). As a consequence, the off-diagonal elements of the phase-space integral matrix  $I_{ij}^\varepsilon$  for waves  $i$  and  $j$  with reflectivity  $\varepsilon$  as defined in Eq. (185) vanish, unless the quantum numbers that determine the  $D$ -functions in the decay amplitudes are the same for both waves, i.e. the two waves have the same  $J^P M^\varepsilon$  quantum numbers and the same isobar and orbital-angular-momentum quantum numbers in the decay chain.<sup>122</sup> For orthogonal decay amplitudes, also the overlap  $\text{Ovl}_{ij}^\varepsilon(m_X, t')$  as defined in Eq. (209) vanishes. Depending on the analyzed final state, the orthogonality of the decay amplitudes is broken by the Bose symmetrization in Eq. (159). In practice, the corresponding off-diagonal elements of  $I_{ij}^\varepsilon$  are often still close to zero. It is important to note that decay amplitudes that correspond to decay chains with different radially excited states of an isobar resonance are in general not orthogonal and the corresponding elements of the integral matrix may have large magnitudes. In this case, the two decay amplitudes correspond to similar phase-space distributions, which may lead to ambiguity and distinguishability issues at the partial-wave decomposition stage (see also Section 5.2.8).

## Appendix C. Angular Distribution for Two-Body Decay

In order to derive the angular distribution for the two-body decay  $r \rightarrow 1 + 2$  in Eq. (147), we consider the special case where  $\vartheta_r = \phi_r = 0$ , i.e. where particles 1 and 2 move in opposite directions along the quantization axis. Hence the corresponding two-particle plane-wave center-of-momentum helicity state  $|0, 0; \lambda_1, \lambda_2\rangle$  is an eigenstate of the  $z$  component  $\hat{J}_z$  of the angular-momentum operator  $\hat{J}$ . The total spin projection of this state is  $\lambda = \lambda_1 - \lambda_2$ , if we assume without loss of generality that

---

<sup>122</sup>Note that the total intrinsic spins  $S_r$  of the daughter particles of the isobars  $r$  in the decay chain appear in Eq. (150) only in Clebsch-Gordan coefficients. Hence the decay amplitudes of two partial waves that differ only in the  $S_r$  are linear dependent, i.e. not orthogonal.

particle 1 moves in the  $+z$  direction. We express the two-particle plane-wave state in terms of angular-momentum helicity states:

$$|0, 0; \lambda_1, \lambda_2\rangle = \sum_{J_r=0}^{\infty} |J_r, \lambda; \lambda_1, \lambda_2\rangle \underbrace{\langle J_r, \lambda; \lambda_1, \lambda_2|0, 0; \lambda_1, \lambda_2\rangle}_{=: C_{J_r}}. \quad (\text{C.1})$$

From this state, we can construct an arbitrary two-particle plane-wave center-of-momentum helicity state by applying the active rotation  $\hat{\mathcal{R}}(\phi_r, \vartheta_r, 0)$ , where  $\vartheta_r$  and  $\phi_r$  describe the direction of particle 1:<sup>123</sup>

$$|\vartheta_r, \phi_r; \lambda_1, \lambda_2\rangle = \hat{\mathcal{R}}(\phi_r, \vartheta_r, 0) |0, 0; \lambda_1, \lambda_2\rangle = \sum_{J_r=0}^{\infty} C_{J_r} \hat{\mathcal{R}}(\phi_r, \vartheta_r, 0) |J_r, \lambda; \lambda_1, \lambda_2\rangle. \quad (\text{C.2})$$

The coefficients  $C_{J_r}$  are fixed by the normalization of the Wigner  $D$ -function and the two-particle states. Together with the transformation property of a spin state under rotations as given in Eq. (B.1), this yields

$$|\vartheta_r, \phi_r; \lambda_1, \lambda_2\rangle = \sum_{J_r=0}^{\infty} \sum_{M_r=-J_r}^{+J_r} \sqrt{\frac{2J_r+1}{4\pi}} D_{M_r, \lambda}^{J_r}(\phi_r, \vartheta_r, 0) |J_r, M_r; \lambda_1, \lambda_2\rangle. \quad (\text{C.3})$$

From the above equation, Eq. (147) follows directly by using the orthonormality of the two-particle states.

## Appendix D. List of Angular-Momentum Barrier Factors

Using the parameterization for the angular-momentum barrier factor  $F_L(z)$  in Eq. (97) from Ref. [56] and the normalization  $F_L(z=1) = 1$ , the barrier factors for the lowest values of  $L$  read

$$F_0^2(z) = 1, \quad (\text{D.1})$$

$$F_1^2(z) = \frac{2z}{z+1}, \quad (\text{D.2})$$

$$F_2^2(z) = \frac{13z^2}{z^2+3z+9}, \quad (\text{D.3})$$

$$F_3^2(z) = \frac{277z^3}{z^3+6z^2+45z+225}, \quad (\text{D.4})$$

$$F_4^2(z) = \frac{12\,746z^4}{z^4+10z^3+135z^2+1575z+11025}, \quad (\text{D.5})$$

$$F_5^2(z) = \frac{998\,881z^5}{z^5+15z^4+315z^3+6300z^2+99\,225z+893\,025}, \text{ and} \quad (\text{D.6})$$

$$F_6^2(z) = \frac{118\,394\,977z^6}{z^6+21z^5+630z^4+18\,900z^3+496\,125z^2+9\,823\,275z+108\,056\,025}. \quad (\text{D.7})$$

## Appendix E. Chung-Trueman Parameterization of the Spin-Density Matrix

The Chung-Trueman parameterization of the spin-density matrix [115] exploits the fact that any Hermitian positive-semidefinite matrix  $\mathbf{A}$  can be written as

$$\mathbf{A} = \mathbf{L} \mathbf{L}^\dagger, \quad (\text{E.1})$$

---

<sup>123</sup>Since a direction is defined by only two angles, we use the convention of Ref. [107] and set the third Euler angle  $\gamma = 0$ . Another commonly used convention is  $\gamma = -\phi_r$  [106].

where  $\mathbf{L}$  is a lower triangular matrix with real-valued and non-negative diagonal entries. This so-called Cholesky decomposition is unique in case  $\mathbf{A}$  is positive-definite. If we reinterpret the wave index  $i$  defined in Eq. (160) as an index that enumerates the various partial waves, we can treat the transition amplitudes  $\bar{\mathcal{T}}_i^r$  in Eq. (168) as elements of an  $N_{\text{waves}} \times N_r$  matrix  $\bar{\mathcal{T}}$ , where  $N_{\text{waves}}$  is the dimension of the spin-density matrix and  $N_r$  its rank, so that

$$\bar{\mathcal{T}} = \begin{pmatrix} \bar{\mathcal{T}}_1^1 & 0 & 0 & \dots & 0 \\ \bar{\mathcal{T}}_2^1 & \bar{\mathcal{T}}_2^2 & 0 & \dots & 0 \\ \bar{\mathcal{T}}_3^1 & \bar{\mathcal{T}}_3^2 & \bar{\mathcal{T}}_3^3 & \dots & 0 \\ \vdots & \vdots & \vdots & \ddots & \vdots \\ \bar{\mathcal{T}}_{N_r}^1 & \bar{\mathcal{T}}_{N_r}^2 & \bar{\mathcal{T}}_{N_r}^3 & \dots & \bar{\mathcal{T}}_{N_r}^{N_r} \\ \vdots & \vdots & \vdots & & \vdots \\ \bar{\mathcal{T}}_{N_{\text{waves}}}^1 & \bar{\mathcal{T}}_{N_{\text{waves}}}^2 & \bar{\mathcal{T}}_{N_{\text{waves}}}^3 & \dots & \bar{\mathcal{T}}_{N_{\text{waves}}}^{N_r} \end{pmatrix} \quad \text{and} \quad \bar{\rho} = \bar{\mathcal{T}} \bar{\mathcal{T}}^\dagger. \quad (\text{E.2})$$

The diagonal elements  $\bar{\mathcal{T}}_i^i$  of  $\bar{\mathcal{T}}$  are real-valued and positive.<sup>124</sup> In addition to the  $N_r$  diagonal elements, the matrix  $\bar{\mathcal{T}}$  contains  $N_r(2N_{\text{waves}} - N_r - 1)/2$  complex-valued off-diagonal elements, which yields a total of  $N_r(2N_{\text{waves}} - N_r)$  real-valued free parameters that need to be determined from data.

## Appendix F. Maximization of the Likelihood Function and Uncertainty Estimation

In order to determine the maximum likelihood estimate for the transition amplitudes, i.e.

$$\{\hat{\mathcal{T}}_i^{r\varepsilon}\} = \arg \max_{\{\mathcal{T}_i^{r\varepsilon}\}} \left[ \ln \mathcal{L}_{\text{ext}}(\{\mathcal{T}_i^{r\varepsilon}\}; \{\tau_{n,k}\}, N) \right], \quad (\text{F.1})$$

using Eq. (206) one has to solve the coupled system of  $(N_r^{\varepsilon=+1} [2N_{\text{waves}}^{\varepsilon=+1} - N_r^{\varepsilon=+1}] + N_r^{\varepsilon=-1} [2N_{\text{waves}}^{\varepsilon=-1} - N_r^{\varepsilon=-1}])$  equations of the form

$$0 = \frac{\partial \ln \mathcal{L}_{\text{ext}}(\{\mathcal{T}_i^{r\varepsilon}\}; \{\tau_{n,k}\}, N)}{\partial \text{Re}[\mathcal{T}_j^{r\varepsilon}]} \Bigg|_{\{\hat{\mathcal{T}}_i^{r\varepsilon}\}} \quad \text{and} \quad 0 = \frac{\partial \ln \mathcal{L}_{\text{ext}}(\{\mathcal{T}_i^{r\varepsilon}\}; \{\tau_{n,k}\}, N)}{\partial \text{Im}[\mathcal{T}_j^{r\varepsilon}]} \Bigg|_{\{\hat{\mathcal{T}}_i^{r\varepsilon}\}} \quad \forall j, r, \text{ and } \varepsilon \quad (\text{F.2})$$

for  $\{\hat{\mathcal{T}}_i^{r\varepsilon}\}$ . However, in practice usually numerical approaches are used to determine the maximum of  $\mathcal{L}_{\text{ext}}$  with respect to the  $\{\mathcal{T}_i^{r\varepsilon}\}$ . Traditionally, the numerical methods find the minimum of a given function. Hence we minimize the negative log-likelihood function  $-\ln \mathcal{L}_{\text{ext}}$ .

The minimization programs usually employ iterative methods to find the minimum. The most widely used minimization algorithm for PWA is the MIGRAD algorithm from the MINUIT or MINUIT2 packages [166, 167]. The algorithm uses an iterative decent method that belongs to the class of quasi-Newton methods, which are generalizations of the secant method to find the root of the first derivative for multi-dimensional functions. Since for these kind of problems, the secant equation does not specify a unique solution, the various methods differ in how they constrain the solution. The MIGRAD algorithm is based on an improved version of the Davidon-Fletcher-Powell (DFP) variable-metric algorithm [340–344]. Since the method depends heavily on the knowledge of the first derivatives, it performs best if they are known precisely. Luckily, the log-likelihood function in Eq. (206) is simple enough to calculate the Jacobian analytically (see e.g. Ref. [140]) or using automatic differentiation [345]. In PWA fits, which may easily have hundreds of free parameters, the MIGRAD algorithm is known to find the minimum reliably.

<sup>124</sup>The corresponding waves are called “anchor waves”, because they define the overall phase(s). Note that apart from differences due to numerical effects, the values of the spin-density matrix elements do not depend on the choice of the anchor waves.

Due to the central limit theorem, the likelihood function in Eq. (196) approaches in the asymptotic limit a multivariate Gaussian in the parameters  $\vec{\theta}$ , with the maximum at  $\hat{\vec{\theta}}$  and the covariance matrix  $\mathbf{V}_{\hat{\vec{\theta}}}$  of  $\hat{\vec{\theta}}$  given by

$$(V_{\hat{\vec{\theta}}}^{-1})_{ij} = E \left[ - \underbrace{\frac{\partial^2 \ln \mathcal{L}(\vec{\theta}; \vec{x})}{\partial \theta_i \partial \theta_j}}_{= H_{ij}(\vec{\theta}; \vec{x})} \right], \quad (\text{F.3})$$

where  $E[ ]$  is the expectation value with respect to  $\vec{x}$  and  $\mathbf{H}$  is the Hessian matrix of the log-likelihood function. In practice, the analytic calculation of the expectation value is often impractical. For sufficiently large  $N$ , a good estimate for  $\mathbf{V}_{\hat{\vec{\theta}}}$  is obtained by calculating the inverse of the Hessian matrix with the measured data at the maximum likelihood estimate, i.e.

$$\hat{\mathbf{V}}_{\hat{\vec{\theta}}} = -\mathbf{H}^{-1}(\hat{\vec{\theta}}; \vec{x}). \quad (\text{F.4})$$

MIGRAD provides a numerical estimate for the covariance matrix. However, the estimate of the HESSE routine of MINUIT, which calculates the covariance matrix according to Eq. (F.4) through inversion of the numerically estimated Hessian matrix of the minimized function, is usually better.

The main caveat of the MIGRAD algorithm is that it requires a comparatively large number of calls of the likelihood function to converge to the minimum. Depending on the number of events in the  $(m_X, t')$  cell and the number of waves in the model, the computation of the log-likelihood function can be computationally expensive. In such cases, the Limited-memory Broyden–Fletcher–Goldfarb–Shanno (L-BFGS) algorithm [344, 346, 347] is a better alternative. It also belongs to the class of quasi-Newton methods and requires an analytic Jacobian of the minimized function. L-BFGS uses a sparse approximation to the inverse Hessian matrix to find the minimum, so that the memory requirements grow only linearly with the number of free parameters. Therefore, it is well suited for PWA fits, which often have a large number of parameters. Another alternative minimization algorithm that is successfully used for PWA fits is called FUMILI [348, 349]. It is based on the conjugate gradient method [344, 350]. Both L-BFGS and FUMILI estimate only the function minimum. The covariance matrix of the parameters at the minimum has to be calculated separately. Due to the simple structure of the log-likelihood function in Eq. (206) the Hessian matrix can be calculated analytically (see e.g. Ref. [140]) or using automatic differentiation [345]. Using Eq. (F.4), this yields a more precise estimate for the covariance matrix compared to numerical methods.

## Appendix G. Numerical Calculation of Integral Matrices

The integral matrices  $I_{ij}^\varepsilon$  and  ${}^{\text{acc}}I_{ij}^\varepsilon$  that are defined in Eqs. (185) and (206), respectively, are calculated using Monte Carlo integration techniques. To this end, we generate  $N_{\text{MC}}$  Monte Carlo events that are uniformly distributed in the  $n$ -body phase space of the final-state particles using e.g. Eq. (A.2) (see Refs. [131, 132] for more details).<sup>125</sup> The integral matrix  $I_{ij}^\varepsilon$  is approximated by

$$I_{ij}^\varepsilon = \int d\Phi_n(\tau_n) \bar{\Psi}_i^\varepsilon(\tau_n) \bar{\Psi}_j^{\varepsilon*}(\tau_n) \approx \frac{V_n}{N_{\text{MC}}} \sum_{k=1}^{N_{\text{MC}}} \bar{\Psi}_i^\varepsilon(\tau_{n,k}) \bar{\Psi}_j^{\varepsilon*}(\tau_{n,k}), \quad (\text{G.1})$$

where  $V_n$  is the volume of the phase space as defined in Eq. (187). To calculate the integral matrix  ${}^{\text{acc}}I_{ij}^\varepsilon$ , the  $N_{\text{MC}}$  phase-space Monte Carlo events are processed through the detector simulation and are then subjected to the event reconstruction and event selection procedure like real data. This

---

<sup>125</sup>These events are hence distributed according to the phase-space density  $\rho_n(\tau_n)$  that is defined in Eq. (138).

yields a sample of  $N_{\text{MC}}^{\text{acc}}$  accepted phase-space Monte Carlo events, which are used to calculate an approximation to the integral matrix

$$\begin{aligned} {}^{\text{acc}}I_{ij}^{\varepsilon} &= \int d\Phi_n(\tau_n) \epsilon(\tau_n) \Psi_i^{\varepsilon}(\tau_{n,k}) \Psi_i^{\varepsilon*}(\tau_{n,k}) \\ &\approx \frac{V_n}{N_{\text{MC}}} \frac{1}{\sqrt{I_{ii}^{\varepsilon} I_{jj}^{\varepsilon}}} \sum_{k=1}^{N_{\text{MC}}} \epsilon(\tau_{n,k}) \bar{\Psi}_i^{\varepsilon}(\tau_{n,k}) \bar{\Psi}_j^{\varepsilon*}(\tau_{n,k}) = \frac{V_n}{N_{\text{MC}}} \frac{1}{\sqrt{I_{ii}^{\varepsilon} I_{jj}^{\varepsilon}}} \sum_{k=1}^{N_{\text{MC}}^{\text{acc}}} \bar{\Psi}_i^{\varepsilon}(\tau_{n,k}) \bar{\Psi}_j^{\varepsilon*}(\tau_{n,k}) . \end{aligned} \quad (\text{G.2})$$

The acceptance weight  $\epsilon(\tau_{n,k})$  for an individual Monte Carlo event is either 1, if the event was detected and selected for the analysis, or 0 otherwise. Hence the acceptance is taken into account by summing only over the accepted phase-space Monte Carlo events. Due to the finite size of the Monte Carlo data samples, the integral matrices have statistical uncertainties. Their size depends on the number of Monte Carlo events, the phase-space volume, and the shape of the amplitudes. The Monte Carlo samples are chosen to be large enough so that these uncertainties are negligible compared to the statistical uncertainties of the real data.

Note that the Monte Carlo approximation for  $I_{ij}^{\varepsilon}$  in Eq. (G.1) is proportional to the phase-space volume  $V_n$  and that consequently the Monte Carlo approximation for  ${}^{\text{acc}}I_{ij}^{\varepsilon}$  in Eq. (G.2) is independent of  $V_n$ . As was discussed in Sections 5.2.4 and 5.2.5, the normalization of the decay and transition amplitudes in Eqs. (186), (188), (191), and (192) fixes only the relative normalization of the transition amplitudes up to an arbitrary common normalization factor that is fixed via Eqs. (203) and (204) by maximizing the extended likelihood function in Eq. (206). We hence obtain the same maximum likelihood estimate for the transition amplitudes when we use the integral matrix  $\tilde{I}_{ij}^{\varepsilon} := I_{ij}^{\varepsilon}/V_n$  instead of  $I_{ij}^{\varepsilon}$  in Eqs. (186) and (188) to normalize the decay amplitudes. This way we do not need to know  $V_n$  in order to perform the partial-wave decomposition, i.e. the first analysis stage.

## Appendix H. Additional Observables

In order to interpret the relative phase  $\Delta\phi_{ij}^{\varepsilon}(m_X, t')$  between two waves  $i$  and  $j$  with reflectivity  $\varepsilon$ , it is important to take into account the *degree of coherence*  $\text{Coh}_{ij}^{\varepsilon}(m_X, t')$  between the two partial-wave amplitudes. This quantity is given by

$$\text{Coh}_{ij}^{\varepsilon}(m_X, t') := \frac{|\varrho_{ij}^{\varepsilon}(m_X, t')|}{\sqrt{\varrho_{ii}^{\varepsilon}(m_X, t') \varrho_{jj}^{\varepsilon}(m_X, t')}} = \sqrt{\frac{\text{Re}^2[\varrho_{ij}^{\varepsilon}(m_X, t')] + \text{Im}^2[\varrho_{ij}^{\varepsilon}(m_X, t')]}{N_i^{\varepsilon}(m_X, t') N_j^{\varepsilon}(m_X, t')}} . \quad (\text{H.1})$$

Note that due to the Cauchy-Schwartz inequality,  $\text{Coh}_{ij}^{\varepsilon} \leq 1$ . Also,  $\text{Coh}_{ii}^{\varepsilon} = 1$  by definition. For PWA models with rank-1 spin-density matrix, i.e.  $N_r^{\varepsilon} = 1$ , all partial-wave amplitudes are fully coherent, i.e.

$$\text{Coh}_{ij}^{\varepsilon}(m_X, t') = \frac{|\mathcal{T}_i^{\varepsilon}(m_X, t') \mathcal{T}_j^{\varepsilon*}(m_X, t')|}{\sqrt{|\mathcal{T}_i^{\varepsilon}(m_X, t')|^2 |\mathcal{T}_j^{\varepsilon}(m_X, t')|^2}} = 1 . \quad (\text{H.2})$$

If the rank of the spin-density matrix is larger than 1, the coherence is in general reduced. In order to interpret resonance signals in the relative phases, the degree of coherence of the respective waves should be close to unity.

Similar to Eq. (210), we can calculate the number of events  $N_{\text{pred}}^{\text{acc}}(m_X, t')$  that it is predicted by the model to be measured by a detector with acceptance  $\epsilon(m_X, t')$  in a given  $(m_X, t')$  cell:

$$\begin{aligned} N_{\text{pred}}^{\text{acc}}(m_X, t') &= \sum_{\varepsilon=\pm 1} \left\{ \sum_i^{N_{\text{waves}}^{\varepsilon}} N_i^{\varepsilon}(m_X, t') {}^{\text{acc}}I_{ii}^{\varepsilon} + \sum_{i,j: i < j}^{N_{\text{waves}}^{\varepsilon}} 2 \text{Re}[\varrho_{ij}^{\varepsilon}(m_X, t') {}^{\text{acc}}I_{ij}^{\varepsilon}] \right\} + N_{\text{flat}}(m_X, t') {}^{\text{acc}}I_{\text{flat}} . \end{aligned} \quad (\text{H.3})$$

Limiting the sums in Eq. (H.3) to a subset of partial wave or even a single wave and comparing the  $N_{\text{pred}}^{\text{acc}}(m_X, t')$  value with the corresponding  $N_{\text{pred}}(m_X, t')$  value from Eq. (210) allows us to study the effect of the detector acceptance on the partial-wave intensities.

## Appendix I. Resonance Parameters of $a_J$ and $\pi_J$ Mesons

In Table I.5, we list the known  $a_J$  and  $\pi_J$  mesons with spin  $J$  in the mass region below  $2.2 \text{ GeV}/c^2$  according to the PDG [5].

## Appendix J. Effect of $\phi_{\text{GJ}}$ Smearing on the Partial-Wave Decomposition of $\pi^-\pi^-\pi^+$

As discussed in Section 7.2, dedicated Monte Carlo simulations show that at low  $t'$  detector resolution leads to a splitting of  $M^\varepsilon = 1^+$  waves in the physics process into  $M^\varepsilon = 1^+$  and  $1^-$  components in the PWA result and to a reduced coherence between  $M^\varepsilon = 0^+$  and  $1^+$  waves. Here we show that these two effects can be explained by a substantial smearing of the  $\phi_{\text{GJ}}$  angle that is defined in Section 5.1.4.

The limiting case of maximal smearing of  $\phi_{\text{GJ}}$ , i.e. when  $\phi_{\text{GJ}}$  cannot be measured, is equivalent to an integration over  $\phi_{\text{GJ}}$ . We study such integrals of products  $\Psi_i^\varepsilon \Psi_j^{\varepsilon*}$  of decay amplitudes. For the diagonal term of an  $M^\varepsilon = 1^+$  wave, we obtain:

$$\frac{1}{2\pi} \int_0^{2\pi} d\phi_{\text{GJ}} |\Psi_{(M=1)}^{(\varepsilon=+1)}(\phi_{\text{GJ}})|^2 = \frac{1}{2} \left[ |\Psi_{(M=1)}^{(\varepsilon=+1)}(\phi_{\text{GJ}})|^2 + |\Psi_{(M=1)}^{(\varepsilon=-1)}(\phi_{\text{GJ}})|^2 \right]. \quad (\text{J.1})$$

Here, both sides of the equation are independent of  $\phi_{\text{GJ}}$ . This means that adding the two intensities with opposite  $\varepsilon$  cancels the  $\phi_{\text{GJ}}$  dependence of the right-hand side while the dependence on the remaining phase-space variables remains unchanged. For the interference term between an  $M^\varepsilon = 0^+$  and a  $1^+$  wave, the integration gives

$$\int_0^{2\pi} d\phi_{\text{GJ}} \Psi_{(M=0)}^{(\varepsilon=+1)}(\phi_{\text{GJ}}) \Psi_{(M=1)}^{(\varepsilon=+1)*}(\phi_{\text{GJ}}) = 0. \quad (\text{J.2})$$

It is important to note that the above equation holds for any value of the remaining phase-space variables.

In a PWA, we fit the model in Eq. (266) to the smeared data. The model is differential in  $\phi_{\text{GJ}}$ , i.e. in the PWA we do not integrate over  $\phi_{\text{GJ}}$ . In order to effectively satisfy Eqs. (J.1) and (J.2), which are a property of the data for the extreme case of maximal smearing, the transition amplitudes must hence fulfill the following conditions: (i) the initial intensity of a pure  $M^\varepsilon = 1^+$  wave splits into equal amounts of  $|\mathcal{T}_{(M=1)}^{(\varepsilon=+1)}|^2$  and  $|\mathcal{T}_{(M=1)}^{(\varepsilon=-1)}|^2$  and (ii) the interference terms  $\mathcal{T}_{(M=0)}^{(\varepsilon=+1)} \mathcal{T}_{(M=1)}^{(\varepsilon=+1)*}$  vanish.

In a realistic case with low  $\phi_{\text{GJ}}$  resolution, the intensity ratio of an  $M^\varepsilon = 1^+$  wave and the corresponding  $1^-$  wave is always larger than one and increases toward higher  $t'$ , where the measurement of the orientation of the production plane and hence of  $\phi_{\text{GJ}}$  is recovered. The small interference terms between the decay amplitudes of waves with  $M^\varepsilon = 0^+$  and  $1^+$  lead to a reduced coherence that is effectively described by  $r_{M=0, M=1}$  in Eq. (266). In the Primakoff region  $t' < 10^{-3} (\text{GeV}/c)^2$ ,  $r_{M=0, M=1}$  has a value of about 0.5 in the peak region of the  $a_2(1320)$  and it is found to increase with increasing  $t'$ .

Table I.5: Resonance parameters of  $a_J$  and  $\pi_J$  mesons in the mass region below  $2.2 \text{ GeV}/c^2$  as given by the PDG [5].

Particle	$J^{PC}$	Mass [MeV/ $c^2$ ]	Width [MeV/ $c^2$ ]
<b>Established states</b>			
$a_0(980)$	$0^{++}$	$980 \pm 20$	50 to 100
$a_1(1260)$	$1^{++}$	$1230 \pm 40$	250 to 600
$a_2(1320)$	$2^{++}$	$1318.3^{+0.5}_{-0.6}$	$107 \pm 5$
$a_0(1450)$	$0^{++}$	$1474 \pm 19$	$265 \pm 13$
$a_4(2040)$	$4^{++}$	$1995^{+10}_{-8}$	$257^{+25}_{-23}$
$\pi(1300)$	$0^{-+}$	$1300 \pm 100$	200 to 600
$\pi_1(1400)$	$1^{-+}$	$1354 \pm 25$	$330 \pm 35$
$\pi_1(1600)$	$1^{-+}$	$1662^{+8}_{-9}$	$241 \pm 40$
$\pi_2(1670)$	$2^{-+}$	$1672.2 \pm 3.0$	$260 \pm 9$
$\pi(1800)$	$0^{-+}$	$1812 \pm 12$	$208 \pm 12$
$\pi_2(1880)$	$2^{-+}$	$1895 \pm 16$	$235 \pm 34$
<b>States omitted from summary table</b>			
$a_1(1420)$	$1^{++}$	$1414^{+15}_{-13}$	$153^{+8}_{-23}$
$a_1(1640)$	$1^{++}$	$1654 \pm 19$	$240 \pm 27$
$a_2(1700)$	$2^{++}$	$1732 \pm 9$	$193 \pm 27$
$a_0(1950)$	$0^{++}$	$1931 \pm 26$	$271 \pm 40$
$\pi_2(2100)$	$2^{-+}$	$2090 \pm 29$	$625 \pm 50$
<b>Further states</b>			
$a_3(1875)$	$3^{++}$	$1874 \pm 43 \pm 96$	$385 \pm 121 \pm 114$
$a_1(1930)$	$1^{++}$	$1930^{+30}_{-70}$	$155 \pm 45$
$a_2(1950)$	$2^{++}$	$1950^{+30}_{-70}$	$180^{+30}_{-70}$
$a_2(1990)$	$2^{++}$	$2050 \pm 10 \pm 40$ $2003 \pm 10 \pm 19$	$190 \pm 22 \pm 100$ $249 \pm 23 \pm 32$
$a_0(2020)$	$0^{++}$	$2025 \pm 30$	$330 \pm 75$
$a_2(2030)$	$2^{++}$	$2030 \pm 20$	$205 \pm 30$
$a_3(2030)$	$3^{++}$	$2031 \pm 12$	$150 \pm 18$
$a_1(2095)$	$1^{++}$	$2096 \pm 17 \pm 121$	$451 \pm 41 \pm 81$
$a_2(2175)$	$2^{++}$	$2175 \pm 40$	$310^{+90}_{-45}$
$\pi_2(2005)$	$2^{-+}$	$1974 \pm 14 \pm 83$ $2005 \pm 15$	$341 \pm 61 \pm 139$ $200 \pm 40$
$\pi_1(2015)$	$1^{-+}$	$2014 \pm 20 \pm 16$ $2001 \pm 30 \pm 92$	$230 \pm 32 \pm 73$ $333 \pm 52 \pm 49$
$\pi(2070)$	$0^{-+}$	$2070 \pm 35$	$310^{+100}_{-50}$
$X(1775)$	$?^{-+}$	$1763 \pm 20$ $1787 \pm 18$	$192 \pm 60$ $118 \pm 60$
$X(2000)$	$?^{?+}$	$1964 \pm 35$ $\sim 2100$ $2214 \pm 15$ $2080 \pm 40$	$225 \pm 50$ $\sim 500$ $355 \pm 21$ $340 \pm 80$

## References

- [1] C. C. W. Taylor, The Atomists: Leucippus and Democritus: Fragments, University of Toronto Press, 1999. URL: <http://www.jstor.org/stable/10.3138/9781442671102>.
- [2] A. Pais, Prog. Theor. Phys. 10 (1953) 457–469. doi:[10.1143/PTP.10.457](https://doi.org/10.1143/PTP.10.457).
- [3] C. D. Anderson, S. H. Neddermeyer, Nature 142 (1938) 878. doi:[10.1038/142878c0](https://doi.org/10.1038/142878c0).
- [4] H. J. Bhabha, Nature 143 (1939) 276–277. doi:[10.1038/143276b0](https://doi.org/10.1038/143276b0).
- [5] M. Tanabashi, et al. (Particle Data Group), Phys. Rev. D 98 (2018) 030001. URL: <https://link.aps.org/doi/10.1103/PhysRevD.98.030001>. doi:[10.1103/PhysRevD.98.030001](https://doi.org/10.1103/PhysRevD.98.030001).
- [6] Quark Masses in M. Tanabashi, et al. (Particle Data Group), Phys. Rev. D 98 (2018) 631–637. URL: <http://pdg.lbl.gov/2019/reviews/rpp2018-rev-quark-masses.pdf>. doi:[10.1103/PhysRevD.98.030001](https://doi.org/10.1103/PhysRevD.98.030001).
- [7] Quark Model in M. Tanabashi, et al. (Particle Data Group), Phys. Rev. D 98 (2018) 287–298. URL: <http://pdg.lbl.gov/2018/reviews/rpp2018-rev-quark-model.pdf>. doi:[10.1103/PhysRevD.98.030001](https://doi.org/10.1103/PhysRevD.98.030001).
- [8] C. Adolph, et al. (COMPASS), Phys. Lett. B 753 (2016) 18–28. doi:[10.1016/j.physletb.2015.11.064](https://doi.org/10.1016/j.physletb.2015.11.064). [arXiv:1503.08935](https://arxiv.org/abs/1503.08935).
- [9] A. S. Kronfeld, Ann. Rev. Nucl. Part. Sci. 62 (2012) 265–284. doi:[10.1146/annurev-nucl-102711-094942](https://doi.org/10.1146/annurev-nucl-102711-094942). [arXiv:1203.1204](https://arxiv.org/abs/1203.1204).
- [10] M. Gell-Mann, Phys. Lett. 8 (1964) 214–215. doi:[10.1016/S0031-9163\(64\)92001-3](https://doi.org/10.1016/S0031-9163(64)92001-3).
- [11] G. Zweig (1964). CERN-TH-401.
- [12] N. Isgur, M. B. Wise, Phys. Rev. Lett. 66 (1991) 1130–1133. doi:[10.1103/PhysRevLett.66.1130](https://doi.org/10.1103/PhysRevLett.66.1130).
- [13] A. V. Manohar, M. B. Wise, Camb. Monogr. Part. Phys. Nucl. Phys. Cosmol. 10 (2000) 1–191.
- [14] E. Klempert, A. Zaitsev, Phys. Rept. 454 (2007) 1–202. doi:[10.1016/j.physrep.2007.07.006](https://doi.org/10.1016/j.physrep.2007.07.006). [arXiv:0708.4016](https://arxiv.org/abs/0708.4016).
- [15] S. Godfrey, N. Isgur, Phys. Rev. D32 (1985) 189–231. doi:[10.1103/PhysRevD.32.189](https://doi.org/10.1103/PhysRevD.32.189).
- [16] D. Ebert, R. N. Faustov, V. O. Galkin, Phys. Rev. D79 (2009) 114029. doi:[10.1103/PhysRevD.79.114029](https://doi.org/10.1103/PhysRevD.79.114029). [arXiv:0903.5183](https://arxiv.org/abs/0903.5183).
- [17] T. Feldmann, P. Kroll, B. Stech, Phys. Rev. D58 (1998) 114006. doi:[10.1103/PhysRevD.58.114006](https://doi.org/10.1103/PhysRevD.58.114006). [arXiv:hep-ph/9802409](https://arxiv.org/abs/hep-ph/9802409).
- [18] G. F. Chew, S. C. Frautschi, Phys. Rev. Lett. 8 (1962) 41–44. doi:[10.1103/PhysRevLett.8.41](https://doi.org/10.1103/PhysRevLett.8.41).
- [19] Y. Nambu, Phys. Lett. B 80 (1979) 372. doi:[10.1016/0370-2693\(79\)91193-6](https://doi.org/10.1016/0370-2693(79)91193-6).
- [20] T. Barnes, S. Godfrey, E. S. Swanson, Phys. Rev. D 72 (2005) 054026. [arXiv:hep-ph/0505002](https://arxiv.org/abs/hep-ph/0505002).
- [21] S. Scherer, M. R. Schindler, Lect. Notes Phys. 830 (2012) 1–338. doi:[10.1007/978-3-642-19254-8](https://doi.org/10.1007/978-3-642-19254-8).
- [22] A. Donnachie, H. G. Dosch, P. V. Landshoff, O. Nachtmann, Pomeron Physics and QCD, 1st ed., Cambridge University Press, 2002.
- [23] B. Ketzer, PoS QNP2012 (2012) 025. doi:[10.22323/1.157.0025](https://doi.org/10.22323/1.157.0025). [arXiv:1208.5125](https://arxiv.org/abs/1208.5125).
- [24] C. A. Meyer, E. S. Swanson, Prog. Part. Nucl. Phys. 82 (2015) 21–58. doi:[10.1016/j.ppnp.2015.03.001](https://doi.org/10.1016/j.ppnp.2015.03.001). [arXiv:1502.07276](https://arxiv.org/abs/1502.07276).
- [25] S. L. Olsen, T. Skwarnicki, D. Ziemska, Rev. Mod. Phys. 90 (2018) 015003. doi:[10.1103/RevModPhys.90.015003](https://doi.org/10.1103/RevModPhys.90.015003). [arXiv:1708.04012](https://arxiv.org/abs/1708.04012).
- [26] V. Mathieu, AIP Conf. Proc. 1735 (2016) 070004. URL: <http://www.indiana.edu/~jpac/>. doi:[10.1063/1.4949452](https://doi.org/10.1063/1.4949452). [arXiv:1601.01751](https://arxiv.org/abs/1601.01751).
- [27] J. J. Dudek, R. G. Edwards, M. J. Peardon, D. G. Richards, C. E. Thomas, Phys. Rev. D 82 (2010) 034508. doi:[10.1103/PhysRevD.82.034508](https://doi.org/10.1103/PhysRevD.82.034508). [arXiv:1004.4930](https://arxiv.org/abs/1004.4930).
- [28] J. J. Dudek, Phys. Rev. D 84 (2011) 074023. doi:[10.1103/PhysRevD.84.074023](https://doi.org/10.1103/PhysRevD.84.074023). [arXiv:1106.5515](https://arxiv.org/abs/1106.5515).
- [29] J. J. Dudek, R. G. Edwards, P. Guo, C. E. Thomas (Hadron Spectrum Collaboration), Phys. Rev. D 88 (2013) 094505. doi:[10.1103/PhysRevD.88.094505](https://doi.org/10.1103/PhysRevD.88.094505). [arXiv:1309.2608](https://arxiv.org/abs/1309.2608).
- [30] M. R. Shepherd, J. J. Dudek, R. E. Mitchell, Nature 534 (2016) 487–493. doi:[10.1038/nature18011](https://doi.org/10.1038/nature18011). [arXiv:1802.08131](https://arxiv.org/abs/1802.08131).
- [31] Lattice Quantum Chromodynamics in M. Tanabashi, et al. (Particle Data Group), Phys. Rev. D 98 (2018) 306–317. URL: <http://pdg.lbl.gov/2018/reviews/rpp2018-rev-lattice-qcd.pdf>. doi:[10.1103/PhysRevD.98.030001](https://doi.org/10.1103/PhysRevD.98.030001).
- [32] C. Gattringer, C. B. Lang, Lect. Notes Phys. 788 (2010) 1–343. doi:[10.1007/978-3-642-01850-3](https://doi.org/10.1007/978-3-642-01850-3).
- [33] R. A. Briceño, J. J. Dudek, R. D. Young, Rev. Mod. Phys. 90 (2018) 025001. doi:[10.1103/RevModPhys.90.025001](https://doi.org/10.1103/RevModPhys.90.025001). [arXiv:1706.06223](https://arxiv.org/abs/1706.06223).
- [34] K. G. Wilson, Phys. Rev. D 10 (1974) 2445–2459. doi:[10.1103/PhysRevD.10.2445](https://doi.org/10.1103/PhysRevD.10.2445).
- [35] S. Borsanyi, et al., Science 347 (2015) 1452–1455. doi:[10.1126/science.1257050](https://doi.org/10.1126/science.1257050). [arXiv:1406.4088](https://arxiv.org/abs/1406.4088).
- [36] S. Perantonis, C. Michael, Nucl. Phys. B 347 (1990) 854–868. doi:[10.1016/0550-3213\(90\)90386-R](https://doi.org/10.1016/0550-3213(90)90386-R).
- [37] G. S. Bali, K. Schilling, Phys. Rev. D 46 (1992) 2636–2646. doi:[10.1103/PhysRevD.46.2636](https://doi.org/10.1103/PhysRevD.46.2636).
- [38] S. Necco, R. Sommer, Nucl. Phys. B 622 (2002) 328–346. doi:[10.1016/S0550-3213\(01\)00582-X](https://doi.org/10.1016/S0550-3213(01)00582-X). [arXiv:hep-lat/0108008](https://arxiv.org/abs/hep-lat/0108008).
- [39] M. Lüscher, Commun. Math. Phys. 105 (1986) 153–188. doi:[10.1007/BF01211097](https://doi.org/10.1007/BF01211097).
- [40] M. Lüscher, Nucl. Phys. B 354 (1991) 531–578. doi:[10.1016/0550-3213\(91\)90366-6](https://doi.org/10.1016/0550-3213(91)90366-6).
- [41] D. J. Wilson, R. A. Briceno, J. J. Dudek, R. G. Edwards, C. E. Thomas, Phys. Rev. D 92 (2015) 094502. doi:[10.1103/PhysRevD.92.094502](https://doi.org/10.1103/PhysRevD.92.094502). [arXiv:1507.02599](https://arxiv.org/abs/1507.02599).
- [42] R. A. Briceno, J. J. Dudek, R. G. Edwards, D. J. Wilson, Phys. Rev. Lett. 118 (2017) 022002. doi:[10.1103/PhysRevLett.118.022002](https://doi.org/10.1103/PhysRevLett.118.022002). [arXiv:1607.05900](https://arxiv.org/abs/1607.05900).

[43] J. J. Dudek, R. G. Edwards, D. J. Wilson (Hadron Spectrum), Phys. Rev. D93 (2016) 094506. doi:[10.1103/PhysRevD.93.094506](https://doi.org/10.1103/PhysRevD.93.094506). [arXiv:1602.05122](https://arxiv.org/abs/1602.05122).

[44] Quantum Chromodynamics in M. Tanabashi, et al. (Particle Data Group), Phys. Rev. D 98 (2018) 141–160. URL: <http://pdg.lbl.gov/2019/reviews/rpp2018-rev-qcd.pdf>. doi:[10.1103/PhysRevD.98.030001](https://doi.org/10.1103/PhysRevD.98.030001).

[45] R. J. Eden, P. V. Landshoff, D. I. Olive, J. C. Polkinghorne, The analytic S-matrix, Cambridge Univ. Press, Cambridge, 1966.

[46] M. E. Peskin, D. V. Schroeder, An Introduction to quantum field theory, Addison-Wesley, Reading, 1995.

[47] A. D. Martin, T. D. Spearman, Elementary Particle Theory, 1st ed., North-Holland Publishing Company, 1970.

[48] U.-G. Meissner, Phys. Rept. 161 (1988) 213. doi:[10.1016/0370-1573\(88\)90090-7](https://doi.org/10.1016/0370-1573(88)90090-7).

[49] Kinematics in M. Tanabashi, et al. (Particle Data Group), Phys. Rev. D 98 (2018) 567–570. URL: <http://pdg.lbl.gov/2018/reviews/rpp2018-rev-kinematics.pdf>. doi:[10.1103/PhysRevD.98.030001](https://doi.org/10.1103/PhysRevD.98.030001).

[50] V. N. Gribov, Strong Interactions of Hadrons at High Energies: Gribov Lectures on Theoretical Physics, volume 27 of *Camb. Monogr. Part. Phys. Nucl. Phys. Cosmol.*, Cambridge University Press, 2008. doi:[10.1017/CBO9780511534942](https://doi.org/10.1017/CBO9780511534942).

[51] G. B. Arfken, H. J. Weber, F. E. Harris, Mathematical Methods for Physicists: A Comprehensive Guide, Elsevier Science, 2011. URL: <https://books.google.de/books?id=J0pHkJF-qcwC>.

[52] Resonances in M. Tanabashi, et al. (Particle Data Group), Phys. Rev. D 98 (2018) 571–575. URL: <http://pdg.lbl.gov/2018/reviews/rpp2018-rev-resonances.pdf>. doi:[10.1103/PhysRevD.98.030001](https://doi.org/10.1103/PhysRevD.98.030001).

[53] M. L. Perl, High Energy Hadron Physics, Wiley-Interscience Publication, Wiley, 1974.

[54] M. Froissart, Phys. Rev. 123 (1961) 1053–1057. doi:[10.1103/PhysRev.123.1053](https://doi.org/10.1103/PhysRev.123.1053).

[55] J. M. Blatt, V. F. Weisskopf, Theoretical Nuclear Physics, Wiley, New York, 1952.

[56] F. von Hippel, C. Quigg, Phys. Rev. D 5 (1972) 624–638. doi:[10.1103/PhysRevD.5.624](https://doi.org/10.1103/PhysRevD.5.624).

[57] G. F. Chew, S. Mandelstam, Phys. Rev. 119 (1960) 467–477. doi:[10.1103/PhysRev.119.467](https://doi.org/10.1103/PhysRev.119.467).

[58] B. W. Lee, Phys. Rev. 120 (1960) 325–330. doi:[10.1103/PhysRev.120.325](https://doi.org/10.1103/PhysRev.120.325).

[59] J.-L. Basdevant, E. L. Berger, Phys. Rev. D19 (1979) 239. doi:[10.1103/PhysRevD.19.239](https://doi.org/10.1103/PhysRevD.19.239).

[60] T. Shimada, A. D. Martin, A. C. Irving, Nucl. Phys. B142 (1978) 344–364. doi:[10.1016/0550-3213\(78\)90209-2](https://doi.org/10.1016/0550-3213(78)90209-2).

[61] I. V. Danilkin, C. Fernandez-Ramirez, P. Guo, V. Mathieu, D. Schott, M. Shi, A. P. Szczepaniak, Phys. Rev. D 91 (2015) 094029. doi:[10.1103/PhysRevD.91.094029](https://doi.org/10.1103/PhysRevD.91.094029). [arXiv:1409.7708](https://arxiv.org/abs/1409.7708).

[62] R. J. Eden, Rept. Prog. Phys. 34 (1971) 995–1053. doi:[10.1088/0034-4885/34/3/304](https://doi.org/10.1088/0034-4885/34/3/304).

[63] D. I. Olive, Il Nuovo Cimento (1955–1965) 26 (1962) 73–102. URL: <https://doi.org/10.1007/BF02754344>. doi:[10.1007/BF02754344](https://doi.org/10.1007/BF02754344).

[64] I. J. R. Aitchison, Nucl. Phys. A 189 (1972) 417–423. doi:[10.1016/0375-9474\(72\)90305-3](https://doi.org/10.1016/0375-9474(72)90305-3).

[65] S.-U. Chung, J. Brose, R. Hackmann, E. Klemp, S. Spanier, C. Strassburger, Annalen Phys. 4 (1995) 404–430. doi:[10.1002/andp.19955070504](https://doi.org/10.1002/andp.19955070504).

[66] S. M. Flatté, Phys. Lett. B 63 (1976) 224. doi:[10.1016/0370-2693\(76\)90654-7](https://doi.org/10.1016/0370-2693(76)90654-7).

[67] S. Weinberg, The Quantum theory of fields. Vol. 1: Foundations, Cambridge University Press, 2005.

[68] J. D. Bjorken, Phys. Rev. Lett. 4 (1960) 473–474. doi:[10.1103/PhysRevLett.4.473](https://doi.org/10.1103/PhysRevLett.4.473).

[69] K. M. Watson, Phys. Rev. 88 (1952) 1163–1171. URL: <https://link.aps.org/doi/10.1103/PhysRev.88.1163>. doi:[10.1103/PhysRev.88.1163](https://doi.org/10.1103/PhysRev.88.1163).

[70] A. Jackura, et al. (JPAC and COMPASS Collaborations), Phys. Lett. B 779 (2018) 464–472. doi:[10.1016/j.physletb.2018.01.017](https://doi.org/10.1016/j.physletb.2018.01.017). [arXiv:1707.02848](https://arxiv.org/abs/1707.02848).

[71] A. Rodas, et al. (JPAC Collaboration), Phys. Rev. Lett. 122 (2019) 042002. doi:[10.1103/PhysRevLett.122.042002](https://doi.org/10.1103/PhysRevLett.122.042002). [arXiv:1810.04171](https://arxiv.org/abs/1810.04171).

[72] P. D. B. Collins, A. D. Martin, Hadron Interactions, 1st ed., Adam Hilger Ltd., 1984.

[73] J. S. Loos, U. E. Kruse, E. L. Goldwasser, Phys. Rev. 173 (1968) 1330–1338. doi:[10.1103/PhysRev.173.1330](https://doi.org/10.1103/PhysRev.173.1330).

[74] H. W. Atherton, L. M. Celnikier, B. French, J. B. Kinson, K. Myklebost, et al., Phys. Lett. B 30 (1969) 494–497. doi:[10.1016/0370-2693\(69\)90182-8](https://doi.org/10.1016/0370-2693(69)90182-8).

[75] C. Patrignani, et al. (Particle Data Group), Chin. Phys. C 40 (2016) 100001. doi:[10.1088/1674-1137/40/10/100001](https://doi.org/10.1088/1674-1137/40/10/100001).

[76] T. Regge, Nuovo Cim. 14 (1959) 951. doi:[10.1007/BF02728177](https://doi.org/10.1007/BF02728177).

[77] R. Newton, The complex  $j$ -plane - complex angular momentum in nonrelativistic quantum scattering theory, 1964.

[78] V. de Alfaro, T. Regge, Potential Scattering, 1965.

[79] A. V. Barnes, D. J. Mellesma, A. V. Tollestrup, R. L. Walker, O. I. Dahl, et al., Phys. Rev. Lett. 37 (1976) 76. doi:[10.1103/PhysRevLett.37.76](https://doi.org/10.1103/PhysRevLett.37.76).

[80] G. F. Chew, S. C. Frautschi, Phys. Rev. Lett. 7 (1961) 394–397. doi:[10.1103/PhysRevLett.7.394](https://doi.org/10.1103/PhysRevLett.7.394).

[81] J. L. Basdevant, E. L. Berger, Phys. Rev. D16 (1977) 657. doi:[10.1103/PhysRevD.16.657](https://doi.org/10.1103/PhysRevD.16.657).

[82] G. N. Fleming, Phys. Rev. 135 (1964) B551–B560. doi:[10.1103/PhysRev.135.B551](https://doi.org/10.1103/PhysRev.135.B551).

[83] F. Niecknig, B. Kubis, JHEP 10 (2015) 142. doi:[10.1007/JHEP10\(2015\)142](https://doi.org/10.1007/JHEP10(2015)142). [arXiv:1509.03188](https://arxiv.org/abs/1509.03188).

[84] M. Mai, B. Hu, M. Doring, A. Pilloni, A. Szczepaniak, PoS Hadron2017 (2018) 140. doi:[10.22323/1.310.0140](https://doi.org/10.22323/1.310.0140).

[85] M. Mikhaseko, Y. Wunderlich, A. Jackura, V. Mathieu, A. Pilloni, B. Ketzer, A. P. Szczepaniak, JHEP 08 (2019) 080. doi:[10.1007/JHEP08\(2019\)080](https://doi.org/10.1007/JHEP08(2019)080). [arXiv:1904.11894](https://arxiv.org/abs/1904.11894).

[86] J. Gasser, H. Leutwyler, Annals Phys. 158 (1984) 142. doi:[10.1016/0003-4916\(84\)90242-2](https://doi.org/10.1016/0003-4916(84)90242-2).

[87] A. S. Carroll, et al., Phys. Rev. Lett. 33 (1974) 932. doi:[10.1103/PhysRevLett.33.932](https://doi.org/10.1103/PhysRevLett.33.932).

[88] A. S. Carroll, et al., Phys. Lett. 80B (1979) 423–427. doi:[10.1016/0370-2693\(79\)91205-X](https://doi.org/10.1016/0370-2693(79)91205-X).

[89] D. Ljung, et al., Phys. Rev. D15 (1977) 3163. doi:[10.1103/PhysRevD.15.3163](https://doi.org/10.1103/PhysRevD.15.3163).

[90] A. Schiz, et al., Phys. Rev. D24 (1981) 26. doi:[10.1103/PhysRevD.24.26](https://doi.org/10.1103/PhysRevD.24.26).

[91] H. H. Bingham, et al., Phys. Lett. 51B (1974) 397–401. doi:[10.1016/0370-2693\(74\)90238-X](https://doi.org/10.1016/0370-2693(74)90238-X).

[92] F. C. Winkelmann, et al., Phys. Rev. Lett. 32 (1974) 121. doi:[10.1103/PhysRevLett.32.121](https://doi.org/10.1103/PhysRevLett.32.121).

[93] R. T. Deck, Phys. Rev. Lett. 13 (1964) 169–173. doi:[10.1103/PhysRevLett.13.169](https://doi.org/10.1103/PhysRevLett.13.169).

[94] P. Abbon, et al. (COMPASS Collaboration), Nucl. Instr. Meth. A 577 (2007) 455–518. [arXiv:hep-ex/0703049](https://arxiv.org/abs/hep-ex/0703049).

[95] P. Abbon, et al. (COMPASS), Nucl. Instr. Meth. A 779 (2015) 69–115. doi:[10.1016/j.nima.2015.01.035](https://doi.org/10.1016/j.nima.2015.01.035). [arXiv:1410.1797](https://arxiv.org/abs/1410.1797).

[96] T. Schlüter, W. Dunnweber, K. Dhibar, M. Faessler, R. Geyer, J. F. Rajotte, Z. Roushan, H. Wohrmann, Nucl. Instrum. Meth. A654 (2011) 219–224. doi:[10.1016/j.nima.2011.05.069](https://doi.org/10.1016/j.nima.2011.05.069). [arXiv:1108.4587](https://arxiv.org/abs/1108.4587).

[97] C. Altunbas, M. Capeáns, K. Dehmelt, J. Ehlers, J. Friedrich, I. Konorov, A. Gandi, S. Kappler, B. Ketzer, R. D. Oliveira, S. Paul, A. Placci, L. Ropelewski, F. Sauli, F. Simon, M. van Stenis, Nucl. Instr. Meth. A 490 (2002) 177–203.

[98] B. Ketzer, A. Austregesilo, F. Haas, I. Konorov, M. Krämer, A. Mann, T. Nagel, S. Paul, in: Nuclear Science Symposium Conference Record, 2007. NSS '07. IEEE, volume 1, IEEE, Piscataway, NJ, 2007, pp. 242–244. doi:[10.1109/NSSMIC.2007.4436323](https://doi.org/10.1109/NSSMIC.2007.4436323).

[99] P. Abbon, et al., Nucl. Instr. Meth. A 567 (2006) 114–117.

[100] T. Schlüter (COMPASS), eConf C110613 (2011) 83. [arXiv:1108.6191](https://arxiv.org/abs/1108.6191).

[101] C. Adolph, et al. (COMPASS Collaboration), Phys. Lett. B 740 (2015) 303–311. doi:[10.1016/j.physletb.2014.11.058](https://doi.org/10.1016/j.physletb.2014.11.058). [arXiv:1408.4286](https://arxiv.org/abs/1408.4286).

[102] C. Adolph, et al. (COMPASS Collaboration), Phys. Rev. D 95 (2017) 032004. doi:[10.1103/PhysRevD.95.032004](https://doi.org/10.1103/PhysRevD.95.032004). [arXiv:1509.00992](https://arxiv.org/abs/1509.00992).

[103] J. D. Hansen, G. T. Jones, G. Otter, G. Rudolph, Nucl. Phys. B 81 (1974) 403. doi:[10.1016/0550-3213\(74\)90241-7](https://doi.org/10.1016/0550-3213(74)90241-7).

[104] D. Herndon, P. Söding, R. J. Cashmore, Phys. Rev. D 11 (1975) 3165. doi:[10.1103/PhysRevD.11.3165](https://doi.org/10.1103/PhysRevD.11.3165).

[105] S. J. Lindenbaum, R. M. Sternheimer, Phys. Rev. 105 (1957) 1874–1879. doi:[10.1103/PhysRev.105.1874](https://doi.org/10.1103/PhysRev.105.1874).

[106] M. Jacob, G. C. Wick, Annals Phys. 7 (1959) 404–428. doi:[10.1016/0003-4916\(59\)90051-X](https://doi.org/10.1016/0003-4916(59)90051-X).

[107] S.-U. Chung, Spin Formalisms — Updated Version III, BNL-76975-2006-IR, 2013. URL: <http://cds.cern.ch/record/1561144>, updated version of CERN-71-08.

[108] J. D. Richman (1984). URL: <http://lib-extopc.kek.jp/preprints/PDF/1984/8409/8409198.pdf>, CALT-68-1148.

[109] R. Kutschke (1996). URL: <http://home.fnal.gov/~kutschke/Angdist/angdist.ps>.

[110] C. W. Salgado, D. P. Weygand, Phys. Rept. 537 (2014) 1–58. doi:[10.1016/j.physrep.2013.11.005](https://doi.org/10.1016/j.physrep.2013.11.005). [arXiv:1310.7498](https://arxiv.org/abs/1310.7498).

[111] E. P. Wigner, Gruppentheorie und ihre Anwendungen auf die Quantenmechanik der Atomspektren, Vieweg, Braunschweig, 1931.

[112] E. P. Wigner, Group Theory and its Application to the Quantum Mechanics of Atomic Spectra, Academic Press, New York, 1959. Translated into English by J. J. Griffin.

[113] M. E. Rose, Elementary Theory of Angular Momentum, John Wiley & Sons, New York, 1957.

[114] R. J. Cashmore, in: 14th Scottish Universities Summer School in Physics: Phenomenology of Particles at High Energies, Middleton Hall (Edinburgh), Scotland, July 29–August 8, 1973, p. 611. URL: <http://www-public.slac.stanford.edu/sciDoc/docMeta.aspx?slacPubNumber=SLAC-PUB-1316>.

[115] S.-U. Chung, T. L. Trueman, Phys. Rev. D 11 (1975) 633. doi:[10.1103/PhysRevD.11.633](https://doi.org/10.1103/PhysRevD.11.633).

[116] R. Odorico, A. Garcia, C. A. Garcia-Canal, Phys. Lett. 32B (1970) 375–379. doi:[10.1016/0370-2693\(70\)90501-0](https://doi.org/10.1016/0370-2693(70)90501-0).

[117] I. Kachaev, et al., Phys. Atom. Nucl. 78 (2015) 1474–1477. doi:[10.1134/S1063778815130153](https://doi.org/10.1134/S1063778815130153).

[118] J. E. Kim, G. Carosi, Rev. Mod. Phys. 82 (2010) 557–602. doi:[10.1103/RevModPhys.82.557](https://doi.org/10.1103/RevModPhys.82.557). [arXiv:0807.3125](https://arxiv.org/abs/0807.3125).

[119] A. Hook, TASI Lectures on the Strong CP Problem and Axions, 2018. [arXiv:1812.02669](https://arxiv.org/abs/1812.02669).

[120] K. Gottfried, J. D. Jackson, Nuovo Cim. 33 (1964) 309–330. doi:[10.1007/BF02750195](https://doi.org/10.1007/BF02750195).

[121] G. Cohen-Tannoudji, P. Salin, A. Morel, Nuovo Cim. A 55 (1968) 412–422. doi:[10.1007/BF02857563](https://doi.org/10.1007/BF02857563).

[122] R. A. Fisher, Phil. Trans. Roy. Soc. Lond. A222 (1922) 309–368. doi:[10.1098/rsta.1922.0009](https://doi.org/10.1098/rsta.1922.0009).

[123] F. James, Statistical Methods in Experimental Physics, 2nd ed., World Scientific Publishing Co., 2006.

[124] A. Stuart, K. Ord, S. Arnold (Eds.), Kendall's Advanced Theory of Statistics, Volume 2A, Classical Inference and the Linear Model, 6th ed., Wiley, 2010.

[125] J. Orear, Notes on statistics for physicists, Technical Report UCRL-8417, Lawrence Berkeley Nat. Lab., Berkeley, CA, 1958. URL: <http://cds.cern.ch/record/104881>.

[126] J. Orear, Notes on statistics for physicists, revised, Technical Report CLNS-82-511, 1982.

[127] R. J. Barlow, Nucl. Instrum. Meth. A297 (1990) 496–506. doi:[10.1016/0168-9002\(90\)91334-8](https://doi.org/10.1016/0168-9002(90)91334-8).

[128] G. Ascoli, et al., Phys. Rev. Lett. 25 (1970) 962. doi:[10.1103/PhysRevLett.25.962](https://doi.org/10.1103/PhysRevLett.25.962).

[129] G. Ascoli, et al., Phys. Rev. D 7 (1973) 669–686. doi:[10.1103/PhysRevD.7.669](https://doi.org/10.1103/PhysRevD.7.669).

[130] D. M. Schmidt, R. J. Morrison, M. S. Witherell, Nucl. Instrum. Meth. A328 (1993) 547–552. doi:[10.1016/0168-9002\(93\)90674-7](https://doi.org/10.1016/0168-9002(93)90674-7).

[131] F. E. James, Monte Carlo phase space, CERN-68-15, 1968. doi:[10.5170/CERN-1968-015](https://doi.org/10.5170/CERN-1968-015).

[132] M. M. Block, Computer Physics Communications 69 (1992) 459–476. doi:[10.1016/0010-4655\(92\)90183-Y](https://doi.org/10.1016/0010-4655(92)90183-Y).

[133] G. Casella, C. P. Robert, M. T. Wells, Generalized Accept–Reject sampling schemes, volume 45 of *IMS Lecture Notes Monogr. Ser.*, Inst. Math. Stat., Beachwood, OH, 2004, pp. 342–347. doi:[10.1214/lnms/1196285403](https://doi.org/10.1214/lnms/1196285403).

[134] Scalar Mesons Below 2 GeV in M. Tanabashi, et al. (Particle Data Group), Phys. Rev. D 98 (2018) 658–663. URL: <http://pdg.lbl.gov/2018/reviews/rpp2018-rev-scalar-mesons.pdf>. doi:10.1103/PhysRevD.98.030001.

[135] F. Niecknig, B. Kubis, S. P. Schneider, Eur. Phys. J. C72 (2012) 2014. doi:10.1140/epjc/s10052-012-2014-1. [arXiv:1203.2501](https://arxiv.org/abs/1203.2501).

[136] S. Teige, et al. (E852), Phys. Rev. D59 (1999) 012001. doi:10.1103/PhysRevD.59.012001. [arXiv:hep-ex/9608017](https://arxiv.org/abs/hep-ex/9608017).

[137] B. Guegan, J. Hardin, J. Stevens, M. Williams, JINST 10 (2015) P09002. doi:10.1088/1748-0221/10/09/P09002. [arXiv:1505.05133](https://arxiv.org/abs/1505.05133).

[138] R. Tibshirani, J. Royal Stat. Soc. B 58 (1996) 267–288. URL: <http://www.jstor.org/stable/2346178>.

[139] K. A. Bicker, Model Selection for and Partial-Wave Analysis of a Five-Pion Final State at the COMPASS Experiment at CERN, Ph.D. thesis, Technische Universität München, 2016. URL: <https://cds.cern.ch/record/2215512/files/CERN-THESIS-2016-102.pdf>, CERN-THESIS-2016-102.

[140] O. J. Drotleff, Model Selection for Partial-Wave Analysis of  $\pi^- + p \rightarrow \pi^- \pi^+ \pi^- + p$  at the COMPASS Experiment at CERN, Master’s thesis, Technische Universität München, 2015. URL: [http://wwwcompass.cern.ch/compass/publications/theses/2015\\_dpl\\_drotleff.pdf](http://wwwcompass.cern.ch/compass/publications/theses/2015_dpl_drotleff.pdf).

[141] F. M. Kaspar, Application and Verification of Model-Selection Techniques for Diffractively Produced Three-Pion Final States, Master’s thesis, Technische Universität München, 2017.

[142] H. Akaike, IEEE Trans. Automat. Contr. 19 (1974) 716–723. doi:10.1109/TAC.1974.1100705.

[143] G. Schwarz, Ann. Statist. 6 (1978) 461–464. doi:10.1214/aos/1176344136.

[144] C. Zemach, Phys. Rev. 140 (1965) B97–B108. doi:10.1103/PhysRev.140.B97.

[145] C. Zemach, Phys. Rev. 140 (1965) B109–B124. doi:10.1103/PhysRev.140.B109.

[146] M. D. Scadron, H. F. Jones, Phys. Rev. 173 (1968) 1734–1744. doi:10.1103/PhysRev.173.1734.

[147] S.-U. Chung, Phys. Rev. D 48 (1993) 1225–1239. doi:10.1103/PhysRevD.48.1225, [Erratum: Phys. Rev. D 56 (1997) 4419].

[148] V. Filippini, A. Fontana, A. Rotondi, Phys. Rev. D 51 (1995) 2247–2261. doi:10.1103/PhysRevD.51.2247.

[149] A. V. Anisovich, A. V. Sarantsev, Eur. Phys. J. A30 (2006) 427–441. doi:10.1140/epja/i2006-10102-1. [arXiv:hep-ph/0605135](https://arxiv.org/abs/hep-ph/0605135).

[150] S.-U. Chung, J. Friedrich, Phys. Rev. D 78 (2008) 074027. doi:10.1103/PhysRevD.78.074027. [arXiv:0711.3143](https://arxiv.org/abs/0711.3143).

[151] M. Mikhaseenko, A. Pilloni, J. Nys, M. Albaladejo, C. Fernandez-Ramirez, A. Jackura, V. Mathieu, N. Sherrill, T. Skwarnicki, A. P. Szczepaniak (JPAC Collaboration), Eur. Phys. J. C78 (2018) 229. doi:10.1140/epjc/s10052-018-5670-y. [arXiv:1712.02815](https://arxiv.org/abs/1712.02815).

[152] E. M. Aitala, et al. (E791 Collaboration), Phys. Rev. D 73 (2006) 032004. doi:10.1103/PhysRevD.73.032004. [arXiv:hep-ex/0507099](https://arxiv.org/abs/hep-ex/0507099).

[153] F. Krinner, D. Greenwald, D. Ryabchikov, B. Grube, S. Paul, Phys. Rev. D 97 (2018) 114008. doi:10.1103/PhysRevD.97.114008. [arXiv:1710.09849](https://arxiv.org/abs/1710.09849).

[154] F. M. Krinner, Freed-Isobar Partial-Wave Analysis, Ph.D. thesis, Technische Universität München, 2018.

[155] R. H. Dalitz, R. G. Moorhouse, Proc. Roy. Soc. Lond. A318 (1970) 279–298. doi:10.1098/rspa.1970.0145.

[156] M. Aghasyan, et al. (COMPASS Collaboration), Phys. Rev. D 98 (2018) 092003. doi:10.1103/PhysRevD.98.092003. [arXiv:1802.05913](https://arxiv.org/abs/1802.05913).

[157] N. A. Törnqvist, Z. Phys. C 68 (1995) 647–660. doi:10.1007/BF01565264. [arXiv:hep-ph/9504372](https://arxiv.org/abs/hep-ph/9504372).

[158] M. R. Ataian, et al. (EHS/NA22 Collaboration), Z. Phys. C 50 (1991) 353–360. doi:10.1007/BF01551447.

[159] G. Ingelman, NATO Sci. Ser. C 534 (1999) 597–624. doi:10.1007/978-94-011-4689-0\_13. [arXiv:hep-ph/9912534](https://arxiv.org/abs/hep-ph/9912534).

[160] K. H. Dederichs, M. A. Faessler, Phys. Lett. B232 (1989) 405–412. doi:10.1016/0370-2693(89)90765-X.

[161] M. A. Faessler, Z. Phys. C58 (1993) 567–574. doi:10.1007/BF01553015.

[162] B. E. Cox, J. R. Forshaw, Comput. Phys. Commun. 144 (2002) 104–110. doi:10.1016/S0010-4655(01)00467-2. [arXiv:hep-ph/0010303](https://arxiv.org/abs/hep-ph/0010303).

[163] C. Daum, et al. (ACCMOR), Phys. Lett. 89B (1980) 276–280. doi:10.1016/0370-2693(80)90029-5.

[164] C. Daum, et al. (ACCMOR Collaboration), Nucl. Phys. B182 (1981) 269. doi:10.1016/0550-3213(81)90123-1.

[165] K. Pearson, Philos. Mag. Ser. 5 50 (1900) 157–175. doi:10.1080/14786440009463897.

[166] F. James, M. Roos, Comput. Phys. Commun. 10 (1975) 343–367. doi:10.1016/0010-4655(75)90039-9.

[167] F. James, M. Winkler, MINUIT home page, 2008. URL: <http://www.cern.ch/minuit>, [Online; accessed 28-May-2018].

[168] M. H. Quenouille, J. Royal Stat. Soc. B 11 (1949) 68–84. doi:10.1017/s0305004100025123.

[169] J. W. Tukey, Ann. Math. Statist. 29 (1958) 614–623. doi:10.1214/aoms/1177706647.

[170] B. Efron, Ann. Statist. 7 (1979) 1–26. doi:10.1214/aos/1176344552.

[171] K. Wolter, Introduction to Variance Estimation, 2nd ed., Springer-Verlag New York, 1985. doi:10.1007/978-0-387-35099-8.

[172] J. Shao, D. Tu, The Jackknife and Bootstrap, 1st ed., Springer-Verlag New York, 1995. doi:10.1007/978-1-4612-0795-5.

[173] M. Mikhaseenko, B. Ketzer, A. Sarantsev, Phys. Rev. D 91 (2015) 094015. doi:10.1103/PhysRevD.91.094015. [arXiv:1501.07023](https://arxiv.org/abs/1501.07023).

[174] F. Aceti, L. R. Dai, E. Oset, Phys. Rev. D 94 (2016) 096015. doi:10.1103/PhysRevD.94.096015. [arXiv:1606.06893](https://arxiv.org/abs/1606.06893).

[175] D. V. Amelin, et al. (VES Collaboration), Phys. Lett. B 356 (1995) 595–600. doi:10.1016/0370-2693(95)00864-H.

[176] M. Mikhaseenko, B. Ketzer, PoS BORMIO2016 (2016) 024. doi:10.22323/1.272.0024.

[177] A. Jackura, M. Mikhaseenko, A. Szczepaniak (JPAC Collaboration), EPJ Web Conf. 130 (2016) 05008. doi:10.1051/epjconf/201613005008. [arXiv:1610.04567](https://arxiv.org/abs/1610.04567).

[178] M. Mikhasenko, A. Jackura, B. Ketzer, A. Szczepaniak (COMPASS and JPAC Collaborations), EPJ Web Conf. 137 (2017) 05017. doi:[10.1051/epjconf/201713705017](https://doi.org/10.1051/epjconf/201713705017).

[179] M. Mikhasenko, A. Pilloni, M. Albaladejo, C. Fernández-Ramírez, A. Jackura, V. Mathieu, J. Nys, A. Rodas, B. Ketzer, A. P. Szczepaniak (JPAC), Phys. Rev. D98 (2018) 096021. doi:[10.1103/PhysRevD.98.096021](https://doi.org/10.1103/PhysRevD.98.096021). [arXiv:1810.00016](https://arxiv.org/abs/1810.00016).

[180] A. Pilloni, J. Nys, M. Mikhasenko, M. Albaladejo, C. Fernández-Ramírez, A. Jackura, V. Mathieu, N. Sherrill, T. Skwarnicki, A. P. Szczepaniak (JPAC), Eur. Phys. J. C78 (2018) 727. doi:[10.1140/epjc/s10052-018-6177-2](https://doi.org/10.1140/epjc/s10052-018-6177-2). [arXiv:1805.02113](https://arxiv.org/abs/1805.02113).

[181] M. Alekseev, et al. (COMPASS Collaboration), Phys. Rev. Lett. 104 (2010) 241803. doi:[10.1103/PhysRevLett.104.241803](https://doi.org/10.1103/PhysRevLett.104.241803). [arXiv:0910.5842](https://arxiv.org/abs/0910.5842).

[182] C. Adolph, et al. (COMPASS), Phys. Rev. Lett. 115 (2015) 082001. doi:[10.1103/PhysRevLett.115.082001](https://doi.org/10.1103/PhysRevLett.115.082001). [arXiv:1501.05732](https://arxiv.org/abs/1501.05732).

[183] G. M. Beladidze, et al. (VES Collaboration), Phys. Lett. B 313 (1993) 276–282. doi:[10.1016/0370-2693\(93\)91224-B](https://doi.org/10.1016/0370-2693(93)91224-B).

[184] V. Dorofeev, et al. (VES Collaboration), AIP Conf. Proc. 619 (2002) 143–154. doi:[10.1063/1.1482444](https://doi.org/10.1063/1.1482444). [arXiv:hep-ex/0110075](https://arxiv.org/abs/hep-ex/0110075).

[185] S.-U. Chung, et al. (E852), Phys. Rev. D60 (1999) 092001. doi:[10.1103/PhysRevD.60.092001](https://doi.org/10.1103/PhysRevD.60.092001). [arXiv:hep-ex/9902003](https://arxiv.org/abs/hep-ex/9902003).

[186] E. I. Ivanov, et al. (E852 Collaboration), Phys. Rev. Lett. 86 (2001) 3977–3980. doi:[10.1103/PhysRevLett.86.3977](https://doi.org/10.1103/PhysRevLett.86.3977). [arXiv:hep-ex/0101058](https://arxiv.org/abs/hep-ex/0101058).

[187] T. Schlüter, The  $\pi^- \eta$  and  $\pi^- \eta'$  Systems in Exclusive 190 GeV  $\pi^- p$  Reactions at COMPASS (CERN), Ph.D. thesis, Ludwig-Maximilians-Universität München, 2012. URL: [https://cds.cern.ch/record/1665412/files/2012\\_phd\\_schlueter\\_3.pdf](https://cds.cern.ch/record/1665412/files/2012_phd_schlueter_3.pdf), CERN-THESIS-2012-370.

[188] T. Schlüter (COMPASS), PoS Hadron2013 (2013) 085. doi:[10.22323/1.205.0085](https://doi.org/10.22323/1.205.0085). [arXiv:1401.4067](https://arxiv.org/abs/1401.4067).

[189] G. Ascoli, R. Cutler, L. M. Jones, U. Kruse, T. Roberts, et al., Phys. Rev. D 9 (1974) 1963–1979. doi:[10.1103/PhysRevD.9.1963](https://doi.org/10.1103/PhysRevD.9.1963).

[190] D. Barberis, et al. (WA102), Phys. Lett. B427 (1998) 398–402. doi:[10.1016/S0370-2693\(98\)00403-1](https://doi.org/10.1016/S0370-2693(98)00403-1). [arXiv:hep-ex/9803029](https://arxiv.org/abs/hep-ex/9803029).

[191] J. Beringer, et al. (Particle Data Group), Phys. Rev. D 86 (2012) 010001 and 2013 partial update for the 2014 edition. doi:[10.1103/PhysRevD.86.010001](https://doi.org/10.1103/PhysRevD.86.010001).

[192] A. D. Martin, et al., Phys. Lett. 74B (1978) 417–421. doi:[10.1016/0370-2693\(78\)90693-7](https://doi.org/10.1016/0370-2693(78)90693-7).

[193] S. A. Sodovsky, On the ambiguities in the partial wave analysis of  $\pi^- p \rightarrow \eta \pi^0 n$  reaction, IHEP-91-75, 1991. URL: <https://lib-extopc.kek.jp/preprints/PDF/1991/9108/9108585.pdf>.

[194] S.-U. Chung, Phys. Rev. D56 (1997) 7299–7316. doi:[10.1103/PhysRevD.56.7299](https://doi.org/10.1103/PhysRevD.56.7299).

[195] E. Barrelet, Nuovo Cim. A8 (1972) 331–371. doi:[10.1007/BF02732655](https://doi.org/10.1007/BF02732655).

[196] K. Peters, E. Klempt, Phys. Lett. B352 (1995) 467–471. doi:[10.1016/0370-2693\(95\)00457-V](https://doi.org/10.1016/0370-2693(95)00457-V).

[197] A. Abele, et al. (Crystal Barrel), Phys. Lett. B404 (1997) 179–186. doi:[10.1016/S0370-2693\(97\)00526-1](https://doi.org/10.1016/S0370-2693(97)00526-1).

[198] A. Bramon, R. Eribano, M. D. Scadron, Eur. Phys. J. C7 (1999) 271–278. doi:[10.1007/s100529801009](https://doi.org/10.1007/s100529801009). [arXiv:hep-ph/9711229](https://arxiv.org/abs/hep-ph/9711229).

[199] S.-U. Chung, et al., Phys. Rev. D 65 (2002) 072001. doi:[10.1103/PhysRevD.65.072001](https://doi.org/10.1103/PhysRevD.65.072001).

[200] A. R. Dzierba, et al., Phys. Rev. D 73 (2006) 072001. doi:[10.1103/PhysRevD.73.072001](https://doi.org/10.1103/PhysRevD.73.072001). [arXiv:hep-ex/0510068](https://arxiv.org/abs/hep-ex/0510068).

[201] S. M. Flatté, Phys. Lett. B 63 (1976) 228. doi:[10.1016/0370-2693\(76\)90655-9](https://doi.org/10.1016/0370-2693(76)90655-9).

[202] M. Ablikim, et al. (BES Collaboration), Phys. Lett. B 607 (2005) 243–253. doi:[10.1016/j.physletb.2004.12.041](https://doi.org/10.1016/j.physletb.2004.12.041). [arXiv:hep-ex/0411001](https://arxiv.org/abs/hep-ex/0411001).

[203] K. L. Au, D. Morgan, M. R. Pennington, Phys. Rev. D35 (1987) 1633. doi:[10.1103/PhysRevD.35.1633](https://doi.org/10.1103/PhysRevD.35.1633).

[204] F. Haas, Two-Dimensional Partial-Wave Analysis of Exclusive 190 GeV  $\pi^- p$  Scattering into the  $\pi^- \pi^- \pi^+$  Final State at COMPASS (CERN), Ph.D. thesis, Technische Universität München, 2014. URL: <https://cds.cern.ch/record/1662589/files/CERN-THESIS-2013-277.pdf>, CERN-THESIS-2013-277.

[205] G. S. Adams, et al. (E852 Collaboration), Phys. Rev. Lett. 81 (1998) 5760–5763. doi:[10.1103/PhysRevLett.81.5760](https://doi.org/10.1103/PhysRevLett.81.5760).

[206] A. Abele, et al. (Crystal Barrel Collaboration), Eur. Phys. J. C 19 (2001) 667–675. doi:[10.1007/s100520100601](https://doi.org/10.1007/s100520100601).

[207] G. Bellini, et al., Phys. Rev. Lett. 48 (1982) 1697–1700. doi:[10.1103/PhysRevLett.48.1697](https://doi.org/10.1103/PhysRevLett.48.1697).

[208] D. V. Amelin, E. B. Berdnikov, S. I. Bityukov, G. V. Borisov, Y. P. Gouz, et al., Phys. Atom. Nucl. 59 (1996) 976–981.

[209] A. V. Anisovich, C. A. Baker, C. J. Batty, D. V. Bugg, V. A. Nikonov, et al., Phys. Lett. B 500 (2001) 222–231. doi:[10.1016/S0370-2693\(01\)00089-2](https://doi.org/10.1016/S0370-2693(01)00089-2). [arXiv:1109.6433](https://arxiv.org/abs/1109.6433).

[210] P. Eugenio, et al. (E852 Collaboration), Phys. Lett. B 660 (2008) 466–470. doi:[10.1016/j.physletb.2008.01.026](https://doi.org/10.1016/j.physletb.2008.01.026).

[211] C. Adolph, et al. (COMPASS Collaboration), Supplemental Material for Phys. Rev. D 95 (2017) 032004. URL: <http://link.aps.org/supplemental/10.1103/PhysRevD.95.032004>.

[212] J. Biel, E. Bleser, T. Ferbel, D. Freytag, B. Gobbi, L. Kenah, J. Rosen, R. Ruchti, P. Slattery, D. Underwood, Phys. Rev. Lett. 36 (1976) 504. doi:[10.1103/PhysRevLett.36.504](https://doi.org/10.1103/PhysRevLett.36.504).

[213] J. Biel, et al., Phys. Lett. 65B (1976) 291–294. doi:[10.1016/0370-2693\(76\)90185-4](https://doi.org/10.1016/0370-2693(76)90185-4).

[214] G. Cohen-Tannoudji, A. Santoro, M. Souza, Nucl. Phys. B125 (1977) 445–466. doi:[10.1016/0550-3213\(77\)90116-X](https://doi.org/10.1016/0550-3213(77)90116-X).

[215] F. Hayot, A. Morel, A. Santoro, M. Souza, *Lett. Nuovo Cim.* 18 (1977) 185–188. doi:[10.1007/BF02785194](https://doi.org/10.1007/BF02785194).

[216] A. B. Kaidalov, *Phys. Rep.* 50 (1979) 157–226. doi:[10.1016/0370-1573\(79\)90043-7](https://doi.org/10.1016/0370-1573(79)90043-7).

[217] The  $a_1(1260)$  and  $a_1(1640)$  in W.-M. Yao, et al. (Particle Data Group), *J. Phys. G* 33 (2006) 575–576. URL: <http://pdg.lbl.gov/2006/listings/m010.pdf>. doi:[10.1088/0954-3899/33/1/001](https://doi.org/10.1088/0954-3899/33/1/001).

[218] P. Gavillet, et al. (Amsterdam-CERN-Nijmegen-Oxford Collaboration), *Phys. Lett. B* 69 (1977) 119. doi:[10.1016/0370-2693\(77\)90148-4](https://doi.org/10.1016/0370-2693(77)90148-4).

[219] D. M. Asner, et al. (CLEO Collaboration), *Phys. Rev. D* 61 (1999) 012002. doi:[10.1103/PhysRevD.61.012002](https://doi.org/10.1103/PhysRevD.61.012002). [arXiv:hep-ex/9902022](https://arxiv.org/abs/hep-ex/9902022).

[220] M. G. Bowler, *Phys. Lett. B* 182 (1986) 400. doi:[10.1016/0370-2693\(86\)90116-4](https://doi.org/10.1016/0370-2693(86)90116-4).

[221] C. Amsler, N. A. Törnqvist, *Phys. Rept.* 389 (2004) 61–117. doi:[10.1016/j.physrep.2003.09.003](https://doi.org/10.1016/j.physrep.2003.09.003).

[222] R. S. Longacre, *Phys. Rev. D* 42 (1990) 874–883. doi:[10.1103/PhysRevD.42.874](https://doi.org/10.1103/PhysRevD.42.874).

[223] Z.-G. Wang (2014). [arXiv:1401.1134](https://arxiv.org/abs/1401.1134).

[224] H.-X. Chen, E.-L. Cui, W. Chen, T. G. Steele, X. Liu, S.-L. Zhu, *Phys. Rev. D* 91 (2015) 094022. doi:[10.1103/PhysRevD.91.094022](https://doi.org/10.1103/PhysRevD.91.094022). [arXiv:1503.02597](https://arxiv.org/abs/1503.02597).

[225] T. Gutsche, V. E. Lyubovitskij, I. Schmidt, *Phys. Rev. D* 96 (2017) 034030. doi:[10.1103/PhysRevD.96.034030](https://doi.org/10.1103/PhysRevD.96.034030). [arXiv:1706.07716](https://arxiv.org/abs/1706.07716).

[226] M. Nielsen, S. J. Brodsky, *Phys. Rev. D* 97 (2018) 114001. doi:[10.1103/PhysRevD.97.114001](https://doi.org/10.1103/PhysRevD.97.114001). [arXiv:1802.09652](https://arxiv.org/abs/1802.09652).

[227] T. Gutsche, M. A. Ivanov, J. G. Körner, V. E. Lyubovitskij, K. Xu, *Phys. Rev. D* 96 (2017) 114004. doi:[10.1103/PhysRevD.96.114004](https://doi.org/10.1103/PhysRevD.96.114004). [arXiv:1710.02357](https://arxiv.org/abs/1710.02357).

[228] J.-L. Basdevant, E. L. Berger (2015). [arXiv:1501.04643](https://arxiv.org/abs/1501.04643).

[229] J.-L. Basdevant, E. L. Berger, *Phys. Rev. Lett.* 114 (2015) 192001. doi:[10.1103/PhysRevLett.114.192001](https://doi.org/10.1103/PhysRevLett.114.192001). [arXiv:1504.05955](https://arxiv.org/abs/1504.05955).

[230] D. Alde, et al. (IHEP-Brussels-Los Alamos-Annecy(LAPP)), *Phys. Lett. B* 205 (1988) 397. doi:[10.1016/0370-2693\(88\)91686-3](https://doi.org/10.1016/0370-2693(88)91686-3).

[231] H. Aoyagi, et al., *Phys. Lett. B* 314 (1993) 246–254. doi:[10.1016/0370-2693\(93\)90456-R](https://doi.org/10.1016/0370-2693(93)90456-R).

[232] D. R. Thompson, et al. (E852 Collaboration), *Phys. Rev. Lett.* 79 (1997) 1630–1633. doi:[10.1103/PhysRevLett.79.1630](https://doi.org/10.1103/PhysRevLett.79.1630). [arXiv:hep-ex/9705011](https://arxiv.org/abs/hep-ex/9705011).

[233] A. Abele, et al. (Crystal Barrel Collaboration), *Phys. Lett. B* 423 (1998) 175–184. doi:[10.1016/S0370-2693\(98\)00123-3](https://doi.org/10.1016/S0370-2693(98)00123-3).

[234] A. Abele, et al. (Crystal Barrel Collaboration), *Phys. Lett. B* 446 (1999) 349–355. doi:[10.1016/S0370-2693\(98\)01544-5](https://doi.org/10.1016/S0370-2693(98)01544-5).

[235] G. S. Adams, et al. (BNL E852 Collaboration), *Phys. Lett. B* 657 (2007) 27–31. doi:[10.1016/j.physletb.2007.07.068](https://doi.org/10.1016/j.physletb.2007.07.068). [arXiv:hep-ex/0612062](https://arxiv.org/abs/hep-ex/0612062).

[236] P. Salvini, et al. (OBELIX Collaboration), *Eur. Phys. J. C* 35 (2004) 21–33. doi:[10.1140/epjc/s2004-01811-8](https://doi.org/10.1140/epjc/s2004-01811-8).

[237] J. Kuhn, et al. (E852 Collaboration), *Phys. Lett. B* 595 (2004) 109–117. doi:[10.1016/j.physletb.2004.05.032](https://doi.org/10.1016/j.physletb.2004.05.032). [arXiv:hep-ex/0401004](https://arxiv.org/abs/hep-ex/0401004).

[238] M. Lu, et al. (E852 Collaboration), *Phys. Rev. Lett.* 94 (2005) 032002. doi:[10.1103/PhysRevLett.94.032002](https://doi.org/10.1103/PhysRevLett.94.032002). [arXiv:hep-ex/0405044](https://arxiv.org/abs/hep-ex/0405044).

[239] D. V. Amelin, et al. (VES Collaboration), *Phys. Atom. Nucl.* 68 (2005) 359–371. doi:[10.1134/1.1891185](https://doi.org/10.1134/1.1891185).

[240] C. A. Baker, et al., *Phys. Lett. B* 563 (2003) 140–149. doi:[10.1016/S0370-2693\(03\)00643-9](https://doi.org/10.1016/S0370-2693(03)00643-9).

[241] G. S. Adams, et al. (CLEO Collaboration), *Phys. Rev. D* 84 (2011) 112009. doi:[10.1103/PhysRevD.84.112009](https://doi.org/10.1103/PhysRevD.84.112009). [arXiv:1109.5843](https://arxiv.org/abs/1109.5843).

[242] F. E. Close, H. J. Lipkin, *Phys. Lett. B* 196 (1987) 245. doi:[10.1016/0370-2693\(87\)90613-7](https://doi.org/10.1016/0370-2693(87)90613-7).

[243] F. Iddir, A. Le Yaouanc, L. Oliver, O. Pene, J. C. Raynal, S. Ono, *Phys. Lett. B* 205 (1988) 564–568. doi:[10.1016/0370-2693\(88\)90999-9](https://doi.org/10.1016/0370-2693(88)90999-9).

[244] F. Iddir, A. Le Yaouanc, L. Oliver, O. Pene, J. C. Raynal, *Phys. Lett. B* 207 (1988) 325–328. doi:[10.1016/0370-2693\(88\)90584-9](https://doi.org/10.1016/0370-2693(88)90584-9).

[245] S.-U. Chung, E. Klemt, J. G. Körner, *Eur. Phys. J. A* 15 (2002) 539–542. doi:[10.1140/epja/i2002-10058-0](https://doi.org/10.1140/epja/i2002-10058-0). [arXiv:hep-ph/0211100](https://arxiv.org/abs/hep-ph/0211100).

[246] D. V. Amelin, et al., *Phys. Atom. Nucl.* 67 (2004) 1408–1415. doi:[10.1134/1.1777297](https://doi.org/10.1134/1.1777297), [Yad. Fiz. 67, 1433 (2004)].

[247] A. R. Dzierba, et al., *Phys. Rev. D* 67 (2003) 094015. doi:[10.1103/PhysRevD.67.094015](https://doi.org/10.1103/PhysRevD.67.094015). [arXiv:hep-ex/0304002](https://arxiv.org/abs/hep-ex/0304002).

[248] A. P. Szczepaniak, M. Swat, A. R. Dzierba, S. Teige, *Phys. Rev. Lett.* 91 (2003) 092002. doi:[10.1103/PhysRevLett.91.092002](https://doi.org/10.1103/PhysRevLett.91.092002). [arXiv:hep-ph/0304095](https://arxiv.org/abs/hep-ph/0304095).

[249] A. Zaitsev (VES Collaboration), *Nucl. Phys. A* 675 (2000) 155–160. doi:[10.1016/S0375-9474\(00\)00238-4](https://doi.org/10.1016/S0375-9474(00)00238-4).

[250] M. Nozar, et al. (CLAS Collaboration), *Phys. Rev. Lett.* 102 (2009) 102002. doi:[10.1103/PhysRevLett.102.102002](https://doi.org/10.1103/PhysRevLett.102.102002). [arXiv:0805.4438](https://arxiv.org/abs/0805.4438).

[251] P. Eugenio, C. Bookwalter (CLAS Collaboration), *AIP Conf. Proc.* 1560 (2013) 421–423. doi:[10.1063/1.4826808](https://doi.org/10.1063/1.4826808).

[252] S. Grabmüller, Cryogenic Silicon Detectors and Analysis of Primakoff Contributions to the Reaction  $\pi^- \text{Pb} \rightarrow \pi^- \pi^- \pi^+$   $\text{Pb}$  at COMPASS, Ph.D. thesis, Technische Universität München, 2012. URL: <https://cds.cern.ch/record/1492155/files/CERN-THESIS-2012-170.pdf>, CERN-THESIS-2012-170.

[253] A. Afanasev, P. R. Page, *Phys. Rev. D* 57 (1998) 6771–6777. doi:[10.1103/PhysRevD.57.6771](https://doi.org/10.1103/PhysRevD.57.6771). [arXiv:hep-ph/9712388](https://arxiv.org/abs/hep-ph/9712388).

[254] A. P. Szczepaniak, M. Swat, *Phys. Lett. B* 516 (2001) 72–76. doi:[10.1016/S0370-2693\(01\)00905-4](https://doi.org/10.1016/S0370-2693(01)00905-4). [arXiv:hep-ph/0105329](https://arxiv.org/abs/hep-ph/0105329).

[255] C. Adolph, et al. (COMPASS Collaboration), *Eur. Phys. J. A* 50 (2014) 79. doi:[10.1140/epja/i2014-14079-8](https://doi.org/10.1140/epja/i2014-14079-8).

[arXiv:1403.2644](https://arxiv.org/abs/1403.2644).

[256] V. A. Shchegelsky, A. V. Sarantsev, A. V. Anisovich, M. P. Levchenko, Eur. Phys. J. A 27 (2006) 199–205. doi:[10.1140/epja/i2005-10266-0](https://doi.org/10.1140/epja/i2005-10266-0).

[257] C. A. Baker, et al., Phys. Lett. B 449 (1999) 114–121. doi:[10.1016/S0370-2693\(99\)00075-1](https://doi.org/10.1016/S0370-2693(99)00075-1).

[258] F. E. Close, P. R. Page, Nucl. Phys. B 443 (1995) 233–254. doi:[10.1016/0550-3213\(95\)00085-7](https://doi.org/10.1016/0550-3213(95)00085-7). [arXiv:hep-ph/9411301](https://arxiv.org/abs/hep-ph/9411301).

[259] T. Barnes, F. E. Close, P. R. Page, E. S. Swanson, Phys. Rev. D 55 (1997) 4157–4188. doi:[10.1103/PhysRevD.55.4157](https://doi.org/10.1103/PhysRevD.55.4157). [arXiv:hep-ph/9609339](https://arxiv.org/abs/hep-ph/9609339).

[260] P. R. Page, E. S. Swanson, A. P. Szczepaniak, Phys. Rev. D 59 (1999) 034016. doi:[10.1103/PhysRevD.59.034016](https://doi.org/10.1103/PhysRevD.59.034016). [arXiv:hep-ph/9808346](https://arxiv.org/abs/hep-ph/9808346).

[261] A. V. Anisovich, C. A. Baker, C. J. Batty, D. V. Bugg, V. A. Nikonov, et al., Phys. Lett. B 517 (2001) 273–281. doi:[10.1016/S0370-2693\(01\)01018-8](https://doi.org/10.1016/S0370-2693(01)01018-8). [arXiv:1109.6817](https://arxiv.org/abs/1109.6817).

[262] A. V. Anisovich, C. A. Baker, C. J. Batty, D. V. Bugg, V. A. Nikonov, et al., Phys. Lett. B 517 (2001) 261–272. doi:[10.1016/S0370-2693\(01\)01017-6](https://doi.org/10.1016/S0370-2693(01)01017-6). [arXiv:1110.0278](https://arxiv.org/abs/1110.0278).

[263] M. Mikhasek, in preparation, Ph.D. thesis, Universität Bonn, 2019.

[264] M. Zielinski, et al., Z. Phys. C16 (1983) 197–204. doi:[10.1007/BF01571606](https://doi.org/10.1007/BF01571606).

[265] C. F. von Weizsäcker, Z. Phys. 88 (1934) 612–625. doi:[10.1007/BF01333110](https://doi.org/10.1007/BF01333110).

[266] E. J. Williams, Phys. Rev. 45 (1934) 729–730. doi:[10.1103/PhysRev.45.729](https://doi.org/10.1103/PhysRev.45.729).

[267] I. Y. Pomeranchuk, I. M. Shumushkevich, Nucl. Phys. 23 (1961) 452–467. doi:[10.1016/0029-5582\(61\)90272-3](https://doi.org/10.1016/0029-5582(61)90272-3).

[268] A. Halprin, C. M. Andersen, H. Primakoff, Phys. Rev. 152 (1966) 1295–1303. doi:[10.1103/PhysRev.152.1295](https://doi.org/10.1103/PhysRev.152.1295).

[269] M. Zielinski, Acta Phys. Polon. B18 (1987) 455. URL: <http://www.actaphys.uj.edu.pl/fulltext?series=Reg&vol=18&page=455>.

[270] G. Fäldt, U. Tengblad, Phys. Rev. C79 (2009) 014607. doi:[10.1103/PhysRevC.79.014607](https://doi.org/10.1103/PhysRevC.79.014607), [10.1103/PhysRevC.87.029903](https://doi.org/10.1103/PhysRevC.87.029903). [arXiv:0807.2700](https://arxiv.org/abs/0807.2700), [Erratum: Phys. Rev. C87 (2013) 029903].

[271] G. Fäldt, Phys. Rev. C82 (2010) 037603. doi:[10.1103/PhysRevC.82.037603](https://doi.org/10.1103/PhysRevC.82.037603). [arXiv:1005.5672](https://arxiv.org/abs/1005.5672).

[272] M. Zielinski, et al., Phys. Rev. D30 (1984) 1855. doi:[10.1103/PhysRevD.30.1855](https://doi.org/10.1103/PhysRevD.30.1855).

[273] V. V. Molchanov, et al. (SELEX), Phys. Lett. B521 (2001) 171–180. doi:[10.1016/S0370-2693\(01\)01194-7](https://doi.org/10.1016/S0370-2693(01)01194-7). [arXiv:hep-ex/0109016](https://arxiv.org/abs/hep-ex/0109016).

[274] N. Jurisic, L. Stodolsky, Phys. Rev. D3 (1971) 724. doi:[10.1103/PhysRevD.3.724](https://doi.org/10.1103/PhysRevD.3.724).

[275] S. Grabmüller (COMPASS), Int. J. Mod. Phys. A26 (2011) 751–753. doi:[10.1142/S0217751X11052736](https://doi.org/10.1142/S0217751X11052736).

[276] J. Friedrich (COMPASS), AIP Conf. Proc. 1322 (2010) 457–462. doi:[10.1063/1.3542025](https://doi.org/10.1063/1.3542025).

[277] Q. Weitzel, Precision Meson Spectroscopy: Diffractive Production at COMPASS and Development of a GEM-based TPC for PANDA, Ph.D. thesis, Technische Universität München, 2008. URL: [https://cds.cern.ch/record/1493534/files/2008\\_phd\\_weitzel.pdf](https://cds.cern.ch/record/1493534/files/2008_phd_weitzel.pdf), CERN-THESIS-2008-180.

[278] J. Beringer, et al. (Particle Data Group), Phys. Rev. D 86 (2012) 010001. doi:[10.1103/PhysRevD.86.010001](https://doi.org/10.1103/PhysRevD.86.010001).

[279] S. Ishida, S. Hinata, M. Oda, K. Takeuchi, K. Yamada, Prog. Theor. Phys. 71 (1984) 806. doi:[10.1143/PTP.71.806](https://doi.org/10.1143/PTP.71.806).

[280] S. Ishida, K. Yamada, M. Oda, Phys. Rev. D40 (1989) 1497. doi:[10.1103/PhysRevD.40.1497](https://doi.org/10.1103/PhysRevD.40.1497).

[281] T. Maeda, K. Yamada, M. Oda, S. Ishida, Int. J. Mod. Phys. Conf. Ser. 35 (2014) 1460454. doi:[10.1142/S2010194514604542](https://doi.org/10.1142/S2010194514604542). [arXiv:1310.7507](https://arxiv.org/abs/1310.7507).

[282] R. P. Feynman (1973).

[283] I. Larin, et al. (PrimEx), Phys. Rev. Lett. 106 (2011) 162303. doi:[10.1103/PhysRevLett.106.162303](https://doi.org/10.1103/PhysRevLett.106.162303). [arXiv:1009.1681](https://arxiv.org/abs/1009.1681).

[284] J. L. Goity, A. M. Bernstein, B. R. Holstein, Phys. Rev. D66 (2002) 076014. doi:[10.1103/PhysRevD.66.076014](https://doi.org/10.1103/PhysRevD.66.076014). [arXiv:hep-ph/0206007](https://arxiv.org/abs/hep-ph/0206007).

[285] L. Capraro, et al., Nucl. Phys. B288 (1987) 659. doi:[10.1016/0550-3213\(87\)90233-1](https://doi.org/10.1016/0550-3213(87)90233-1), [,703(1987)].

[286] J. Huston, et al., Phys. Rev. D33 (1986) 3199. doi:[10.1103/PhysRevD.33.3199](https://doi.org/10.1103/PhysRevD.33.3199).

[287] T. Jensen, et al., Phys. Rev. D27 (1983) 26. doi:[10.1103/PhysRevD.27.26](https://doi.org/10.1103/PhysRevD.27.26).

[288] D. Carlsmith, et al., Phys. Rev. Lett. 56 (1986) 18. doi:[10.1103/PhysRevLett.56.18](https://doi.org/10.1103/PhysRevLett.56.18).

[289] C. Chandee, et al., Phys. Rev. Lett. 51 (1983) 168. doi:[10.1103/PhysRevLett.51.168](https://doi.org/10.1103/PhysRevLett.51.168).

[290] M. Zielinski, et al., Phys. Rev. Lett. 52 (1984) 1195. doi:[10.1103/PhysRevLett.52.1195](https://doi.org/10.1103/PhysRevLett.52.1195).

[291] B. Collick, et al., Phys. Rev. Lett. 53 (1984) 2374–2377. doi:[10.1103/PhysRevLett.53.2374](https://doi.org/10.1103/PhysRevLett.53.2374).

[292] S. Cihangir, et al. (FERMILAB-MINNESOTA-ROCHESTER), Phys. Lett. 117B (1982) 119–122. doi:[10.1016/S0370-2693\(82\)90886-3](https://doi.org/10.1016/S0370-2693(82)90886-3).

[293] E. N. May, J. Abramson, D. E. Andrews, R. Busnello, J. R. Harvey, F. Lobkowicz, C. A. Nelson, M. N. Singer, E. H. Thorndike, M. E. Nordberg, Phys. Rev. D16 (1977) 1983–1985. doi:[10.1103/PhysRevD.16.1983](https://doi.org/10.1103/PhysRevD.16.1983).

[294] J. Pisut, M. Roos, Nucl. Phys. B6 (1968) 325–352. doi:[10.1016/0550-3213\(68\)90001-1](https://doi.org/10.1016/0550-3213(68)90001-1).

[295] J. L. Rosner, Phys. Rev. D23 (1981) 1127. doi:[10.1103/PhysRevD.23.1127](https://doi.org/10.1103/PhysRevD.23.1127).

[296] I. G. Aznauryan, K. A. Oganesyan, Sov. J. Nucl. Phys. 47 (1988) 1097.

[297] N. Kaiser, J. M. Friedrich, Eur. Phys. J. A36 (2008) 181–188. doi:[10.1140/epja/i2008-10582-9](https://doi.org/10.1140/epja/i2008-10582-9). [arXiv:0803.0995](https://arxiv.org/abs/0803.0995).

[298] N. Kaiser, Nucl. Phys. A848 (2010) 198–217. doi:[10.1016/j.nuclphysa.2010.08.014](https://doi.org/10.1016/j.nuclphysa.2010.08.014). [arXiv:1007.5277](https://arxiv.org/abs/1007.5277).

[299] N. Kaiser (nkaiser@ph.tum.de, private communication, 2013).

[300] C. Adolph, et al. (COMPASS Collaboration), Phys. Rev. Lett. 108 (2012) 192001. doi:[10.1103/PhysRevLett.108.192001](https://doi.org/10.1103/PhysRevLett.108.192001). [arXiv:1111.5954](https://arxiv.org/abs/1111.5954).

[301] P. Jasinski, Analysis of diffractive dissociation of  $K^-$  into  $K^- \pi^+ \pi^-$  on a liquid hydrogen target at the COMPASS

spectrometer, Ph.D. thesis, Johannes Gutenberg Universität Mainz, 2012. URL: <https://cds.cern.ch/record/1493570>, CERN-THESIS-2012-191.

[302] S. Wallner, in preparation, Ph.D. thesis, Technische Universität München, 2020.

[303] Yu. Khokhlov, et al., EPJ Web Conf. 37 (2012) 01029. doi:[10.1051/epjconf/20123701029](https://doi.org/10.1051/epjconf/20123701029).

[304] D. Ryabchikov, et al., AIP Conf. Proc. 1701 (2016) 040020. doi:[10.1063/1.4938637](https://doi.org/10.1063/1.4938637).

[305] I. Kachaev, D. Ryabchikov, EPJ Web Conf. 130 (2016) 04003. doi:[10.1051/epjconf/201613004003](https://doi.org/10.1051/epjconf/201613004003).

[306] D. Riabchikov, I. Kachaev (VES group), PoS Hadron2017 (2018) 033. doi:[10.22323/1.310.0033](https://doi.org/10.22323/1.310.0033).

[307] D. Ryabchikov (VES group, COMPASS), EPJ Web Conf. 212 (2019) 03010. doi:[10.1051/epjconf/201921203010](https://doi.org/10.1051/epjconf/201921203010).

[308] G. Collaboration, Proposal to Jefferson Laboratory PAC30 (2006). URL: <https://halldweb.jlab.org/doc-public/DocDB>ShowDocument?docid=1226>.

[309] H. Al Ghoul, et al. (GlueX), AIP Conf. Proc. 1735 (2016) 020001. doi:[10.1063/1.4949369](https://doi.org/10.1063/1.4949369). arXiv:[1512.03699](https://arxiv.org/abs/1512.03699).

[310] S. Dobbs (GlueX), PoS ICHEP2016 (2017) 1243. doi:[10.22323/1.282.1243](https://doi.org/10.22323/1.282.1243).

[311] S. Dobbs (GlueX), PoS Hadron2017 (2018) 047. doi:[10.22323/1.310.0047](https://doi.org/10.22323/1.310.0047). arXiv:[1712.07214](https://arxiv.org/abs/1712.07214).

[312] A. Austregesilo (GlueX), Int. J. Mod. Phys. Conf. Ser. 46 (2018) 1860029. doi:[10.1142/S2010194518600297](https://doi.org/10.1142/S2010194518600297). arXiv:[1801.05332](https://arxiv.org/abs/1801.05332).

[313] T. Britton (GlueX), EPJ Web Conf. 199 (2019) 01004. doi:[10.1051/epjconf/201919901004](https://doi.org/10.1051/epjconf/201919901004).

[314] M. Battaglieri, et al. (CLAS Collaboration), Proposal to Jefferson Laboratory PAC37 (2011). URL: [http://www.jlab.org/exp\\_prog/proposals/11/PR12-11-005.pdf](http://www.jlab.org/exp_prog/proposals/11/PR12-11-005.pdf).

[315] A. Celentano, Acta Phys. Polon. Supp. 6 (2013) 769–775. doi:[10.5506/APhysPolBSupp.6.769](https://doi.org/10.5506/APhysPolBSupp.6.769).

[316] B. Khazin, Nucl. Phys. Proc. Suppl. 181–182 (2008) 376–380. doi:[10.1016/j.nuclphysbps.2008.09.068](https://doi.org/10.1016/j.nuclphysbps.2008.09.068).

[317] M. N. Achasov, et al., Nucl. Instrum. Meth. A449 (2000) 125–139. doi:[10.1016/S0168-9002\(99\)01302-9](https://doi.org/10.1016/S0168-9002(99)01302-9). arXiv:[hep-ex/9909015](https://arxiv.org/abs/hep-ex/9909015).

[318] M. N. Achasov, et al., Nucl. Phys. Proc. Suppl. 225–227 (2012) 66–68. doi:[10.1016/j.nuclphysbps.2012.02.015](https://doi.org/10.1016/j.nuclphysbps.2012.02.015).

[319] D. M. Asner, et al., Int. J. Mod. Phys. A 24 (2009) 1–794. arXiv:[0809.1869](https://arxiv.org/abs/0809.1869).

[320] A. J. Bevan, et al. (Belle and BABAR Collaborations), Eur. Phys. J. C 74 (2014) 3026. doi:[10.1140/epjc/s10052-014-3026-9](https://doi.org/10.1140/epjc/s10052-014-3026-9). arXiv:[1406.6311](https://arxiv.org/abs/1406.6311).

[321] W. Altmannshofer, et al. (Belle-II) (2018). arXiv:[1808.10567](https://arxiv.org/abs/1808.10567).

[322] R. Aaij, et al. (LHCb), Eur. Phys. J. C73 (2013) 2373. doi:[10.1140/epjc/s10052-013-2373-2](https://doi.org/10.1140/epjc/s10052-013-2373-2). arXiv:[1208.3355](https://arxiv.org/abs/1208.3355).

[323] M. F. M. Lutz, et al. (PANDA Collaboration) (2009). arXiv:[0903.3905](https://arxiv.org/abs/0903.3905).

[324] E. Aker, et al. (Crystal Barrel), Nucl. Instrum. Meth. A321 (1992) 69–108. doi:[10.1016/0168-9002\(92\)90379-I](https://doi.org/10.1016/0168-9002(92)90379-I).

[325] T. A. Armstrong, et al. (E760), Nucl. Phys. B373 (1992) 35–54. doi:[10.1016/0550-3213\(92\)90448-K](https://doi.org/10.1016/0550-3213(92)90448-K).

[326] T. A. Armstrong, et al. (E760), Phys. Rev. D47 (1993) 772–783. doi:[10.1103/PhysRevD.47.772](https://doi.org/10.1103/PhysRevD.47.772).

[327] T. A. Armstrong, et al. (E760), Phys. Rev. D52 (1995) 4839–4854. doi:[10.1103/PhysRevD.52.4839](https://doi.org/10.1103/PhysRevD.52.4839).

[328] G. Garzoglio, et al., Nucl. Instrum. Meth. A519 (2004) 558–609. doi:[10.1016/j.nima.2003.10.089](https://doi.org/10.1016/j.nima.2003.10.089).

[329] U. Wiedner, Prog. Part. Nucl. Phys. 66 (2011) 477–518. doi:[10.1016/j.ppnp.2011.04.001](https://doi.org/10.1016/j.ppnp.2011.04.001). arXiv:[1104.3961](https://arxiv.org/abs/1104.3961).

[330] C. Amsler, et al., Phys. Lett. B342 (1995) 433–439. doi:[10.1016/0370-2693\(94\)01515-E](https://doi.org/10.1016/0370-2693(94)01515-E).

[331] C. Amsler, et al. (Crystal Barrel), Phys. Lett. B355 (1995) 425–432. doi:[10.1016/0370-2693\(95\)00747-9](https://doi.org/10.1016/0370-2693(95)00747-9).

[332] A. Abele, et al. (Crystal Barrel), Phys. Lett. B380 (1996) 453–460. doi:[10.1016/0370-2693\(96\)00574-6](https://doi.org/10.1016/0370-2693(96)00574-6).

[333] A. Abele, et al. (Crystal Barrel), Phys. Lett. B385 (1996) 425–432. doi:[10.1016/0370-2693\(96\)01059-3](https://doi.org/10.1016/0370-2693(96)01059-3).

[334] B. Adams, et al. (2018). arXiv:[1808.00848](https://arxiv.org/abs/1808.00848), CERN-SPSC-2019-003 (SPSC-I-250).

[335] P. Bernard, P. Lazeyras, H. Lengeler, V. Vaghin (1968). doi:[10.5170/CERN-1968-029](https://doi.org/10.5170/CERN-1968-029), CERN-68-29.

[336] W. K. H. Panofsky, W. Wenzel, Rev. Sci. Instrum. 27 (1956) 967. doi:[10.1063/1.1715427](https://doi.org/10.1063/1.1715427).

[337] A. Citron, G. Dammertz, M. Grundner, L. Husson, R. Lehm, H. Lengeler, D. E. Plane, G. Winkler, Nucl. Instrum. Meth. 155 (1978) 93–96. doi:[10.1016/0029-554X\(78\)90190-8](https://doi.org/10.1016/0029-554X(78)90190-8).

[338] K. S. Kölbig, Beta-Term in Wigner's D-Function, CERNLIB-U501, 1989. URL: <https://cds.cern.ch/record/2050877>, CERN Program Library Short Writeups.

[339] D. A. Varshalovich, A. N. Moskalev, V. K. Khersonskii, Quantum Theory of Angular Momentum: Irreducible Tensors, Spherical Harmonics, Vector Coupling Coefficients,  $3nj$  Symbols, World Scientific, Singapore, 1988. doi:[10.1142/0270](https://doi.org/10.1142/0270).

[340] W. C. Davidon, ANL-5990, 1959. doi:[10.2172/4222000](https://doi.org/10.2172/4222000).

[341] W. C. Davidon, SIAM Journal on Optimization 1 (1991) 1–17. doi:[10.1137/0801001](https://doi.org/10.1137/0801001).

[342] R. Fletcher, M. J. D. Powell, The Computer Journal 6 (1963) 163–168. doi:[10.1093/comjnl/6.2.163](https://doi.org/10.1093/comjnl/6.2.163).

[343] R. Fletcher, The Computer Journal 13 (1970) 317–322. doi:[10.1093/comjnl/13.3.317](https://doi.org/10.1093/comjnl/13.3.317).

[344] J. Nocedal, S. J. Wright, Numerical Optimization, 2nd ed., Springer-Verlag, New York, NY, USA, 2006. doi:[10.1007/978-0-387-40065-5](https://doi.org/10.1007/978-0-387-40065-5).

[345] A. Griewank, A. Walther, Evaluating Derivatives: Principles and Techniques of Algorithmic Differentiation, Other Titles in Applied Mathematics, second ed., Society for Industrial and Applied Mathematics, 2008. doi:[10.1137/1.9780898717761](https://doi.org/10.1137/1.9780898717761).

[346] J. Nocedal, Math. Comput. 35 (1980) 773–782. doi:[10.1090/S0025-5718-1980-0572855-7](https://doi.org/10.1090/S0025-5718-1980-0572855-7).

[347] D. C. Liu, J. Nocedal, Mathematical Programming 45 (1989) 503–528. doi:[10.1007/BF01589116](https://doi.org/10.1007/BF01589116).

[348] S. N. Dymov, V. S. Kurbatov, I. N. Silin, S. V. Yaschenko, Nucl. Instrum. Meth. A 440 (2000) 431–437. doi:[10.1016/S0168-9002\(99\)00758-5](https://doi.org/10.1016/S0168-9002(99)00758-5).

[349] I. M. Sitnik, Comput. Phys. Commun. 185 (2014) 599–603. doi:[10.1016/j.cpc.2013.08.001](https://doi.org/10.1016/j.cpc.2013.08.001).

[350] M. R. Hestenes, E. Stiefel, J. Research Nat. Bur. Standards 49 (1952) 409–436. doi:[10.6028/jres.049.044](https://doi.org/10.6028/jres.049.044).